Plasma chemistry modelling of an atmospheric pressure argon plasma jet with air impurities for plasma medicine applications

Proefschrift voorgelegd tot het behalen van de graad van doctor in de Wetenschappen aan de Universiteit Antwerpen te verdedigen door

Wouter Van Gaens

Promotor
Prof. dr. Annemie Bogaerts

Faculteit Wetenschappen
Departement Chemie
Antwerpen 2014

Universiteit
Antwerpen

Universiteit Antwerpen

Faculteit Wetenschappen
Departement Chemie

Plasma chemistry modelling of an atmospheric pressure argon plasma jet with air impurities for plasma medicine applications.

Proefschrift voorgelegd tot het behalen
van de graad van doctor in de Wetenschappen
aan de Universiteit Antwerpen
te verdedigen door

Wouter Van Gaens

Promotor: Prof. Dr. Annemie Bogaerts

Antwerpen, 2014

Dit proefschrift werd geëvalueerd door de promotor, de voorzitter en de leden van de doctoraatscommisie en de doctoraatsjury:

promotor:	Prof. Dr. A. Bogaerts (Universiteit Antwerpen)
commisie:	Prof. Dr. K. Van Alsenoy (Universiteit Antwerpen)
	Prof. Dr. P. Van Espen (Universiteit Antwerpen)
jury:	Prof. Dr. E. Neyts (Universiteit Antwerpen)
	Prof. Dr. Ir. G.M.W. Kroesen
	(Technische Universiteit Eindhoven)
	Prof. Dr. D. O'Connell (University of York)
	Prof. Dr. J.-M. Pouvesle (Université d'Orleans)

Contents

Acknowledgements

First, in this small but certainly not insignificant section, I want to thank everybody who contributed to this thesis in any possible way.

Up till now, prof. Annemie Bogaerts played the most crucial role in my early academic career. She gave me the opportunity to do my bachelor, master and PhD thesis under her supervision. During this period she made me the scientist I am today. By using constructive criticism she pushed me to gain more knowledge and make the good scientific choices. I admire the way she processes all the work that comes with such a large research group and her willingness to always make time for her PhD students, even if her schedule is more than saturated. I will remember especially the many (many!) chances she gave me to visit international conferences.

The Institute for the Promotion of Innovation through Science and Technology Flanders (IWT Flanders) is acknowledged for financial support by means of a fellowship. In this context, I explicitly thank everybody who helped me during the application procedure for this IWT fellowship.

Furthermore, the CalcUA computing facilities of the University of Antwerp are acknowledged.

Next, I want to express my sincerest gratitude to Mark Kushner and his co–workers for inviting me to the University of Michigan, teaching me how to use their codes and to help me when I experienced any problems afterwards. I also thank Mark for the interesting discussions and his advice in general.

Subsequently, the fruitful collaborations with the people of Eindhoven and Greifswald need to be acknowledged. In particular, I feel very grateful for getting to know Peter Bruggeman who was in some ways a second supervisor.

The nice atmosphere at work was also very important for me, especially during difficult moments. I would therefore like to thank all my present and former colleagues from the PLASMANT group. When I think about Evi, Maxie, Axel, David, Wouter, Stefaan, Ming, Maksud, Antonin, Ramses, Wesley, Peter, Tom, Christophe, Stefan and Robby, I know that they became even a little bit more than just colleagues.

Some of them even deserve some extra recognition. Stefan and Tom (supported by Christophe during busy periods) were the best mentors I could have imagined during my bachelor and master thesis, respectively. Further-

more, I am eternally grateful to Péter Simon who transformed from a quiet guy in my office to a key success factor in my PhD, especially regarding technical issues with the numerical simulations. Concerning Robby, who simultaneously started his PhD and whom I shared the office with for four years, I would need at least two extra pages to enumerate the things I learned from him and this is certainly not only work related. Without these people my PhD would have looked completely different.

For a variety of technical, financial and administrative issues at PLAS-MANT I could always count on the excellent help of Luc and Nelly.

Finally, all the people from my personal life deserve my gratitude: those who became good friends during my studies, through KDA or while spending countless hours on the bike.

Evidently, I cannot forget to mention the support I received from my parents (and the rest of the family). First, you encouraged me in the choice for university studies, which was not so evident at that point. Later on, at home, you created the perfect living environment for a PhD student.

My last and deepest thanks is to Stefanie, simply for always being there for me and to put me at ease precisely the way I need it.

Wouter Van Gaens, September 2014

Chapter 1

Introduction

1.1 Atmospheric pressure plasmas

The plasma state of matter is a gas that (partially) consists of free charge carriers, *i.e.* ions and electrons. These free charges make the plasma electrically conductive and strongly responsive to electromagnetic fields and surfaces. This state is normally unstable under the conditions here in the Earth's troposphere where we live (*e.g.* temperature and pressure). Nevertheless, there are a few examples of naturally occurring plasmas such as lightning, flames and the northern light (*Aurora Borealis*). Indeed, energy has to be fed to the plasma in order to sustain it. If the energy source is removed, the ions and electrons will recombine and the plasma will quench in a timescale of nanoseconds up to milliseconds, depending on the conditions.

Thus, plasmas can be created artificially and this is often done by applying an electric field (by means of a powered electrode) in order to accelerate the charge carriers which then gain energy. Moreover, through collisions they form new charged particles and in the cascade that follows a plasma is formed. Depending on the background gas, this plasma also consists of excited atoms and molecules, dissociation products, radicals and photons. This unique feature opens the door to a large variety of useful applications. Among the best known are light bulbs, plasma displays and fusion reactors. There are many different types of artificial plasmas and an important distinction has to be made regarding the thermodynamic equilibrium within plasmas. When all plasma species have a similar temperature, the term LTE or 'Local Thermodynamic Equilibrium' is being used. In this case high temperatures of several thousand Kelvin (or even up to millions of Kelvin) are achieved and the plasma is called 'hot' or 'thermal'. Obviously, this yields very high ionisation degrees or even a fully ionized gas.

However, it is also possible to establish a non-LTE regime where only electrons are highly energetic and the gas is not heated more than a few hundred Kelvin. For example when the electric field is created by applying a radio frequent AC voltage to the electrodes, the electrons will easily be accelerated

due to their small mass but the ions, having a much higher mass, cannot keep up with the quickly alternating field, and remain almost motionless. The energy is then transferred to the heavy particles mainly by elastic collisions. However, the amount of energy that is transferred in a collision between electrons and heavy particles is small, because of the high mass ratio (like a ping-pong ball rapidly hitting a wall). As a result, the electron temperature stays much higher than the heavy particle temperature, or gas temperature. Moreover, the ionization degree stays low and the densities of the neutral species are much higher than of the charged species, causing the neutral chemistry to be extremely important.

The non–LTE regime can easily be maintained at low pressure since the number of collisions is small but at higher pressures (such as atmospheric pressure) the total energy transfer eventually might become significant. Indeed, the minimum electric field to achieve breakdown at atmospheric pressure is typically quite large and to prevent that the plasma becomes unstable and uncontrollable after the discharge is ignited, several techniques can be utilized:

- By covering the electrode(s) with a dielectric material (electrical insulator), charges from the plasma can accumulate on this surface and create a counteracting electric field. The net electric field therefore becomes lower again and the electrons are accelerated less. Because of this charge accumulation, it is not possible to sustain the plasma by a DC voltage but an AC voltage is required. This type of self–controlled plasma source is called a dielectric barrier discharge (DBD). The discharge can be either diffuse (homogeneous) or filamentary depending on the conditions (electrode geometry, operating gas, dielectric material, *etc.*)

- Another way is by miniaturization, the so-called 'micro plasmas'. Micro plasmas are discharges with sizes in the order of micrometre up to millimetre. Due to the high surface to volume ratio, the energy losses of the plasma species to the surrounding are relatively large (compared to the energy gain within the volume).

- Transition to LTE can also be prevented by 'pulsed plasmas'. In these plasma sources the electrons are only accelerated for a short time. In this way the discharge (partially) recombines during the off-period, before a transition can occur.

- Finally, it is possible not to keep the gas confined within the space where the power is deposited. By introducing a flow through the device, the plasma species are simply blown out into the surroundings or towards a target. Therefore, this technique also has the advantage that new applications become possible as the plasma treatment does not necessarily have to occur within the plasma device itself. Note that all 'plasma jets', like those described in this thesis, make use of this technique.

It is important to mention that these methods can also be combined. Indeed, all of them have been utilized in the construction of many different types of low temperature atmospheric pressure plasma jets, especially in the field of biomedical applications, which is the subject of this thesis. Note that low temperature in this context means not more that a few hundred Kelvin and even close to room temperature for therapeutic applications.

The presence of molecular gases like oxygen, water and nitrogen in the plasma (directly in the feed gas and/or by mixing with ambient air when the discharge is blown out of the device) yields small amounts of biologically active species, from short– (ns) to long– (s) lived, most of them are also naturally present in human systems and their biochemical pathways. Besides the charged and neutral species, other plasma agents like electromagnetic fields and (V)UV also interact with the object that needs to be treated. This diversity creates a synergistic effect that cannot be achieved by these components individually.

1.2 Plasma jet devices

1.2.1 Plasma jets reported in literature

Various types of plasma jets with different configurations have been reported [2–16] (and references below), where most of the jets are working with noble gas (helium or argon) mixed with a small percentage of reactive gases, such as oxygen, water or air. In fact, this variety of configurations is one of the major problems in the field; each setup has its own advantages and disadvantages and the slightest difference can have a considerable influence on the plasma chemistry, as will be demonstrated further in this work. As a result, it is very difficult to compare the different experiments performed all over the world and this prevents even faster developments in
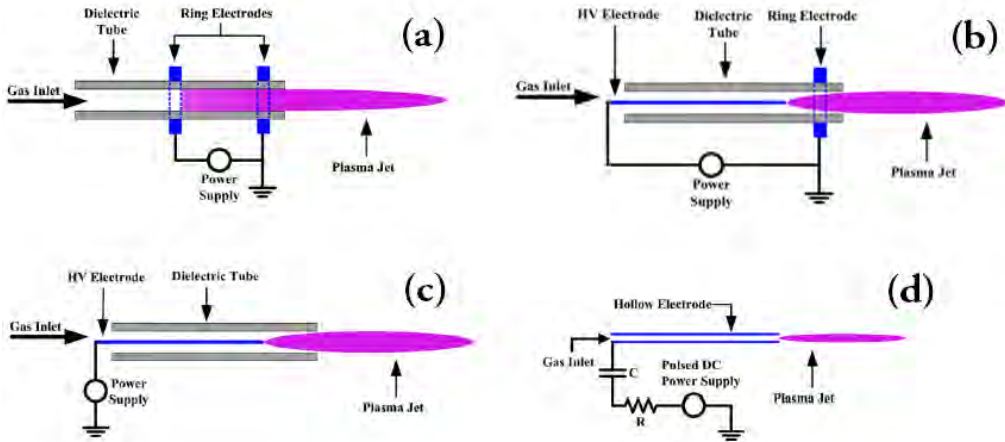
Figure 1.1: Schematics of different plasma jet designs, figures are adopted from [1].

the field.

Especially the electrode setup can be very different, the powered electrode can be either ring-shaped like in figure 1.1(a) – placed around the dielectric tube, which guides the gas flow – or it can be a coaxially placed electrode within the tube like in figure 1.1(b). In the latter case, this electrode can be either a solid pin or a hollow needle (possibly even with a secondary gas feed through its core, besides the gas feed through the dielectric tube). In some cases the powered electrode itself is also covered by a dielectric material. Note that the sharp tip of a needle electrode offers the advantage that it enhances the electric field locally.

Some jets are constructed just with this powered electrode (figure 1.1(c)), but most also feature a grounded ring electrode around the dielectric tube (figures 1.1(a)–1.1(b)) or as a plate in front of the tube exit (positioned perpendicular) with a hole through which the plasma can propagate (see section 1.2.2 below).

Still, when a plasma is to be launched in open space beyond the electrodes where the applied electric field is normally quite low, it is extremely difficult to sustain the plasma. The length of the active plasma region where the density of free charges is still significant is typically about 0.5 to 2 centimetre. However, this distance can be extended by at least half a meter by using flexible catheter-like silicon or polyimide capillaries, making it suit-

able for endoscopic purposes, *e.g.* the plasma gun [17]. Nevertheless, after the plasma propagates through the capillary and it enters the ambient air, the plasma extinguishes at least as fast as without the capillary.
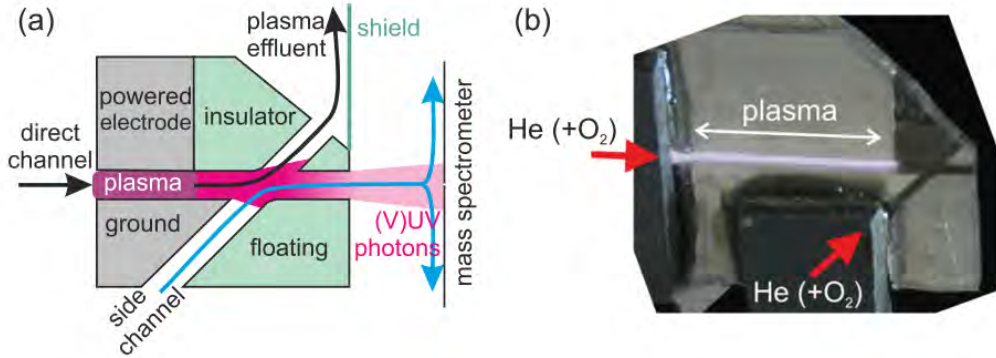
Figure 1.2: Sketch (a) and photo (b) of the X–jet, adopted from [22].
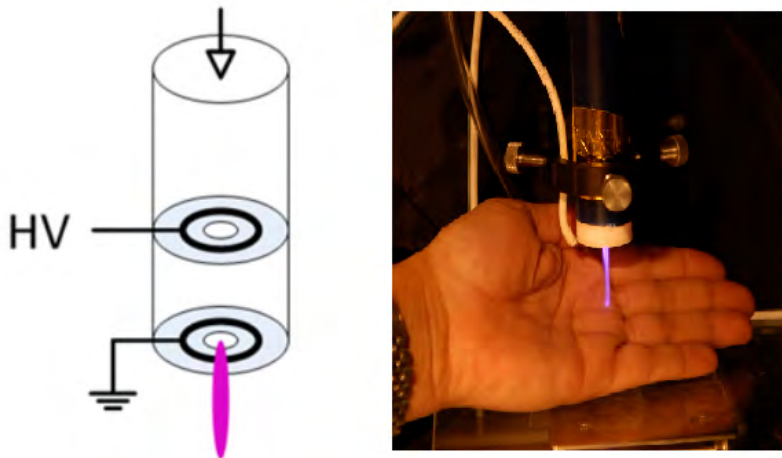
Figure 1.3: Sketch (left) and photo (right) of the plasma pencil, adopted from [23].

Two other important plasma jets have a remarkably different setup, *i.e.* the μAPPJ developed by Schultz-von-der-Gathen and co-workers [18] and the plasma pencil developed by Laroussi and co-workers [19]. The first is designed with two parallel metal plates which act as the electrodes and is primarily developed to easily enable optical diagnostic measurements in

between the electrodes. Furthermore, this group continued with the development of the μAPPJ by constructing the X-Jet (see figure 1.2) which allows the separation of the different plasma components (UV, charged particles and neutrals) [20]. Note that the μAPPJ setup is currently being adapted and tested to act as a benchmark plasma jet device in the framework of the COST Action MP1101 on Bioplasma [21]. This is an important initiative, since it is not likely that all the different research groups will give up their own devices and the associated diagnostics, however, currently they cannot be compared properly.

The plasma jet developed by Laroussi (see figure 1.3) has one of the largest discharge volumes, *i.e.* in the cubic centimetre range. The discharge develops within a cylindrical region, created by two glass disks inserted in a glass tube with the same diameter. By varying the distance between the disks, the discharge gap and volume can be reduced or enlarged. A thin copper ring is attached to the surface of each of the disks and connected to the power supply. Furthermore, both disks are perforated in order to create a flow through these millimetre-sized holes. This yields a plasma jet which is very long (up to 5 cm). Finally, this nanosecond pulsed device is especially important because the phenomenon of 'plasma-bullets' (see below) was first reported for this device [24].

The plasma needle developed by Stoffels *et al* [26] (see figure 1.4) was one of the first devices used for plasma medicine applications. It is part of a category of jets where the dielectric material is only present to guide the gas flow (figure 1.1(c)) or it is simply not present at all (figure 1.1(d)). In the latter design, the gas is fed through a hollow needle that is connected to the power supply in order to create a discharge at the needle tip [27]. Note that this extremely compact hollow needle device is ideally suited to operate in very narrow spaces such as the root canal of a tooth. A variant on this hollow needle device enveloped by an insulating capillary also exists [28].

When bringing a biological sample in close proximity to these needle type jets, a discharge develops between them, since the sample acts as a additional electrode and affects the electric circuit and the electric field orientation. In fact, because of this characteristic, significant currents might go trough the sample and the devices should be used with caution. In order to overcome this problem, a resistor and capacitor are placed between the power supply and the electrode for controlling the discharge current and voltage on the electrode.

In this context, a distinction can be made between direct and indirect
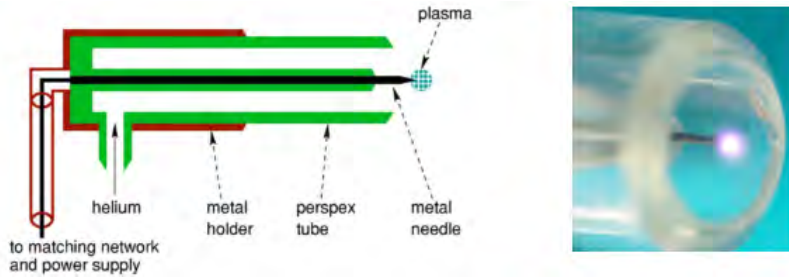
Figure 1.4: Sketch (left) and photo (right) of the plasma needle, adopted from [23].

plasma treatments. When the target is very close to or in contact with the plasma jet a conductive current over the sample can arise, the electric field on the sample might be considerable (electroporation [29]) and ions are not yet recombined, so a significant charged particle flux towards the sample is possible. However, when only the neutral, long living species are important for the application, it might be better to employ indirect treatment, *e.g.* by keeping the distance between the device and the target sufficiently large.

An important disadvantage of plasma jets is that the surface area of the treatment is relatively small, considering that wounds eligible for plasma treatment might be as large as several squared centimetre. Obviously, this could be solved by moving the jet along the treatment area, but this procedure is quite slow. Instead, several jets could be used in parallel, *i.e.* the so-called 1D or 2D jet-arrays, which are for example experimentally studied by Kong et al [30,31]. However, the interaction between the individual jets is very complex and not well studied yet. Some modelling efforts on this topic were performed by Kushner and co-workers [32].

In almost all jets categorized above, power is delivered in a variety of ways: AC (kHz-MHz) and DC, both possibly nanosecond pulsed. In some cases microwaves are being used, *e.g.* [4,33,34]. Note that the microwave driven plasma device of [34] is an atypical plasma jet, as the surface area of the torch is in the order of centimetres in order to cover the surface of wounds entirely (see figure 1.5). To this end, the device is composed of a aluminium cylinder with an inner diameter of 4 mm and contains multiple electrodes. Typical voltage amplitudes are between a few hundred volts and several kilovolts. This operating parameter highly depends on the electrode setup and operating gas, which determine the breakdown voltage, but also on the

Figure 1.5: Photo of the MicroPlaster device (ADTEC Plasma Technology Co. Ltd., Hiroshima/London).

desired plume length, the gas temperature and the plasma intensity, which are required for the different applications (see below). Indeed, sterilization requires for example very large amounts of reactive species, in contrast to 'soft' therapeutic applications such as wound healing or cancer treatment. The typical flow speeds that are being used vary from 0.5 to 10 L/min. Note that the resulting flow velocity on the sample should not be too high. Indeed, *ex-vivo* studies report that (even without plasma) desiccation can be achieved since the protecting media is blown away at the point of contact [35].

Additionally, the flow regime is an issue that is drawing a lot of attention recently. Normally, it can be assessed relatively easily from the Reynolds number whether a flow is turbulent or laminar [36,37]. However, it appears that the electric field applied by the electrodes and the presence of charged plasma species in the jet, result in electrostatic forces that have a considerable influence on the transition point. Obviously, the mixing of ambient gas with the jet is much higher for a turbulent jet and might therefore result in a different chemical cocktail arriving at the sample.

1.2.2 Plasma jets studied in this work

Many of the setups mentioned above are operated with helium as background gas. However, in this work we focus on RF driven argon sources.
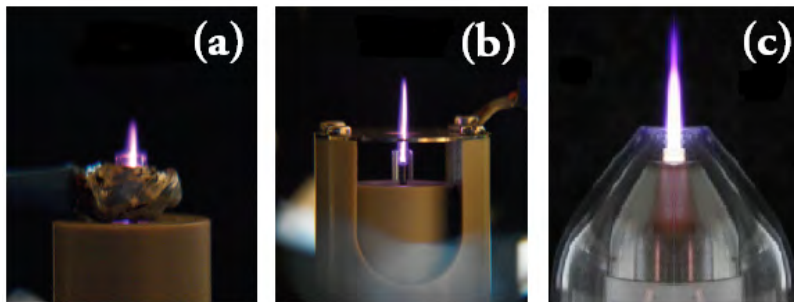
Figure 1.6: Photograph of the different RF driven plasma jets, operated in argon, that are studied in this work: (a) Eindhoven jet with grounded ring electrode, (b) Eindhoven jet with perforated grounded plate electrode in front of the nozzle and (c) the commercial kinpen device including its gas curtain. For all these jets, power is delivered by means of a powered pin electrode coaxially inserted inside the dielectric tube. Note that the scale is not the same for these three pictures; the plasma jet diameter is in all three cases approximately 2 mm.

We evaluated both the non-commercial version developed at the University of Technology in Eindhoven by Bruggeman and co–workers [38–42] (see figure 1.6(a) and (b), chapters 2–5) and the commercially available kinpen (neoplas GmbH, Germany) [43, 44] (see figure 1.6(c), chapter 6). Note that all three jets are variations on the schematic in figure 1.1(b) above. For the plasma jet depicted in figure 1.6(b), the grounded ring electrode around the dielectric tube is replaced by a grounded metal plate in front of the nozzle. A hole in this electrode assures that the plasma jet can freely propagate. This modification yields an electric field that is more in line with the flow direction. Further specifications will be given in the next chapters.

The kinpen device, on the other hand, offers the unique feature that it can be operated with a gas curtain of ‘shield gas’ (*i.e.*, dry air), which yields control over the atmosphere around the active plasma effluent zone. This allows excluding the influence of laboratory conditions (*e.g.* air humidity) and to have better control on the effluent chemistry. Note that comprehensive pre-clinical and first clinical studies have been performed with this device, both *in–vivo* and *in–vitro*, and CE certification has been granted.

There are several reasons why it can be interesting to use argon and not helium. For example, it has been shown for the pulsed and continuous RF plasma jet, operated in argon, that the power density in plasma is larger

(for the same total deposited power), as well as the UV–flux and electron density [39]. Furthermore, the argon plasma jet is the longest and the most contracted, whereas helium plasma jets are usually more diffuse. This all results in a different chemical cocktail and these properties can thus be exploited in terms of the biomedical application. Finally, argon might be more interesting in terms of commercial applications, simply because it is significantly cheaper than helium.

1.2.3 Plasma bullet phenomenon
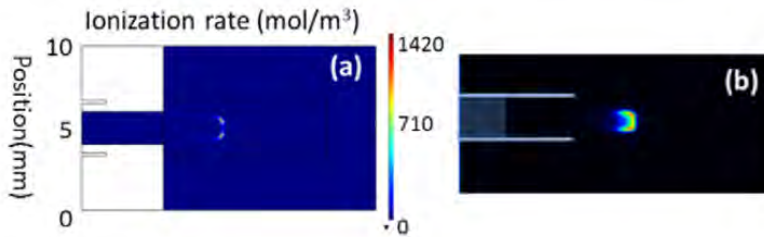
Figure 1.7: Simulation (a) and photograph (b) of a plasma bullet by Liu *et al* [45]

When the existence of 'plasma–bullets' (see figure 1.7) was first detected by very fast imaging cameras [46], it was believed that these were plasma packages travelling individually, hence their name. Because these packages are travelling so fast, *i.e.* several orders of magnitude faster than the gas flow velocity, and since the repetition rate is related to the voltage pulse or AC frequency, they are observed by the naked eye as a continuous plume. It was hypothesized that these bullets propagate by a mechanism of photo-ionization in front of the bullet head, therefore explaining the fast movement.

First numerical efforts by Naidis *et al* proved that these wave fronts indeed propagate at very high speeds through the helium channel that develops in the ambient air, in this case by including a rudimentary photo-ionisation function [47]. Nevertheless, later simulations (all performed for a pre–developed helium channel in ambient air) suggest that photo-ionisation processes might not be crucial for the propagation of these ionization fronts, as the existence of a pre-ionisation channel (created by previous bullets) was sufficient for their propagation [48, 49]. Nevertheless, including the photo-ionisation phenomena does affect the velocity of the ionization wave [50],

although a higher velocity can also be obtained by using a higher degree of pre-ionisation.

Anyway, the development of any ionization wave requires both an electric field high enough in its front (to be able to ionize the gas) and the presence of seed electrons just ahead of the front of the ionization wave. The latter could be caused both 'instantaneously' by photo-ionization or by a pre-ionized channel created by preceding bullets.

Note that the large electric field at the head of the ionization wave is associated with the significant positive space charge of the head compared to the surroundings.

Furthermore, it was shown by Yousfi *et al* that the ionization rate rapidly drops when helium is significantly diluted by air (above 1%) [51]. Therefore, this explains why the mixing of helium with ambient air limits the bullet propagation both in the radial and axial direction. In fact, Breden *et al* suggested that the ionizing cross reactions between helium and air species are crucial for guiding the wave front and that the ionisation is the highest at the edge of the streamer (thus explaining the ring-shaped wave front). Less work has been performed on the actual development of the discharge in the device before transitioning into a streamer or ionisation wave. For some of the modelled setups it was experimentally observed that the ionisation intensity inside the tube is the highest at the inner dielectric surface of the tube (note that the setup is quite similar in most of these modelling papers). As a matter of fact, when Breden et al performed simulations in ambient helium they observed that the plasma (formed within the dielectric tube during the rise time of the voltage pulse) propagated along the surface of the dielectric during the rest of the pulse, without transitioning into a streamer. Similar results were recently obtained by Liu *et al* [45].

Finally, it needs to be mentioned that Kushner and co-workers simulated the propagation of these ionization waves through flexible capillary channels, impinging upon a target, through branched tubes and across different channels, thereby mimicking experiments performed with the plasma gun of GREMI (Orléans) [53–55]. The same research group also studied ionization waves launched from single and multiple plasma jets (pin-electrode setup) after a steady state was obtained for the neutral fluid flow of helium containing 2% oxygen into ambient humid air. Note that this work does include photo-ionization processes. They found that the jets interact through electrostatic, hydrodynamic and photolytic means [56].

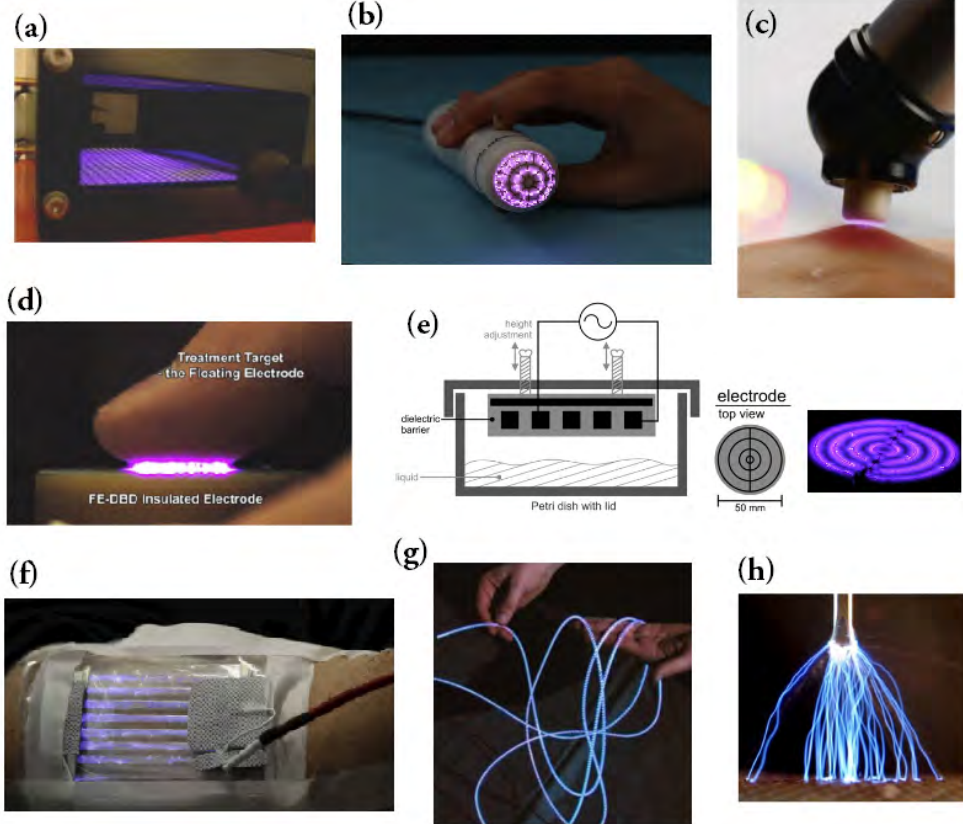Figure 1.8: (a) HandPlaster and (b) MiniFlatPlaster (ADTEC Plasma Technology Co. Ltd., Hiroshima/London), (c) PlasmaDerm (CINOGY GmbH Duderstadt, GE), (d) FE-DBD (Drexel University, Philadelphia, USA), (e) surface DBD and (f) Flexible surface-DBD and (g) bifilar helix electrode configuration (INP Greifswald, GE), (h) needle-to-plane corona (Comenius University, Slovakia). The figures are adopted from [43].

1.2.4 Other atmospheric pressure plasma sources used in plasma medicine

Although many plasma jets mentioned above exhibit DBD-like properties, there is a range of actual DBD devices that do not rely on any gas flow to launch the biologically active particles towards the sample. Moreover, they often operate with atmospheric humid air as the operating gas without the use of noble gases.

In principle there must be at least one electrode covered by a dielectric material but, once more, many variants exist. A clear advantage compared to plasma jets is that large surfaces can be handled, *e.g.* the HandPlaSter [52] (figure 1.8(a)) with a surface micro discharge at the top and the bottom of a partially open device in order to insert objects. Interesting is also the MiniFlatPlaSter (figure 1.8(b)) which incorporates the high voltage power supply inside the device itself and is built for portable usage [57], as does the PlasmaDerm® [58] (figure 1.8(c)).

Also spectacular are the floating electrode (FE–) DBD [59] (figure 1.8(d)) where the sample itself acts as the counter electrode, and the micro plasma arrays [60] where many miniaturized DBD discharges co-operate to enable one homogeneous large area treatment.

A surface-DBD specifically designed for systematic biomedical *in–vitro* experiments in Petri dishes is built by the INP in Greifswald [61] (figure 1.8(e)). This institute also developed several other flexible DBD-devices for treating non-flat surfaces [43] (figure 1.8(f)).

Another DBD-based setup to generate a plasma discharge inside a long flexible tube (like the plasma gun mentioned above) is the bifilar helix electrode configuration around a PTFE tube, creating a discharge inside of several meters long catheters [62] (figure 1.8(g)). This electrode configuration was primarily developed as an alternative construction of endoscopes to guarantee a better decontamination. However, since a plasma plume develops at the end of the catheter, it might also be used for endoscopic treatments like the plasma gun mentioned above.

Finally, we would like to mention the existence of corona discharges suitable for plasma medicine applications, *e.g.* those developed by Machala and co-workers (figure 1.8(h)). Such devices can be used both as a method of direct treatment [63] or as a way to treat a liquid sample [64]. In this context it has to be mentioned that plasma treated water, the so-called 'plasma activated water' (PAW) can retain its antibacterial properties for several days [65].

1.3 Plasma medicine applications

The recent literature on all the different biomedical applications is very large, extremely diverse and multi-disciplinary. Moreover, the number of research groups involved in the field of plasma medicine and the number of papers published in this area keeps growing strongly. However, since the actual biological experiments are beyond the scope of this work, we will only make a short summary here. Indeed, in our research we focus on the complex chemical gas phase reaction kinetics of noble gas/humid air mixtures, yet keeping the applications in mind.

The beneficial effects of plasma are attributed to synergistic effects of the different plasma components, or at least several of them:

- Reactive oxygen and nitrogen species (RONS): The various atoms and molecules generated by the plasma can directly oxidize biomolecules, induce chemical changes in the cell medium (*e.g.* affecting the pH) or trigger a biological response on the cellular/tissue level (*e.g.* induced apoptosis by inflicting some level of DNA-damage [66] or accelerate the wound healing process [67]). The possible effects of the RONS are summarized in an extensive paper by Graves [68].

- UV-radiation: Intense UV-C radiation can enhance the sterilizing effect of the plasma, nevertheless it can be harmful for animals and humans as it induces DNA strand breakages which, if not properly repaired, can lead to cancer. However, the levels of UV-C generated in the devices used for therapeutic applications should be low enough, in order not to have this effect [69]. Additionally, UV radiation itself is known to generate RONS by photolysis in water, especially in the presence of O_3, H_2O_2, HNO_2 and HNO_3 [68].

- Electromagnetic fields: electroporation of cells can occur if the electric field strength is sufficient [29]. Obviously, this might lead to an enhanced delivery of oxidative species or signalling molecules into the cell. This is of course only relevant for direct plasma applications. Furthermore, modest electric fields can even influence the cell signalling pathways by themselves, *e.g.* stimulate release of growth factors which favour cell proliferation and thus the wound healing process.

- Charged species: In principle, high amounts of membrane charging could lead to the rupture of cells or organelles. However, in general, the concentration of neutral species is far larger than that of charged species in these types of plasmas. For indirect plasma treatments the amount of charged species is even negligible. Nevertheless, the superoxide anion, O_2^- is identified as an important species in the biological signalling pathways within an organism, as well as NO_2^-, NO_3^- and $ONOO^-$ [68]. Note, however, that these charged species are also formed in the liquid when neutral molecules like NO, NO_2 and H_2O_2 are transferred from the plasma to the liquid phase [64, 70, 71].

Among the first investigations of plasma interaction with a biological sample, is the work of Fridman and co–workers. The researchers proved that a cocktail of plasma species can enhance blood coagulation by promoting the polymerization of fibrinogen monomers, even in the absence of heat and/or a pH change. Additionally, they also demonstrated sterilization effects of their FE-DBD device [72].

Treatment with cold atmospheric plasma was proven to be highly effective against gram-negative bacteria, gram-positive bacteria, spores, biofilm-forming bacteria [73], viruses [74] and fungi [74]. Nevertheless, experiments showed that cold atmospheric plasmas are far more effective against gram-negative than gram-positive bacteria. The plasma species can cause severe peroxidation of cell membrane components or damage the extracellular polysaccharide matrix in which bacteria are embedded. Additionally, cold atmospheric plasmas have also been used to destroy prions [75]. Therefore, cold atmospheric plasma might fill specific niches that exist in conventional sterilization techniques, *e.g.* areas that are difficult to access, materials that are heat sensitive, *etc.*

This automatically brings us to the application field of dentistry [76]. Indeed, cavities are generally quite difficult to access and heat damage to dental pulp must be prevented. Moreover, dental plaques are clear examples of biofilms that need to be destroyed whereas the use of toxic products has to be avoided. Additionally, plasma treatment offers a new approach for root canal disinfection, which is still one of the major problems in dentistry. This is because conventional techniques often still fail (around 10%) due to the complicated structure of the root canal. Plasma jets, however, are know to propagate relatively easily through such narrow and irregular dielectric channels, possibly even in the surrounding microscopic channels

of the porous dentin tissue. Furthermore, the use of plasma is not limited for antimicrobial purposes but it is also exploited for tooth bleaching and the surface treatment of dental implants, for example to enhance the biocompatibility.

First reports of plasma mediated manipulation of mammalian cells were published by Stoffel *et al* [77, 78]. Experiments *in–vitro* showed that cells could be detached by plasma treatment without a huge loss in viability. Furthermore, the researchers showed for the first time that it is possible to induce apoptosis with plasma. Apoptosis is the normal way of disposing of cells which are old or damaged (under the influence of toxins, oxidative or mechanical stress) or if the DNA can not be repaired properly. Indeed, it has been demonstrated that reactive oxygen species, generated in the plasma, induce double strand breaks in the DNA [79–81], which can thus be correlated to the triggering of apoptosis [82]. Alternatively, apoptosis can also be triggered by targeting the mitochondrial membrane [66, 83], since these cell organelles are primary coordinators of the apoptotic process. Note that very intense plasma treatments might lead to necrosis and the associated severe inflammation in the surrounding tissue. Additionally, the researchers were also the ones taking the first steps towards plasma applications in dentistry (i.e. treatment of dental cavities) by using the plasma as a disinfectant for typical oral bacteria [84] (see above).

The possibility of inducing apoptosis by plasma facilitates a new therapeutic approach for cancer treatment as well. Two recent reviews [85, 86] summarize the many investigations for different tumor cell types, both *in–vivo* and *ex–vivo*. Very interesting is that several studies report a certain degree of selectivity for killing cancer cells compared to normal cells; more information on this can also be found in the latter review.

A significant amount of progress in the field of cancer treatment was achieved by Vandamme *et al* at GREMI (University of Orléans) by means of *in-vivo* and even endoscopic studies with the plasma gun device [87]. Some of their recent work even demonstrates synergistic effects of plasma treatment and classical radiotherapy, where plasma facilitates tumor blood vessel normalization and tissue oxygenation [88].

As already mentioned above, plasmas are not necessarily only destructive. On the contrary, 'soft' plasmas (*i.e.* limited species flux to the target) can be used to stimulate the wound healing process by enhancing endothelial cell proliferation and the angiogenesis process [89]. The treatment of burn wounds is for example studied by Kroesen and co-workers [90].

Nastuta et al [91] related several of the beneficial effects to the reactive oxygen species. Besides, the role of nitric oxide (NO) in different stages of the wound healing process is already known for a long time [92]. Indeed, plasma treatment can provide a method of supplying this species exogenously, in synergy with other plasma effects such as disinfection.

As a result, cold atmospheric pressure plasma treatment is a promising new approach in the area of chronically infected wounds like chronic ulcers [93]. Indeed, this is still one of the major problems in dermatology (in 15% to 20% of the cases healing does not occur, even with optimal care) [94] and might become even more important due to the rising prevalence of diabetes and antibiotic resistance, among other causes. It must be mentioned in this context that higher order organisms (eukaryotic cells) have better resistance mechanisms to withstand external stress caused by reactive oxygen species, and plasma treatment is therefore more harmful for bacteria [95].

In the field of dermatology, plasma treatment also proved to be effective for other skin afflictions, such as eczema [96], Herpes Zoster [97] and Hailey-Hailey disease [98].

Finally, we would like to conclude this section with some safety concerns. There are only few reports on the potential detrimental effects of current, temperature, species toxicity and UV-irradiation, yet to our knowledge they are conclusive on the fact that plasmas are not harmful if the dosage (treatment time and plasma intensity) can be kept below a certain threshold [57, 95, 99, 100]. Limits for gaseous O_3, NO and NO_2, which can be toxic in high concentrations, have not been exceeded. No microscopically detectable histological changes induced by plasma treatment were registered compared with untreated skin up to a depth of several hundreds of micrometre, nor on the cellular level measured by electron microscopy. Finally, the level of UV-C (usually measured in W.m^{-2}) is significantly below the threshold values defined by the authorities.

Several clinical trials with the MicroPlaSter device (Adtec) have been concluded after extensive testing on hundreds of patients in German hospitals [97, 101]. Moreover, the PlasmaDerm® device is currently undergoing official clinical trials in Germany [96] as well. Furthermore, the kinpen device received CE marking (for electromagnetic compatibility), thus fulfilling the EU consumer safety, health or environmental requirements [99].

1.4 Aim of this thesis

Due to the diversity of the plasma devices and the generated plasma agents, a lot of studies and many different techniques are required, so that the efficiency and safety of the technology can be improved.

Important is that not all information can be acquired by experimental techniques alone, for example, because species densities might be below the detection limit, because some areas in the setup are difficult to access or when the method itself is influencing the plasma significantly. Furthermore, experimental measurements are expensive and time consuming. Numerical simulations, on the other hand, can offer a large amount of valuable information relatively fast and cheaply, once they are thoroughly benchmarked. The goal of this thesis is therefore to construct a chemical model that is able to mimic argon APPJs. By examining three different plasma jets with a commonly used electrode configuration, our work should cover a considerable part of the different APPJs that are currently being employed. The final goal is to find both differences and similarities in the resulting plasma chemistry when varying the device geometry or the operating conditions.

Chapter 2

Model Description

Preface

In this chapter we describe the features of the numerical model used in this thesis and present the $Ar/O_2/N_2/H_2O$ reaction chemistry set we developed, including a case study. This chapter is based on our paper published in 2013 which was, to our knowledge, the first with such an extended argon/humid air chemistry focussing on the formation of biomedically active species, *i.e.* N, O, OH, $O_2(^1\Delta_g)$, O_3, H_2O_2, N_xO_y, H_xNO_y, O_2^-. Most of them are identified as possibly important reactive oxygen species (ROS) and reactive nitrogen species (RNS), as reported in a recent review by Graves [68].

Since many different plasma jet configurations exist [1], it is difficult to come up with a general model, valid for all configurations. The way the power is deposited, the position of the plasma jet nozzle exit, the speed of humid air diffusion into the noble gas stream, different gas flow speeds and so forth, all influence the chemistry significantly. Therefore, our zero-dimensional (0D) model is used in a semi-empirical way to mimic the experimental conditions. In this chapter we use the plasma jet device developed by Bruggeman and co-workers [38] and the experimental conditions of [40] as a basis.

2.1 Overview of related modelling

Most of the numerical work in the field of plasma medicine is based on the 0D reaction kinetics approach (hence volume averaged) or on the 1D– and 2D–fluid approach.

0D or global models offer the advantage over more sophisticated models that they enable one to analyse the most important chemical phenomena, while maintaining the computational load low. Eliasson and Kogelschatz [102,103] used this numerical technique to describe the chemistry of ozone formation in an oxygen discharge at high pressure and low temperature. One year later, the same authors also clarified ozone generation for dry air conditions [104], upgrading the previous reaction scheme containing 70 collisions and 16 species to 143 collisions and 30 species. This dry air chemistry was further expanded in the work of Kossyi *et al* [105] who proposed a set of 450 electron impact and heavy particle collisions. A few years later, a humid air plasma chemistry was reported by Gentile and Kushner [106], in which a total of 400 reactions and 56 species were considered. More importantly, these authors focussed on N_xO_y plasma remediation, and many of these species also play an important role in biomedical applications. During the 90's and early 00's a series of publications containing chemical kinetic reference data was published by several authors affiliated to the National Institute of Standards and Technology (NIST, Maryland, US) [107–115, 188]. In this way the most important data for non-thermal humid air plasmas became easily accessible (additionally it also contains carbon based particles).

More recently, this knowledge was further used for modelling non-thermal atmospheric pressure micro discharges used in plasma medicine applications. Indeed, dry or humid air is sometimes used directly as the main background gas, usually with DBD configurations. Two modelling studies, with a specific focus on the plasma chemistry, were recently published by Sakiyama *et al* [116] and Babaeva *et al* [117]. The first one concerns two coupled zero-dimensional (0D) models to describe a surface micro discharge with 50 species and 600 reactions. One of the 0D models describes the plasma zone near the electrodes, with a high electric field and thus comprises balance equations for both neutral and charged species, whereas the other model only describes the neutrals and highlights the chemistry of the long-lived species. The model of Babaeva provides more insight in the effect of filaments on the chemical formation of species and the particle fluxes towards wounded skin. For this purpose the results of a 2D fluid model were used

as input for a 0D model calculation and vice versa. The 2D fluid is able to describe streamer development in air between the electrode and the tissue which acts as a floating electrode, however, only for short timescales due to the computational load [29,118]. The 0D model is used in a complementary way to evaluate what chemical species are formed on the long term from the short-lived chemical species created in the streamers simulated in 2D. Also interesting is that the authors included a cellular structure in the model, mimicking actual skin tissue, and looked at the induced electric fields in the context of electroporation. Later, this work was extended to wounds covered by liquid, possibly containing blood platelets [119].

Similarly, Naidis coupled his 2D fluid model describing the streamer or 'bullet' behaviour of the He plasma jet (see 1.2.3 in the previous chapter) with a small 0D kinetics model (He/H_2O) for describing the OH radical production mechanism inside the device, thus not in the effluent [120]. Since recent modelling efforts concerning the plasma bullet phenomenon were already summarized in the previous chapter, this will not be repeated here.

An interesting 0D numerical study was reported by Liu *et al* [121] with a much larger He/H_2O chemistry set containing 46 species and 577 reactions. In this publication, the authors also suggest several reduced chemistries that can be used to run complex simulations faster.

An example of such a model is the work of Waskoenig *et al* [122] for a He/O_2 mixture with 16 species and 116 reactions. This code was developed to comprise chemical and physical phenomena across the gap between the two parallel plate electrodes (hence 1D) of a micro-scaled radio-frequency driven atmospheric pressure plasma jet device (μAPPJ), designed for plasma medicine applications. Results of a similar model were reported by McKay *et al* [123] but with the addition of water to the helium-oxygen mixture. In this study, a very large reaction chemistry set of 61 species and 878 reactions was implemented in the 1D fluid model.

As mentioned in the previous chapter, the μAPPJ can be used in the X–jet configuration to separate reactive species from UV [20, 22]. For this setup, a 2D fluid model was used to describe the neutral gas flow and a few chemical reactions were integrated to evaluate the density of O atoms and O_3 produced in the effluent. However, no actual plasma chemistry (electron kinetics) was included.

The chemistry of the μAPPJ was further studied by Murakami *et al* [124–126], by means of a global model. The lower complexity of the latter enabled these authors to do a faster kinetic analysis of a He/O_2/N_2/H_2O/CO_2

mixture with 59 species and 1048 reactions.

Another plasma medicine tool that has been studied numerically is the plasma needle, initially by Brok *et al* and later by Sakiyama and Graves. Brok was the first one to model in 2D (in the field of plasma medicine at least) and his simulations ran for a fixed He/N_2 gas ratio over the entire simulation domain, neglecting the gas flow and using only a limited plasma chemistry [25]. The approach of Sakiyama and Graves was similar, yet already more advanced as they used an unstructured mesh (and not a Cartesian mesh like in Brok's work) which enabled a high resolution close to the needle electrode tip. Therefore, these authors were able to model the sheath accurately and they found that the corona discharge at low power exhibits a transition to a glow discharge at a critical power, spreading back along the needle surface [127, 128]. Consequently, they studied this discharge type with an asymmetric electrode in a more fundamental way in 1D spherical coordinates, *e.g.* looking at the validity of the local field approximation, the influence of nitrogen impurities and secondary electron emmission [129, 130]. Finally, they published the results of a 2D fluid calculation that considered the neutral gas flow (*i.e.* ambient air diffusion, here represented by N_2) [131].

The only other numerical study of an argon plasma jet was recently published by Schmidt-Bleker *et al* [132] for the kinpen device. They used a relatively simple 0D approach, combined with a reduced reaction scheme, to model the chemistry of the effluent without including the electron dynamics. Using some of our findings reported later in this chapter, they assume that reactive species (*e.g.* O radicals, nitrogen metastables and OH radicals) mainly originate from collisions of argon metastables and excimers with O_2, N_2 and H_2O. Subsequently, long-lived species like O_3 and NO_2 are formed in the effluent. The authors used a certain initial density for the argon species that best matched their FTIR measurements. By varying the shield gas humidity and composition (*i.e.* O_2/N_2 ratio) they obtained valuable insights regarding the chemistry of the plasma jet effluent.

Up to this point only gas phase simulations were enumerated, however, biological samples are usually covered by a liquid medium. The chemical cocktail in the gas phase is not necessarily the same after the gas phase species are transferred to the liquid phase. This has been studied by global models as well [71, 133], implementing a set of liquid phase reactions and their associated rate constants. In the work of Hamaguchi [133] the flux of reactive oxygen and nitrogen species towards the liquid (*i.e.* the initial

conditions for the 0D model of the liquid) is estimated, based on their typical gas phase concentrations in a representative plasma medicine device and on the Henry's Law constant, which determines how easily a species dissolves in water. In the work of van Gils *et al* [71] the flux is determined using an optimization algorithm to find the values at which the end concentrations of nitrate and nitrite correspond to the values found in the ion chromatography measurements of the plasma treated liquid. These works yield very interesting insights, for example, it was found that pH can affect the liquid chemistry drastically and therefore has a considerable impact on the bactericidal effect.

The interaction of plasma with a thin water layer was even simulated in 2D by Tian and Kushner. The water layer (with liquid phase chemistry) is represented by an extremely dense gas and is separated from the actual gas phase (with gas phase chemistry) by a boundary layer. Transport of RONS across this boundary is allowed according to Henry's Law constant. Even water evaporation from the liquid layer and photolysis of water molecules into OH_{liq} (triggered by photons created in the plasma above the liquid layer) was taken into account. The authors also found that ROS are readily consumed by hydrocarbons in the liquid, thus affecting their concentrations. Finally, it is worth mentioning a completely different type of modelling in the field of plasma medicine, *i.e.* molecular dynamics. With this technique (at least when implementing an appropriate reactive force field) interaction mechanisms between the plasma species and biological cells can be studied on a more fundamental (atomic) level. In our research group Yusupov *et al* investigated the interaction of OH, H_2O_2, O, O_3 with peptidoglycan which is a key building block of the bacterial cell wall [134,135] and evaluated if this leads to the destruction of this biomolecule. Furthermore, they examined the interaction of several reactive oxygen species with water, whether they can travel through the water layer and if they eventually reach the surface of biomolecules [136]. The interaction of O and OH radicals with lipids, more specifically with α-linolenic acid as a model for the free fatty acids present in the upper skin layer was investigated by Van der Paal *et al* [137]. A good review on such atomistic simulations for plasma–biomolecule and plasma–tissue interactions was recently published by Neyts *et al* [138].

In this thesis we make use of a zero-dimensional (0D) reaction kinetics model to describe the chemical processes for an argon plasma jet including the behaviour of humid air components. It is in many aspects different from any of the models cited above.
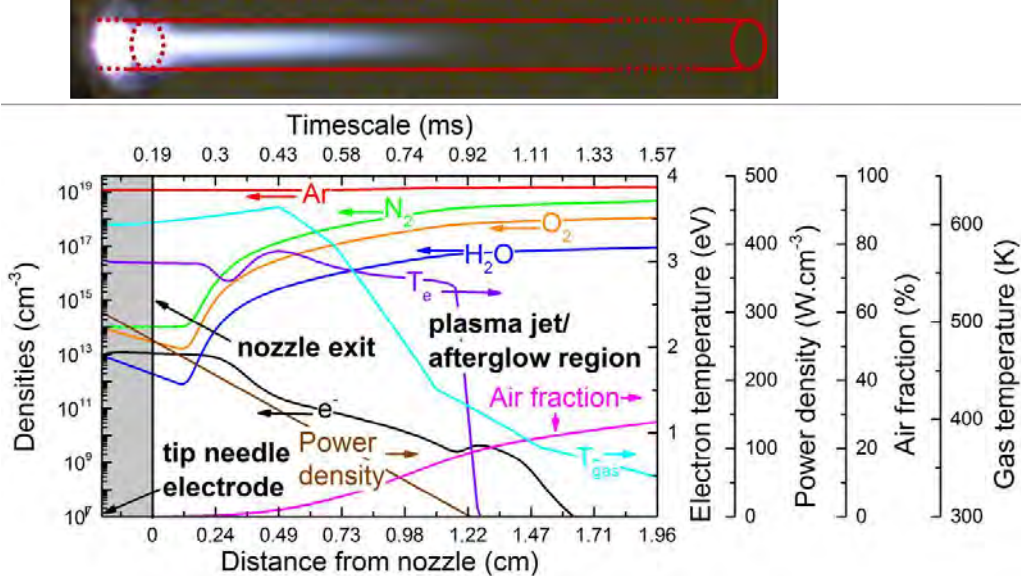
Figure 2.1: Plasma characteristics as a function of the distance from the nozzle, along the plasma jet axis. The profiles of the power deposition, gas temperature and humid air densities/fractions in argon due to diffusion are fitted to experimental values, whereas the average electron energy (T_e) and electron density (e^-) are calculated values. The interior of the plasma jet device is represented by the grey area, beginning at the needle electrode tip. This zone ends at the nozzle exit (indicated with axial position = 0 cm) and is followed by a region where the plasma jet propagates into ambient air. Approximately at 1.2 cm from the nozzle exit, when the power density dropped to zero, the plasma jet becomes an afterglow. Note that the time and distance dimensions are correlated with an externally calculated velocity profile.

2.2 Model description

The model is based on the Global_Kin code, developed by Kushner and co-workers [139], which we modified to be able to fit certain plasma properties to experimental values. Thus, the model can be considered to be semi-empirical.

2.2.1 Pseudo-one-dimensional plug flow

First of all the 'pseudo-one-dimensional plug flow' approximation will be discussed. In this way it is possible to represent the time dependent evolution of species densities (as is typically the case in a 0D model) as a spatial dependence, hence, as a function of the position in the plasma jet device and effluent. This approach was previously successfully applied in [140] for a He/O_2 discharge. We assume that the tube of the plasma jet device, the plasma jet itself and the afterglow region in the far effluent can be represented by a long cylinder (see figure 2.1), where constant atmospheric pressure conditions rule. The magnitude of the flow velocity determines the change of position of a volume averaged (0D) plug element, *i.e.* a cylindrical segment, along the jet stream. In our approach, we assume that axial transport of mass and energy due to drift and concentration gradients is negligible in comparison to axial transport by convection. Furthermore, no species transport in the radial direction is considered in this approach. Due to the very high axial flow speed (typically in the order of 10^3 cm.s^{-1}) compared to the radial flow speed, this seems acceptable for the first few cm's after the nozzle exit. As an additional source of information, not only the length scale is plotted in figure 2.1 but also the corresponding time scale. Note that this time scale is within the millisecond range, which is not much longer than the time-scales necessary for the formation of long–lived species formation processes, but is much shorter than the typical operating duration of DBD discharges with a stationary gas [116, 117]. We want to stress once more that the original dependency in our 0D model is density versus time and that the distance dependency is not an extra dimension solved by the equations.

Evidently, the flow velocity should decrease along the jet symmetry axis. This is due to gas expansion and obstruction by the relatively stationary surrounding atmosphere. Therefore, the gas flow velocity was fitted to the

fluid dynamics simulation results that we performed with a 2D fluid dynamics model [141], as a function of the distance from the nozzle exit. This 2D fluid simulation only considers the neutral background gas species (Ar, O_2, N_2, H_2O), thus electric field forces of the plasma have no influence on the flow field calculation.

The relation between the time scale and the length scale is thus not simply the initial velocity at the nozzle exit as a constant factor (*i.e.* 2900 cm.s^{-1} as determined by the pressure, temperature, cross section of the device and flow rate of the feed gas), but the time correlates with position through the variable flow speed, *i.e.* a non-linear decreasing value along the jet effluent obtained from the 2D fluid model.

2.2.2 Species continuity equation

The following continuity equation is solved for all plasma species included in the model (see tables 2.1 and 2.2 below):

$$\frac{dn_i}{dt} = \sum_j \left[\left(a_{ij}^R - a_{ij}^L \right) k_j \prod_l n_l^L \right] + S_{\text{diff}}(i) \qquad (2.1)$$

$$(\text{with } S_{\text{diff}}(i) = 0 \text{ if } i \neq \text{Ar}, N_2, O_2 \text{ or } H_2O)$$

where n_i is the density of species i, a_{ij}^R and a_{ij}^L are the right-hand side and left-hand side stoichiometric coefficients of species i in reaction j, k_j is the reaction rate coefficient and n_l^L is the density of the lth species in the left-hand side of reaction j. All these coefficients are input values, obtained from literature, according to a predefined reaction scheme (see Appendix A). Note that each new time step dt describes the length of the next volume averaged segment of the plug flow cylinder. In addition, since fluid dynamics are not included in this model, the humid air diffusion (from the surroundings into the argon flow) is handled by adding a production/loss term, S_{diff}, for Ar, N_2, O_2 and H_2O. This makes that argon is gradually being replaced by a humid air mixture starting from the nozzle exit. Of course, these artificial source terms will vary along the jet effluent. In this way, the mixing speed used in our calculations, can be adapted to obtain the same impurity levels as experimentally measured. These experimental data, as a function of distance from the nozzle, are taken from literature [22, 142]. Moreover, our 2D fluid dynamics simulations confirm the reported impurity measurements. The simulated profile of the humid air fraction in argon can be seen

in figure 2.1.

2.2.3 Electron energy density equation

In the model electrons are assumed to be mainly heated by Joule heating, under the influence of an electric field. The time evolution of the electron energy is calculated from

$$
\begin{aligned}
\frac{d}{dt}\left(\frac{3}{2}n_e k_b T_e\right) \;=\; & \overrightarrow{j}\cdot\overrightarrow{E} + \sum_l n_e k_l N_l \Delta\varepsilon_i \\
& - \sum_i \frac{3}{2}n_e \nu_{mi}\left(\frac{2m_e}{M_i}k_b\left(T_e - T_i\right)\right)
\end{aligned}
\tag{2.2}
$$

where n_e is the electron density, k_b is Boltzmann's constant, T_e is the electron temperature, $\overrightarrow{j}$ and $\overrightarrow{E}$ are the current density and the electric field in the discharge, k_l is the reaction rate coefficient for the lth electron impact process, N_l is the density of the gas phase collision partner and $\Delta\varepsilon_i$ is the corresponding change in the electron energy. ν_{mi} is the electron momentum transfer collision frequency with species i , m_e is the electron mass and T_i and M_i are the temperature and mass of species i. In an experimental setup, the value of the electric field throughout the plasma jet is greatly dependent on the applied electrode voltage, the electrode configuration, *etc.* Moreover, it fluctuates in time. Unfortunately, this complexity cannot be captured by a 0D kinetics model. Therefore, the Joule heating term is determined by an estimated power deposition density (W.cm^{-3}) which is also an input parameter in our model. The temporal/spatial evolution of this input value is given in figure 2.1. This profile is assuming a maximum power density at the needle electrode tip at 2 millimetres before the nozzle exit, *cf.* the experimental setup [38], and the value decreases linearly along the plasma jet flow. Note that the electron density is about one order of magnitude smaller than reported in the experimental work performed for this device, with a maximum value of 10^{13} cm^{-3}. However, this can be understood because our simulations are spatially averaged over the cylinder segment, whereas in the experiment local densities are measured. Furthermore, processes that can generate extra electrons, for example secondary electron emission at the needle electrode tip, can not easily be included in this simple model.

Finally, propagating ionisation wave fronts, *i.e.* the so–called plasma bullets with photo-ionisation as an additional electron source (see chapter 1), can not be taken into account either, but might result in a higher electron density as well.

To measure the power deposition profile further from the needle tip is highly non-trivial. We know, however, from literature that plasma jets typically show UV-*vis* light emission over a distance in the order of maximum a few cm. For the experimental conditions of [40], which we attempt to mimic, light can be observed until 1.2 cm after the nozzle exit. Since our calculations predict that the electron density and excited state densities rapidly drop when the power deposition becomes small, we adopted a power density profile that linearly goes to zero at 1.2 cm in our case study, see figure 2.1. It should be noted that the total power deposition in the model is exactly matching the experimental value. The resulting value of the electron temperature (also see figure 2.1) is only slightly higher than the values reported in literature, typically around 1 - 2.5 eV [144, 145]. This is expected since the electron density is probably somewhat underestimated (see above), thus the same power is distributed over fewer electrons.

The electron energy value, calculated from equation 2.2, is used to determine the reaction rate coefficients for most electron impact reactions. For this purpose a look-up table of these coefficients as a function of a wide range of electron temperatures is constructed by an internal Boltzmann equation solver using electron collision cross sections obtained from literature (see Appendix A). It is important to mention that these look-up tables need to be regularly updated by running the Boltzmann code again, because of the drastic change in background gas composition due to humid air diffusion. In practice, in our model the Boltzmann solver was updated every 10 μs, for a typical time step of the calculations of 0.1 ns.

2.2.4   Gas temperature

The gas temperature is very important for the formation of biomedically important species from humid air components. A good example is the depletion of atomic oxygen either by ozone formation or NO_x formation, dependent on the temperature [146]. In a needle type plasma jet the gas temperature typically varies largely, both in the radial and axial direction, as demonstrated in [40]. Indeed, the gas temperature can be – in terms of

biomedical applications – quite high close to the needle tip. Nevertheless, it will also drop quickly in the next few millimetres. To mimic the experimental conditions of [40] accurately, the gas temperature profile is fitted to the experimentally measured values. More details on the fitting method can be found in chapter 4. This gas temperature profile is illustrated in figure 2.1 as well.

Note that the jet can also operate at lower power regimes and this results in a lower gas temperature. In this way the device would be even more suitable for direct therapeutic applications, where the distance between the device and the object can only be a few millimetres. We will show results of our simulations at lower gas temperatures in the next chapter.

It should be mentioned that gas heating can also be calculated by the model itself, simply from the reaction enthalpy, and this resulted in similar values as obtained in the experiment, up till 5 millimetres from the nozzle exit. However, beyond that distance, the calculated gas temperature decreases much more slowly than the experimentally obtained profile. Naturally, this is caused by the fact that our model does not capture cooling processes like gas expansion and diffusion of cold surrounding air into the plasma jet. Therefore, we decided to perform the simulations for the gas temperature profile shown in figure 2.1.

Finally, it is worth to mention that our model adjusts the gas species densities for gas temperature changes while maintaining constant pressure, assuming ideal gas law. Nevertheless, this effect proved to have only a small influence on the formation of biomedical species.

2.2.5   Reaction chemistry

Since we are mainly interested in the biomedically active components, often present at ppm levels or even lower, we have to take a very large chemistry set into account. However, at some point a decision has to be made about which species should be included and which will be neglected. Species containing carbon – created out of atmospheric CO_2 – were for example not taken into account. Furthermore, species can sometimes not be included because their corresponding reaction rate coefficients are uncertain or even unknown at all. The species that are included in the model are presented in table 2.1.

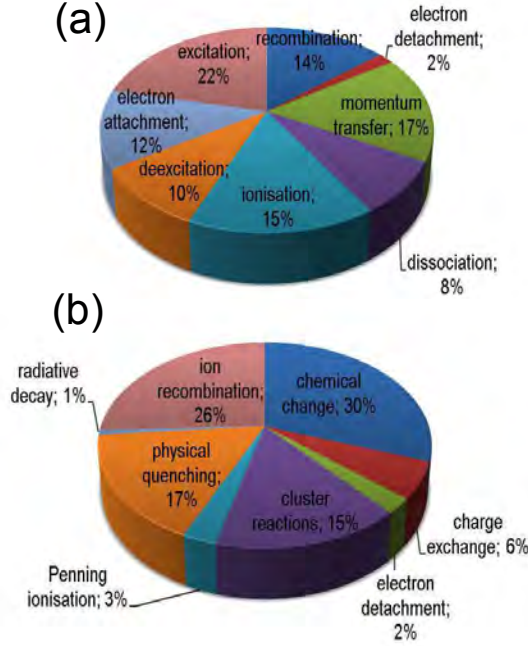Several electronically, rotationally and vibrationally excited states are in-

Figure 2.2: Different reaction types included in the model for (a) electron impact collisions and (b) heavy particle reactions, with their relative contributions to the reaction set.

cluded in our model. Electronically excited states are important to consider because they often play a crucial role in the plasma chemistry, for example in stepwise electron impact or Penning ionization. Note that, at atmospheric pressure, due to a high collision frequency, it is unlikely that high electronic energy levels become populated and therefore these are not included. Rotational and vibrational excitations, on the other hand, are important processes since these reactions affect the electron energy distribution function significantly. Note that in this reaction set, rotationally and vibrationally excited states only participate in electron impact excitation and de-excitation reactions, as well as in physical quenching by the background gas. The reason is that the rotational and vibrational energy at atmospheric pressure is usually too low to induce a chemical change in its collision partner. We would like to point out that, if a particle has multiple vibrational states, they are all grouped in one species in our model.

We consider three factors for the selection of excited states in our model:

Table 2.1: Plasma species included in the model

Ground state neutrals	Excited state neutrals	Charged species
Ar	$Ar(^4S[^3P_2])$, $Ar(^4S[^3P_1])$, $Ar(^4S[^3P_0])$, $Ar(^4S[^1P_1])$, $Ar(^4P)$ [a], $Ar_2^*(a^3\sum_u^+)$	e^-, Ar^+, Ar_2^+, ArH^+
N, N_2	$N(^2D)$, $N_{2,rot}$, $N_{2,vib(1-8)}$, $N_2(A^3\sum_u^+)$, $N_2(a'^1\sum_u^-)$	N^+, N_2^+, N_3^+, N_4^+
O, O_2, O_3	$O(^1D)$, $O_{2,rot}$, $O_{2,vib(1-4)}$, $O_2(a^1\Delta_g)$, $O_2(b^1\sum_g^+)$	O^+, O_2^+, O_4^+, O^-, O_2^-, O_3^-
NO, NO_2, N_2O, NO_3, N_2O_3, N_2O_4, N_2O_5	$N_2O_{vib(1-3)}$	NO^+, NO_2^+, NO_2^-, NO_3^-
H, H_2, OH, H_2O, HO_2, H_2O_2	H^* [b], $H_{2,rot}$, $H_{2,vib(1-2)}$, H_2^* [c], OH(A), $H_2O_{vib(100,010,001)}$	H^+, H_2^+, H_3^+, OH^+, H_2O^+, H_3O^+, H^-, OH^-
NH, HNO, HNO_2, HNO_3, HNO_4		

[a] This species groups the electronically excited states ^4P, ^5D, ^5S and ^5P
[b] This species groups the electronically excited states with n=2-4
[c] This species groups the electronically excited states $(b^3\sum_u^+)$ and $(c^3\Pi_u)$

Table 2.2: Water clusters included in the model

$H_4O_2^+$, $H_2O_3^+$, $H_5O_2^+$, $H_7O_3^+$, $H_9O_4^+$, $H_{11}O_5^+$, $H_{13}O_6^+$, $H_{15}O_7^+$
$H_2NO_2^+$, $H_4NO_3^+$, $H_6NO_4^+$

metastability, high cross sections and low energy threshold for excitation from the ground state, or states that have been reported to be important in this type of plasmas. For example, for the hydrogen molecules, the magnitude of the vibrational excitation cross sections roughly drops with one order of magnitude for each next vibrational quantum number, although the threshold value remains quite low. As a result, these collisions are not included.

Besides the species shown in table 2.1, the possibility of positive water ion

clustering is included in our reaction set as well and these species are given in table 2.2. The presence of water clusters in atmospheric plasma jets was experimentally demonstrated by [148]. A water clustering reaction scheme was previously implemented by Liu and Bruggeman [121] for a helium/water discharge. Water clustering is also implemented in the chemistry sets of recent papers by Murakami [126] and Babaeva [117]. In our investigation water clustering with NO_x^+ ions is additionally implemented.

The 84 species shown in table 2.1 and 2.2 interact with each other by means of 279 electron impact reactions and 1601 heavy particle reactions. The latter consist of 249 water ion clustering and recombination reactions. We would like to stress that water clustering reaction rate coefficients are very dependent on pressure and temperature, as reported in [113]. As pressure and temperature are variables in our calculations, it is necessary to use the reported rate coefficient dependencies, which are deviating from the Arrhenius expression. This resulted in very important changes for clustering pathways and is a strong indication that temperature and pressure effects should not be disregarded.

Bruggeman *et al* [149] demonstrated the presence of negative water clusters for a capacitively coupled atmospheric pressure RF excited glow discharge in helium/water mixtures. However, there is not so much chemical data available as for the positive water ion clustering and therefore negative ion clustering is not included in our model. Thus, the reader should interpret the negative species densities like O^-, O_2^- and NO_3^- with caution, especially in the far effluent, as the densities of these species might be lower in reality, due to possible clustering reactions.

For both the electron impact reactions and heavy particle reactions, 8 different types can be distinguished, as illustrated in figure 2.2. The relative contributions of these processes to the total chemistry set are also displayed in this figure. The complete reaction chemistry set can be found in Appendix A. One can see that reactions are taken from a large selection of papers (several were already cited in the introduction). Firstly, this is because there are no papers or databases available that contain all species we want to describe. Secondly, this enabled us to cross check the values of the Arrhenius parameters between as many references as possible. For several important reactions, a range of rate coefficient values was assembled, and a sensitivity study allowed us to determine the effect of this variation and to define which value is best used.

We used a specific order for the reaction list. In this way every reaction

has its specific place in the list, which also makes the search for a specific reaction easier and implicitly shows which reactions are 'missing': either because they are unavailable in literature or because they are simply too slow under the conditions of interest. Furthermore, we have split the complete set in subsets of argon-, oxygen-, nitrogen-, dry air-, humid air- and finally water clustering chemistries. In this way, specific parts of the reaction set can be easily extracted by the reader. The order in each subset is based upon reactants and (with some exceptions) as follows: the lightest reactants first, ground state before excited states (lowest internal energy first) followed by charged species and finally positive before negative charges.

At last, we also want to mention that the table in Appendix A provides a reduced chemistry set, which can be of use for high level computational models (e.g. 3D fluid or hybrid models) where the size of the reaction chemistry set is an issue in terms of simulation time. For this reduction, only reactions were selected that contribute for more than 10% to the total formation or destruction of a species, *i.e.* the relative contribution of the reaction. In this way, it was possible to reduce the number of reactions to 744, without any change in the species densities in our simulations. These reactions are indicated with the symbol 'A'. When a further reduction would be necessary, it is possible to retain only 519 reactions if 30% relative contribution is used as a criteria. However, in this case density changes of important species like O_3 become significant (factor 2). This subset is indicated by the symbol 'B'.

Three important issues are addressed in this reduction of the chemistry set. First, it should be realized that any reaction could become important or negligible during a specific part of the calculation, so it is dangerous to reduce the set with rates integrated over the complete simulation. Therefore we checked in every time step whether the 10% relative contribution criteria was exceeded. Second, the reduction is only done for reactions and not for species, since every species can be of interest in the biomedical applications (either directly or otherwise they might act as an intermediate form). Note that it is certainly possible to reduce the set further, but that would be at the expense of the amount of information and/or accuracy. Third, our reduction takes a very broad parameter range for both temperature, power and feed gas humidity into account (data not shown). So the reduction of the reaction set was done for each parameter study independently, and afterwards the most important reactions for each case were merged. In this way the reduced set is valid for our complete parameter range. Indeed, the

chemistry in humid air, for example, proves to be quite different from the chemistry in dry air.

To study the reaction mechanism in detail, the reaction analysis module, implemented in the modified Global_Kin code by Aerts *et al* [147], is used.

Table 2.3: Conditions for the basic case study of which the results can be found in figures Figures 2.3–2.6, unless specifically stated otherwise in the text.

Gas feed (*cf.* experiment)	2 slm
Air impurities in gas feed (estimated)	10 ppm O_2/N_2, 1 ppm H_2O
Relative humidity (estimated)	50 %
Initial flow speed, *i.e.* at the nozzle exit (calculated)	2917 cm.s^{-1}
Initial gas temperature, *i.e.* at needle tip position (*cf.* experiment)	600 K
Total deposited power (*cf.* experiment)	6.5 W

2.3 Basic case study: results and discussion

Here, we will show the calculation results of this model for the conditions listed in table 2.3. The parameters are chosen in such a way that the simulations mimic the experimental conditions of the plasma jet device specified above [40], as closely as possible. Although the experimental device can be operated with different kinds of gas admixtures, we opted in this chapter for the simplest case, *i.e.* without an initial concentration of oxygen, nitrogen or water in the argon gas feed. However, some ppm levels of these gases are added to represent the impurities in the feed gas itself. Note that these impurities are largely destructed in the first few millimetres (see figure 2.1), until atmospheric air diffusion into the jet becomes predominant and the power is dropping, so the dissociation degree becomes lower. Evidently, reactive plasma species will be created in similar proportions to the impurity levels. An important parameter for experimental work is the relative humidity, which can in principle vary between 10 and 100% on a daily basis or dependent on the location. We assume 50% relative humidity for the basic case study. Figures 2.3–2.5 show all the calculated species densities as a function of the distance from the the nozzle exit, up till 2.5 cm. Note

that the figures display the calculated values starting from the position of the needle electrode tip, *i.e.* 2 millimetres inside the device, although the simulation begins even earlier. Since the corresponding time scale is also very important to interpret the chemistry, it is shown as well. It appears that several densities, *e.g.* of O_3 and NO_x species, reach a relatively 'stable' value after 2 ms. This is because these species have typical lifetimes that exceed the simulated time frame by several orders of magnitude, as was also confirmed by our longer calculations of several seconds (not shown). It is not relevant to show these results because of two reasons: first, plasma jets are usually directly applied at a distance of maximum a few cm and second, the calculation results would be inaccurate since the propagating velocity of the jet and the mixing speed of the gas for the far effluent is not available yet (in contrast to our later work reported in the last chapter).

The electron density is included in every figure, not only as a point of reference because different y-axis scales had to be used, but the behaviour of various species is of course also strongly correlated with the profile of the electron density and vice versa. In the first few millimetres, the electron density profile drops linearly (difficult to see since the figures are presented in a logarithmic scale) with nearly the same slope as the drop in power density. After about 3 millimetres behind the nozzle, the density starts to decrease very fast. This is due to the rapidly increasing speed of air diffusion into the argon stream. Note that, in about the same distance, the jet flow velocity drops to about 50% of its initial value, so that the surrounding air can diffuse 'faster' into the argon stream (see air fraction profile in figure 2.1). Free electrons efficiently attach to various oxygen, water and NO_x species, as a consequence of the increased amount of air components in the jet, and this explains the significant drop in electron density. Our simulations predict that electron impact dissociative attachment of oxygen molecules is the dominant process at these conditions. The importance of this process also explains the slight increase of the electron density at a position of 1.2 cm from the nozzle. At that point the power density goes to zero and as a result T_e quickly goes to room temperature as well. Consequently, there are few electrons left with enough energy to dissociate oxygen species and therefore dissociative attachment rates rapidly decrease in this area. Electron attachment in three body collisions, *e.g.* $e^- + O_2 + M \rightarrow O_2^- + M$, are not fast enough to completely take over the role of the dissociative attachment as a loss process for free electrons. On the other hand, the electron formation reactions do not depend so much on the value of T_e, since

in that region they are mainly formed by electron detachment reactions like $O + O_3^- \rightarrow O_3 + e^-$. Thus, the net formation of free electrons strongly rises in this area and one could consider the negative ions as a reservoir of free electrons that is able to create free electrons for a considerable amount of time. Note that, until 1.2 cm from the nozzle, the dominating electron loss processes are not a real neutralisation of negative charge, but rather free electrons going to the negative ion reservoir.

Another interesting fact that follows from our calculation, is that throughout the entire effluent region, the main source for the total positive charge is due to convection and not due to the creation of electron-ion pairs in chemical reactions. This is caused by the rapidly decelerating flow speed, which makes that the outgoing flux of positive charge is much less than the incoming flux, for a cylinder segment of the plasma jet effluent.

In the following text the numbers of the mentioned reactions, are referring to the numbering in the reaction list from Appendix A.

2.3.1 Argon species chemistry

Molecular argon species are expected to be much more abundant than the atomic states at atmospheric pressure, due to efficient three-body association collisions (*e.g.* reactions 309 and 314 from the table in Appendix A). This can indeed be seen from figure 2.3.A. Besides, Ar_2^+ is significantly formed by electron impact ionization of the excimer as well (reaction 49). For the atomic states, the long living $Ar(^4S[^3P_2])$ metastable state clearly has the highest density. Generally, these states are directly formed by electron impact excitation, for example through reaction 2. Atomic ions, on the other hand, are formed through a stepwise ionization pathway, based on electron impact excitation, followed by electron impact ionization (in this case mainly by reaction 17 and 45).

It is clear that the densities of argon ions, metastables and the excimer state quickly drop at almost the same rate as the electron density. This is because energetic argon species easily transfer their energy to various air species. Note that different types of processes are involved, including charge and energy transfer reactions (*i.e.* physical & chemical quenching) and Penning ionisation processes. The energy is usually not transferred back since the excited energy levels of argon are quite high: 10.6 eV for the excimer, 11.5 eV for the $Ar(^4S)$ levels and even 15.7 eV is necessary to ionise argon. Most energy levels of air species are at lower energies. An exception are the
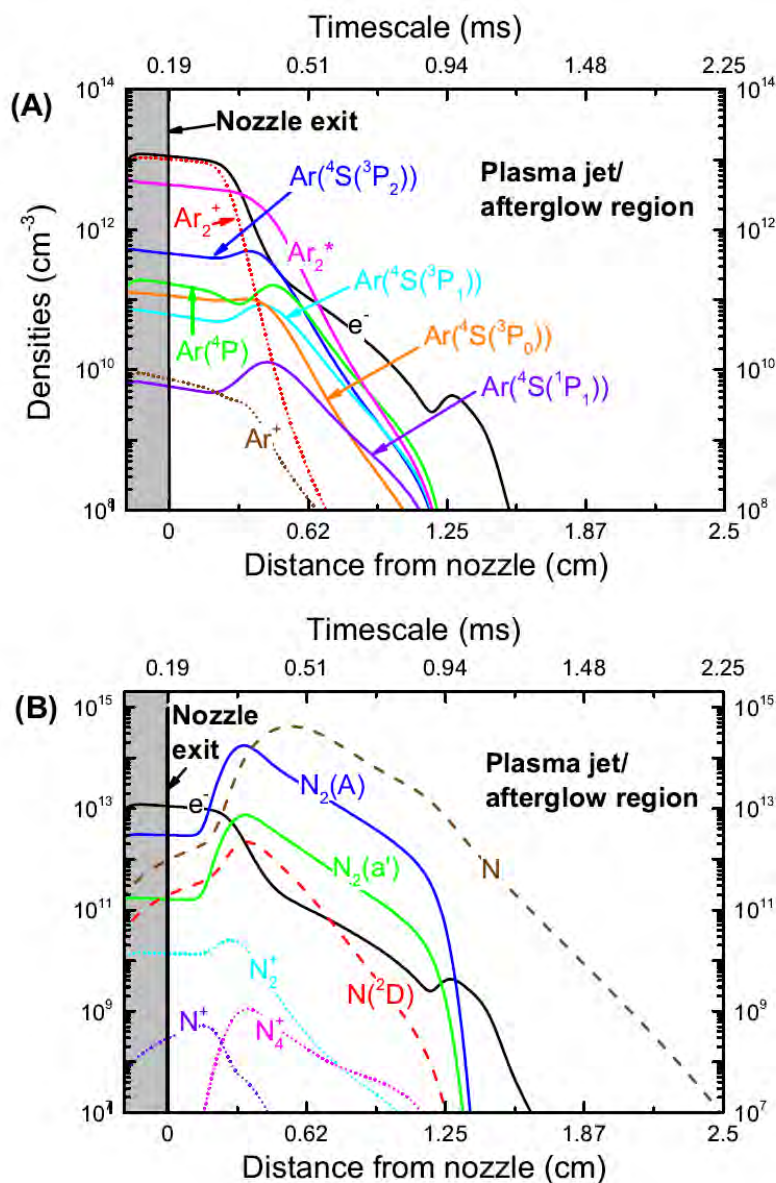
Figure 2.3: Densities along the symmetry axis of the plasma jet: (A) argon species, (B) nitrogen species. Molecules are indicated by a solid line, radicals by a dashed line and ions by a dotted line. Note that the time and distance dimensions are correlated with an externally calculated velocity profile.

energy levels of different nitrogen ions, which lie close to the argon ionization threshold, and therefore reaction 637 (N_4^+ + Ar $\rightarrow$ Ar^+ + 2 N_2) becomes the most important argon ion source when air diffusion becomes significant. The dominant processes for the destruction of the different argon species by air impurities are, at 0.5 cm from the nozzle (for each reaction, the relative contributions to the total loss is indicated after the colon):

- $Ar(^4S[^3P_2])$ + O_2 $\rightarrow$ 2 O + 2 Ar (321): 31%
  $Ar(^4S[^3P_2])$ + N_2 $\rightarrow$ 2 N / $N_2(A)$ + 2 Ar (327-328): 24/24%
  $Ar(^4S[^3P_2])$ + H_2O $\rightarrow$ H + OH + 2 Ar (977): 3%

- Ar_2* + O_2 $\rightarrow$ 2 O + 2 Ar (427): 36%
  Ar_2* + N_2 $\rightarrow$ $N_2(A)$ + 2 Ar (429): 42%
  Ar_2* + H_2O $\rightarrow$ H + OH + 2 Ar (1005): 6%

- Ar_2^+ + O_2 $\rightarrow$ O_2^+ + 2 Ar (434): 37%
  Ar_2^+ + H_2O $\rightarrow$ H_2O^+ + 2 Ar (1008): 49%
  Ar_2^+ + H_2O $\rightarrow$ ArH^+ + OH + Ar (1009): 12%

- Ar^+ + N_2 $\rightarrow$ N_2^+ + Ar (414): 74%

2.3.2 Nitrogen species chemistry

When ambient nitrogen is diffusing into the jet, it is easily excited to the first electronic state $N_2(A)$, mainly by electron impact collisions (reaction 157). Indeed, this excited state is among the most dominant nitrogen species as can be seen from figure 2.3.B. $N_2(A)$ is easily quenched back to the ground level in superelastic collisions (reaction 167) or by gas species (reaction 618). Another destruction pathway is also very important, although significantly slower than 167 and 618: the reaction with atomic oxygen, where NO is formed (reaction 647). This reaction is in the first few millimetres after the nozzle exit the main production pathway for NO (see below, section 2.3.5). Note that it is probably less fast at lower temperatures because the rate coefficient is quite temperature dependent. The production and loss processes for the $N_2(a')$ excited level are similar as for $N_2(A)$ and this explains why the trends of the density profiles are alike.

The nitrogen radical (N) is mainly formed through the chemical quenching of argon by N_2 (*e.g.* reaction 328) and the reaction between $N_2(A)$ and O, generating NO and N (see above). N easily reacts further with molecular

oxygen to form NO through reaction 729. However, it can also be destructed by NO to form N_2 again (reaction 849). A considerable fraction of N is also excited by electrons to $N(^2D)$ through reaction 138. This species can react further in a similar way as the ground state, but it can also be physically quenched to the latter. The only remarkable difference is that the excited $N(^2D)$ state easily reacts with H_2O, and this forms the largest source of NH (reaction 1496). All these fast reactions result in a significant drop for the N atom density, starting at a distance of 0.6 cm from the nozzle. At a distance of 1.5 cm the density is already three orders of magnitude lower than the maximum density of 4×10^{14} cm^{-3}. This might be important information, since high N densities can, for example, be necessary in sterilization applications, thus, the distance between the device and the object can be crucial.

Nitrogen ions (N_2^+) are mainly formed either by charge transfer of Ar^+, Penning ionization by excited argon levels or stepwise electron impact ionisation (reactions 414, 329 and 169 respectively) depending on the effluent region. In their turn they transfer this charge to H_2O (reaction 1501). This is indeed one of the two most important ways for the generation of H_2O^+ ions, next to the direct charge transfer between Ar_2^+ and H_2O (reaction 1008). A small amount of N_2^+ associates with N_2 and is thus converted into N_4^+ by means of reaction 590. The role of the main N_4^+ destruction pathway was already discussed in the argon chemistry mechanism.

The other nitrogen species do not play a significant role in the discharge.

2.3.3 Oxygen species chemistry

Looking at the oxygen species profiles in figure 2.4.A, one can see that the $O_2(a)$ and $O_2(b)$ excited states, as well as O atoms and O_3 are formed at high densities. The dissociation degree, *i.e.* , the ratio of atomic over molecular oxygen, is about 6% at a distance of 7 millimetres from the nozzle, which is 25 times higher than the maximum nitrogen dissociation degree. Oxygen atoms are created mainly by electron impact dissociation (reaction 79 and 80: both cross sections sum up to the correct value) and by collisions of O_2 with excited N_2 (reaction 736 and 741). In the far effluent O atoms are fully generated from the reaction between singlet oxygen $(O_2(a))$ and ozone (O_3) (reaction 522). In reality O might also be generated by UV radiation that penetrates far into the effluent, as previously stated in [142], but this effect can not be included in the model. In contrast to the N atoms, the
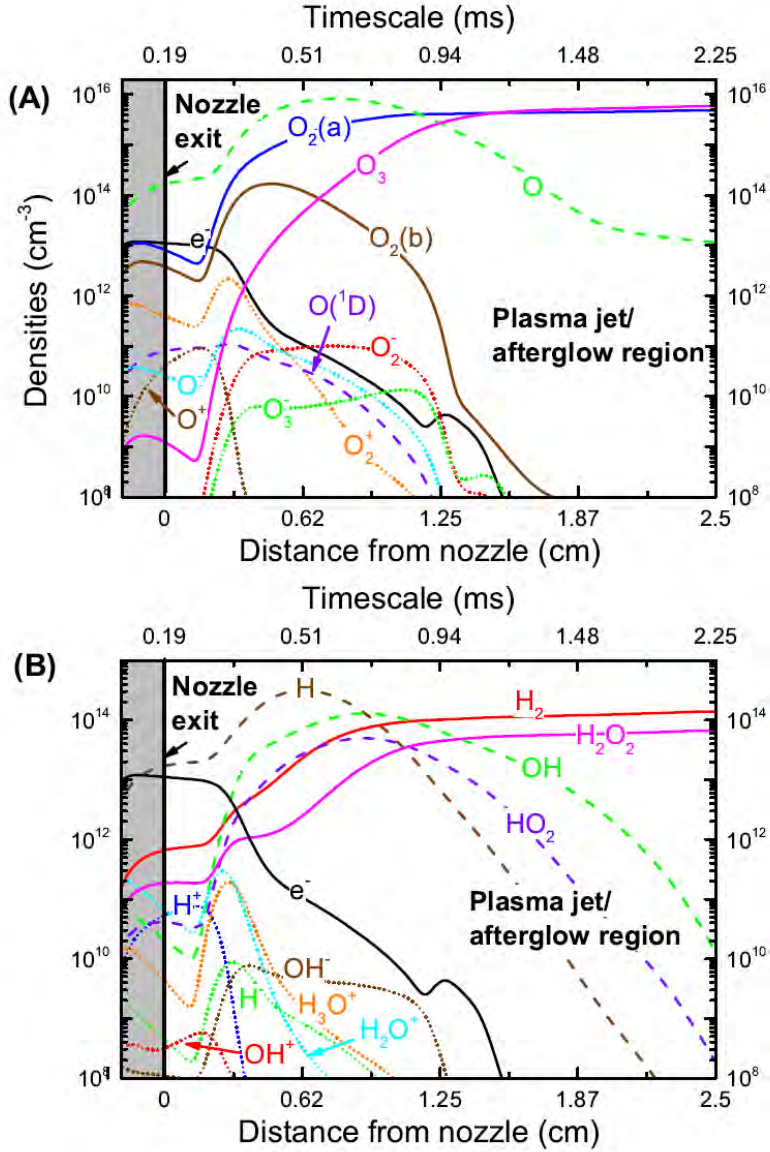
Figure 2.4: Densities along the symmetry axis of the plasma jet: (A) oxygen species, (B) water species. Molecules are indicated by a solid line, radicals by a dashed line and ions by a dotted line. Note that the time and distance dimensions are correlated with an externally calculated velocity profile.

O atoms are abundant even in the far effluent. Even at a distance of 2.5 cm from the nozzle the density has only dropped by 3 orders of magnitude compared to the maximum value of 10^{16} cm^{-3}. This has also been observed experimentally by Schaper *et al* [150] for a helium plasma jet. The main loss mechanism in the first part of the effluent, when a large amount of H atoms are present, are the consecutive reactions 1022, 1452 and 1303. In the first reaction HO$_2$ is formed out of H and O$_2$, in the next step HO$_2$ reacts with O to form OH and O$_2$ and in the last step OH is converted back into H by reacting with O. The net result is the conversion of 2 O into O$_2$. Later in the effluent, when the gas temperature is lower and H is depleted by other processes, the formation of ozone is the main loss for atomic oxygen (reactions 456-461). The excitation to O(^{1}D) as a loss mechanism does not seem to have an important role in the discharge. Although this excited level is easily generated by electron impact collisions (reaction 53), it is physically quenched back to the ground state at almost the same rate (reaction 475). Furthermore, the internal energy of O(^{1}D) is 1.97 eV which is not very large in comparison to typical bond energies, so the chance of breaking bonds and as a consequence the probability of forming new species is indeed rather small.

The same is valid for the two molecular electronically excited states O$_2$(a) and O$_2$(b) which lie at 0.98 eV and 1.63 eV respectively. For these two states, the first electronically excited molecular state, O$_2$(a), is by far the most abundant and is mainly formed by electron impact (reaction 76) and an energy transfer where N$_2$(A) is involved (reaction 737). The role of the O$_2$(a) chemical quenching by O$_3$ in the production of O in the late effluent was already mentioned above, but in the first part of the effluent O$_2$(a) is destroyed mainly by dissociation reactions (reactions 98, 99, 751). O$_2$(b) reacts in a similar manner.

Ozone (O$_3$) is created through three-body association reactions between molecular and atomic oxygen (reactions 456-461). On the other hand, O$_3$ also reacts efficiently with O atoms, to form O$_2$ again (reaction 464). This indicates that the O$_3$ generation is somewhat 'buffered', and producing more O will only generate slightly more O$_3$ or even decrease its density. Destruction pathways with NO$_x$ or OH are less important since these species are not generated in large enough quantities (see below).

Both O$_3$ and O$_2$(a) are known to cause oxidative stress in a biological system [68]. However, the densities shown here might apply only to the gas phase since biological samples are always surrounded by water and, even

after a drying process, the gas species first have to pass a liquid interface. Especially for O_3 this is known to be a slow process [151]. $O_2(a)$ is clearly a long living species, but will be quenched much more quickly once it passes a liquid interface.

The generation of O_2^+ ions is caused by charge transfer with Ar_2^+ (reaction 434). Further in the effluent this role is taken over by direct electron impact ionization (reaction 78), but at a much lower rate. The cations either recombine with the most abundant anions (*e.g.* reaction 497), or they undergo dissociative electron-ion recombination (reaction 124). More important is the fast generation of $H_2O_3^+$ in a water clustering reaction 1710, as will be explained in section 2.3.6. The atomic oxygen ion, O^+ is generated by charge transfer by various species ($H^+/N_2^+/N_4^+$, reaction 1110/652/653 respectively). When such high energetic ions are largely depleted, direct electron impact ionisation of O becomes important (reaction 54). O^+ is an important species for the formation of NO^+, see below.

A very interesting property of oxygen containing discharges is the efficient electron attachment process due to the electronegativity of oxygen. In our simulations, anions are mainly created through electron impact dissociative attachment of O_2 forming O^- (reaction 82). In a next step, the negative charge of O^- is transferred to O_2 generating O_2^- (reaction 490) which is the dominant negative charge carrier from 0.5 cm up to 1.3 cm from the nozzle, but O_3^- is formed out of O^- as well (reaction 491). The latter is the main production channel of ozone anions and this species is one of the most important species for NO_3^- production, see below. The main loss channels for O_3^- are however two reactions with O ($\rightarrow 2\ O_2 + e^-$ and $\rightarrow O_2 + O_2^-$, 466 and 465 respectively). Note that the density ratio of O^- against O_2^- is also determined by reaction 462 where the electron is given back from O_2^- to O^-. Finally, it is important to mention the dominant role of reactions 455 and 463 in the creation of free electrons from anions, where O^-/O_2^- and O associate to form O_2/O_3 (note that H^- is almost equally important for the creation of free electrons, see below). O_2^- is apparently not present in large quantities, about 5 ppb at maximum, yet this species is also reported to be important in therapeutic applications [68].

2.3.4 Water species chemistry

The density profiles of the different water species created in the discharge are plotted in figure 2.4.B. First of all, note that the generation of H and OH

is rather complex and closely linked and many other species are involved. Just after the nozzle exit, the most important pathway for H generation is the dissociative electron-ion recombination of H_2O^+ (reaction 267 and 268) where an O and OH are formed as well. A few millimetres further from the nozzle, when the water levels start rising due to diffusion, H is primarily created through H_2O dissociation (reaction 262 and 1005) and OH dissociation (reaction 246, 250, 1303, 1309 and 1565). The H atoms reach a maximum density at a distance of 6 millimetres from the nozzle, but will eventually completely disappear in the next 2 cm by conversion into OH and eventually to hydrogen peroxide (HO), see below. The loss to OH is mainly caused by reaction with O_3 (1031) as mentioned earlier or through the consecutive reactions 1022 and 1084, where HO_2 acts as an intermediate.

OH itself is mainly formed by dissociative electron-ion recombination of H_2O^+ as mentioned above (268) and from H_2O reactions with electronically excited Ar species (reactions 977, 1005), Ar_2^+ (reaction 1009) and $N(^2D)$ (reaction 1496), with an additional H generated in the first three reactions and NH for the latter. When these species are depleted, OH is primarily formed in a collision between H and O_3 (1031). The OH formed in these processes reacts further with N (1309) and O (1303) to generate H radicals again. Stepwise electron impact dissociation of OH, where OH(A) acts as the intermediate, can also be important (typically dependent on the background gas composition) but it is generally not crucial. Later in the effluent, OH molecules start to dimerize quickly, forming hydrogen peroxide in reactions 1338-1343. First, it is important to mention that H_2O_2 production is limited by the presence of OH and O (reaction 1348 and 1558). Second, we want to stress the relevance of reaction 1346 where OH and HO_2 react with each other to form water and oxygen molecules. This reaction can be considered as competing with OH or H_2O_2 production. Additionally, the rate coefficient of this reaction is inversely proportional with temperature. Knowing that a low temperature is desirable for the biomedical applications, the rate of this process will be fast.

All the water species mentioned up to now are strong oxidizing agents in biological samples. Some might even influence the ROS signalling in and between cells [68]. Note that H_2 is also formed in large quantities but it is not reactive and has probably no biological effect. However, since two reactive water species are needed for its formation (1083), this process reduces the biological reactivity of the plasma.

As far as the important positive ions are concerned, H_2O^+ receives its charge

from Ar_2^+ (1008). H_2O^+ easily loses its charge to oxygen species (reaction 1523), but there is an additional destruction channel leading to the formation of a hydronium cation (H_3O^+) by a reaction with neutral water molecules (1507). Indeed, after the nozzle exit H_3O^+ is primarily created in this way, next to a proton transfer reaction between ArH^+ and H_2O (reaction 1509). Later in the effluent H_3O^+ is mainly formed out of $H_2O_3^+$ (reaction 1713). Other ions like OH^+, H^+, H_2^+ and H_3^+ do not play a significant role in the discharge.

Negatively charged water species are formed by electron impact dissociative attachment of H_2O, through reaction 260 forming H^- which reacts with another H_2O resulting in the generation of OH^- (reaction 1183). H^- and OH^- ions usually lose their electron by a collision with a neutral species, where a free electron is created (reaction 1148 for H^- or reactions 1082 and 1402 for OH^-).

2.3.5 NO_x species chemistry

The NO_x reaction mechanism is quite complex and is very dependent on various species from the nitrogen, oxygen and water chemistries. As a result, the most important destruction and formation pathways are varying as a function of the distance from the nozzle. The density profiles are shown in figure 2.5.A.

Nitrogen monoxide (NO) has the highest density, about 4×10^{14} cm^{-3}. This species is formed through various pathways: reaction of O with $N_2(A)$ (reaction 647) is initially the most important one, but at a distance of 6 millimetres from the nozzle exit this role is taken over by reactions 729 and 1309: O_2 + N and OH + N. While NO is being formed, it is also continuously converted into NO_2 by associative three-body collisions with O (reactions 655-659). A balance is created between these two species, since NO_2 is destroyed by O in reaction 661, forming NO again. Reaction 1048 where H reacts with NO_2 to form NO and OH, has a similar function and the generated OH will even be used to generate more NO by reaction 1309, as mentioned before. Even so, reaction 1048 will only have a limited effect because H rather rapidly disappears compared to O and OH. Note that also the gas temperature plays a crucial role in the ratio between these two species, since the back reaction 661 is proportional with temperature and reactions 655-659 contain an inverse relationship, where NO is converted into NO_2. Thus, lower temperatures will favour NO_2 formation. Interest-
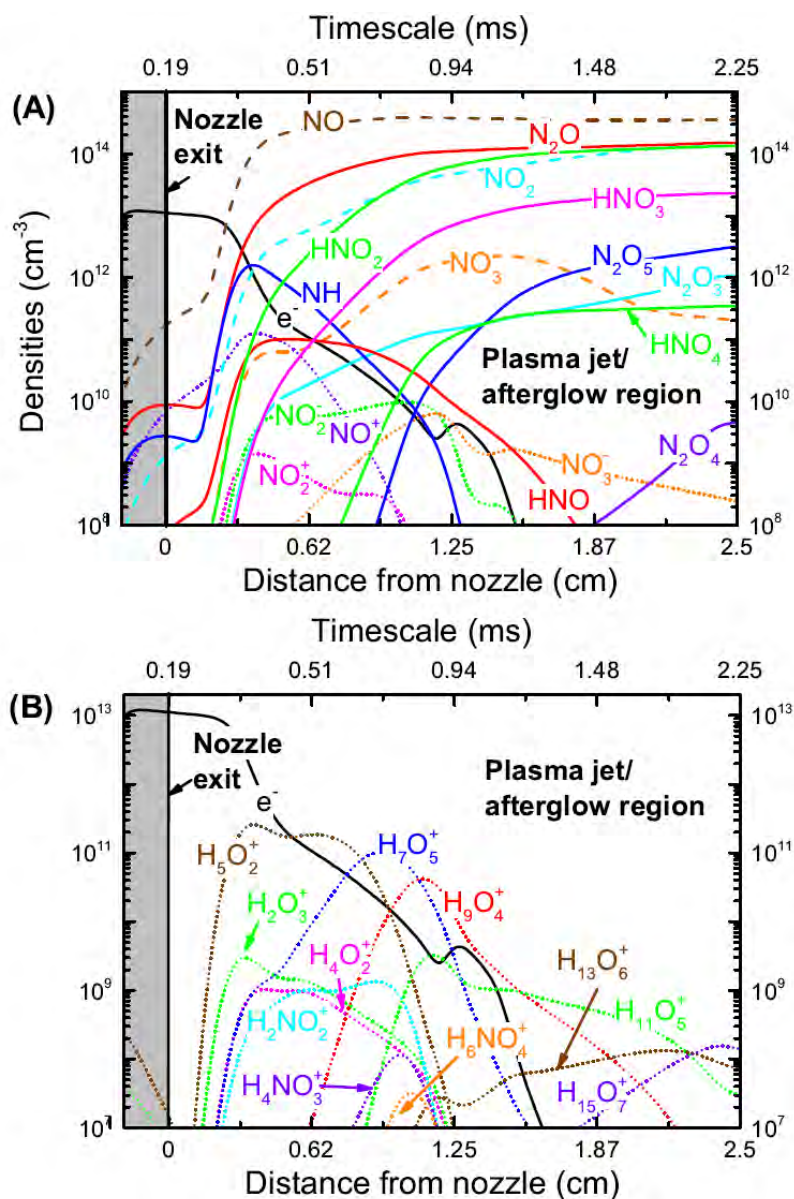
Figure 2.5: Densities along the symmetry axis of the plasma jet: (A) NO_x species and (B) ionic water clusters. Molecules are indicated by a solid line, radicals by a dashed line and ions by a dotted line. Note that the time and distance dimensions are correlated with an externally calculated velocity profile.

ingly, both species also associate with each other to form N_2O_3 (reaction 910). The time scale is, however, too short to form large amounts of N_2O_3 and it is quite easily destroyed by breaking up again into NO and NO_2 in collisions with the background gas (reaction 971).

With respect to the biomedical applications, we want to stress that varying the treatment distance will affect the NO and even more the NO_2 flux that reaches the object, since the density of these species increases gradually as a function of distance from the nozzle (by several orders of magnitude over the total simulated distance). Note that NO_2 can be toxic, and therefore not more than 5 ppm over an 8 h period is recommended [95].

N_2O is formed competitively with the NO_x mentioned above, because it is also created through $N_2(A)$, by a reaction with molecular oxygen, *i.e.* reaction 739. The reaction rate is lower than for $N_2(A)$ + O, where NO is created, but this is compensated by the much higher density of O_2 compared to O. This explains why the N_2O density is quite high as well. It is noteworthy that N_2O is again destroyed by the same $N_2(A)$ species (reactions 875 and 876). We have no information on N_2O being a biologically important species (neither as a reactive nitrogen species (RNS), as a signalling molecule or causing toxic effects), though it can be used as an anaesthetic. The nitrate radical, NO_3, is considered as a RNS [68]. It is formed through an associative three-body collision between O and NO_2 (reactions 662-666). Its concentration reaches at maximum only 0.1 ppm, since it is quite efficiently destroyed again by O, NO and H, forming NO_2 (reactions 672, 919 and 1060). Moreover, NO_3 is also largely converted into N_2O_5 (which is a RNS as well) in the far effluent by association with NO_2 (reaction 943), especially when the temperature goes down since the back reaction N_2O_5 $\rightarrow NO_2 + NO_3$ (973) is strongly correlated with temperature.

The role of NH and HNO will not be discussed in detail here. They do not reach a high density nor do they act as an important chemical intermediate, except for the pathways that already have been explained above. This is, however, not the case for the other HNO_x species, since HNO_2 reaches 10 ppm in the jet effluent, HNO_3 reaches 1 ppm and HNO_4 10 ppb (all at 1.5 cm from the nozzle exit). Figure 2.5.A clearly indicates that it is be possible to largely avoid these species if the treating distance would be kept small when applying a plasma jet.

HNO_2 is mainly formed by the association of OH and NO (reactions 1319-1323). On the other hand, it is also efficiently destroyed by O and OH radicals creating NO_2 (reactions 1593 and 1353). For HNO_3, reactions 1326-

1331 ($OH + NO_2 + M$) and reactions 1460-1465 ($HO_2 + NO + M$) are the main sources, while it is predominantly lost by collisions with OH and O, yielding the formation of NO_3 (reaction 1354 and 1598). Moreover, HNO_3 reacts at a reasonably high rate with O_2^- (reaction 1601) and NO_2^- (reaction 1603), creating NO_3^-. This explains why NO_3^- is the dominant negative charge carrier in the far effluent.

Finally our simulations indicate that HNO_4 is formed through NO_2 and HO_2 association (reactions 1473-1478). This species is lost in two, almost equally fast reactions; *i.e.* by collisions with OH forming NO_2, H_2O and O_2 (reaction 1356), as well as through collisions with the background gas (1605) forming NO_2 and HO_2 again. Evidently, the latter is only possible when the temperature is significantly deviating from room temperature in certain regions of the effluent, due to its temperature dependent reaction rate.

It was mentioned before that NO_3^- will be formed through O_2^- and NO_2^- via HNO_3 (reaction 1601 and 1603). The importance of the $O_3 + NO$ channel (reaction 827) was stated above as well. We would like to add that the $NO_2 + O_3$ pathway (reaction 813) is equally important. Which reaction dominates is very dependent on the distance to the nozzle. This is valid for NO_2^- itself as well. At first, it is formed by $NO + O^- + M$ (reaction 719). Later in the effluent, when O_2^- becomes the most important anion, the O_2^- reaction with NO_2 (reaction 793) starts being dominant for NO_2^- formation. At the point where the densities O^- and O_2^- have become low, this anion is not created any more. The main effective charge loss for both negative ions NO_2^- and NO_3^- (so not charge transfer between each other) is simply recombination reactions with the most abundant positive ion at that point. NO_x^+ ions (mainly NO^+) are created through collisions of various species with O^+ (reaction 691) and O_2^+ (reaction 756 and 758), but these reactions are not very fast, so the densities remain low. Therefore, we can conclude that these species do not play an important role in the chemistry at the conditions under study.

2.3.6 Water clustering chemistry

Our calculation results plotted in figure 2.5.B reveal that as soon as the air concentration in the jet starts to increase significantly, the positive ions are almost immediately clustering with water, in spite of the fact that declustering, *e.g.* reaction 1718, is still very fast in this area (where the temperature

is still high). In this way the water clusters quickly become the most important charge carriers, as is clear from the figure. Furthermore, the clusters keep increasing in size as a function of the distance from the nozzle. The first important cluster $H_5O_2^+$ is simply formed out of the reaction of H_3O^+ with H_2O (reaction 1717). The hydronium ion itself is created from H_2O^+ (see above, reaction 1507). Clearly, the formation of $H_2O_3^+$ (water clustering of O_2^+, reaction 1710) is less efficient and this is attributed to the following efficient reactions: $H_2O_3^+ + H_2O$ yielding $H_4O_2^+$ (1714) and $H_2O_3^+ + H_2O$ yielding H_3O^+ (1713). Additionally, $H_4O_2^+$ also leads to $H_5O_2^+$ formation through reaction 1716. This all explains why only the $H^+.(H_2O)_x$ water clusters survive. All clusters, regardless of their size, recombine with electrons and anions (O^-, O_2^-, NO_3^- depending on their densities as a function of the distance) causing a gradual decrease in the total amount of positive and negative ions of about three orders of magnitude within 2 ms. $NO^+.(H_2O)_x$ will not be discussed in detail since these species do not reach a high density.

2.3.7 Electron energy gain and loss

In this model, the mean electron temperature T_e is used to determine practically all rate coefficients for the electron-heavy particle collisions, either by an Arrhenius expression or by energy dependent cross sections (where the Boltzmann solver provides lookup tables for a wide range of T_e values with corresponding rate coefficients). For this reason the calculation of the electron temperature is very important. The value is obtained from the electron energy density equation, see equation 2.2, and is plotted in figure 2.1. The second term and third terms on the right side consider the electron energy density gain and loss due to all different inelastic and elastic electron collisions. Evidently, the number of inelastic reactions is great, moreover the species densities and chemical pathways are rapidly changing along the plasma jet stream. Figure 2.6 clarifies which are the most important contributions for changes in the electron energy density, as a function of distance from the nozzle.

It is clear that the main source of electron energy gain throughout the effluent is continuously the power input into the plasma. However, for a short period, when air entrainment becomes important (3 - 5 millimetres from the nozzle), the sum of de-excitations from different excited nitrogen states (reactions 1.2-1.5 in figure 2.6(a)) adds up to 10% of the total energy gain. The effect of any other species or processes is negligible.
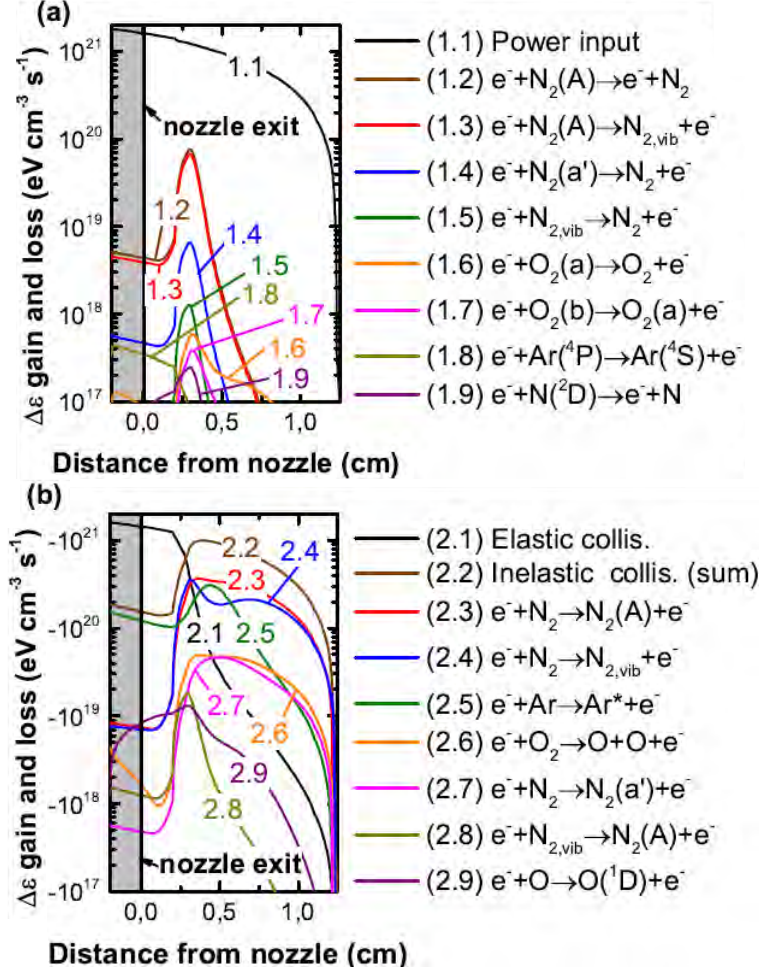
Figure 2.6: Dominant electron energy density gain (a) and loss (b) terms ($\Delta\varepsilon$) along the symmetry axis of the plasma jet, where $\varepsilon=\left(\frac{3}{2}n_e k_b T_e\right)$ (see equation 2.2). Ar* and $N_{2,vib}$ are the sum of all electronically excited states of argon and of the vibrationally excited states of nitrogen included in the model respectively.

As long as air species are not more than impurities in the argon background gas, elastic collisions with argon atoms are the largest drain of electron energy, with a relative contribution of about 90%. Inelastic collisions with argon atoms have only a minimal effect of less than 10%. Note that in figure 2.6(b), reactions 2.3-2.9 are the predominant contributions to the total inelastic reactions, which is represented by profile 2.2. Figure 2.6 shows that the ratios of the different contributions completely shift when air entrainment becomes significant. In this case, inelastic collisions, more specifically nitrogen vibrational and electronical excitation, become the largest energy loss processes (reactions 2.3-2.4). Due to these nitrogen excitations, T_e is initially slightly going down at this point (see figure 2.1 above). However, only one millimetre further, T_e is going up again. A detailed analysis of our simulation results indicates that this is caused by the extremely rapid drop in electron density (again see figure 2.1 above). This drop causes the absolute value of the elastic loss term (third term on the right side of equation 2.2) to decrease faster than the increase of the absolute value of the inelastic loss terms. Therefore, the derivative of the electron energy density as a function of time becomes positive again, which explains the rise in T_e. Indeed, after some more time (at 5 millimetres from the nozzle) T_e starts dropping once more and this is exactly where the slope of the electron density profile flattens. Note that the total energy loss and gain rates are almost exactly cancelling each other and the slightest change in either of these values has a large effect on T_e. The maximum in the energy loss process 2.5 (at 4 millimetres) can be explained through the T_e profile: the rate coefficient of argon excitation increases strongly for higher T_e values. The opposite is true for vibrational excitations of nitrogen molecules, thus explaining the dip in the energy loss process 2.4. The reason why there is no maximum observed for electronic excitation of nitrogen (process 2.3) is because the increase of both the rate coefficient as a function of T_e and the nitrogen density (due to diffusion) are rather small in comparison to the steep drop in electron density. Since the rate of reaction 2.3 is a product of these three factors, it drops and therefore the energy loss due to this reaction becomes less important in this region.

Finally, we want to stress that this information is maybe not directly transferable to the 'real' value of the electron temperature at a certain distance. Indeed, the model still uses some crude approximations like spatial averaging, and also time fluctuations (RF) of the electric field are not taken into account. However, the figure still gives an idea of how the electron temper-

ature is determined in this model and what are the dominant loss and gain terms caused by the air component reactions. Additionally, the importance of including rotational or vibrational states is demonstrated.

2.4   Conclusion

In this chapter, a 0D chemical kinetics model is presented to study an experimental plasma jet setup. In the 0D model, the time dependent evolution of species densities is converted into a spatial dependence, hence, as a function of the position in the plasma jet device and effluent. The argon feed gas flows into the open atmosphere, assuming 50% relative humidity and for this purpose, an extended reaction chemistry set for a argon/humid air mixture was developed, which considers 84 different species, including biomedically active species (ROS and RNS), and 1880 reactions (see Appendix A).

Free electrons are mainly created through electron impact ionization of the argon excimer, Ar_2^*, which is created through association reactions of argon metastables with the background gas. When the argon species flow into the ambient humid air, they are chemically quenched by the air molecules, thereby mainly forming atomic species. The calculation results show that high O, H, and N densities in the jet can even already partially be formed within the device, out of ppm impurities in the gas feed. From a distance of 0.25 cm behind the nozzle exit, ambient air diffusion starts to influence all density profiles drastically. The densities of all implemented biomedically active species increase strongly from that point on. The highest density is reached by atomic oxygen at 0.8 cm (8×10^{15} cm^{-3}). From that point, the density decreases again since this species is (mainly) associating with O_2 forming O_3, which becomes the dominant species in the effluent (5×10^{15} cm^{-3}), where the power density and gas temperature are decreasing rapidly. The other radicals (*i.e.* N, H and OH) are more efficiently quenched than O and they are predominantly converted into HO_2 and NO. All the chemically reactive species recombine and form 'long–lived neutrals' (at the simulated time scales), mainly $O_2(a)$, H_2, N_2O, NO_2, H_2O_2, HNO_2 and HNO_3 (next to ozone and NO as mentioned before), through various pathways. Their densities vary between 2×10^{13} cm^{-3} and 4×10^{15} cm^{-3}, which corresponds to concentrations between 1 and 200 ppm. The negatively charged species are created through dissociative attachment of oxygen and water molecules. By means of association or charge transfer reactions with neutrals, O_2^- and

later in the effluent NO_3^- dominate over the other anions. Dissociative attachment processes are also the main cause of the rapid decrease of the electron density from 0.3 cm beyond the nozzle exit. Note that negative cluster formation, which is not included in the model, might affect the anion densities. Positive ions are mainly created through charge transfer with argon ions, but they are quickly converted into $H_3O^+.(H_2O)_x$ water clusters. Furthermore, we identified the dominant electron energy gain and loss contributions. Our calculations show that, as long as the electron density is high and air is only present in ppm concentrations, elastic collision losses with Ar are dominant. Afterwards, when air entrainment becomes significant, energy losses by inelastic collisions become the most important; electronic excitation of nitrogen, vibrational excitation of nitrogen and electronic excitation of argon atoms have the highest contributions. Therefore, we conclude that the vibrational states have to be included to determine the electron temperature as accurately as possible in these kind of simulations.

Chapter 3

Reaction pathways of the biomedically active species in an Ar plasma jet

Preface

For helium plasma jets it was already demonstrated both experimentally and numerically that the chemical properties of the plasma jet can be manipulated by controlling the voltage amplitude [153, 154], pulsing [155], the electrode configuration [156], addition of oxygen/nitrogen/water admixtures [123, 157–160] and the gas flow speed [161]. Moreover, also the humidity, both in and out of the discharge chamber, plays a role [126, 162, 163], but is quite difficult to control.

The number of research groups working on argon plasma jets and the number of published works [38, 40–42, 71, 164–168], on the other hand, is lower, while modelling work for argon as the background gas is practically absent. In this thesis we therefore simulate the gas phase reaction kinetics of an argon plasma jet flowing into an open atmosphere of humid air. In the previous chapter we described the model in detail, but the plasma was more generally described, for a basic case study. In the present chapter, we focus in detail on the plasma generation of the biomedically active species (or gas phase precursors for important liquid phase species) and the influence of the operating conditions. Moreover, we vary the most important operating conditions like ambient air humidity, energy input and gas temperature and investigate the effect of each of these parameters on the chemical pathways of species relevant for plasma medicine applications. Note that it can be very challenging in experimental work to study the effect of only one parameter, because changing one parameter often influences another one.

In the next section we start with some extra numerical details that specifi-

---

cally apply for this chapter. Subsequently we evaluate the formation of the most abundant biologically active agents. This analysis is done separately for three distinct regions in the plasma jet: inside the device, the active plasma jet and the far effluent. This also includes the effect of the variation of ambient air humidity, power input and gas temperature.

3.1 Additional comments on the model

For this chapter we chose once more to mimic the plasma jet conditions of the needle type argon plasma jet developed by Bruggeman and co-workers at the Technical University of Eindhoven [38] (see figure 1.6). This device is well studied and can be used for biomedical application studies.

The input parameters for our zero-dimensional (0D) model, used in this chapter are practically the same as in the previous one, as can be seen from figure 3.1 (comparing with figure 2.1). Note that also the flow velocity is now depicted in the figure. Like in the previous chapter, we use the reaction set presented in Appendix A, however, with a few exceptions which are listed in Appendix B. These modifications have only a minor influence on the calculated plasma properties and are implemented here only for completeness and/or consistency. Obviously, this all results in nearly the same electron density and temperature profile.

Our results are analysed by an in house developed software tool, which enables an automatic identification of the most dominant reaction pathways. Additionally, with this tool it is possible to produce reaction pathway plots (see section 3.2.15) using the open source software 'Graphviz' [169].

Note that this work mainly provides qualitative insights in the complex reaction mechanisms of the biomedically active species within a wide range of experimental conditions. Nevertheless, our model can even provide relatively accurate quantitative predictions of the species densities as will be shown in the next chapters.
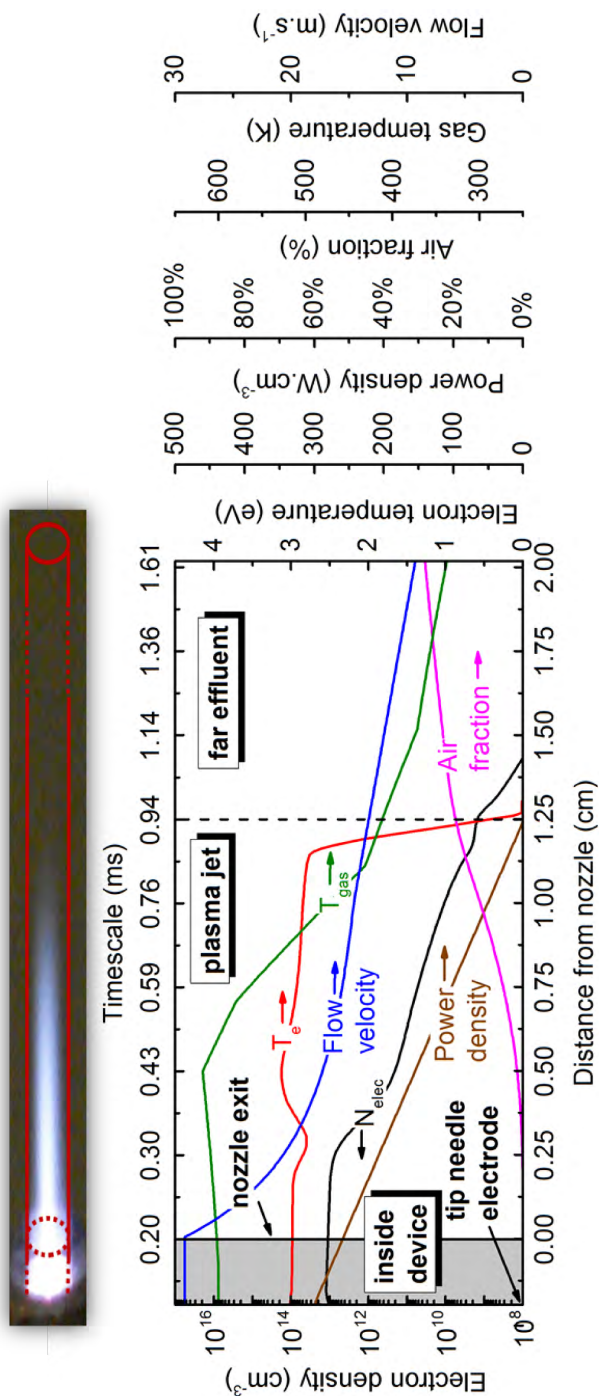
Figure 3.1: Plasma characteristics along the axial symmetry axis of the plasma jet which is shown at the top. The electron temperature (T_e) and electron density (N_{elec}) result from the calculation. The profiles of the power density, gas temperature, humid air fraction diffusing into the argon stream and gas flow velocity are fitted to experimental values. The interior of the plasma jet device is represented by the gray area, beginning at the needle electrode tip. This zone ends at the nozzle exit (indicated with axial position = 0.0 cm) and is followed by a second region where the plasma jet propagates into the ambient air. Around 1.2 cm from the nozzle exit, when the power density has reached a value of zero, the plasma jet becomes an afterglow, which we call 'far effluent' throughout this chapter.

Table 3.1: Parameter range and initial conditions at the start of the simulation, *i.e.* at 5 mm before the nozzle exit and 3 mm before the needle tip where the power deposition is maximum.

Initial electron density		10^8 cm^{-3}
Initial electron temperature		0.1 eV
Typical time step		0.1 ns
Update frequency Boltzmann solver		10 μs
Impurities in gas feed (estimated)		10 ppm O$_2$, 10 ppm N$_2$, 1 ppm H$_2$O
Parameters	Relative humidity	0 - 50 - 100%
	Total deposited power	2 - 6.5 - 20 W
	Gas temperature profile	300 K *const* - 600 K *max* - 800 K *max*

3.2 Results and discussion

In this section the production and loss processes of the different biomedically important species are analysed for three distinct regions of the plasma jet: inside the device with high power deposition (close to the needle electrode tip), in the plasma jet region with ambient air diffusion (still some power deposition and a significant electron density) and finally in the far effluent where the densities of both the charged species and the most reactive species have become very low. We will only analyse the reaction kinetics for the biomedically active species, with the exception of N$_2$(A) which is a key species for producing biomedically active species. The density profiles of these species are illustrated in figure 3.2, and the initial conditions and parameter range for which the calculations are performed are listed in table 3.1. Note that gas temperature profile '300 K' assumes room temperature throughout the plasma jet, whereas '800 K' and '600 K' refer to the peak temperature just after the nozzle exit (*i.e.* experimentally measured; more details in [40] and chapter 4).

The rates and the relative contributions of the various production and loss pathways for each species can be found in figures 3.3-3.16. The top figures illustrate the densities of the species for each of the distinct regions of the plasma jet simulation (see above). The values are spatially averaged for each specific region. A spatially resolved density profile for each of these
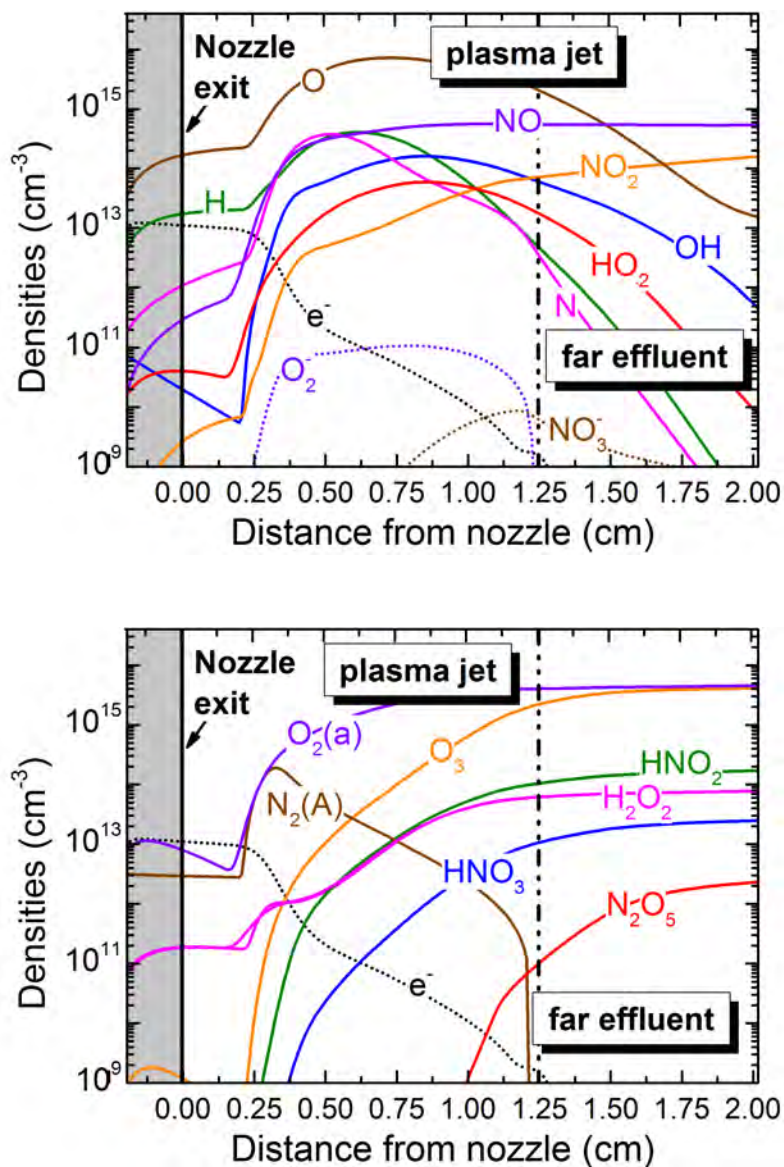
Figure 3.2: Density profiles of the biomedically active species and the species directly relevant for their reaction mechanisms, along the symmetry axis of the plasma jet. The radicals are plotted together with the charged species in the top graph and are indicated by a full line and a dotted line, respectively. In the bottom graph we present the metastable and the longer living molecules, indicated by a full line.

species can be consulted in figure 3.2 above. In the bottom graphs, the color bars represent the relative contributions of each production/loss reaction to the total production/loss of that species, again spatially averaged throughout each region. This total formation/loss rate is also presented on this graph (with the white dots, ∘), so the absolute rates of each reaction can be deduced. Note that reactions with contributions of less than 10% are excluded and this is why the bars sometimes do not completely add up to 100%.

Figures 3.3-3.16 also show the effect of variations in power, ambient air humidity and gas temperature evolution, compared to the conditions of the 'basic case' of 50% relative humidity, 6.5 Watt total applied power and the gas temperature profile from figure 3.1. The data of the conditions of this 'basic case' are indicated by stars (★) in the top graphs and with the hatched bars in the bottom graphs.

Finally, it is worth mentioning that if species densities (top figures) and absolute total rate values (white dots in bottom figures) do not fall within the range displayed in the figures, the relative rates (colour bars) in the bottom figures become irrelevant. This is because the rates and the densities are then too low, so that the corresponding reaction mechanisms (see legend) are unimportant.

First we will discuss in detail the production and loss mechanisms for the biomedically important species individually. We will emphasize the differences in the three different regions of the plasma jet and at varying operating conditions. However, note that varying the relative humidity of the ambient air will only start affecting the species densities after the nozzle exit (hence no effect for the region 'inside the device'). In a last section we will summarize the overall pathways for the production and loss of all the species.

3.2.1 $N_2(A^3\sum_u^+)$ metastable nitrogen

Although this electronically excited state of molecular nitrogen is not considered as a biomedically active species, we would like to discuss the reaction pathways of this species first (see figure 3.3) since it will later prove to be important for the air chemistry. One of the reasons is that its internal energy lies below the argon excitation levels and energy transfer from excited argon atoms to nitrogen molecules is possible. Because the N_2 density in the argon stream rapidly rises due to ambient air diffusion, the rate of such

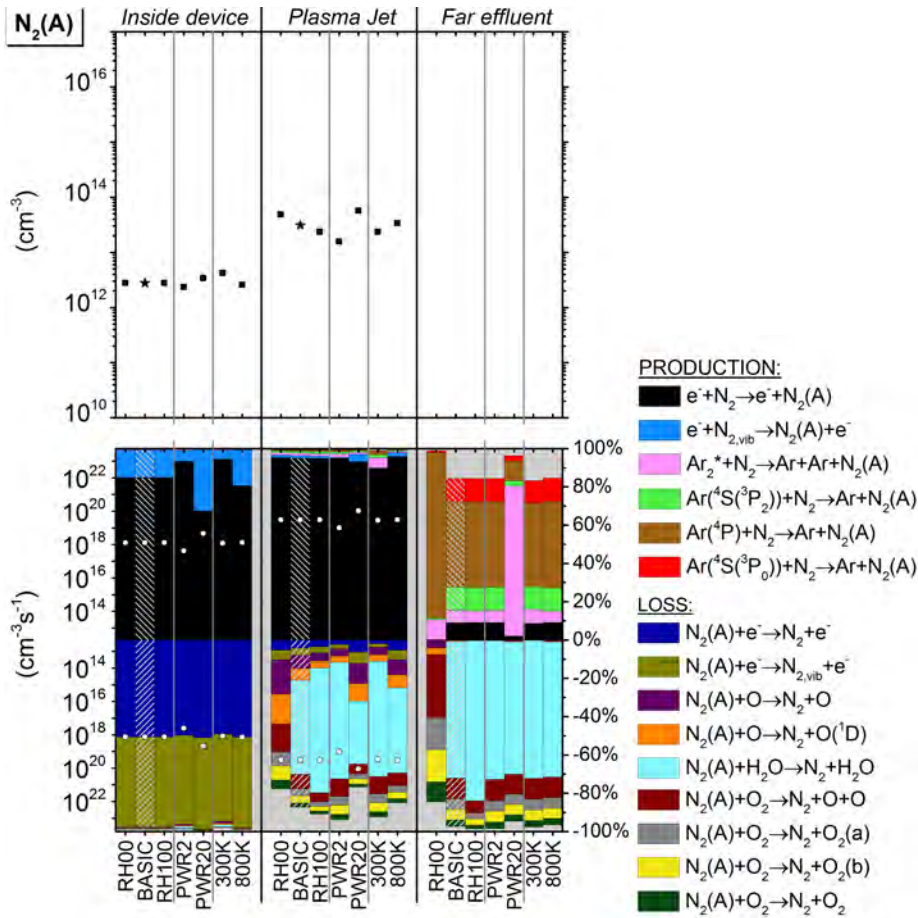Figure 3.3: Top graph: nitrogen metastable spatially averaged densities (cm^{-3}) for the three distinct regions of the plasma jet and for different operating conditions. The calculation results are presented for the 'basic' case (indicated with ★ symbols) which corresponds to 50% relative humidity (RH), 6.5 Watt applied power (PWR) and the gas temperature profile fitted to the experimental measurements. Additionally, the results for variations in RH (0% and 100%), PWR (2W and 20W) and gas temperature profile (indicated by their maximum of 300K and 800K) are shown. Bottom graph: the colour bars represent the spatially averaged relative contributions of the dominant reactions to the total production/loss (linked to the right y-axis with production in the upper half and loss in the lower half of the figure) for the same three regions and the same operating conditions. The (○) symbols indicate the spatially averaged absolute total production/loss rates (cm^{-3}s^{-1}), linked to the left y-axis. In this bottom graph, the results of the 'BASIC' case are indicated by hatched colour bars.

reactions increases significantly after the nozzle exit. Moreover, the energy content of $N_2(A)$ (6.17 eV) is sufficient to induce chemical changes in other molecules upon collisions (a typical single covalent bond energy is $\sim$ 2-5 eV). Note that singlet oxygen, $O_2(a^1\Delta_g)$, usually reaches a higher density in air plasmas but its internal energy of 0.98 eV is barely enough to cause any bond to break. As a consequence this species is not so important in the gas phase reaction mechanism of $Ar/O_2/N_2$ mixtures, although it might have a biochemical effect and thus be crucial for the applications.

Inside the device and in the first few mm after the nozzle exit, $N_2(A)$ is created by electron impact excitation reactions at all conditions investigated, mainly directly from the ground state but also to some extent stepwise through the vibrationally excited N_2 molecules:

$$e^- + N_2 \rightarrow e^- + N_2(A) \tag{1.1}$$

$$e^- + N_{2,vib} \rightarrow e^- + N_2(A) \tag{1.2}$$
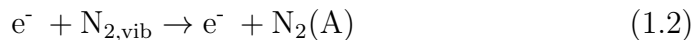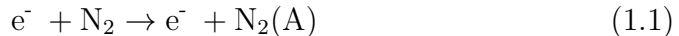
Clearly, de-excitation by electron impact reactions (*i.e.* the reverse of reactions 1.1 & 1.2) has only a slightly lower rate, which results in a limited net production for $N_2(A)$. Note that these are electron impact collisions with gas feed impurities as there is no ambient air diffusion in this region yet.

When the argon flows out of the device, it mixes with the ambient atmospheric air and the N_2 density rises, which results in an acceleration of all electron impact excitation reactions, although the electron density is already dropping. This is especially the case for reaction 1.1 which is now responsible for more than 95% of the formation of $N_2(A)$. Evidently, also the O_2 and H_2O densities are rising (and as a consequence also atomic O), so quenching of $N_2(A)$ by these species now dominates over electron impact de-excitation. Quenching by water molecules (reaction 1.3) turns out to be the most efficient:

$$N_2(A) + H_2O \rightarrow N_2 + H_2O \tag{1.3}$$
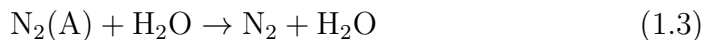
The observed mechanism easily explains why the $N_2(A)$ density increases with power in the active plasma jet (see top left graph of figure 3.3), because for higher power values the electron density and temperature increase, which in turn accelerate electron impact excitation.

The observed trend as a consequence of relative humidity variation in the active plasma jet is explained by the importance of quenching by H_2O (reaction 1.3). The $N_2(A)$ density appears to be indeed much higher for dry

ambient air conditions.

The effect of different gas temperature profiles is only small; the reason for the slightly higher $N_2(A)$ density for the higher temperature profile in the active plasma jet region, is simply that the density of the quenchers is lower. Recall that in our simulations we assume constant atmospheric pressure, so a higher temperature leads to lower densities.

In the far effluent region the $N_2(A)$ is largely consumed and this region will therefore not be discussed for this species.
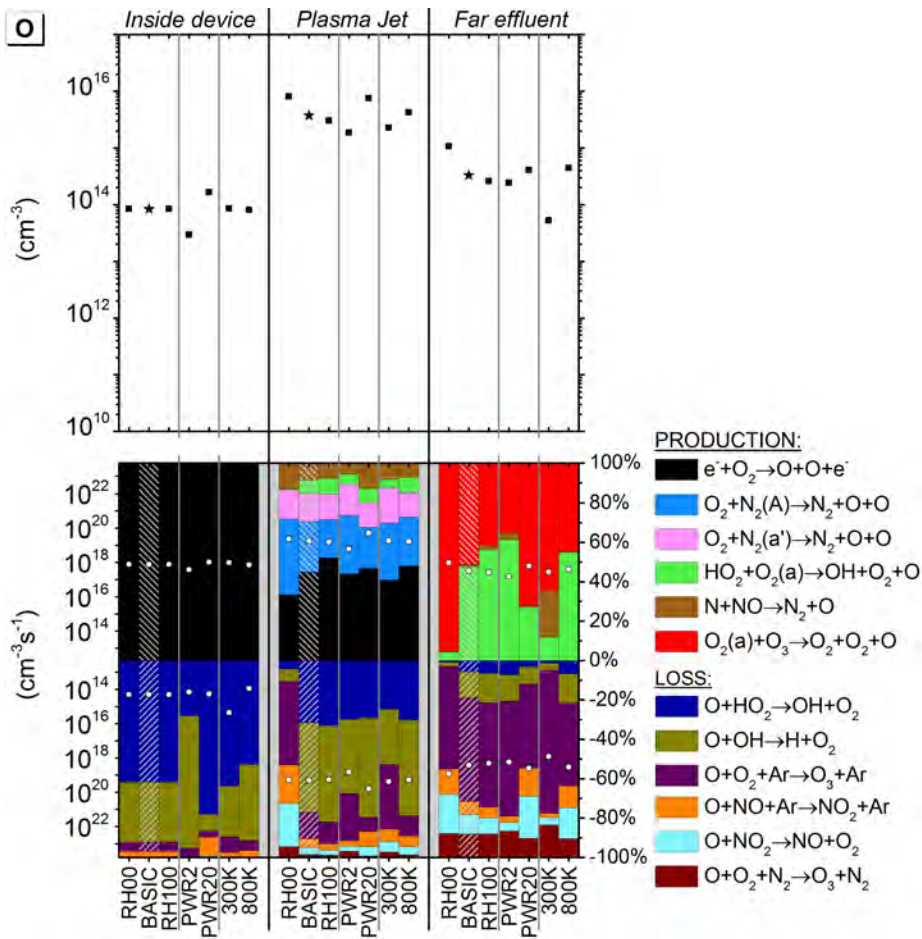
Figure 3.4: Similar graphs as in figure 3.3 but for O atoms.

3.2.2 O atom

One of the dominant (bio-)reactive species formed in plasma jet micro-discharges is the oxygen atom. First, we want to point out that electron impact excitation to $O(^1D)$ by reaction 2.1 and de-excitation by reaction 2.2 are filtered out of the data presented in figure 3.4, as they have practically no net effect on the chemistry. This is because $O(^1D)$ is quenched back to the ground state mainly by physical and not chemical quenching. Additionally, to our knowledge no other (chemically) important electronically excited states are created in significant quantities by this quenching process.

$$e^- + O \rightarrow e^- + O(^1D) \tag{2.1}$$
$$O(^1D) + M \rightarrow O + M \tag{2.2}$$

Inside the device O is predominantly formed by electron impact dissociation of O_2. This direct dissociation process is quite efficient since its cross section is favourable at the governing average electron temperature [170], especially compared with the cross sections of inelastic electron impact collisions with the other impurities: nitrogen and water [171, 172].

Therefore, high O densities are rapidly formed due to the efficient production, as well as the absence of significant loss processes inside the device. We see two reasons for this. First, the temperature in this region is quite high (about 600 K due to the needle electrode geometry) prohibiting association reactions of O with background gas species, *e.g.* ozone formation, which would obviously result in the loss of O atoms. The rate coefficient of this reaction indeed drops drastically with rising temperature:
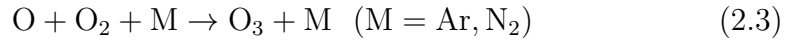
$$O + O_2 + M \rightarrow O_3 + M \quad (M = Ar, N_2) \tag{2.3}$$
$$k = 6.40 \times 10^{-35} exp(663.0/T_{gas}) \, cm^6 s^{-1}$$

Second, the humid air plasma components that react heavily with O and thus contribute to the loss of oxygen atoms, are only present in ppm levels and lower in the device. These reactants are mainly OH and HO_2 and NO_x. In the active jet region electron impact dissociation of molecular oxygen even accelerates, although the electron density is already decreasing. The rate increases because large amounts of ambient O_2 mix with the argon plasma. Nevertheless, this production channel through electron impact is less dominant in this region as dissociation by collisions with N_2 metastables ($N_2(a')$ and $N_2(A)$) also becomes important, again due to ambient air

diffusion. It should be noted that these species are created by electron impact themselves (see above).

As a consequence, the rise in O density is great but nonetheless limited by fast destruction processes with H containing species and 3-body association with O_2 (reaction 2.3) in this area.

In the far effluent the contribution of loss reaction 2.3 increases because the O_2 level keeps increasing due to diffusion and the rate coefficient rises as the temperature drops. Besides, OH and HO_2 species are largely depleted in this region and their role as O quencher is only partially taken over by NO and NO_2. Evidently, the O production is much lower in this region since no highly energetic electrons, or $N_2(A)$ metastable molecules, are left in the far effluent. Our simulations show that the production of O atoms is now dominated by collisions between $O_2(a)$ and O_3:

$$O_2(a) + O_3 \rightarrow O_2 + O_2 + O \tag{2.4}$$

Besides, the reaction between $O_2(a)$ and HO_2 (see figure 3.4 as well) is only important in the very beginning of the far effluent, because the HO_2 concentration decreases rapidly in this region (see figure 3.2).

The rate coefficient of reaction 2.4 has exactly the right value to cause a slow but long release of O. Moreover, most of the O is again converted into O_3 through reaction 2.3, which again leads to O as long as there is sufficient $O_2(a)$ present.

An increase in power leads to a clearly higher O density in all three regions (see top graph of figure 3.4) and this is again related to the increased electron impact reaction rates leading to more O_2 dissociation, directly from electron impact or indirectly through the N_2 electronically excited states $N_2(a')$ and $N_2(A)$ (as described above). However, the difference becomes smaller again towards the far effluent region and this results from the higher power as well, since this causes an increased generation of molecules that destroy O atoms, *e.g.* OH, NO_2 and HO_x (which are to a large extent created from O atoms themselves, see sections below).

The relative humidity has a drastic effect on the O density in the active plasma jet and the far effluent. More specifically, the O density increases for lower relative humidities. This is attributed to the higher production rates due to less quenching of $N_2(A)$ (see above) and, at the same time, lower loss rates because the densities of the most important quenchers, OH and HO_2, decrease for lower water concentration (see below).

Finally, the gas temperature profile has a strong influence on reaction 2.3,

more precisely the rate coefficient of this dominant loss reaction drops with rising temperature. This explains why the O density increases with temperature, as is clear from figure 3.4. The effect becomes even more pronounced towards the far effluent region where reaction 2.3 is the only dominant loss process remaining.
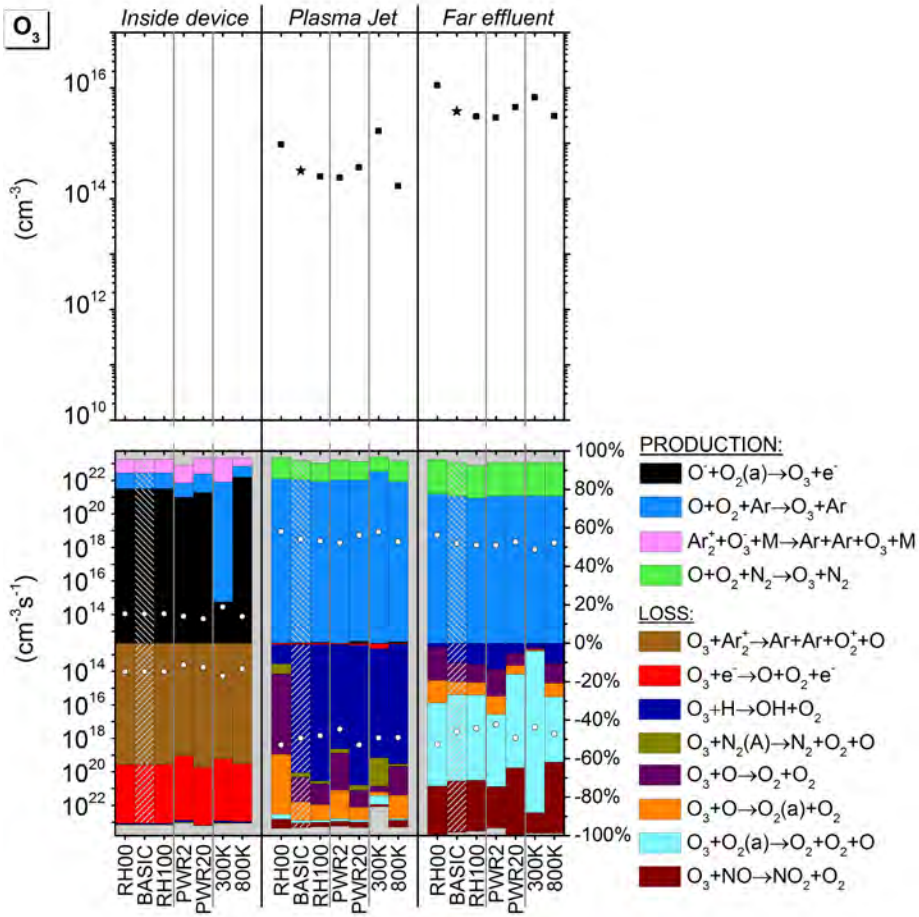

Figure 3.5: Similar graphs as in figure 3.3 but for O_3.

3.2.3 O_3

One can see from figure 3.5 that inside the device the density of O_3 is negligible at all conditions investigated. Furthermore, the production and loss rates are very low and therefore they will not be discussed.

In the active plasma jet region, where the gas is rapidly cooled and ambient air diffusion starts, this drastically changes as the formation rate rapidly increases due to the 3-body association reaction between O and O_2 (reaction 2.3), with either Ar or N_2 as third body. The net production is, however, still limited by the presence of highly reactive species like O and H, which cause the destruction of ozone through reactions 3.1, 3.2 and 3.3:

$$O + O_3 \rightarrow O_2 + O_2 \tag{3.1}$$
$$k = 8.00 \times 10^{-12} \exp(-2060.0/T_{gas}) \, \mathrm{cm^3 s^{-1}}$$

$$O + O_3 \rightarrow O_2 + O_2(a) \tag{3.2}$$
$$k = 1.00 \times 10^{-11} \exp(-2300.0/T_{gas}) \, \mathrm{cm^3 s^{-1}}$$

$$H + O_3 \rightarrow OH + O_2 \tag{3.3}$$

Ono and Oda [173] also stressed the importance of reaction 3.3 as the first step of a 'catalytic' reduction of ozone, where H acts as the catalyst. The second step is a reaction of the produced OH with O:

$$OH + O \rightarrow H + O_2 \tag{3.4}$$

Indeed, this second reaction is crucial as it additionally destroys an O atom which would normally form O_3 again in reaction 2.3.

The production rate of O_3 in the far effluent (mainly due to reaction 2.3) remains high since the lower O density (see figure 3.4 above) is being compensated by both an increasing O_2 density (due to ambient air diffusion) and an increasing rate coefficient (due to gas cooling). Moreover, the loss processes become less efficient in the far effluent region because H atoms are depleted (*cfr.* reaction 3.3) and, as already mentioned, the O density is dropping as well. Besides, destruction of ozone by these O atoms only occurs at elevated temperatures due to the strong temperature dependence of the rate coefficient of reactions 3.1 and 3.2 above. As a consequence of these three factors, the destruction is now dominated by collisions with less reactive, but long-lived NO and $O_2(a)$ species. This causes the ozone density to generally keep rising up to about 2 cm from the nozzle exit for the basic case study (see figure 3.2). Note that this distance might shift by

a few mm's, when varying the conditions.

Ozone appears to be more abundant at dry ambient air conditions, both in the active plasma jet and in the far effluent, since the O density is higher and thus also the formation rate. Additionally, the influence of loss reaction 3.3 rapidly decreases when approaching dry ambient air conditions. As a result the ratio of formation to destruction increases.

We see that the effect of power on the ozone density is quite small, both for the active plasma jet and for the far effluent. This is remarkable because ozone formation is very dependent on the O density which significantly rises with power, as explained in the previous section and *cfr.* figure 3.4. However, since this species is also involved in the destruction mechanism (reaction 3.1-3.4), higher O levels at higher powers only lead to a slight increase of the ozone density. Note that also the H density increases with power (see below), thus reaction 3.3 also contributes to a quite high destruction for the high power case study.

The temperature effect in the ozone production mechanism is very pronounced in the active plasma jet and related to the temperature dependence of the rate coefficients of reactions 2.3, 3.1 and 3.2. Indeed, the production rate (reaction 2.3) increases when the temperature is lower, while the loss rates (reaction 3.1 and 3.2) drop, hence causing a higher ozone density at lower temperature. However, we want to stress that, even the two elevated temperature cases reach temperatures close to 300 K in the far effluent (*cfr.* experimental data). Therefore, ozone formation is in fact, mostly, only 'delayed' in the high temperature cases and thus the density difference becomes smaller again towards the far effluent region.

3.2.4 $O_2(a)$

Inside the device, both the production and loss of the $O_2(a)$ state are governed by electron impact reactions, see figure 3.6. Clearly, the difference between production and loss is small and this results in a limited net production and a low $O_2(a)$ density.

In the active plasma jet region, the $O_2(a)$ density increases because the production through electron impact excitation accelerates due to the rising O_2 concentration (ambient air diffusion), which is thus more important than the drop in the electron density. Nevertheless, we see that the relative importance of electron impact excitation decreases by ambient air diffusion,
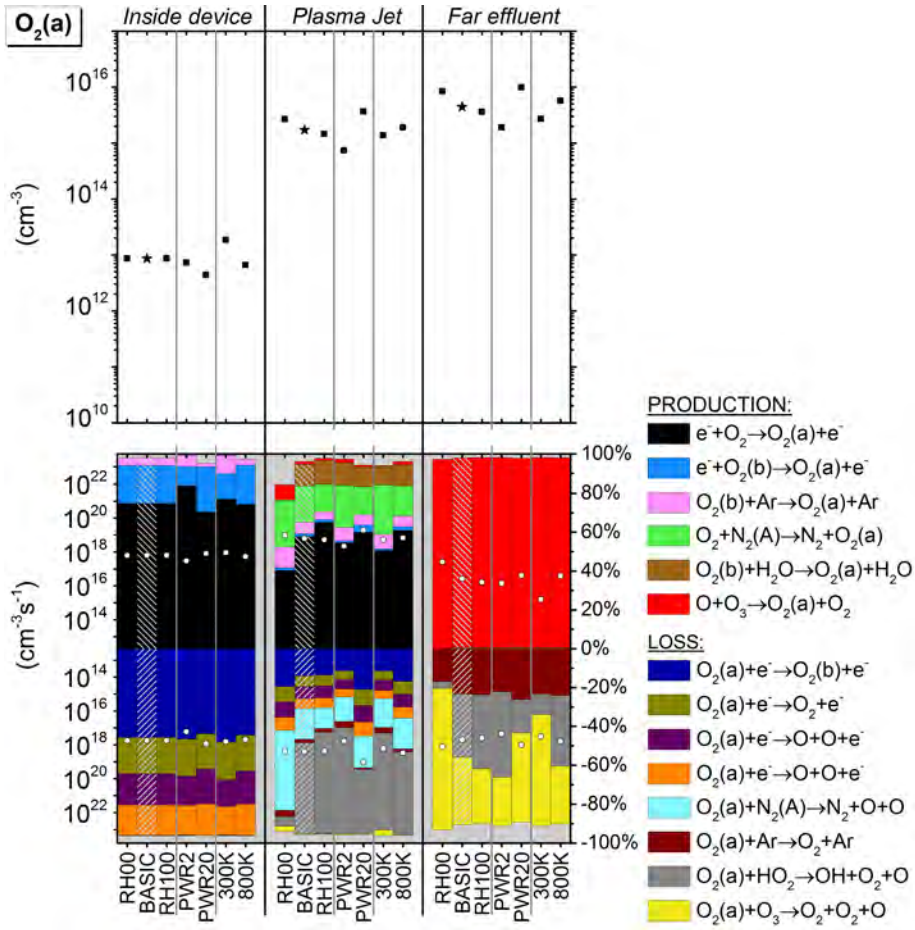
Figure 3.6: Similar graphs as in figure 3.3 but for $O_2(a)$.

since indirect processes, *i.e.* reactions involving $N_2(A)$, are now no longer negligible. Note, however, that $N_2(A)$ is also primarily created by electron impact excitation of the nitrogen ground state.

A decreasing importance of electron impact processes and an increasing importance of collisions with $N_2(A)$ is also seen for the loss processes in the first part of the active plasma jet region. Nonetheless, somewhat further in this region we see that quenching by HO_2 starts dominating the destruction pathway, where this species has a high concentration (see figure 3.2). Throughout the far effluent region HO_2 will become depleted and only chemical quenching by ozone and physical quenching by Ar will remain as significant loss processes.

For the production in the far effluent we see from figure 3.6 that only the reaction between O and O_3 (reaction 3.2 above) yields the formation of $O_2(a)$ far from the nozzle exit, as a consequence of the absence of energetic electrons and $N_2(A)$ metastables in that area.

It is worth to mention that $O_2(a)$ in fact only starts to be important for the chemistry of other species towards the far effluent, as its internal energy is rather low (0.98 eV) and only weak bonds can be broken. For example, $O_2(a)$ becomes, besides O atoms, a dominant quencher of HO_2 in that region (see section 3.2.7 below). Moreover, we want to stress that in these reactions OH is produced. Later it will be demonstrated that OH reacts further into HNO_2 and thus $O_2(a)$ indirectly accelerates the formation of HNO_2. A second chemical pathway where $O_2(a)$ acts as an important quencher, is the destruction of ozone in the far effluent, as already mentioned above (reaction 2.4).

In the active jet region we see that lowering the ambient air humidity results in a higher $O_2(a)$ concentration. This can mainly be attributed to the production processes, more specifically to an increased generation of $N_2(A)$ and the consecutive energy transfer to O_2, as the humidity has no effect on the total loss rate of $O_2(a)$ itself. The latter can be explained by the fact that a lower quenching by HO_2 is compensated by a higher quenching by $N_2(A)$ for more dry conditions.

The higher density of $O_2(a)$ at lower ambient air humidity in the far effluent is mainly related to the effect on the O_3 and the O densities (which demonstrate the same behaviour, see above), since these species are involved in the only significant production mechanism. Still, we observe that the effect is rather limited for $O_2(a)$ because O_3 is also an important quencher of $O_2(a)$ in this region, hence this counteracts the observed trend.

The influence of power variation in the active plasma jet is once again straightforward, since the $O_2(a)$ production is induced by electron impact reactions, directly or indirectly through $N_2(A)$, so a higher power results in a higher $O_2(a)$ concentration. The majority of $O_2(a)$ is produced in this area and by these reactions, thus the effect is even observable in the far effluent.

Our simulations demonstrate only a small effect of gas temperature variation in the active plasma jet region because the $O_2(a)$ pathways are dominated by electron impact reactions here, which are practically temperature independent. However, in the far effluent a lower $O_2(a)$ density for the 300K case can be observed. Indeed, at lower temperature, both the O density in this region and the rate coefficient of reaction 3.2 are lower, causing a lower production rate, whereas for the loss rates, the lower concentration of the HO_2 quencher is compensated by an increase in the density of the O_3 quencher.

3.2.5 N atom

First of all, we need to point out that for figure 3.7 the excitation and de-excitation reactions to the $N(^2D)$ state were filtered out to show the chemically most relevant reactions. This $N(^2D)$ state has a negligible limited effect on the N reaction chemistry, with the following exception:

$$H_2O + N(^2D) \rightarrow OH + NH \tag{5.1}$$

$$O + NH \rightarrow H + NO \tag{5.2}$$

Thus, we see that NH immediately reacts further with O atoms to form NO, just as N would do (see below) but on a much smaller scale. Note that H_2O and O are much more abundant and do not 'feel' the reactions with N and NH. Furthermore, we will see in the following sections from figures 3.8 and 3.10 that the consecutive reactions 5.1 and 5.2 are not a dominant production pathway for OH or H atoms either. As a result, we conclude that this pathway has no influence on the chemistry of other species.

Figure 3.7 shows that the production of N atoms inside the device and in the active plasma jet is mainly due to the dissociation of N_2 upon collision with metastable (or higher excited) argon atoms (reaction 5.3), in contrast to O_2 dissociation which is dominated by electron impact processes (see
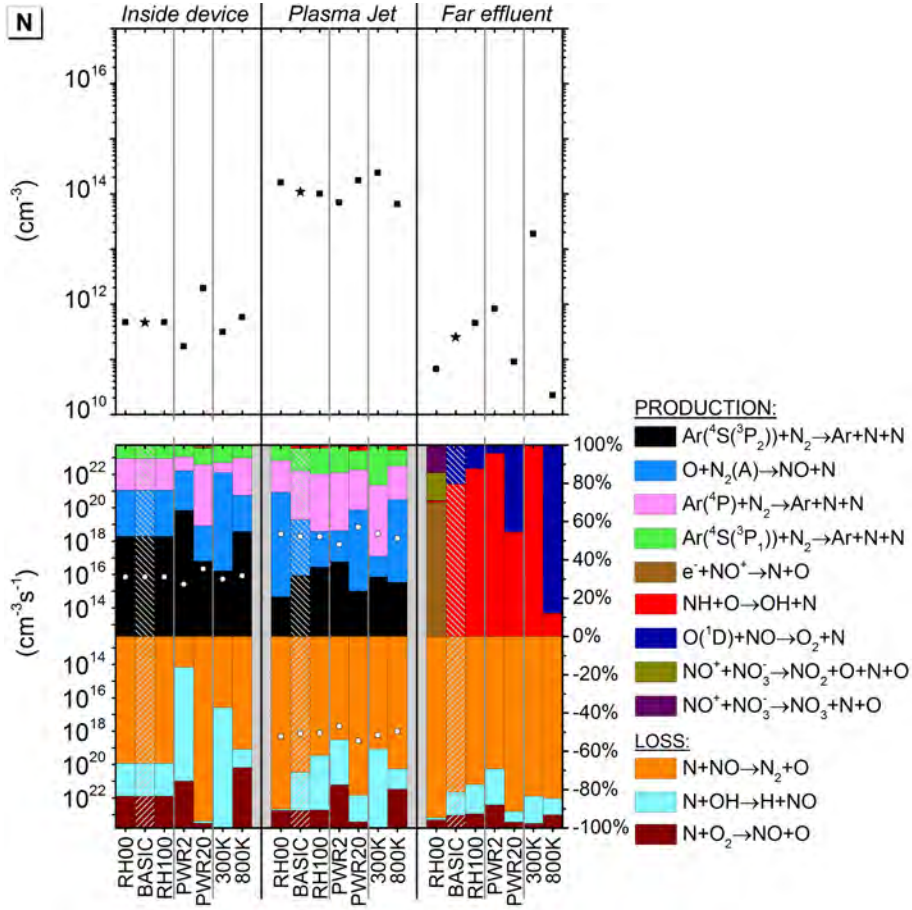
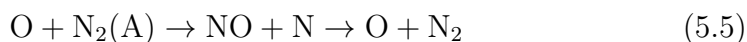Figure 3.7: Similar graphs as in figure 3.3 but for N atoms.

section 3.2.2). A second important source for N atoms inside the device is the collision of nitrogen metastables ($N_2(A)$) with O atoms (reaction 5.4). Clearly, this reaction type needs 'activation' of N_2 to $N_2(A)$ by electron impact excitation (see section 3.2.1 above).

$$Ar^* + N_2 \rightarrow Ar + 2N \qquad (5.3)$$
$$O + N_2(A) \rightarrow NO + N \qquad (5.4)$$

Inside the device N_2 is only present in ppm levels and the formation of N atoms is therefore limited. In the active plasma jet region the rates of the aforementioned reactions with argon species rapidly increase. Obviously, this is due to ambient N_2 diffusing into the jet, causing the N_2 concentration to rise drastically. Reaction 5.4 accelerates almost equally for the 'basic' case and this can be attributed to the fact that both reactants of this reaction also (temporary) become available in higher quantities here (see sections above). The increase in the loss processes (*i.e.* collisions with NO, OH and O_2) is, however, not as large, which explains the rapidly rising N density in the active plasma jet.

At the beginning of the far effluent region, the N density has dropped again to about 10^{11} cm^{-3} as the N production quickly stops because Ar metastables and $N_2(A)$ are very efficiently quenched by various diffusing ambient air components. Additionally, the rate coefficients of the dominant loss reactions (*i.e.* collisions with OH and NO) are large and these quenchers reach about the same density as N itself at the end of the plasma jet region.

We also want to stress the importance of the following reaction paths for the active plasma jet:

$$O + N_2(A) \rightarrow NO + N \rightarrow O + N_2 \qquad (5.5)$$
$$\text{and}$$
$$O_2 + N \rightarrow NO + O \quad \text{followed by} \qquad (5.6)$$
$$NO + N \rightarrow O + N_2 \quad \text{with} \qquad (5.7)$$
$$k = 8.20 \times 10^{-11} \exp(-410.0/T_{gas}) \text{ cm}^3\text{s}^{-1}$$

The first pathway does not result in any net production of N, and in fact simply leads to quenching of $N_2(A)$. The second pathway (5.6 & 5.7), yields the destruction of two N atoms. In both pathways, reaction 5.7 is crucial and its rate coefficient is highly temperature dependent (*i.e.* rising with higher temperature). It explains why the net N production, and hence the

N density, is significantly lower for the high temperature cases both in the active plasma jet and especially in the far effluent.

The effect of relative humidity variation in the active plasma jet is governed by both the production and the loss; the rate of N production (reaction 5.4) increases for dry ambient air (due to higher concentrations of both reactants, see above) and the loss of N atoms by collisions with OH (which has a lower density at low humidity, see below) is reduced. This results in a higher N density. However, towards the far effluent the effect on the N density is not determined by a production process anymore but by the loss upon collisions with NO (reaction 5.7). As this quencher is more abundant at low relative humidity, the trend for the far effluent becomes opposite (*i.e.* a significantly lower N concentration at lower humidity).

This opposite trend is also observed when varying the power. Applying more power generates more $N_2(A)$ and O, as well as Ar*, both inside the device and in the active plasma jet, hence increasing the N density in both regions. Nevertheless, towards the far effluent, the higher power has generated much more quenchers (see sections on NO and OH below) and the trend is reversed; the N concentration now drops significantly faster at higher power.

3.2.6   H atom

Figure 3.8 shows that the production of the H atoms inside the device is dominated by electron impact reactions, *i.e.* dissociation of OH and dissociative recombination with H_2O^+. Important is that Ar_2^+ and H_2O are always involved, although this can not be deduced only from figure 3.8. The first mechanism is with OH as an intermediate:

$$Ar_2^+ + H_2O \rightarrow ArH^+ + Ar + OH \qquad (6.1)$$
$$e^- + OH \rightarrow e^- + OH(A) \rightarrow e^- + O + H \qquad (6.2)$$
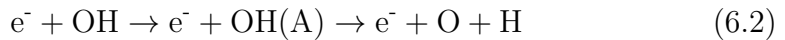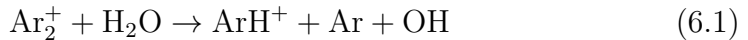
The second pathway has H_2O^+ as an intermediate:

$$Ar_2^+ + H_2O \rightarrow H_2O^+ + Ar + Ar \qquad (6.3)$$
$$e^- + H_2O^+ \rightarrow O + H + H \qquad (6.4)$$
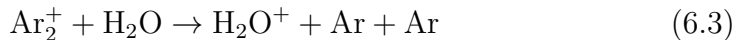
The loss reactions in this region are of minor importance compared to the production, resulting in a significant H production within the device, in spite of the low water impurity concentrations.
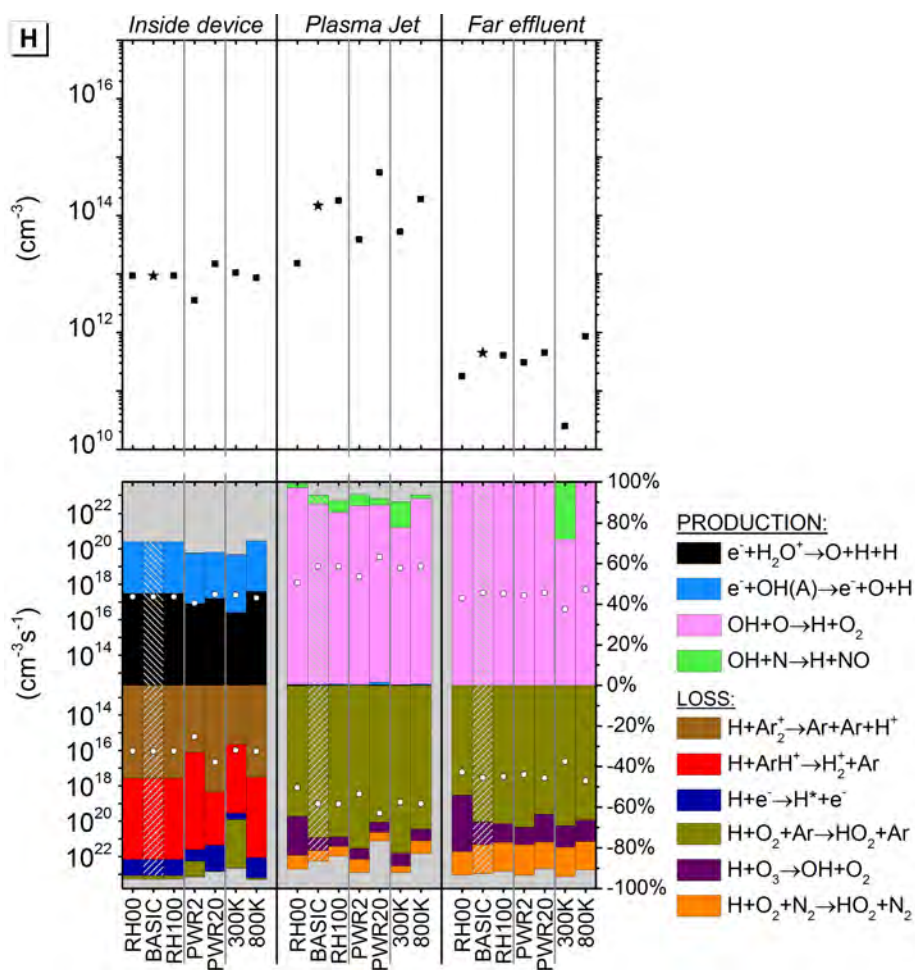
Figure 3.8: Similar graphs as in figure 3.3 but for H atoms.

When humid air starts diffusing into the jet, the production first increases due to the higher H_2O concentration, but only for a very short time, as Ar_2^+ is no longer generated in large quantities. Afterwards, there is in fact no production of 'new' H atoms anymore. Indeed, figure 3.8 demonstrates that the H atoms are predominantly generated from OH radicals, both in the active plasma jet and in the far effluent, by reactions 6.5 and 6.6, as long as the densities of O and N atoms remain sufficiently high:

$$OH + O \rightarrow H + O_2 \tag{6.5}$$

$$OH + N \rightarrow H + NO \tag{6.6}$$

Actually, we will see later that the OH radicals are mainly produced from H atoms in these regions, so it is a regeneration process. This can already be partially inferred from figure 3.8, because the H atoms are lost mainly to HO_2 through reaction 6.7, in both the active plasma jet and far effluent.

$$H + O_2 + M \rightarrow HO_2 + M \tag{6.7}$$

$$k = 6.09 \times 10^{-32} \left(\frac{T_{gas}}{300} \right)^{-0.80} cm^6 s^{-1}$$

These HO_2 molecules will react further to OH (see section 3.2.7 below). Additionally, direct conversion of H atoms into OH radicals by ozone contributes for about 10% to the total loss:

$$H + O_3 \rightarrow OH + O_2 \tag{6.8}$$

In the far effluent region the N and O densities are reduced to too low levels to maintain the crucial steps of the regeneration process (reactions 6.5 and 6.6) and the H density becomes very low.

The fact that Ar_2^+ is a key component in the formation mechanism of H atoms obviously explains why the H atom density increases for a higher applied power, both inside the device and in the active plasma jet, because the Ar_2^+ density is very dependent on the electron density and electron temperature, which rise with power.

The importance of the 3-body association reaction 6.7 for the loss of H atoms is the main reason why the H density is lower in both the active plasma jet and the far effluent, when the jet is cooler. The rate of this reaction typically drops significantly for a higher gas temperature, due to the reaction rate coefficient and the density of the third collision partner M.

The effect of ambient air humidity variation is of course trivial for all hydrogen containing species, as their density evidently increases with water concentration.
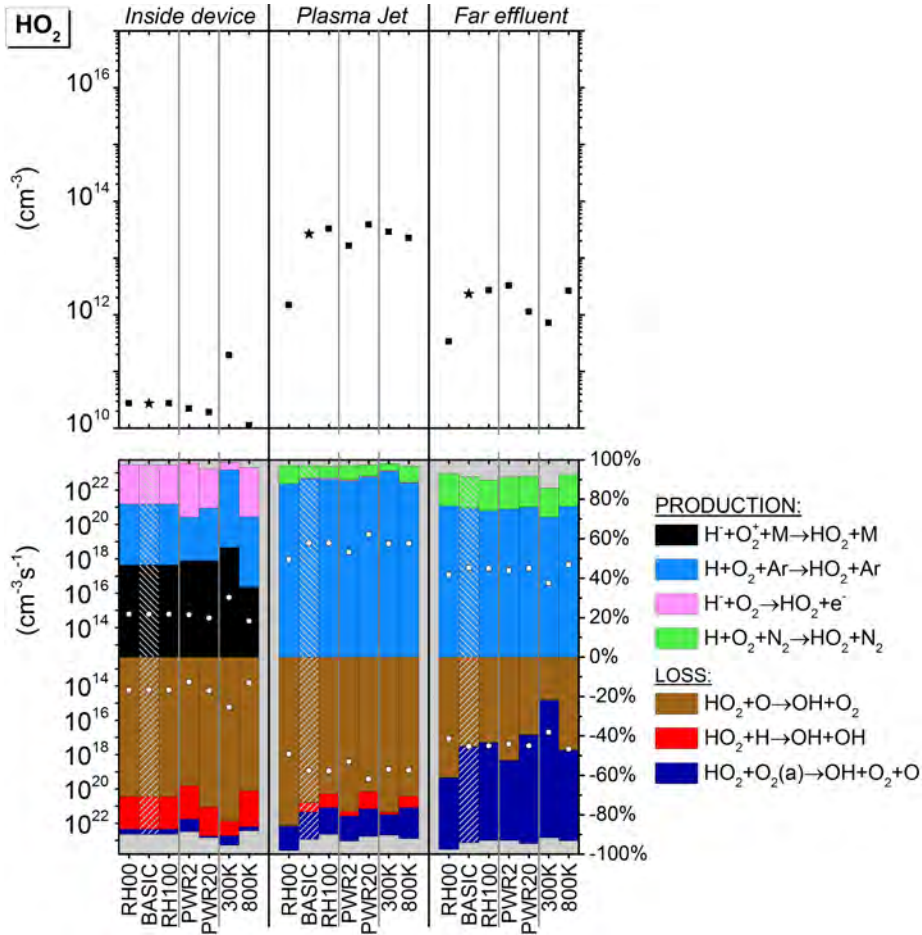

Figure 3.9: Similar graphs as in figure 3.3 but for HO_2.

3.2.7 HO_2

In figure 3.9 we see that the HO_2 density is negligible within the device. The explanation is that the temperature is simply too high for efficient associative 3-body collisions between H and O_2 (reaction 6.7). Additionally,

the H and O_2 densities are still rather low in this region.

The situation drastically changes when the argon flows into the open atmosphere and ambient air diffusion starts, since the temperature now rapidly cools down. Moreover, the H and O_2 concentrations are now sufficient for significant HO_2 production through reaction 6.7. However, the rapid depletion of H further away from the nozzle prohibits the maintenance of such high rates in the far effluent (see section 3.2.6), explaining the drop in the HO_2 density.

The loss processes shown in figure 3.9 confirm that HO_2 is indeed converted into OH (as mentioned in the previous section). In the active plasma jet this occurs predominantly by reaction pathway 7.1 and to some extent by reactions 7.2 and 7.3, whereas in the far effluent only reactions 7.1 and 7.2 play a role. The rate coefficient of reaction 7.1 rises upon lower gas temperature and this compensates for the gradual decrease of the O density. Furthermore, reaction 7.2 becomes gradually more important in the far effluent, because $O_2(a)$ is a long-lived species within this time scale (see section 3.2.4), whereas H is not.

$$HO_2 + O \rightarrow OH + O_2 \tag{7.1}$$
$$HO_2 + O_2(a) \rightarrow OH + O_2 + O \tag{7.2}$$
$$HO_2 + H \rightarrow OH + OH \tag{7.3}$$
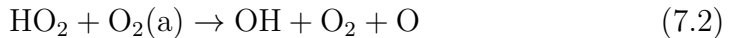
The effect of power on the HO_2 concentration in the active plasma jet is not very large compared to the effect on the H density (see figure 3.8) since both production and loss are strongly enhanced by increasing power. The reason why the HO_2 density drops faster towards the far effluent at high power is that the production arises from the very short living H atoms, whereas the destruction is regulated mainly by longer living species O and $O_2(a)$. The HO_2 density is thus determined by the loss reactions with O and $O_2(a)$ which are generated in higher quantities for higher powers.

It is remarkable that the temperature variation has only a small effect on the density of HO_2 in the active plasma jet. The explanation is that the higher density of H atoms at higher temperatures, counteracts the drop in the rate coefficient for the 3-body association reaction (reaction 6.7). Similarly, the increase in O density compensates for the lower rate coefficient of the main destruction pathway, *i.e.* reaction 7.1, in the high temperature case. In the far effluent a much stronger temperature dependence of the HO_2 density is observed, as the density clearly increases with temperature.

Note that the temperature difference between the cases is only small in this region and the rate coefficients are thus similar. Therefore, the effect on the HO_2 concentration must be related directly to the more rapid depletion of H atoms at low temperatures (see section 3.2.6) and hence a smaller production rate of HO_2.

Finally, the effect of ambient air humidity is again evident, as HO_2 is also a derivation product of H_2O, so its density drops significantly at dry air conditions.
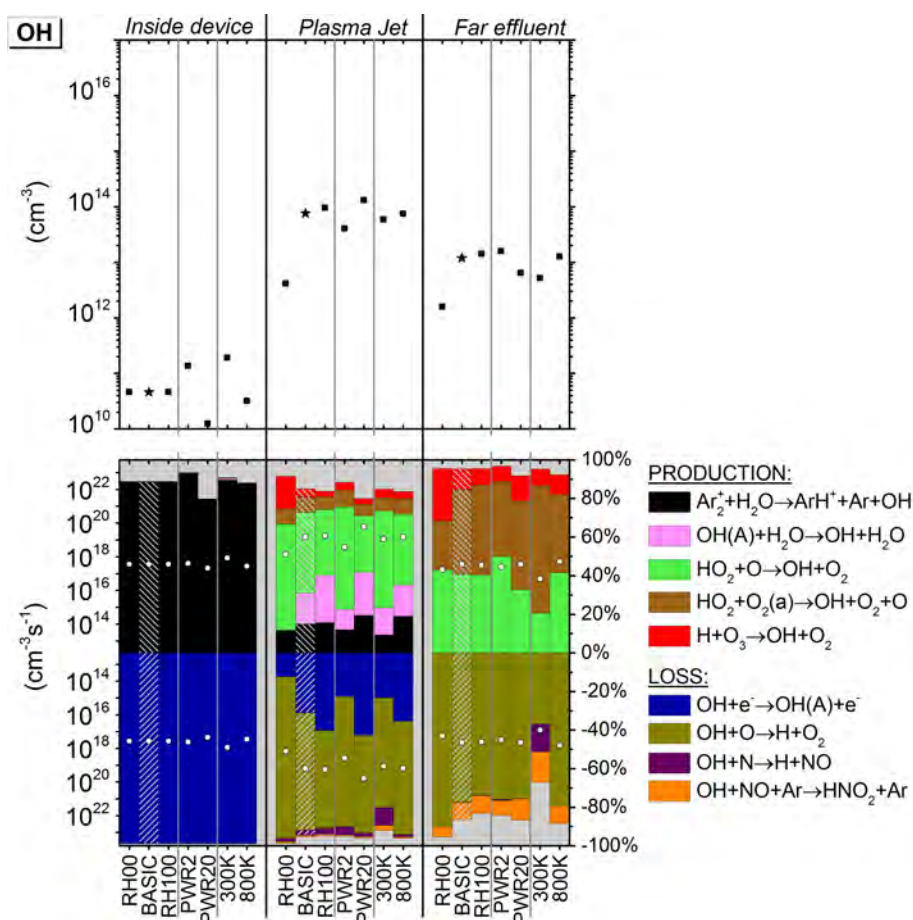
Figure 3.10: Similar graphs as in figure 3.3 but for OH.

3.2.8 OH

The production of OH radicals inside the device is by collisions of Ar_2^+ with H_2O (see reaction 6.1 above). A large fraction of the OH radicals is electronically excited to OH(A), which is the only dominant loss process for OH in this region (see figure 3.10). This OH(A) state is more easily dissociated by electron impact than ground state OH (see reaction 6.2). Still, most of the OH(A), about 80% (data not shown), will simply decay radiatively back to the ground state. Nevertheless, as a result of the efficient electron impact excitation, most of the OH is present in the form of OH(A): about a 6-fold higher density. All this results in a low OH density inside the device.

In the active plasma jet region and the far effluent, the pathways for water species become more complex and involve many different reactive species. OH is not as efficiently dissociated anymore by electron impact reactions (through OH(A); reaction 6.2) and H is gradually being converted into OH, mainly through HO_2 that acts as an intermediate species (see reaction 6.7, followed by reactions 7.1 and 7.2 presented above) as well as by the direct pathway (reaction 6.8 mentioned above).

Nevertheless, a lot of OH is still converted back into H, both in the active plasma jet and the far effluent, but now mainly through reaction 6.5 and to a lower extent by reaction 6.6, as long as the densities of the collision partners O and N remain high. When the densities of the reactive species O and N have sufficiently dropped in the far effluent, the regeneration of H will stop and OH is converted into HNO_2, HNO_3 and H_2O_2 (the last two processes only contribute for a few % and are therefore not shown in figure 3.10).

The regeneration of H and 'recycling' of OH was also observed by Komuro et al [174] in an air streamer discharge. A similar reaction scheme was identified, although the conditions were very different (gas composition, power regime and a stationary gas).

The importance of the OH loss reaction to HNO_2 was already stressed in Fresnet et al [175]. Additionally, the author identified this reaction as a dominant loss pathway for NO as well (see also section 3.2.9 on NO below). The study concerned a pulsed parallel plate discharge in $N_2/H_2O/NO$ mixtures.

Because OH is mainly produced from HO_2 (see above), the density trend for OH under influence of power and temperature, is practically the same as for HO_2. More specifically, in the plasma jet region the OH density

clearly increases with power but is not so much affected by temperature. The explanation is that a higher density of the reactants, due to a higher temperature, is compensated by a decrease in the production reaction rate coefficient for the main reactions, resulting in an almost equal production for all temperature cases (identical explanation for the destruction). Note that in the far effluent OH simply follows the density trend of its precursor HO_2 and the quenchers of HO_2 (in particular O and O_2(a)), *i.e.* increases with temperature (the temperature influence on the rate coefficient is irrelevant as the temperature is practically the same for the three different temperature profiles in this region).

Again the effect of ambient air humidity is obvious, as OH is derived from H_2O.

3.2.9 NO

Inside the device the impurity levels are too low to create a high amount of the reactive species out of which NO can be formed. Moreover, figure 3.11 illustrates that NO is efficiently dissociated by electron impact and argon excimers. As a result the NO concentration remains very low inside the device. Therefore, we will not discuss the production and loss processes of NO in this region further.

The pathways drastically change when the argon discharge flows into the open humid air atmosphere: plenty of OH, N, O and N_2(A) become available and a large amount of NO is now rapidly formed from these species (their origin was explained in detail in the sections above)

The formation of NO through NO_2 in the active plasma jet region, however, needs to be interpreted with caution since this species is formed from NO itself by an associative 3-body reaction between O and NO (see also below and section 3.2.10). The reactions of NO_2 with O and H, as shown in figure 3.12, therefore have to be considered as a regeneration pathway and not as the production of 'new' NO.

$$H + NO_2 \rightarrow OH + NO \qquad (9.1)$$
$$O + NO_2 \rightarrow NO + O_2 \qquad (9.2)$$

Clearly, this comment is even more valid for the far effluent region where only these two pathways (and especially reaction 9.2) are able to generate
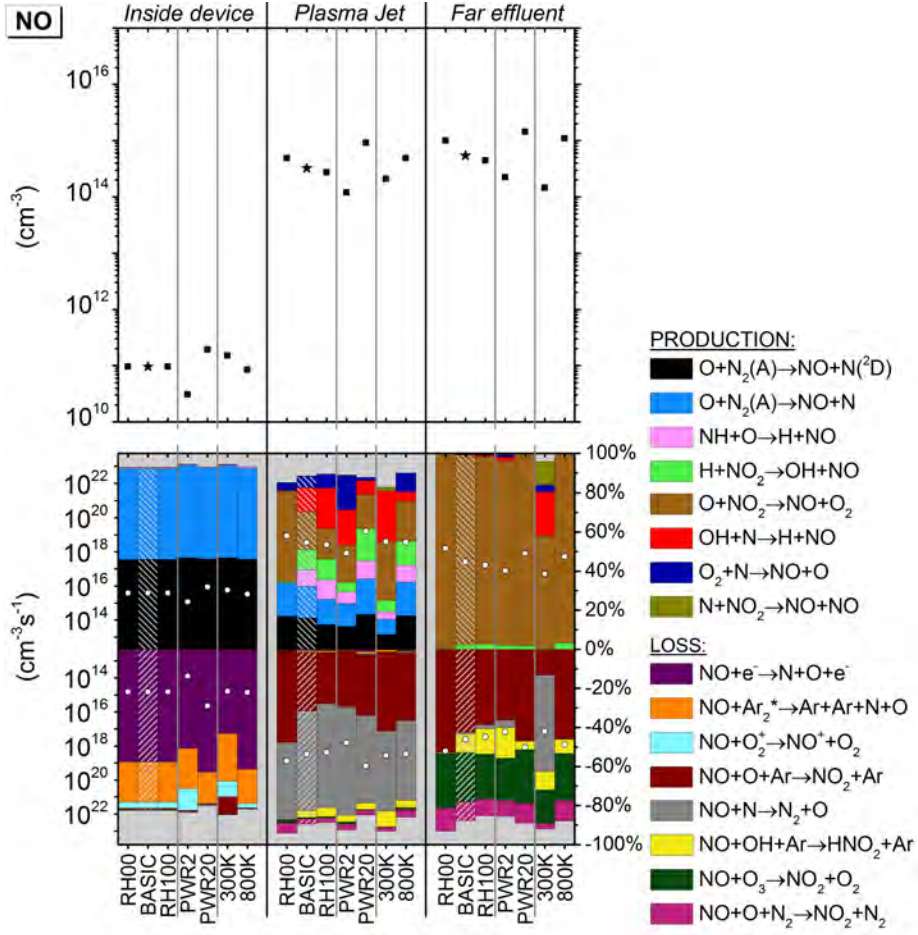
Figure 3.11: Similar graphs as in figure 3.3 but for NO.

NO.

As a consequence, our simulations indicate that four pathways are responsible for the creation of 'new' NO in the active plasma jet, *i.e.* reaction 5.2 listed in section 3.2.5, and the following three processes:
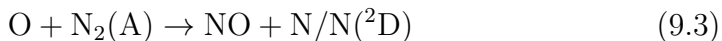
$$O + N_2(A) \rightarrow NO + N/N(^2D) \tag{9.3}$$

$$OH + N \rightarrow H + NO \tag{9.4}$$

$$O_2 + N \rightarrow NO + O \tag{9.5}$$

Figure 3.11 shows that reaction 9.3 is the most important of these four. Concerning the loss processes, the formation of NO_2 upon a 3-body association reaction between O and NO is important both in the active plasma jet and the far effluent, as mentioned earlier:

$$O + NO + M \rightarrow NO_2 + M \tag{9.6}$$

$$k = 1.00 \times 10^{-31} \left(\frac{T_{gas}}{300} \right)^{-1.60} \text{cm}^6\text{s}^{-1}$$

Moreover, reaction 9.7 is the second important loss process for NO in the active plasma jet region:

$$N + NO \rightarrow N_2 + O \tag{9.7}$$

$$k = 8.20 \times 10^{-11}\exp(-410.0/T_{gas}) \text{ cm}^3\text{s}^{-1}$$

This reaction is quite important because it leads to a rapid decrease in both the reactivity and bio-reactivity of the plasma jet, since one of the reaction products is stable molecular nitrogen.

The rates of the two loss processes diminish towards the far effluent because of the density drop of the atomic O and N quenchers. This is especially true for the reaction with N atoms, of which the concentration is low in the far effluent. Besides, the rate coefficient of the 3-body association reaction between O and NO does not rise so strongly with decreasing temperature (see reaction 9.6 above) compared to other reactions of this type that were discussed in previous sections. Thus, it cannot compensate entirely for the decreasing O density in the region far from the nozzle exit and hence the rate of this process drops as well. This makes that the conversion of NO to NO_2 upon collision with O_3, which is a long-lived species, gains importance in the far effluent. Additionally, as long as there is still OH available, some

NO is also converted into HNO_2, again by an associative 3-body reaction. A variation in the relative humidity of the ambient air has only a limited effect on the NO density. The reason is two-fold: first, NO is lost by collisions with species that are also responsible for the production (*i.e.* N and O atoms). Thus, a higher density of such reactive species at dry conditions leads to both a higher production and a higher loss. In the far effluent we see exactly the same phenomena where NO is created from O and lost mainly by collisions with O and O_3. The latter is of course directly generated from O. Second, the generation of NO is facilitated by multiple pathways. In the case of high humidity, reactions 9.4 and 5.2 partially compensate for the decreasing production through reactions where N, O and $N_2(A)$ are involved. The effect of power on the NO densities is more pronounced and the net production increases at higher power, explaining the rise in NO concentration, although the different relative contributions do not change drastically. The effect of gas temperature in the active plasma jet region is quite complex. The difference in density as a function of the three temperature profiles must be attributed to the loss processes because the total production rate is practically the same for all temperature cases, as can be seen from table 3.2. This table explains how the different NO production pathways behave under the influence of temperature in the plasma jet region. The conclusion is that the net effect on the total production rate is indeed very small, because different trends compensate each other. The total loss rate, on the other hand, drops upon increasing temperature, due to the lower rates of the associative 3-body reactions between O and NO (reaction 9.6). The other important loss channel (*i.e.* reaction 9.7) stays more or less constant with increasing temperature, since the increasing reaction rate coefficient compensates for a lower N density (see section 3.2.5). Overall, as the production rate stays more or less constant, and the loss rate drops at higher temperature, this explains the higher NO density at higher temperature in the active plasma jet.

In the far effluent region, the effect of the different temperature profiles is more straightforward, as the temperature is now close to 300K in all the cases and most of the reactive species are depleted. Production is now dominated by reaction 9.2 and due to the higher density of O in the high temperature cases, this reaction causes a higher regeneration of NO from NO_2. Moreover, the effect is enhanced by loss reaction 9.7 which is very slow for the high temperature cases, due to more rapid depletion of N (see section 3.2.5). Hence, both the higher production rate and lower loss rate

Table 3.2: Effect of increasing temperature on the production rates of NO in the plasma jet region

Reaction	Rate coeff.	Reactant 1	Reactant 2	Total
5.2	-	NH ($\downarrow$)	O_2 $\uparrow$	($\uparrow$)
9.1	$\uparrow$	H $\uparrow$	NO_2 $\downarrow$	($\uparrow$)
9.2	$\downarrow$	O $\uparrow$	NO_2 $\downarrow$	($\downarrow$)
9.3	$\uparrow$	O $\uparrow$	$N_2(A)$ ($\uparrow$)	($\uparrow$)
9.4	-	OH ($\uparrow$)	N $\downarrow$	$\downarrow$
9.5	$\uparrow\uparrow$	O_2 -	N ($\downarrow$)	$\uparrow$

explain the increase of the NO concentration in the far effluent for the higher temperature cases.

3.2.10 NO_2

The NO_2 density is negligible inside the device, so we do not discuss the production and loss processes in this region.

As explained in the previous section, the production of NO_2 in the active plasma jet and the far effluent is dominated by reaction 9.6 with Ar as third body. From figure 3.12 we can see that, in the far effluent, NO oxidation by O_3 or NO_3 also become significant, as these two species have reached a high concentration in the far effluent.

The two NO regeneration processes upon collision with H or O (*i.e.* reactions 9.1 and 9.2) are clearly the most important loss processes for NO_2 in the active plasma jet, whereas in the far effluent only the quenching by O atoms (reaction 9.2) remains due the absence of H.

The NO_2 density in the active plasma jet and the far effluent rises for dry air conditions, as well as with increasing power. These effects can simply be explained by the fact that O, NO, O_3, which are the main species out of which NO_2 is formed demonstrate, the same trend. Even the increased quenching by H atoms (which also demonstrates a density rise) cannot compensate for it. Note that O is involved in both the predominant loss and formation reactions, which limits the net effect.

The effect of gas temperature is more complex. We see that in the active plasma jet the NO_2 concentration drops at higher temperature, whereas
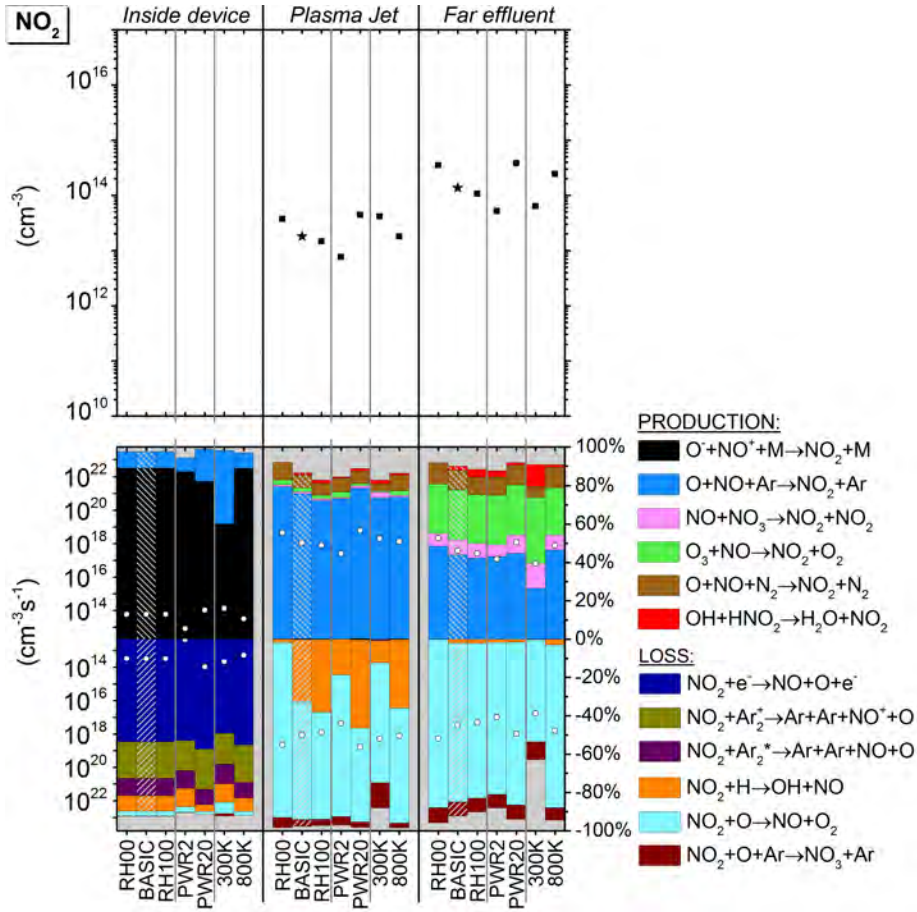
Figure 3.12: Similar graphs as in figure 3.3 but for NO_2.

the effect is opposite in the far effluent. This can be explained as follows: in the active plasma jet NO_2 formation is inhibited for high temperature cases because of the temperature dependent rate coefficient of production reaction 9.6 (although the densities of both NO and O increase with temperature) and at the same time the main quenching mechanism of NO_2, *i.e.* reaction 9.2, becomes relatively faster (see table 3.2). Note that the latter is partially compensated by a deceleration of further oxidation of NO_2 into NO_3 as a loss process at higher temperature.

Nevertheless, the temperature effect in the plasma jet region is indeed only temporary; in the far effluent the NO oxidation into NO_2 becomes more efficient in the higher temperature case, because the O atoms are much less converted into O_3 in such a case.

3.2.11 N_2O_5

For N_2O_5, we only focus on the production and loss processes in the far effluent because its density is negligible inside the device as well as in the active plasma jet.

The generation of N_2O_5 is straightforward. For the formation and the destruction there is only one relevant mechanism (see figure 3.13):

$$NO_2 + NO_3 + M \leftrightarrow N_2O_5 + M \qquad (11.1)$$

$$k_{forward} = 2.80 \times 10^{-30} \left(\frac{T_{gas}}{300}\right)^{-3.50} cm^6.s^{-1}$$

$$k_{backward} = 1.33 \times 10^{-03} \left(\frac{T_{gas}}{300}\right)^{-3.50}$$
$$\exp(-11000.0/T_{gas}) \, cm^3.s^{-1}$$

Due to the very high temperature dependence of these reaction rate coefficients, the balance will shift to the right at low temperatures whereas the balance is shifted to the left at elevated temperatures. Hence, this explains the higher N_2O_5 concentration for the low temperature case. Indeed, except for the 300 K case N_2O_5 formation starts only in the far effluent when the temperature is very close to room temperature.

N_2O_5 production is favoured at higher power and in dry ambient air since these conditions give rise to higher densities of the reactants.
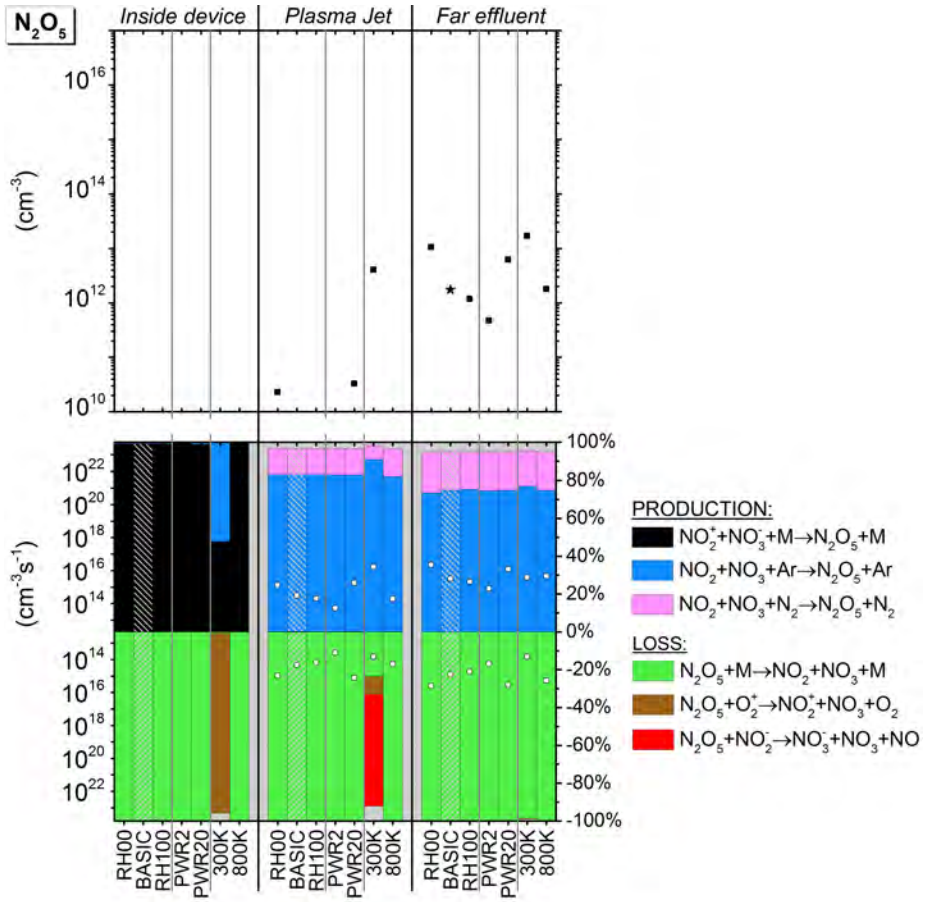
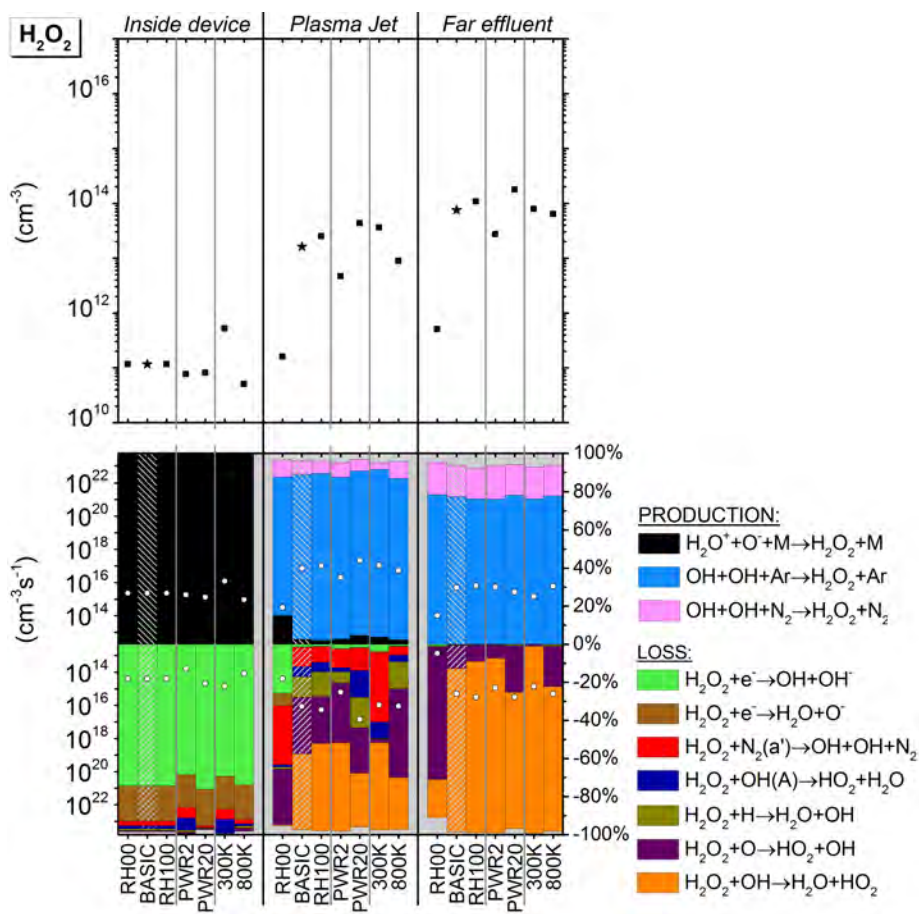Figure 3.13: Similar graphs as in figure 3.3 but for N_2O_5.

Figure 3.14: Similar graphs as in figure 3.3 but for H_2O_2.
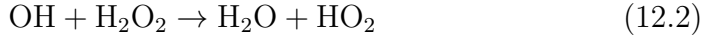
3.2.12 H_2O_2

H_2O_2 production is again of minor importance inside the device, so we concentrate only on the pathways in the active plasma jet and the far effluent. Figure 3.14 shows that H_2O_2 is predominantly created by a 3-body association reaction in both these regions:

$$OH + OH + M \rightarrow H_2O_2 + M \qquad (12.1)$$
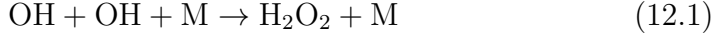
$$k = 8.00 \times 10^{-31} \left(\frac{T_{gas}}{300} \right)^{-0.80} cm^6.s^{-1}$$

Thus, this reaction can not take place inside the device, as the temperature in this area is simply too high for a significant rate coefficient. Moreover, the OH density is still rather low in this region.

The main destruction pathways of H_2O_2, again both in the active plasma jet and in the far effluent, are collisions with OH (reaction 12.2) and O (reaction 12.3), which both have a rate coefficient that rises with temperature:

$$OH + H_2O_2 \rightarrow H_2O + HO_2 \qquad (12.2)$$

$$k = 4.53 \times 10^{-12} exp(-288.9/T_{gas}) \, cm^3.s^{-1}$$

$$H_2O_2 + O \rightarrow HO_2 + OH \qquad (12.3)$$

$$k = 1.79 \times 10^{-13} \left(\frac{T_{gas}}{300} \right)^{2.92} exp(-1394.0/T_{gas}) \, cm^3.s^{-1}$$

This explains the drop in H_2O_2 concentration upon higher temperature, especially in the active plasma jet. Clearly, the rate coefficient of reaction 12.3 has a much higher gas temperature dependency and therefore its relative importance compared to reaction 12.2 becomes smaller in the far effluent where the gas temperature is close to 300 K for all temperature profiles. Note that in reaction 12.3 the number of reactive species created is 2 (HO_2 + OH) whereas in reaction 12.2 only 1 reactive species is formed (HO_2, besides H_2O). We can conclude that reaction 12.2 thus reduces the H_2O_2 production (above we explained that HO_2 leads to OH again, hence by reaction 12.1 also to H_2O_2).

Figure 3.14 shows that H_2O_2 is extremely sensitive to the ambient air humidity: the density is very low at dry air conditions. Indeed, the rate of the only production type (reaction 12.1) is proportional to the square of the OH density (which is very dependent on the relative humidity itself

as demonstrated above), whereas for the destruction mechanism there are alternative quenchers available (*i.e.* O, $N_2(a')$ and electrons) with densities that are not as dependent on the ambient air humidity.

The highest net production occurs at the end of the active plasma jet region, thus the OH converted into H_2O_2 in that area will mainly determine the final hydrogen peroxide concentration.

As shown in section 3.2.8, the OH density increases with power in the active plasma jet, and the rise in density of the quenching species upon higher power can not compensate for this effect. As a result, H_2O_2 is also more abundant at higher power, both in the active plasma jet and in the far effluent.

As mentioned above, we observe a faster conversion of OH into H_2O_2 at low temperature. The higher concentration of hydrogen peroxide in the active plasma jet for a lower temperature can be explained by the strongly temperature dependent rate coefficient of the loss reaction 12.3. Indeed, much less of the produced H_2O_2 is converted back into OH (or the OH precursor HO_2) at low temperature. Nevertheless, this is largely not more than a delay of hydrogen peroxide production, because in the far effluent these differences in H_2O_2 concentration between the three different temperature cases almost disappear.

3.2.13 HNO_2

The HNO_x species in a plasma treated (humid) biological sample might originate either from liquid chemistry (*i.e.* reactions between various reactive nitrogen species and hydrogen species) or they might be transferred directly from the gas phase. Our simulations demonstrate that HNO_2 is certainly formed in considerable quantities by gas phase reactions, although the efficiency of mass transfer to the liquid phase still remains an open question [71].

Inside the device, the HNO_2 densities are negligible, so once more we only focus on the chemistry in the active plasma jet and the far effluent.

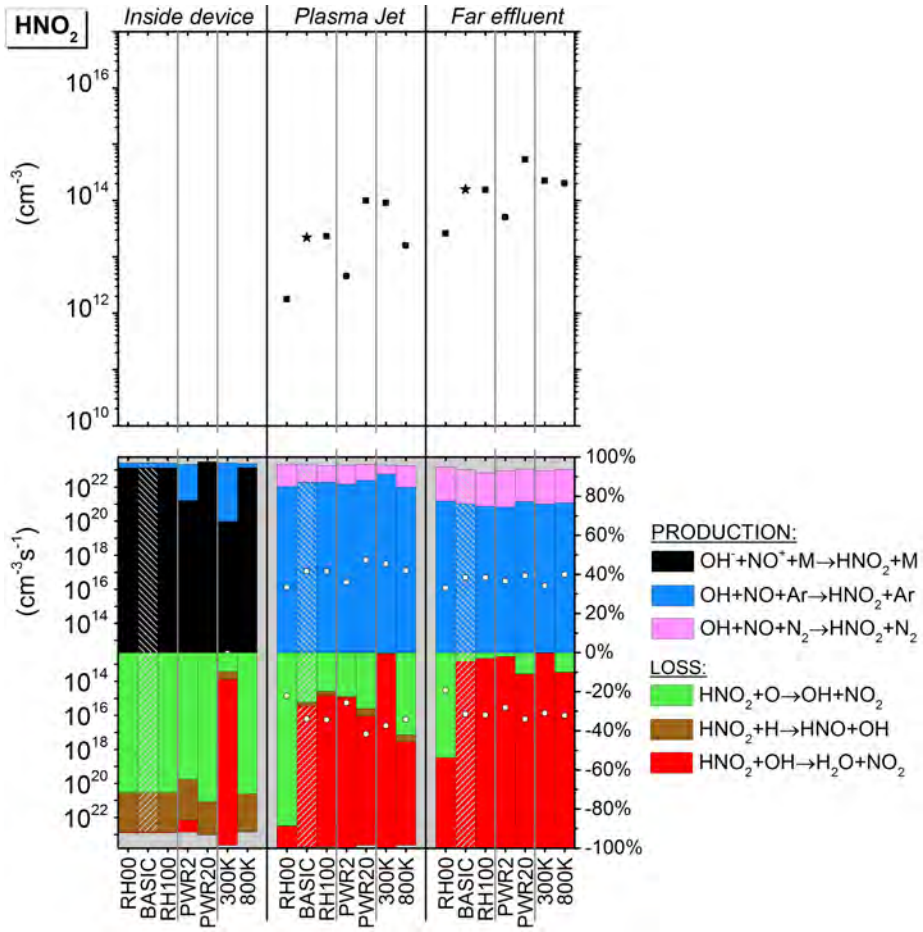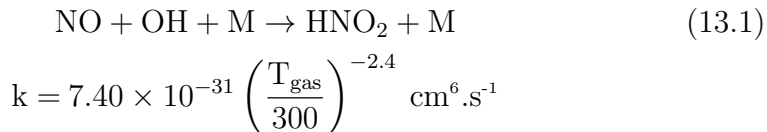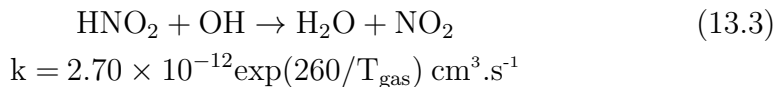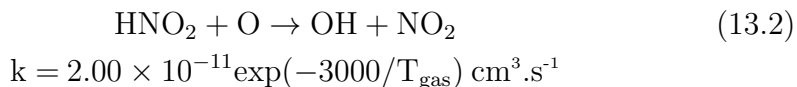Figure 3.15 shows that HNO_2 is mainly formed by associative 3-body colli-

Figure 3.15: Similar graphs as in figure 3.3 but for HNO_2.

sions between OH and NO, throughout the entire effluent region:

$$NO + OH + M \rightarrow HNO_2 + M \qquad (13.1)$$

$$k = 7.40 \times 10^{-31} \left(\frac{T_{gas}}{300} \right)^{-2.4} cm^6.s^{-1}$$

The loss mechanism is dominated by collisions of HNO_2 with O and OH, *i.e.* conversion of HNO_2 into NO_2 by hydrogen abstraction:

$$HNO_2 + O \rightarrow OH + NO_2 \qquad (13.2)$$

$$k = 2.00 \times 10^{-11} exp(-3000/T_{gas}) \, cm^3.s^{-1}$$

$$HNO_2 + OH \rightarrow H_2O + NO_2 \qquad (13.3)$$

$$k = 2.70 \times 10^{-12} exp(260/T_{gas}) \, cm^3.s^{-1}$$

Apparently, hydrogen abstraction by O atoms can only occur at elevated temperatures (its rate coefficient rises drastically with temperature), whereas abstraction by OH is enhanced by lower temperatures (its rate coefficient drops with temperature). This explains why roughly only quenching by OH remains in the far effluent (except in dry air, where the OH concentration is very low).

The HNO_2 formation is the highest at the end of the active plasma jet. This is because of three reasons; first, the densities of both reactants, OH and NO, are high enough for significant production (see figure 3.2). Second, the temperature dropped sufficiently to avoid quenching by O and third, the gas is not yet cool enough for efficient quenching by the OH radicals. In the far effluent, these OH radicals are already largely depleted and both the production and loss become low.

Furthermore, HNO_2 is clearly more abundant for a higher applied power and more humid ambient air, both in the active plasma jet and the far effluent. This behaviour is trivial because both reactants, OH and NO, have a higher density at those conditions (see sections 3.2.8 and 3.2.9 for more details). Note that the increase in HNO_2 density upon rising humidity is especially large at low air humidities.

The HNO_2 concentration in the active plasma jet is clearly higher for the lower temperature case and can be explained as follows. First, the production rises because the rate coefficient of reaction 13.1 increases drastically (although the OH and NO concentrations are a bit lower at low temperature). Second, the rate increase of loss reaction 13.3 is not as large, because

the increased rate coefficient is largely compensated by the decrease in the OH density. Third, the loss by collisions with O becomes negligible (mainly due to its rate coefficient).

However, in the far effluent the HNO_2 density difference between the temperature cases is again reduced. The reason is that HNO_2 production is now significantly faster for the higher temperature profiles due to the higher concentrations of OH and NO (the temperature effect on the rate coefficient is for all temperature profiles the same in this area, as already repeatedly explained), while the most dominant loss reaction 13.3 stays slow for all three temperature cases in this region (low rate coefficient close to room temperature).

3.2.14 HNO_3

The production mechanism of HNO_3 in the active plasma jet and the far effluent is remarkably similar to the HNO_2 pathway. In this case, OH associates with NO_2 instead of with NO:

$$OH + NO_2 + M \rightarrow HNO_3 + M \qquad (14.1)$$
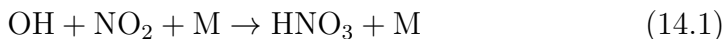
Only a minor part of the production is through NO (about 10%, depending on the conditions):

$$HO_2 + NO + M \rightarrow HNO_3 + M \qquad (14.2)$$
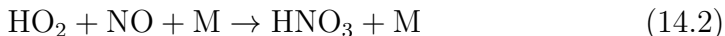
The loss rates are clearly lower than the total production rate throughout the entire effluent and will therefore not be discussed, although it is worth mentioning that HNO_3 is involved in the production of NO_3^- which is in literature identified as a possible biomedically active agent [68]

Again, the HNO_3 concentration greatly increases with higher power and ambient air humidity, both in the active plasma jet and the far effluent, simply because the reactants are more abundant. As was the case for HNO_2, only a few percent of ambient air humidity is sufficient to let the HNO_3 concentration rise drastically.

Furthermore, the much higher HNO_3 density at lower temperature in the active plasma jet is primarily determined by the production reaction 14.1, because the rate coefficient of this 3-body associative collision is typically higher at low temperature. Nevertheless, in the far effluent, this temperature effect is reduced, since the densities of both reactants, OH and NO_2, are
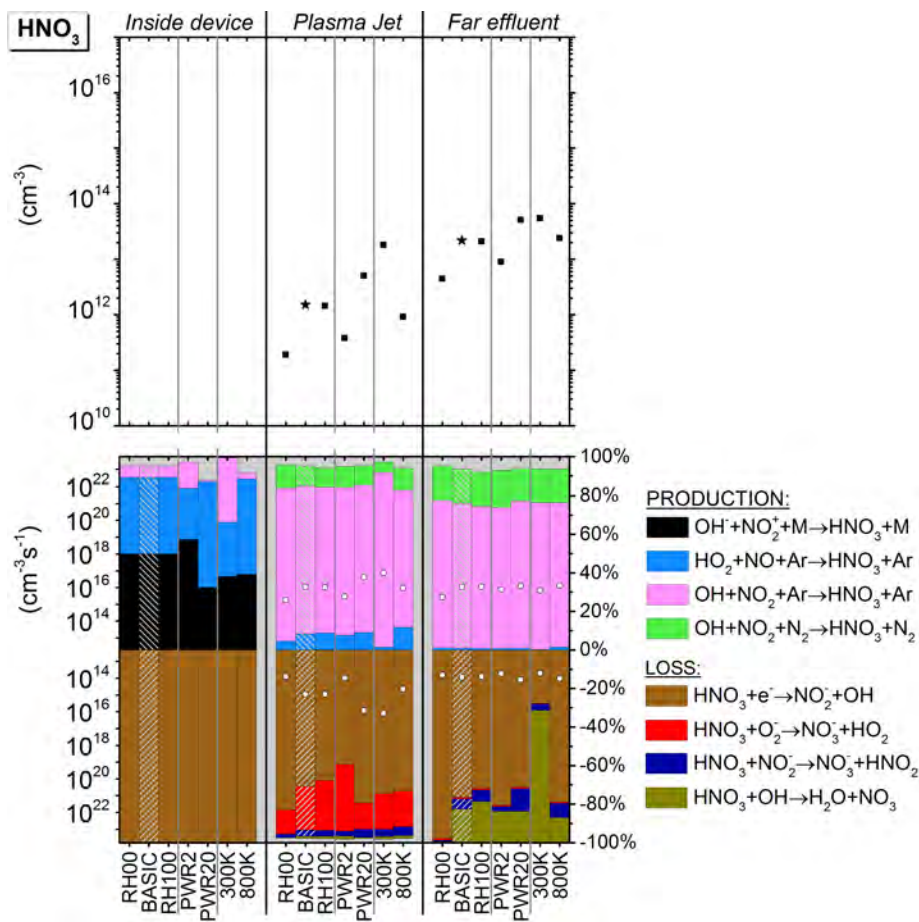
Figure 3.16: Similar graphs as in figure 3.3 but for HNO_3.

higher for the higher temperature profiles, which results in a higher HNO_3 production.

3.2.15 Summary of the chemical pathways

Figures 3.17, 3.18 and 3.19 visualize the production and loss pathways in a qualitative way and give a good overview of the complete reaction chemistry of the biomedically active species. The species connections in these figures are labelled and these labels will be mentioned throughout this section, so that the pathway plots and this summary are complementary.

The pathway plots are constructed from the 'basic case' simulation with 50% relative humidity, 6.5 Watt total applied power and the gas temperature profile from figure 3.1. Pathway visualization plots for other conditions are not included in this chapter, but can be consulted upon request.

We want to stress that for the interpretation of these graphs a few remarks should be kept in mind. For example in the figures showing the production mechanisms: when a connection is made between species A and C, which represents a reaction in the form of A + B → C + D, this means that there is at least one important production reaction for C out of A, but it says nothing about the possible collision partners, B in this case. It neither suggests that this reaction is important as a loss for A as well, because the plot only illustrates the production mechanisms.

A similar comment can be made for the connections in the loss mechanisms. For instance, the connection from NO to O in figure 3.18 (center graph) is only important as a loss pathway for NO, but the connection is not a dominant production pathway for O, since the density of NO is significantly lower than the O densities. Hence, there is no production arrow going from NO to O in the left graph.

The reason why we chose to show the production and loss mechanisms in separate figures is because showing only the net reaction pathways, *i.e.* summation of formation and destruction rates, could possibly hide a lot of interesting information and can even hide important mechanisms. Also, note that a connection often represents several reactions. Additionally, when there is more than one connection arriving at a certain species, the arrows have a pen width in relation to their relative contribution to the total formation/loss. Finally, it is important to mention that we use a 10% cut-off for the arrow connections in the pathway plots to reduce the complexity of the figure.

- Nitrogen metastables ($N_2(A)$) turn out to be very important for the generation of biomedical species. They are probably always present in biomedical plasma sources, as it is impossible to exclude nitrogen from the gas feed (ppm impurity levels) and because nitrogen is a basic component of the ambient air that diffuses into the argon stream (percentage levels in the plasma jet). The electronically excited $N_2(A)$ state is formed rapidly by electron impact of N_2 molecules, both inside the device and especially in the active plasma jet due to humid air diffusion (see label **a1** in figures 3.17 and 3.18). The $N_2(A)$ density of 3×10^{12} cm^{-3} inside the device rises to a maximum of 2×10^{14} cm^{-3} at 0.3 cm from the nozzle exit (see figure 3.2). $N_2(A)$ is mainly lost by electron impact de-excitation inside the device, and is quenched by H_2O in the active plasma jet. Both processes again lead to the N_2 ground state (see label **a2** in figures 3.17 and 3.18). The $N_2(A)$ density becomes negligible towards the far effluent region for all conditions under study, hence there is no arrow connection between N_2 and $N_2(A)$ in figure 3.19.

- The O atom density is in the order of 10^{14} cm^{-3} within the device. This indicates that most of the molecular oxygen impurities are dissociated. The O atoms are, in the absence of nitrogen admixtures in the gas feed, created by electron impact dissociation in this region (label **b1** in figure 3.17). In the active plasma jet, when higher amounts of nitrogen become available, O_2 dissociation reactions by collisions with $N_2(A)$ and $N_2(a')$ (label **b2** in figure 3.18) become equally important as the electron impact process. Therefore, the O atom density rises by typically more than two orders of magnitude in the active plasma jet (at maximum 8×10^{15} cm^{-3} for the 'basic' case of figure 3.2). Water species like OH and HO_2 are responsible for the loss of O atoms in all three regions, forming O_2 again (label **b3** in figure 3.17 - 3.19). Another important destruction reaction is the formation of O_3 by association of O atoms with O_2. The rate coefficient of this reaction is highly dependent on the temperature, thus this process is more important towards the far effluent where the gas is cooler (label **b4** in figures 3.18 and 3.19). Note that a significant amount of O atoms keeps being formed even far from the nozzle exit, by collisions between $O_2(a)$ and O_3 (label **b5** in figure 3.19). Therefore, the O atom density gradually drops in the far effluent but is still considerable towards the

end of the simulated domain (2×10^{13} cm⁻³ in figure 3.2).

- The O_3 concentration is negligible inside the device, but rises rapidly after the nozzle exit (by 3-body association between O and O_2; label **c1** in figures 3.18 and 3.19) and it even becomes one of the most abundant species in the far effluent (4×10^{15} cm⁻³ in figure 3.2) Note that, in the beginning of the active plasma jet, the net O_3 production is limited due to the high H density in that region, which reacts heavily with O_3 forming OH and O_2 (label **c2** in figure 3.18). In the far effluent, however, the loss processes (predominantly collisions with O_2(a) and NO, labels **c3** and **c4** in figure 3.19, respectively) are rather slow, explaining the high O_3 concentration in this region.

- O_2(a) is, both inside the device and in the active plasma jet, created primarily by electron impact excitation (label **d1** in figures 3.17 and 3.18). Inside the device, O_2(a) is mainly lost by electron impact de-excitation, forming ground state O_2 molecules again (see label **d₋₁** in figure 3.17). Note that in the active plasma jet, it is additionally produced by energy transfer from N_2(A) (label **d2** in figure 3.18). In this region O_2(a) is mainly quenched by HO_2 (label **d3** in figure 3.18). The maximum O_2(a) density (4×10^{14} cm⁻³ in figure 3.2) is reached at the end of the active plasma jet because formation in the far effluent is negligible compared to the loss (*i.e.* collisions with O_3; label **d4** in figure 3.19). Even so, this loss of O_2(a) is rather slow and, therefore, O_2(a) is also long-lived (at these time scales).

- N atoms are only formed inside the device and in the active plasma jet, mainly by dissociation of N_2 by electronically excited Ar atoms (see label **e1** in figures 3.17 and 3.18). These reactions accelerate after the nozzle exit, where the nitrogen levels increase, explaining the higher N density in the active plasma jet (at maximum 4×10^{14} cm⁻³ in figure 3.2). In the far effluent, the formation of N is almost negligible, explaining why no arrow points towards N in figure 3.19. The N atoms are in all three regions easily converted into NO by reaction with OH or O_2 (see labels **e2** and **e3** in figures 3.17-3.19). Moreover, a large part of the produced N is also converted back into N_2 upon reaction with this generated NO (see label **e4** in figures 3.17-3.19).

- The H atoms are produced from a series of steps that begin with col-

lisions between Ar_2^+ and H_2O (label **f1** in figures 3.17 and 3.18). The H formation is especially prominent in the first few mm's after the nozzle exit due to humid air diffusion, explaining why the H atom density is the highest in the active plasma jet (at maximum 4×10^{14} cm^{-3} in figure 3.2). The H atoms are very efficiently converted into OH, either directly but especially indirectly (through HO_2; label **f2** in figures 3.17 - 3.19). However, the H density does not get depleted before the far effluent because the OH radicals are continuously converted back into H atoms upon collision with O atoms, especially in the active plasma jet (label **f3** in figure 3.18).

- As just mentioned, HO_2 is the intermediate species out of which OH is (re)created, after H generation. It is produced by a 3-body association reaction between H and O_2 (label **g1** in figures 3.17-3.19). Nevertheless, this process is only fast in the active plasma jet where H atoms are abundant, resulting in a density of maximum 6×10^{13} cm^{-3} in this region (see figure 3.2). Subsequently, HO_2 is converted into OH by collisions with O atoms (label **g2** in figures 3.17-3.19), or with $O_2(a)$ (label **g3** in figures 3.18 and 3.19). The contribution of the latter process increases towards the far effluent.

- The OH radical density only starts rising after the nozzle exit, because inside the device it is efficiently dissociated by electron impact (label **h1** in figure 3.17) soon after its generation by Ar_2^+ and H_2O collisions (label **h2** in figures 3.17 and 3.18). In the active plasma jet region, where the OH density reaches its maximum value (1.5×10^{14} cm^{-3}, see figure 3.2), it is additionally (and mainly) dissociated upon collision with O atoms, thereby producing H atoms. In the far effluent only this quenching by O atoms remains (label **h3** in figures 3.18 and 3.19). Nevertheless, most of the OH is always regenerated from these H atoms (mainly through the HO_2 intermediate as mentioned above, label **h4** in figures 3.18 and 3.19). Towards the far effluent, OH is definitively removed because the generation of HNO_2 from OH and NO now also becomes important (label **h5** in figure 3.19). The same applies for the formation of HNO_3 and H_2O_2 but because the contribution is lower than the cut-off, this cannot be seen in figures 3.18 and 3.19.

- The production of H_2O_2 is negligible inside the device, but in the ac-

tive plasma jet and far effluent it proceeds through the 3-body association reaction of two OH radicals (label **i1** in figures 3.18 and 3.19). The rate of this process is the largest in the active plasma jet, where the OH radicals are the most abundant. Therefore, H_2O_2 reaches its maximum density at the end of this region (almost 10^{14} cm^{-3}, see figure 3.2), and it remains more or less constant in the far effluent. The loss of H_2O_2 is primarily due to collisions with H (forming H_2O and OH; label **i2** in figure 3.18), with O (forming HO_2 and OH; label **i3** in figure 3.18) and with OH (forming H_2O and HO_2; label **i4** in figure 3.18 and 3.19). H_2O_2 is a long-lived species in the far effluent because the rates of these loss processes rapidly drop, especially the first two processes. Note that the reactions with H and OH create water and thus reduce the reactivity of the plasma.

- The production and loss mechanisms of NO and NO_2 are tightly coupled. Their densities are very small inside the device, so the reaction pathways for that region are not discussed here. NO is generated through various processes in the first mm's after the nozzle exit, *i.e.* from $O+N_2(A)$ (label **j1** in figures 3.17 and 3.18), from OH+N (label **j2** in figure 3.18) and from O_2+N (label **j3** in figure 3.18). Subsequently, it can be either quenched by N back into N_2+O (label **j4** in figure 3.18) or be converted into NO_2 by a 3-body association reaction with O atoms (label **j5** in figure 3.18 and 3.19). However, most of the NO_2 is converted back into NO by collision with O and H atoms (*i.e.* label **j6** in figures 3.18 and 3.19 and label **j7** in figure 3.18, respectively). NO is long-lived on the simulated time scale with a high density (6×10^{14} cm^{-3}) because its loss reactions are slow in the far effluent. Indeed, the N density is depleted, the O density is also decreasing, and only O_3 still has a high concentration, but this last quenching reaction is rather slow (label **j8** in figure 3.19). Nevertheless, the NO_2 density keeps slowly rising in the far effluent because of these last two processes.

- The N_2O_5 production only occurs by a 3-body association reaction between NO_2 and NO_3 at low temperatures (label **k1** in figures 3.18 and 3.19). Therefore, it is negligible inside the device. Furthermore, since the two reactants need some time to build up in the plasma jet effluent, we only observe significant N_2O_5 densities in the far effluent

(about 2×10^{12} cm^{-3}). Note that the loss of N_2O_5 is dominated by the reverse reaction, forming NO_2 and NO_3 again (see label $\mathbf{k_{-1}}$ in figures 3.18 and 3.19).

- Finally, HNO_2 and HNO_3 are again negligible inside the device, and also reach their highest density in the far effluent (2×10^{14} cm^{-3} and 2.5×10^{13} cm^{-3}, respectively). Their production mechanism inside the active plasma jet and far effluent is very similar, *i.e.* through a 3-body association reaction between OH and NO forming HNO_2 (label $\mathbf{l1}$ in figures 3.18 and 3.19) and between OH and NO_2 forming HNO_3 (label $\mathbf{l2}$ in figures 3.18 and 3.19). The much higher concentration of NO compared to NO_2 is the main reason why HNO_2 is more abundant than HNO_3. This is in spite of the fact that HNO_2 is partially destroyed by collision with O atoms (forming OH and NO_2; label $\mathbf{l3}$ in figure 3.18) and OH (forming H_2O and NO_2; label $\mathbf{l4}$ in figures 3.18 and 3.19), whereas HNO_3 does not seem to have significant loss processes.
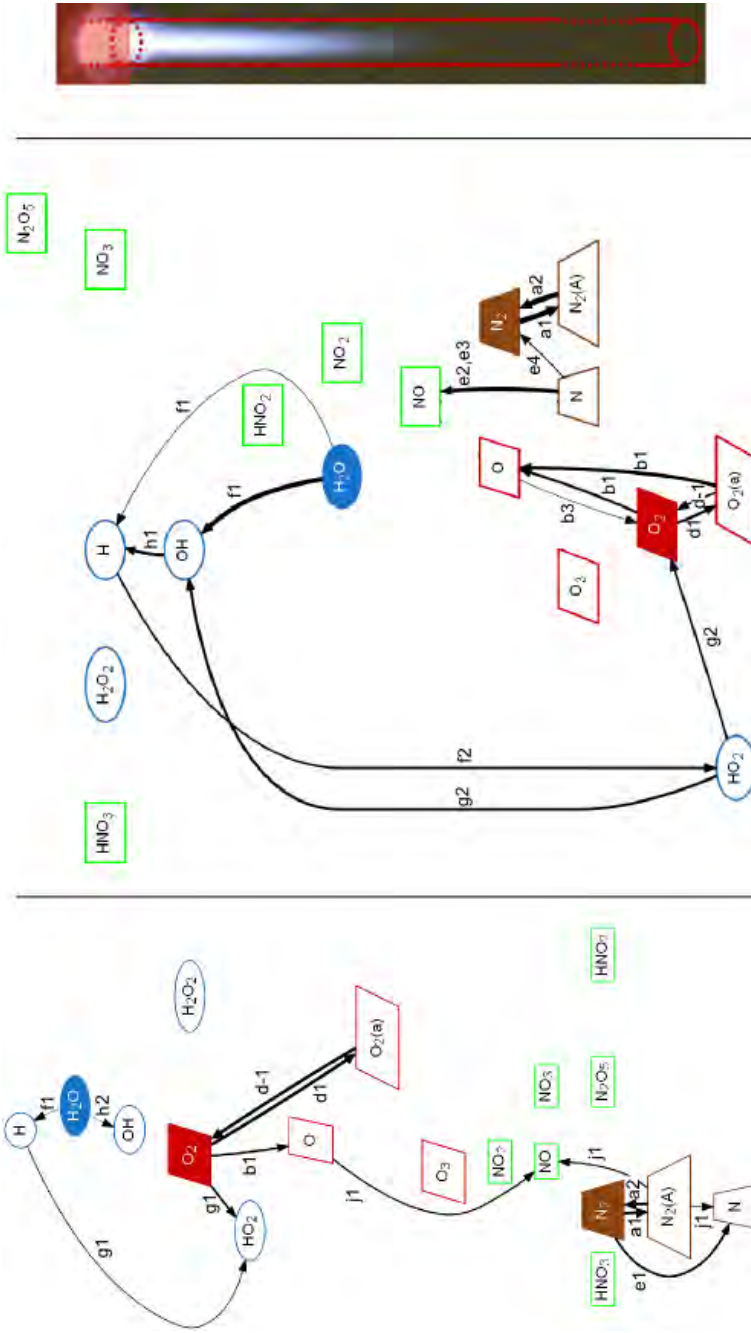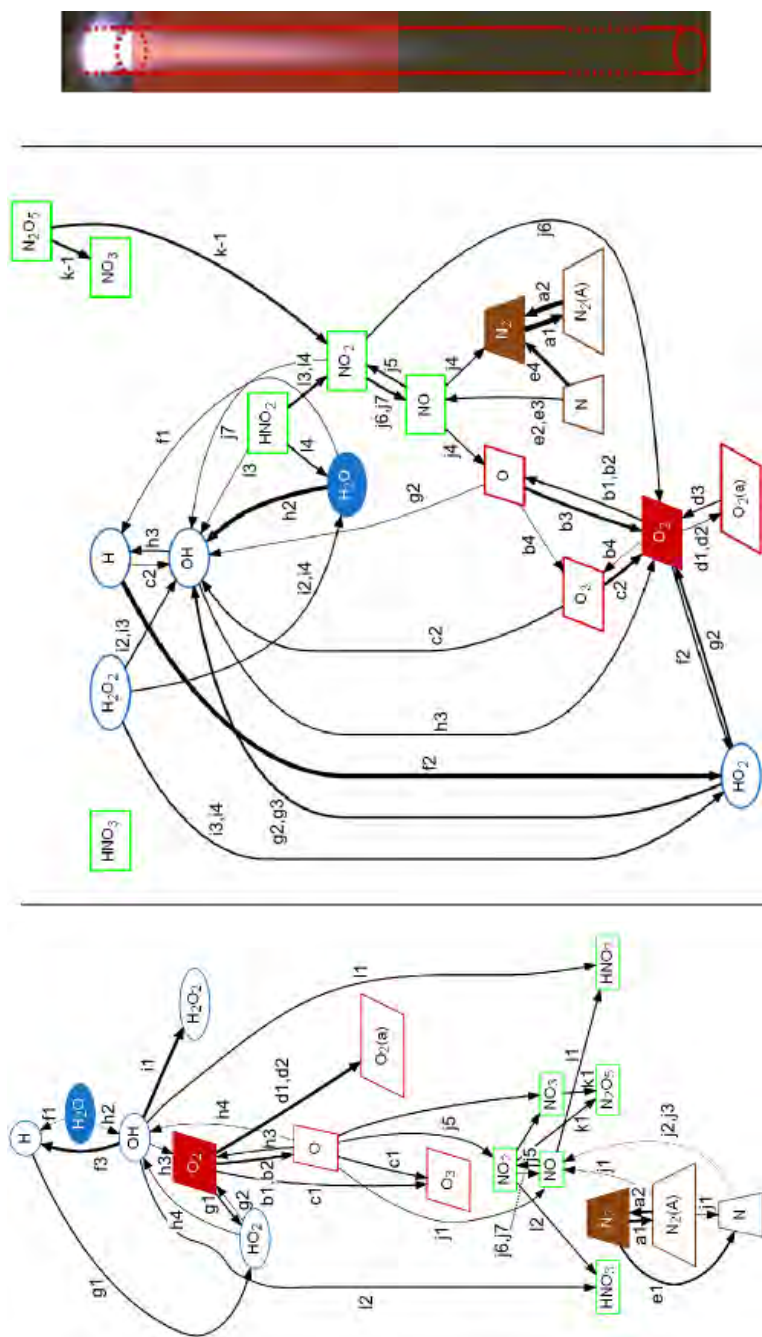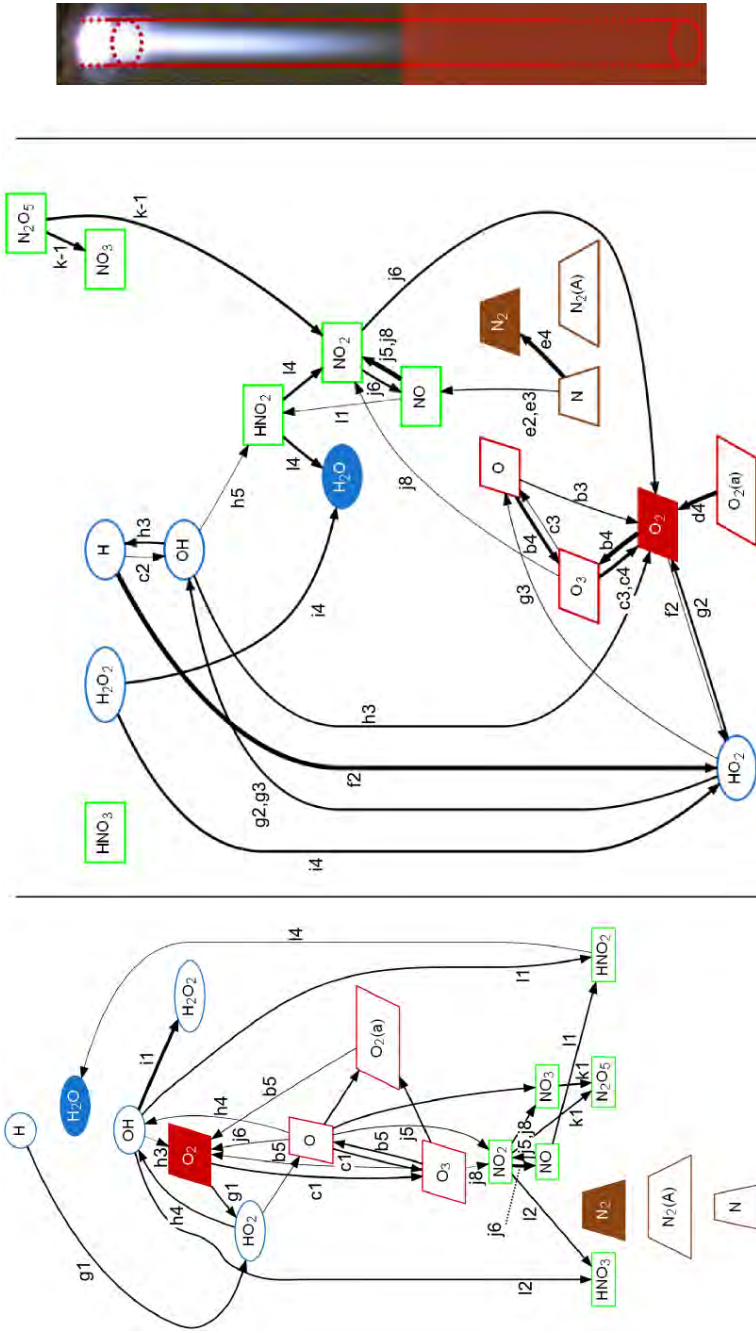
Figure 3.17: The dominant reaction pathways of the production (left figure) and loss (center figure) mechanisms of the most important biomedically active species inside the plasma jet device (deduced from the spatially averaged rates over the highlighted region, see figure at the right) for the so-called 'basic' case (see text and figures 3.3-3.16). The pathways are explained further in section 3.2.15 by the labels next to the arrow connections. The oxygen species are represented by red parallelograms, the nitrogen species by brown trapezia, the water species by blue circles and the nitrogen oxides by green rectangles. Some of the biomedical species have a low density in this region, hence they are not connected with other species.

Figure 3.18: The dominant reaction pathways of the production (left figure) and loss (center figure) mechanisms of the most important biomedically active species in the active plasma jet region (deduced from the spatially averaged rates over the highlighted region, see figure at the right) for the so-called 'basic' case (see text and figures 3.3-3.16). The pathways are explained further in section 3.2.15 by the labels next to the arrow connections. The oxygen species are represented by red parallelograms, the nitrogen species by brown trapezia, the water species by blue circles and the nitrogen oxides by green rectangles.

Figure 3.19: The dominant reaction pathways of the production (left figure) and loss (center figure) mechanisms of the most important biomedically active species in the far effluent (deduced from the spatially averaged rates over the highlighted region, see figure at the right) for the so-called 'basic' case (see text and figures 3.3-3.16). The pathways are explained further in section 3.2.15 by the labels next to the arrow connections. The oxygen species are represented by red parallelograms, the nitrogen species by brown trapezia, the water species by blue circles and the nitrogen oxides by green rectangles. $N_2(A)$ and N have a low density in this region, hence they are not connected with other species.

Table 3.3: Effect of varying the conditions on the densities of the biomedical species. Note that the densities under consideration here, are the spatially averaged values over the three different plasma jet regions, see figures 3.3-3.16. Hence, some very local effects might be filtered out.

Species	Relative humidity ↑			Power ↑			Peak gas temperature ↑		
	Inside device	Active plasma jet	Far effluent	Inside device	Active plasma jet	Far effluent	Inside device	Active plasma jet	Far effluent
$N_2(A)$	-	↓	▨	(↑)	↑	▨	(↓)	(↑)	▨
O	-	↓	↓	↑	↑	(↑)	-	(↑)	↑
O_3	▨	↓	↓	▨	(↑)	(↑)	▨	↓↓	↓
$O_2(a)$	-	(↓)	↓	(↓)	↑	↑	↓	(↑)	↑
N	-	(↓)	↑↑	↑↑	↑	↓↓	↑	↓↓	↓↓↓
H	-	↑↑	↑	↑	↑↑	(↑)	(↓)	↑	↑↑
HO_2	▨	↑↑	↑↑	▨	↑	↓	▨	(↓)	↑
OH	-	↑↑	↑↑	↓↓	↑	↓	↓↓	(↑)	↑
NO	-	(↓)	(↓)	↑	↑	↑	(↓)	↑	↑
NO_2	▨	↓	↓	▨	↑	↑	▨	↓	↑
N_2O_5	▨	▨	↓↓	▨	▨	↑↑	▨	▨	↓↓
H_2O_2	▨	↑↑↑	↑↑↑	▨	↑↑	↑↑	▨	↓	(↓)
HNO_2	▨	↑↑	↑↑	▨	↑↑	↑↑	▨	↓	-
HNO_3	▨	↑↑	↑↑	▨	↑↑	↑	▨	↓↓	↓

As mentioned above, figures 3.17-3.19 illustrate the reaction pathways at the 'basic' case of 50% relative humidity, 6.5 Watt applied power and the gas temperature profile plotted in figure 3.1. Varying these conditions affects the densities of the biomedical species, which is schematically illustrated in table 3.3, and can be summarized as follows:

- Increasing the ambient air humidity results in a lower concentration for all the non H-containing species. This is mostly due to more

quenching of $N_2(A)$ by water, hence, less $N_2(A)$ is available for the generation of the non H-containing biomedical species. Obviously, the densities of the H-containing species rise for higher air humidities. We see that close to dry air conditions, the effect is the largest. For the HNO_x species there is even practically no effect of humidity except for close to dry air conditions. This is caused by the opposite trend for the H- and non H-containing reactants, both necessary for HNO_x formation.

- The generation of all biomedical species increases in the active plasma jet when applying more power. However, due to the high density of reactive species at high power they clearly destroy each other much faster. Therefore, the concentrations of most of the atomic and molecular radicals even become again lower towards the far effluent, at high power. Nevertheless, the stable long-lived neutrals typically have a higher density in the far effluent for higher powers.

- A higher gas temperature in the active plasma jet results in only a slightly higher concentration of O, $O_2(a)$, OH and NO. For these last two species this is a result of multiple processes compensating each other, but for the first two species this is because they are formed directly or indirectly (by argon or nitrogen metastables) by temperature independent electron impact processes. The latter is in fact also the case for N and H but the loss processes of these species are clearly favored (for N) and disabled (for H) by a high temperature. Additionally, we observe that a low temperature favors the oxidation of NO into NO_2 and also enhances the association of NO_2 with NO_3 forming N_2O_5. Finally, we found that a high temperature profile only delays the formation of H_2O_2 and the HNO_x species but does not prevent this.

3.3 Conclusion

In this chapter the production and destruction pathways are analysed for the most important neutral biomedically active species, *i.e.* O, O_3, $O_2(a)$, N, H, HO_2, OH, NO, NO_2, N_2O_5, H_2O_2, HNO_2 and HNO_3.
For almost all species it was shown that the pathways change as a function of the distance from the nozzle exit. The net production of the species is

usually high either inside the device, in the active plasma jet or in the far effluent. Indeed, we demonstrated that some processes and pathways are very local, *e.g.* destruction of ozone by H. We have also shown that for some species the formation mechanism consists of multiple different pathways at the same time, *e.g.* for NO.

Air impurities in the gas feed seem to be easily excited by electron impact inside the device, forming $O_2(a)$ and $N_2(A)$. Furthermore, O_2 is efficiently dissociated by electron impact and H_2O by collisions with argon species. Hence, also H and O atoms are abundant inside the device, certainly when keeping in mind the low air impurities. The N atom density on the other hand remains lower. After the nozzle exit, the gas mixes with ambient (humid) air and the densities of H, O and N atoms drastically rise. However, further in the active plasma jet the production of these species reaches a maximum, since the electron and argon species densities are dropping. Subsequently, the atoms are now converted into NO (mainly produced from $N_2(A)+O$), NO_2 (formed by NO oxidation), OH (or its precursor HO_2, both created from H) and O_3 (association between O and O_2). These processes are further accelerated by the decreasing gas temperature when moving further away from the nozzle exit. Moreover, most of these molecules are efficiently dissociated by electron impact inside the device and/or by collision with the atoms in the active plasma jet. However, this becomes of minor importance in the far effluent. Furthermore, towards the far effluent, the OH radicals dimerize into H_2O_2 or associate with the NO_x species into stable HNO_2 and HNO_3 molecules. Note that the NO and NO_2 molecules themselves are only partially converted into N_2O_5 and HNO_x. More importantly, the reaction of NO and NO_2 with O_3 in the far effluent is too slow to reduce the NO_x species densities at the given time scales. Finally, we see that $O_2(a)$ reacts only slowly with other species as well (in contrast to $N_2(A)$ which is efficiently quenched by water and has a low concentration further in the plasma jet). Thus, $O_2(a)$ becomes, together with O_3, the most abundant long-lived species. Obviously, it would be very interesting to see how a specific air/water admixture to the gas feed can prevent/stimulate the generation of certain biomedically active species.

We conclude that the chemical pathways are more complex than usually presumed and that the different species groups (*i.e.* derivation products from either oxygen, nitrogen or water) intensively interact, even in the case of ppm gas impurity levels or minor ambient air humidities. Thus, it is extremely important to consider all possible reactions with all possible humid

air species.

Our parameter study showed that the species concentrations can easily vary by one order of magnitude, but usually not much more than that.

Chapter 4

Analysis of the O_3 density and reaction pathways in a needle-type atmospheric pressure plasma jet

Preface

The development of our semi-empirical 0D model was done in parallel with validation studies of experimental measurements. Indeed, the fitting of the parameters like temperature and power density needs to be done with caution, considering the large amount of physical assumptions that are made in our numerical approach. For example, how to convert the 2D spatially resolved gas temperature measurement (with a significant gradient in the radial direction of the jet) into a 1D profile. Besides, exactly the same applies for the mixing of ambient air with the argon discharge flowing out of the discharge chamber.

Additionally, spatially resolved power density measurements, a measurement of a related plasma property or numerically obtained values (in order to make a good estimation) are lacking in the literature. Thus, in this chapter and the subsequent ones we indirectly evaluate the best approach by comparing the calculated species densities with the experimentally measured values. For this chapter we specifically focus on the formation of ozone in the plasma jet and its effluent.

Important to mention is that a validation of the reaction set also proved to be critical. Indeed, the reaction rate coefficients reported in literature for identical reactions often vary significantly and their accuracy is extremely difficult to asses. This is sometimes even the case for crucial reactions.

4.1 Experimental setup

An image of the operating plasma jet used in this chapter is depicted in figure 4.1(a). The APPJ geometry is the same as for the RF excited DBD-like sources described in the previous two chapters. However, this image specifically shows a jet with O_2 gas admixed to the argon feed gas, flowing through a quartz tube (inner diameter of 1.8 mm) and around the needle electrode (diameter of 1 mm) positioned in the centre of the tube.

A grounded copper ring is placed outside the quartz tube to obtain the aforementioned DBD–like configuration. This can be seen from figure 4.1(b), which illustrates the geometry schematically.

The plasma jet is placed vertically, parallel with the axis of the gravitational force, faced up, and without surrounding objects, to ensure a minimal disturbance of the flow. Actually, the plasma jet looks like the flame of a candle. In addition, about half a metre above the plasma jet is a ventilator, which does not affect the jet effluent but ensures that the produced O_3 is not accumulating around the jet effluent.

All the measurements shown in this work are for a 2 slm argon flow with 2% O_2 mixture (in the previous two chapters no admixtures were used) and the dissipated plasma power is 6.5 W. Note that the plasma used in this work is time modulated, so this dissipated plasma power is an average value. The power measurement is performed as described in detail in [38].

The O_3 density is measured by UV absorption (mercury lamp which emits the 254nm UV line). Since the expected absorption signal is very low, a lock-in amplifier needs to be used as it is capable of measuring small variations precisely if the variation is modulated by a known frequency. This kind of modulation is achieved by the modulation of the RF signal with the light source continuously on. In this way, the small absorption signal is subsequently modulated. As the plasma–off time should be long enough to ensure that the gas flow flushes away the ozone produced in the plasma, a low frequency plasma modulation of 50 Hz is used. Given the diameter of the quartz tube of 1.8 mm and the gas flow of 2 slm, the velocity of the gas flow is estimated to be at least 10 m.s^{-1} at 300 K. This means that the O_3 is removed by the flow over a length of 25 mm in 2.5 ms. According to this estimation, a plasma-off time of 10 ms is enough for the gas flow to flush away the produced ozone. Further details on the absorption measurement are described in [40] and are not mentioned here because they are beyond the scope of this work.
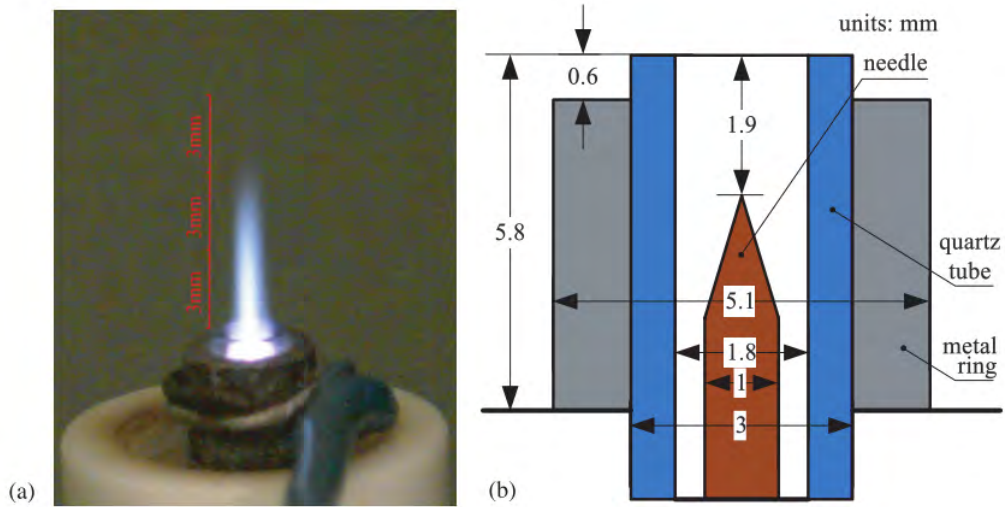
Figure 4.1: Schematic of the nozzle of the plasma jet (a) and an image of the operating plasma source (b). The APPJ is operating with a 2 slm argon flow mixed with 2% O_2 and the plasma dissipated power is 6.5 W

The gas temperature plays an important role in the ozone production and destruction [181]. To analyse the effect of the gas temperature on the ozone density distribution, Rayleigh scattering is performed to measure the gas temperature distribution in the jet. Details about the measurement setup can be consulted in [40].

4.2 Model input

For this investigation, the 0D plug-flow model as described in chapter 2 is again used. In fact, the experimental conditions described in section 4.1 are used as a basis for the fundamental case study of the plasma jet reaction chemistry described in chapter 2. Note that both investigations were performed simultaneously. Hence, most of the plasma parameters of figure 4.2 are quite similar as those depicted in figure 2.1, with the following exception. Here, 2% oxygen is admixed to the gas feed whereas the simulations of chapter 2 were performed with pure argon as a feed gas (including ppm air impurities) to keep it as general as possible. Therefore, we assumed for the simulations of this chapter that the mixing rate is the same as the one displayed in figure 2.1 and that a different initial gas feed composition thus
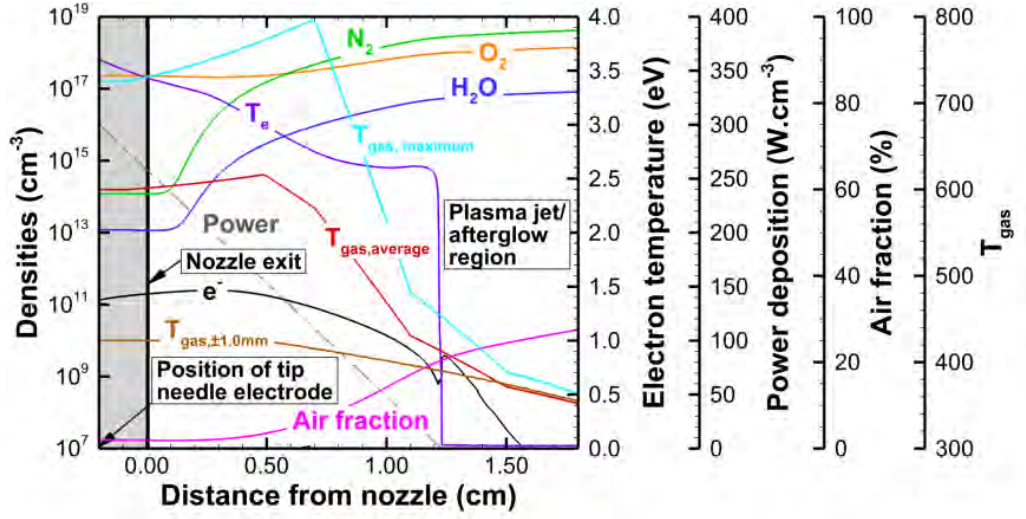
Figure 4.2: Plasma characteristics as a function of the axial position along the plasma jet axis. Both the experimental input parameter of the gas temperature (*i.e.* 3 alternative profiles, see text), the assumed power deposition profile, the air fraction and the resulting values of electron density and temperature are depicted here. The interior of the plasma jet device is represented by the grey area, beginning at the needle electrode tip. This zone ends at the nozzle exit (indicated with axial position = 0.0 cm) and it is followed by the plasma jet propagating in the surrounding air. Around 1.2 cm from the nozzle exit, when the power density has reached a value of zero, the plasma jet becomes an afterglow.

does not affect the diffusion of ambient air into the jet significantly. Note that the addition of 2% oxygen to the feed gas influences the chemistry, as well as the electron temperature and density. These values are also shown in figure 4.2.

Once more, we want to point out that we assume a linear correlation between the power density and the distance from the nozzle exit, which is probably not exactly consistent with reality, but better experimental or modelling data was not available at this point. Important is that the total power deposition in the model matches exactly the experimentally measured value of 6.5 W.

In the following sections the assumption concerning the gas temperature profile will be further clarified. As previously stated, since the gas temperature evolution in the jet is essential to model the plasma chemistry correctly (especially for O$_3$ [146]), it was not calculated (*e.g.* from contributions of reaction enthalpy) but fitted to the experimentally measured gas temperature. Three different profiles are considered (see figure 4.2 as well): a temperature at a radial position 1mm off-axis, a maximum temperature at the symmetry axis, and a temperature radially averaged over all values in between -1mm and +1mm from the jet axis. These represent a lower limit, upper limit and average temperature, respectively (see below).

4.3 Results and discussion

4.3.1 The gas temperature

Figure 4.3 shows the two-dimensional distribution of the gas temperature as experimentally measured. On every different axial plane, the maximum gas temperature is always located on the axis of symmetry. In the radial direction, the temperature decreases quickly within $\pm$ 1 mm off–axis, *i.e.*, the tube radius. In the axial direction, between z = 8–13 mm, the gas temperature decreases quickly towards room temperature. Remarkably the maximum gas temperature is found at a distance of about 7 mm from the nozzle, which corresponds to the location at which significant mixing of air into the jet occurs. The exact mechanisms are not clear and it needs to be mentioned that the increase in temperature beyond the nozzle exit is close to the experimental accuracy of the temperature measurement ($\pm$ 20 K). Nonetheless, a similar small increase in the gas temperature is found
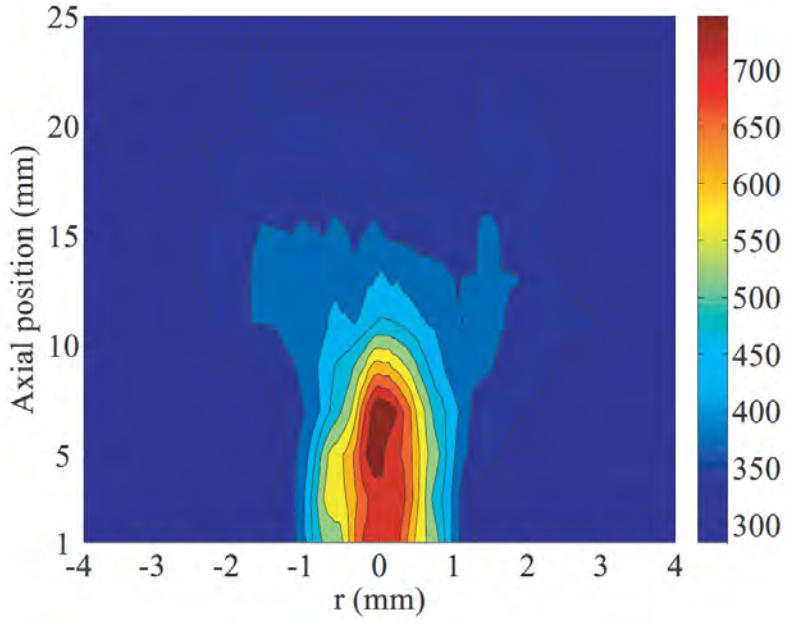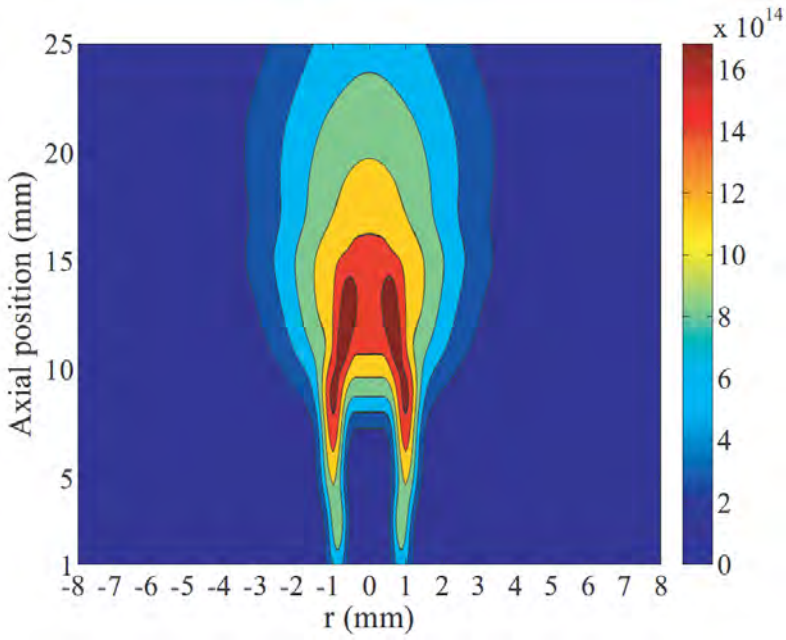
Figure 4.3: Spatially resolved gas temperature (K).

Figure 4.4: Experimentally obtained ozone density by UV absorption (cm^{-3})

in the model calculations and the heating seems to be caused by chemical reactions having excess energy in addition to the reaction products (*i.e.*, reaction enthalpy).

The observed gas temperature is larger compared with the results for *e.g.* the RF Ar based jet (kinpen) developed at the INP institute in Greifswald [195] (see also chapter 6 below). However, the actual power dissipated in the plasma (6.5W) in this work is expected to be larger than the power of the kinpen. Certainly, the discrepancy is not due to the different technique of the gas temperature determination. Indeed, different techniques of obtaining the gas temperature have been compared in detail in previous investigations of this plasma jet setup [38].

4.3.2 Ozone density

Figure 4.4 shows the experimentally measured ozone density obtained from the absorption measurements as described in [40]. The distribution of the ozone density consists of two different zones. In the zone close to the nozzle, *i.e.* in the ionizing plasma, the peak density of ozone is 1 mm off-axis. In the second zone further downstream and outside the ionizing plasma, the maximum density of ozone is on the axis of symmetry. The maximum density of ozone, produced by the APPJ, is 1.9×10^{15} cm^{-3} at axial position z = 13 mm from the nozzle.

Comparing figures 4.3 and 4.4, a strong correlation between the gas temperature and the ozone density is found. Indeed, in the hot plasma region, the ozone density is smaller compared with the colder effluent and the radial edges of the plasma plume, which also have a temperature lower than the gas temperature at the axis of symmetry. By means of a chemical analysis it is investigated below if there is any causality between the observed phenomena.

4.3.3 Analysis of O$_3$ production and destruction mechanisms

Due to our numerical approach, the simulations yield for each time–step radially averaged O$_3$ densities (cm^{-3}) for a volume that is as wide as the tube radius and as long as the movement in the axial direction within that time–step due to the gas flow. Hence, this data is only resolved in the axial direction (*i.e.* along the symmetry axis of the jet) whereas the experiments
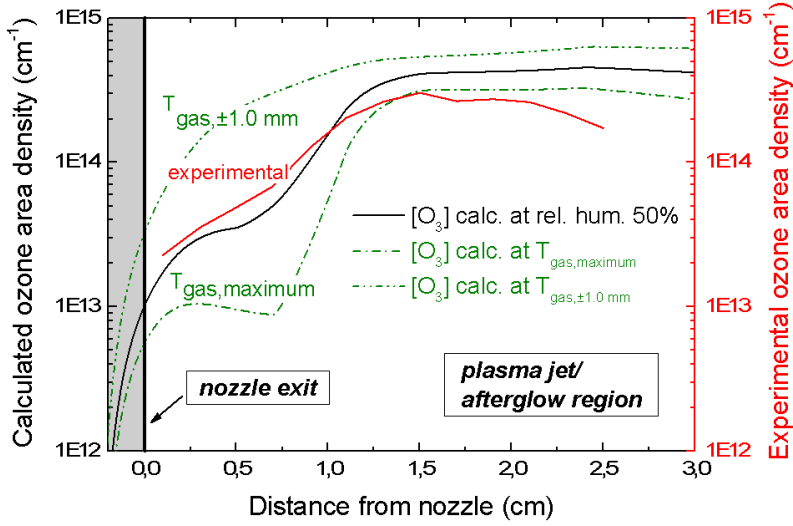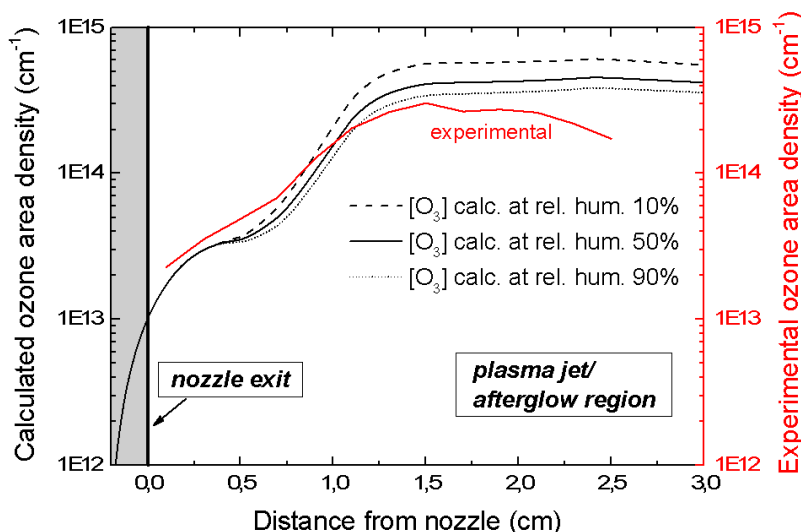
Figure 4.5: Comparison of calculated and experimentally obtained O_3 area densities as a function of the axial position. The calculated area densities depicted by the black line are obtained for $T_{gas,average}$ (see figure 4.2) and relative humidity 50% of the surrounding atmosphere. The two green O_3 area density profiles are calculated with different gas temperature profiles (see figure 4.2 as well).

provide data with radial resolution as well. Therefore, both the spatially averaged model results and the spatially resolved measured values of the ozone density are converted into area densities (cm^{-1}) for each axial plane. Note that the radial resolution of the experimental measurements is thus not considered in the comparison displayed in figures 4.5 and 4.6.

Both the measurements and the model indicate that the highest density of O_3 is found in the downstream region of the effluent outside the active plasma region (beyond 12 mm). The dependence of the O_3 density as a function of the axial position and the absolute O_3 density are well captured by the model (using an average gas temperature in the jet). The model shows that the absolute O_3 densities strongly depend on the temperature value. Indeed, as shown in figure 4.5, using a maximum, average or off-axis gas temperature yields a significant difference in the absolute O_3 densities. It is further checked that a change in humidity of the air, which diffuses into the Ar–O_2 effluent does not have a significant influence on the obtained O_3 densities (depicted in figure 4.6).

Figure 4.6: Comparison of calculated and experimentally obtained O$_3$ area densities as a function of the axial position. The calculated area densities depicted by the solid black line are obtained for T$_{gas,average}$ (see figure 4.2) and relative humidity 50% of the surrounding atmosphere. The dashed and dotted O$_3$ area density profiles are obtained for the humidity of the ambient air equal to 10% and 90%, respectively.

Finally, the assumption for the power deposition profile was checked, using lower/higher maximum power density values and/or a more/less steep slope, while maintaining a total power deposition of 6.5 W (results not shown). This resulted in deviations for the other biomedical species O, NO and OH densities (also involved in the O$_3$ production and destruction, see below) with a maximum of a factor 2, but the changes in the O$_3$ density were only about 25% at maximum. The above results show that the production and destruction processes of O$_3$ can be determined by the zero-dimensional model.

The most important ozone production and destruction reaction rates are shown in figures 4.7 and 4.8, respectively. In addition, the densities of the species involved in the production and destruction pathways are shown in figure 4.9.

The three-body association reaction of O atoms with molecular oxygen and Ar as a third body (see reaction 1 in figure 4.7) has the most important contribution to the production of ozone. This is due to the very high O
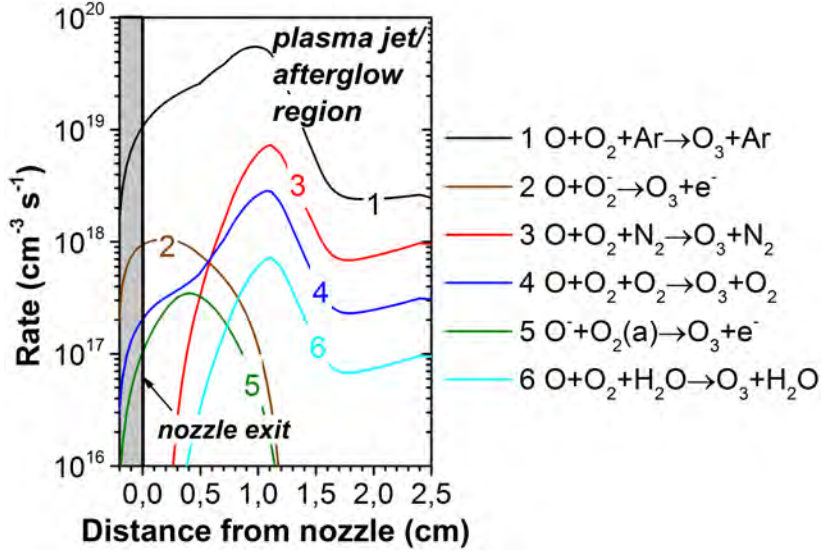
Figure 4.7: O_3 production rates of the dominant pathways, as calculated by the model

Table 4.1: Reactions and the corresponding rate constants

	Reaction	Rate constant[a]	Ref
(1)	$O + O_2 + Ar \to O_3 + Ar$	$6.4 \times 10^{-35} \exp(663/T_{gas})$	[170]
(2)	$O + O + Ar \to O_2 + Ar$	$5.2 \times 10^{-35} \exp(900/T_{gas})$	[112]
(3)	$O + O_3 \to O_2 + O_2$	$8.0 \times 10^{-12} \exp(-2060/T_{gas})$	[188]

[a] Units for the two– and three–body reactions are $cm^3 s^{-1}$ and $cm^6 s^{-1}$.

density with a maximum up to 3×10^{17} cm^{-3}. However, the gas temperature in the present jet is approximately two times higher (700K compared with below 400K in the case of [196]); hence, the local plasma dissipated power will be larger and it can be expected that the same will be valid for the O density as well. On the other hand, since the electron energy is possibly slightly overestimated by our model (see chapter 2), the dissociation rate might be somewhat overestimated too. According to the Boltzmann solver calculations, the dissociation rate might be reduced to half its value with an average electron temperature of 2 eV instead of 3 eV.

Nevertheless, in the region of the plasma close to the nozzle the high temperature inhibits an even faster rate for the three-body formation of O_3.
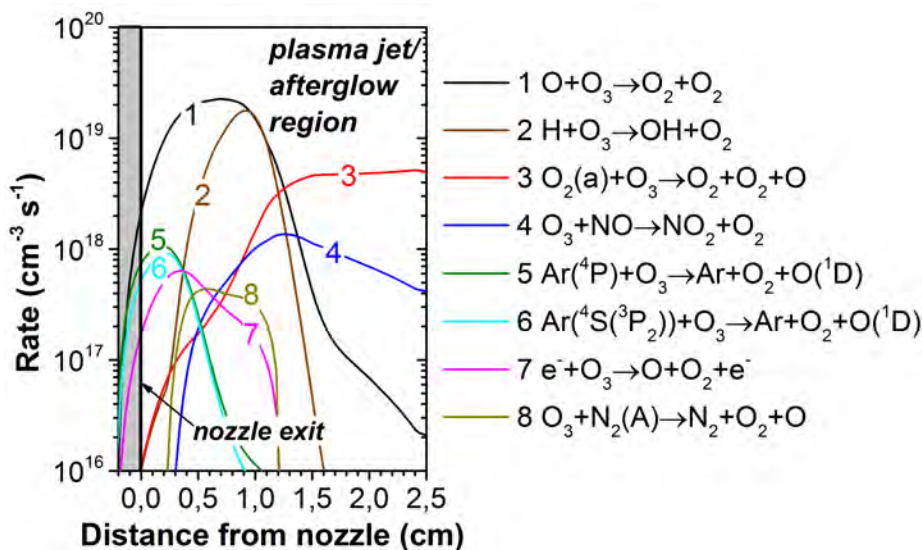
Figure 4.8: O_3 destruction rates of the most dominant pathways, as calculated by the model

Indeed, this reaction type is typically strongly inversely dependent on the temperature (see reaction 1 in table 4.1). Moreover, in this region O_3 is also significantly destroyed by the abundance of O atoms. Nevertheless, more downstream (approximately 10 mm from the nozzle), when humid air entrainment becomes more important, the destruction of ozone by H atoms also becomes significant.

The density of these two atomic species drops significantly in the far effluent, which allows for the increase in the O_3 density. Note that a significant decrease of O and H atoms is found in the model at about 13 mm from the nozzle, which corresponds to the location of the maximum O_3 density found in the experiment. As a result, the destruction of O_3 in the far effluent becomes significantly slower and is determined by long–lived species such as NO and $O_2(a)$.

The calculations predict that the densities of H and O will increase upon rising gas temperature (this dependency is not shown in the figures), but also the rate coefficients of their reactions with ozone will increase, which results in a much higher destruction rate of ozone. Additionally, the rate coefficients for association of O and O_2, thereby forming O_3, are inversely proportional with the gas temperature, which illustrates again that O_3 for-
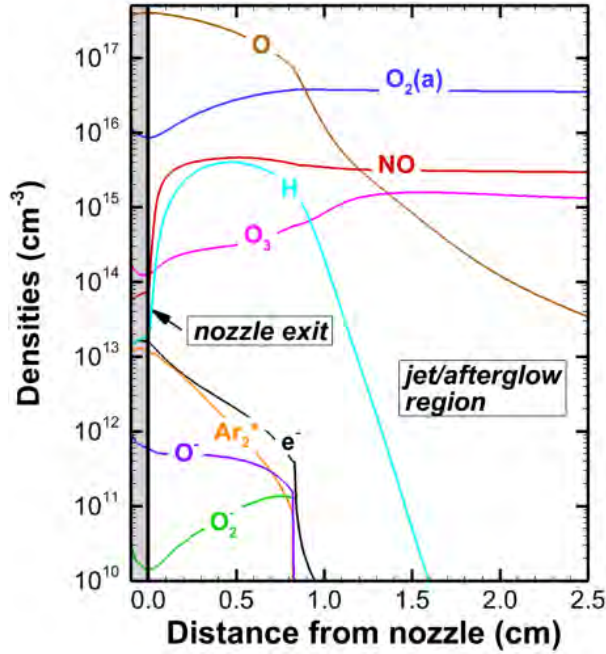
Figure 4.9: Densities of the main species involved in the O_3 formation and destruction pathways, as calculated by the model

mation is extremely sensitive to temperature effects. Again, this effect can clearly be seen in figure 4.5, where the ozone density profiles for three different temperature conditions are plotted.

Interestingly, the model predicts that O atoms are, in the far effluent, mainly created by a collision between $O_2(a)$ and O_3. Note that it is the only significant destruction pathway for both $O_2(a)$ and O_3 in this region. In fact, its reaction rate is low, since its rate coefficient is proportional with temperature and the jet effluent has cooled down to nearly room temperature in that area. Thus, this explains why $O_2(a)$ and O_3 are long-lived species at these time scales. We also want to stress that the O atoms generated by this process, are readily converted back into ozone, since O association with O_2 at room temperature is much faster than the reactions 2 and 3 shown in table 4.1.

Thus, although a direct (inverse) correlation seems to be observed between the gas temperature and the O_3 density, the depletion of O_3 in the plasma core is not attributed to thermal dissociation of O_3 (i.e., $O_3 + M \rightarrow$

118

O + O$_2$ + M) but it is caused by the generation of atomic oxygen and hydrogen, and due to a low reaction rate for the association of O atoms and O$_2$ at high gas temperatures (reaction 1). Indeed, this causes the depletion of O$_3$ in the plasma core.

4.4 Conclusions

The same RF driven DBD–like plasma jet geometry as discussed in the previous chapters, operating at 6.5 W is investigated, but this time with Ar + 2% O$_2$ as the feed gas. Spatially resolved ozone densities and gas temperatures are obtained by UV absorption and Rayleigh scattering, respectively. Significant gas heating in the core of the plasma up to 700K is found and the elevated gas temperature is correlated by a decrease in O$_3$ density. The maximum O$_3$ density is found at 13 mm from the nozzle, downstream of the plasma and equals 2×10^{15} cm^{-3}.

The production and destruction reactions of O$_3$ in the plasma jet as a function of the distance from the nozzle obtained from our 0D model are presented in detail. In the core of the plasma the O$_3$ is produced from O and O$_2$ in three-body reactions while the O$_3$ dissociation induced by atomic species (O and H) is found to be the most important loss process. In the far effluent, where the O density is significantly reduced, O$_3$ is produced less efficiently and the destruction of O$_3$ is due to long-lived species such as NO and O$_2$(a).

The boundary between the two zones with different O$_3$ chemistry is determined by the significant drop of O and H at about 13 mm from the nozzle. This location corresponds with the position where the temperature steeply drops and where the maximum O$_3$ density is observed experimentally. Indeed, it is shown by the model that the gas temperature and the O and H concentrations strongly determine the O$_3$ density. For instance, the reaction rates involved in the destruction and especially the production of O$_3$ (*i.e.*, mainly by the three-body association reaction 1) are temperature dependent. Still, it needs to be emphasized that thermal dissociation of O$_3$ is not causing the depletion of O$_3$ in the core of the plasma.

Chapter 5

Analysis of the O and NO density and reaction pathways in a needle-type atmospheric pressure plasma jet: effect of the electrode geometry and water impurities

Preface

Depending on the type of plasma medicine application, certain plasma agents are desired more than others. For example, nitrogen oxide (NO), oxygen atoms (O) and ozone (O_3) are identified to play a key role in wound healing [95] and sterilization applications [197]. In order to assure the safety of the devices, a detailed knowledge of the chemical cocktail is crucial. Furthermore, it is necessary to investigate how the chemical composition of the jet can be controlled by altering the operating conditions (geometry, gas feed, *etc.*). Numerical simulations can provide this information but at the same time it is necessary to benchmark the model by experimental results. For the work reported in this chapter we make use of the same 0D model to study the reaction mechanism for NO and O in a power modulated RF driven plasma jet for two distinct electrode configurations. We will show that the electrode configuration largely affects the power deposition profile, which results in a different chemistry and species density distribution in the effluent. Walsh *et al* already reported on the contrasting characteristics of such different plasma jet types [198], although mainly by optical emission spectroscopy.

Additionally, we will also investigate in more detail the possible effect of RF power modulation on the chemistry, by comparing the densities calculated by the model with the experimental data.

The next sections will elaborate on the reaction kinetics for both O and NO. Finally, the influence of feed gas humidity will be discussed.

5.1 Experimental setup

In the present chapter we also consider the RF driven micro discharge with needle electrode as in the previous chapters, but with two different grounded electrode configurations (see figure 1.6(a) and (b)). These APPJs were previously characterized for a range of different operating conditions at the Eindhoven University of Technology by Hofmann et al [38, 39], Zhang et al [40] and van Gessel et al [33, 41, 165]. Furthermore, the setups were also used in biological studies [71, 166].

The grounded electrode can be ring-shaped and in that case it is placed over the glass tube. In the alternative setup the electrode consists of a metal plate with a small hole in the center, through which the plasma jet can freely propagate, and which is positioned 3 mm from the nozzle exit. Both configurations are displayed schematically in figure 5.1. It is clear that the electric field is orientated in a different direction for these two configurations (cross field on the left and linear field jet on the right) and this will strongly impact the chemistry in the effluent, as we will demonstrate in this chapter. For this specific study, an argon gas feed of 1.0 slm is again used, mixed with 2% of dry air. This argon gas mixture flows freely into a stationary humid air environment. The plasma is operated at a frequency of 13.9 MHz and modulated at 20 kHz with a 20% duty cycle.

Experimentally, the total power deposited in the plasma is determined by correcting the total power for the power dissipated in the matching box as described in [38]. The resulting value for the plasma dissipated power is used in the numerical simulations to match the experimental conditions. Although experiments were performed for several different plasma dissipated powers, we will study the plasma at approximately 3.5 W dissipated power as a representative case in this chapter.

The experimental data in this work are obtained by Rayleigh scattering to measure the gas temperature, laser induced fluorescence (LIF) to measure the NO density in $situ$, and two-photon absorption laser-induced fluorescence (TALIF) to measure the O density. Moreover, a calibration step enabled the determination of absolute species densities. Finally, Raman
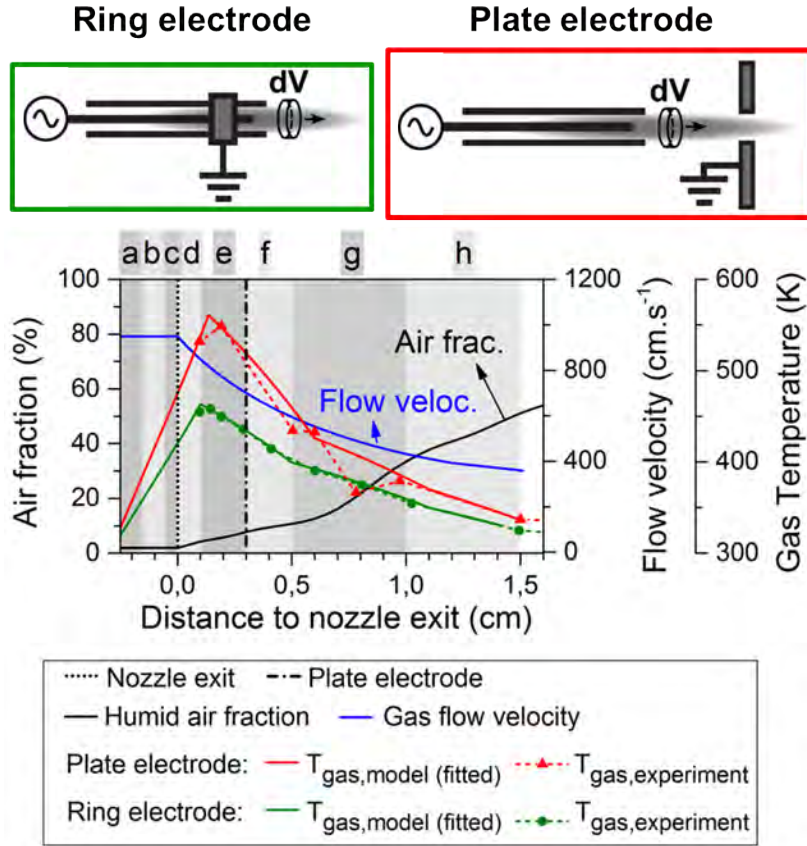
Figure 5.1: Schematic diagrams of the two different plasma needle configurations considered in this study, and input data used in the model (graph): humid air fraction diffusing into the argon stream (the same for both configurations; black curve); estimated flow velocity profile at the jet symmetry axis, based on 2D fluid flow calculations (again the same for both configurations; blue curve); and gas temperature profiles used in the model, for the two different electrode geometries, as obtained from the experiments (red and green curves, solid and dashed lines, respectively).

scattering was used for evaluating the humid air fraction in the argon effluent. More details about these diagnostics and the measurement conditions and procedures can be found in [33, 41, 165, 199].

Table 5.1: Modified reaction scheme for O_3, which now includes $O_{3,vib}$ as a separate species, compared to our previous modelling work. Reactions are taken from [200]. Units for the two– and three–body reactions are $cm^3 s^{-1}$ and $cm^6 s^{-1}$.

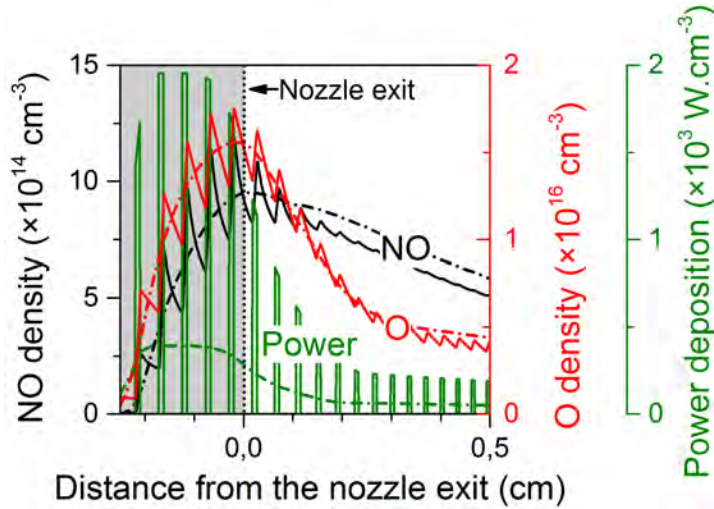| Nr.	Reaction	Rate coefficient
(A.1)	$O + O_2 + Ar \rightarrow O_3 + Ar$	$2.10 \times 10^{-35} \exp(663/T_{gas})$
(A.2)	$O + O_2 + Ar \rightarrow O_{3,vib} + Ar$	$4.30 \times 10^{-35} \exp(663/T_{gas})$
(A.3)	$O_{3,vib} + O \rightarrow O_2 + O_2$	$8.00 \times 10^{-12} \exp(-507/T_{gas})$
(A.4)	$O_{3,vib} + O_2(a) \rightarrow O_2 + O_2 + O$	$2.60 \times 10^{-10} \exp(-1287/T_{gas})$
(A.5)	$O_{3,vib} + O_2 \rightarrow O_3 + O_2$	3.00×10^{-15}
(A.6)	$O_{3,vib} + O \rightarrow O_3 + O$	2.00×10^{-13}

Figure 5.2: Power deposition profile experienced by a random volume element travelling along the effluent in the case of a 20% duty cycle (full green curve; right axis). The resulting NO and O density profiles inside the plasma jet device (grey region) and in the first few millimetres after the nozzle exit are also displayed (full black and red curve, respectively). Additionally, also the calculated profiles for an equivalent continuous power deposition are shown by the dash-dotted curves.

5.2 Model description

The reaction set of the model that is used in this chapter is almost identical to the one used in chapter 3. The only update is the addition of a vibrationally excited state for ozone, $O_{3,vib}$ which resulted in more accurate model results. The reactions with this species are shown in table 5.1.

In literature it is described that 2/3 of the three-body association reactions of O and O_2 forming O_3 generate this vibrationally excited state of ozone [104, 200]. Most of these $O_{3,vib}$ molecules fall back to the ground state by physical quenching (A.5-6), but several chemical quenching reactions (A.3-4) are slightly accelerated as well, compared to the corresponding reactions of ground state O_3 molecules, which results in a lower overall O_3 density. The fact that this $O_{3,vib}$ reaction mechanism was not included in our previous investigations, can explain why the model of chapter 4 predicted less destruction of O_3 in the far effluent than experimentally observed

The plasma properties like gas temperature, gas flow velocity and ambient humid air diffusion (as a function of the position in the effluent), specific for these ring and the plate electrode plasma jet geometries [41, 165], are updated and displayed in figure 5.1.

As the air humidity is not controlled in the lab environment, we estimate that the air humidity is about 50% relative humidity. Furthermore, the gas feed humidity is set to contain 100 ppm H_2O (see also section 5.3.5).

Very important is that the experiments show that the gas temperature profile is very different for the two distinct plasma jet configurations. Obviously, the gas temperature significantly affects the chemistry, as many reaction rate coefficients are a function of this parameter (see previous chapters).

The experiments indicate that the gas temperature starts decreasing in the effluent at 1 to 2 mm from the nozzle exit. It is worth mentioning that from the measurements, however, it remains unresolved whether the temperature at this position is at the maximum, because inside the discharge tube no measurements have been performed. For the majority of this chapter we assume for the calculations that a maximum in the gas temperature profile is indeed reached at this position (*i.e.* 1 mm from the nozzle exit). Moreover, we presume that the gas temperature begins to increase at the needle tip position (*i.e.* where also the power deposition is high), starting from room temperature, as this is the temperature of the gas when entering the tube. We hypothesize that the time is too short for a significant temperature rise in the device before this position (at least at this power), because of the

high flow speed.

Nevertheless, at this stage we are not able to fully exclude the possibility that the gas temperature does not start rising earlier or more rapidly nearby the needle electrode. This is especially the case for the ring electrode configuration where most of the power is deposited within the plasma jet device, as we will demonstrate further in this chapter. At the end of section 5.3.2 we will comment on the possible effect of such a temperature profile on the formation of O and NO.

Crucial in this work is that the power deposition, as a function of the distance from the powered electrode, is not assumed to be linear like in the previous chapters. Indeed, we will demonstrate that the power deposition profile is significantly different for the two plasma jet configurations.

This chapter also features the time modulation of the power deposition (kHz). This modification implies that the duty cycle of 20% is now taken into account, while maintaining the same time-averaged power deposition of 3.5 W. To achieve this, we multiplied the power deposition profile with a factor 5, but this power is 'ON' only 20% of the time. Indeed, this is the power that a gas segment would feel, flowing along the powered needle electrode and beyond. However, the next segment (that follows the previous one) experiences a power deposition at different positions along the effluent. Therefore, we performed simulations for five different kHz modulated power profiles, averaged the results and compared this average with the experimental data for the NO and O density. This is acceptable because the absolute density measurements are performed with high temporal resolution but are always accumulations of a large number of laser shots and thus are intrinsically averaged in the same way.

One of these five modulated power profiles is shown in figure 5.2 for the ring electrode geometry. Note that the power is instantaneously five times higher than the time-averaged power deposition, plotted in the remainder of this chapter (figures 5.4, 5.5 and 5.6).

One can see that the O and NO densities vary by a factor of 2-3 at maximum during the duty cycle, and these variations are only observable inside the plasma jet device or in the first few millimetres after the nozzle exit. The corresponding data for the grounded plate electrode geometry are very similar and not shown.

It turns out that, after averaging the five different power modulated profiles, we observe rather small differences in the species density profiles compared to the simulations with a five times lower, but continuous power (*i.e.* max-

imum 20% difference, dependent on the position in the effluent, see figure 5.2). This is because in general the chemistry for O and NO only scales up, but the relative importance of the various reactions does not change drastically. Indeed, within this power range, when delivering more energy to the electrons by increasing the power, the electron temperature and the electron energy distribution function does not change much. Thus, the ionisation degree of the plasma must rise to maintain the same electron energy density. Therefore, the reaction rates of all electron impact reactions for the generation of the reactive species rise as the density of one of the reactants has increased (*i.e.* the electrons) while the rate coefficients stay the same, so the same chemical pathways continue to be favoured. The experiments of van Gessel *et al* [165] indeed demonstrated that the electron temperature only slightly changes when the power increases fivefold.

Finally, it should be mentioned that the power deposition profile shown in figure 5.2 includes the kHz modulation but not the RF frequency used in the experiment. This should be acceptable, as we study primarily the neutral chemistry which is much slower than the RF period. Thus, it should be sufficiently accurate that the total deposited power for the calculations is equivalent to the experimentally measured plasma power deposition, as long as the bulk chemistry does not change by neglecting the RF frequency. Recall that the previous chapter already demonstrated that this assumption is valid under the given conditions (at least for ozone).

Note that we identify several specific regions (a-h) in most of the figures presented in this chapter (for example see figure 5.1). This will be used in sections 5.3.3–5.3.4 to show how the dominant chemical reactions change throughout the effluent.

5.3 Results and discussion

5.3.1 Time modulation of the $N_2(A)$ density

As a validation of our approach concerning the power modulation (see section 5.2), we will first discuss the calculated densities of species that are strongly affected by this power modulation. More specifically, we will investigate the $N_2(A)$ molecules, as they are very important precursors for both NO and O production. One can see that the $N_2(A)$ density exhibits a

much more pronounced time modulation than the NO and O ground state densities (see figure 5.2 above and figure 5.3 below). Indeed, Van Gessel *et al* [41] and Zhang *et al* [199] found that both the NO and O ground state densities are not strongly affected by the power modulation and are constant as a function of time.

In the work of van Gessel *et al* [41] it was reported that, during the calibration, a lifetime of 24 ns was obtained for NO(A) in the plasma, *i.e.* the electronically excited state of NO. However, the authors did not observe that the density of this species was modulated by the RF cycle (period of 72 ns) although its lifetime is shorter than the RF cycle. The NO(A) is thus most likely not created by electron impact excitation. Therefore, the authors argued that excitation to the NO(A) state is most likely to occur by a collision with $N_2(A)$:

$$NO + N_2(A) \rightarrow NO(A) + N_2 \tag{1.1}$$

Because $N_2(A)$ is a metastable state, this would explain why the NO(A) density is unaffected by multiple RF cycles as well as its slow decay (about 0.7 μs) after the RF power is turned off [41].

Note, however, that the NO(A) state is not included in our model. This is justified because the NO(A) state has a low energy content and does not react much differently than the NO ground state itself. Therefore, we decided to implement the total quenching of $N_2(A)$ by NO simply as follows:

$$NO + N_2(A) \rightarrow NO + N_2$$
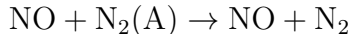
More importantly, as we already demonstrated in chapter 3, O and H_2O are the dominant quenchers of $N_2(A)$ and not NO.

Figure 5.3 illustrates the calculated species densities of NO, O and $N_2(A)$ when a voltage pulse with a 20% duty cycle is applied. Although NO(A) is not included, one can easily see that in about 1 μs after the voltage pulse (power is switched on for 10 μs) the calculated $N_2(A)$ density drops by several orders of magnitude. This is very similar to the experimental 0.7 μs decay time of NO(A), which is in principle created from $N_2(A)$ (see reaction (1.1)). Therefore, we can conclude that there is a good (yet indirect) correlation between the model and the experiments, concerning the voltage pulses.

In addition, in the work of van Gessel *et al* [41] it was shown that the NO(A) density keeps increasing during the pulse. This might seem contradicting
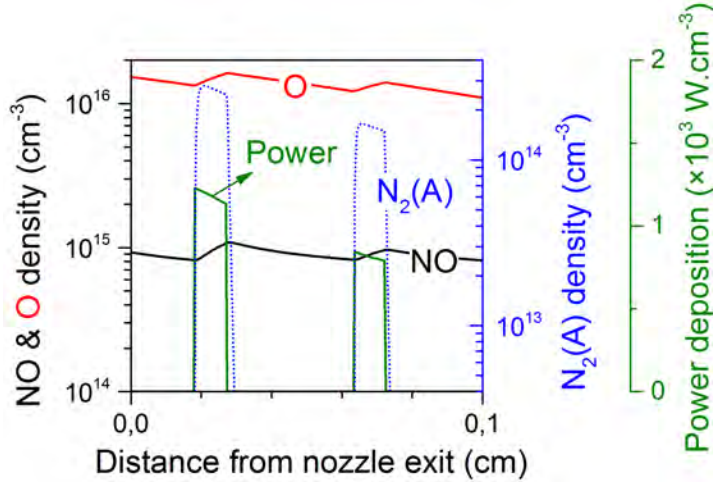
Figure 5.3: Densities of NO, O (black and red curve, respectively; left axis), and $N_2(A)$ (blue dotted curve; first right axis) in the first mm after the nozzle exit, for a random volume element travelling along the effluent in the case of a 20% duty cycle. The power deposition resulting from these voltage pulses is also displayed (green curve; second right axis)

with our calculations, because the $N_2(A)$ density slightly drops in the second part of the voltage pulse. However, the ground state NO molecules, which are the other reactant in reaction (1.1), keep increasing during the pulse, so the overall reaction rate for NO(A) production will indeed continue to increase while the power is on. The reason for the rise in the ground state NO density can be found in the increasing O density during the pulse, as O atoms are involved in several NO production pathways (see section 5.3.3).

5.3.2   Power deposition profiles and their effect on the NO and O density profiles

In our previous studies, we assumed a triangular power deposition profile with a maximum at the electrode and a gradually decreasing slope throughout the effluent. This was done both for simplicity and due to the lack of experimental data. However, such a profile does not perfectly represent the electric field for the grounded ring electrode nor for the grounded plate electrode. Obviously, in the latter case the electric field is directed more

towards the effluent, so a significant power deposition is also expected further in the effluent. For the ring electrode case we will show later in this section that almost all of the power is deposited more closely to the powered electrode needle tip.

To investigate the power deposition profile, we performed a sensitivity study on the effect of several different power deposition profiles on the calculated NO and O density profiles which are also experimentally obtained.

More specifically, we studied the case where all power is deposited very close to the powered needle electrode tip (*cf.* ring electrode configuration), as well as the case where the power deposition gradually starts increasing at the needle tip and reaches a maximum even beyond the grounded plate electrode (*cf.* plate electrode configuration), and several different profiles in between. The calculated NO and O density profiles can then be compared with the experimental data for the two electrode configurations, see figures 5.4–5.7. Because the chemistry of the O atoms is related to the NO formation, we will first discuss figure 5.4 for NO and figure 5.5 for O for the ring electrode configuration before analysing the results of the plate electrode in figures 5.6 and 5.7.

The first power deposition profile from the top graph of figure 5.4, where almost no power is deposited beyond the nozzle exit, results in a narrow NO peak before the nozzle exit. This NO density profile does not agree well with the experimental density profile. The result suggests a deficiency of reactive species, out of which NO is generated (such as N and N_2 metastables, see section 5.3.3), already shortly after the nozzle exit. The overestimated NO density in the far effluent is more difficult to explain and requires a detailed understanding of the reaction chemistry, which will be analysed further in this chapter.

In the bottom graph of figure 5.4 the maximum NO density is found several millimetres beyond the nozzle exit, hence pointing out that initially too few reactive nitrogen species, out of which NO is formed, are generated. Moreover, the maximum density is clearly lower than the experimentally measured maximum value. Further in the effluent, the NO density drop is clearly too steep. We will demonstrate later in this chapter that this can be related to an over-production of O atoms in that region, see also figure 5.5. The intermediate case of figure 5.4 matches the experimental NO profile both quantitatively and qualitatively. Here, most of the power is still deposited inside and close to the discharge tube, but it drops more gradually to low values at 0.3 cm from the nozzle exit (the power deposition becomes
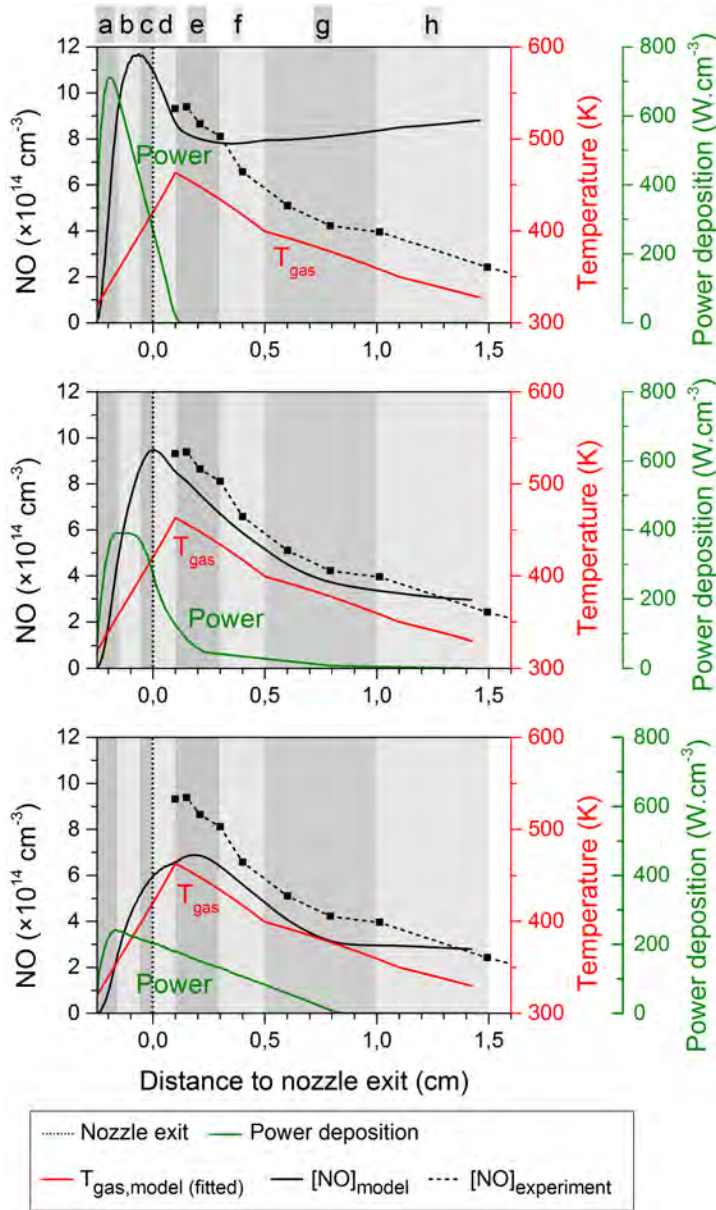
Figure 5.4: Calculated NO density profiles (black solid lines, left axis) for three different power deposition profiles (green curves, right axis). Also shown are the experimental NO density profile (black dashed lines), and the fitted gas temperature profile (red curves) for the ring electrode configuration.

zero at 0.8 cm from the nozzle exit).

When consulting the calculated O density profiles for the different power deposition profiles in figure 5.5, it becomes clear that the power deposition of the middle graph shows once more the best agreement with the experimental data. For the top case the decrease in power deposition is too abrupt, resulting in an O density drop that is too steep. In the bottom case the power is distributed over a too large region and the maximum O density is therefore clearly too low compared to the experimental values.

The quantitative difference between simulated and experimentally measured densities is only a factor 2 at maximum, which can be expected given the assumptions of our model and the uncertainty on the input data, for example the rate coefficients and the accuracy of the density measurements.

In figure 5.6 the calculated NO density profiles for the plate electrode configuration are evaluated, again for three different power deposition profiles. An important feature of this type of plasma jet configuration is that the jet is longer. Recall that the electric field direction is more in line with the symmetry axis of the jet, so the power deposition is expected to be more homogeneous throughout the effluent.

The power deposition profiles from the top and middle graph of figure 5.6 result in quite similar NO density profiles. The calculated values correspond well with the experimental data. In the middle graph the profile shows a maximum density at exactly the same position in the effluent as in the experiment. However, experimentally it was found that the power density remained constant with increasing power as a corresponding increase in plasma size with increasing power was found [38]. This suggests that the power profile of the top graph of figure 5.6 corresponds better to the experiment, although the agreement of the simulated and experimentally measured NO density is not as good. Furthermore, the power deposition profile of the top graph is based on the profile of the middle graph of figure 5.4, but more extended in the effluent. Finally, the simulated and experimental O density profiles for the plate electrode configuration are also more consistent when using the power deposition profile of the top graph in figure 5.7. Therefore, we will use this specific case for the chemical analysis in the next section.

The bottom graph of figures 5.6 and figures 5.7 clearly shows that too much power is deposited far away from the nozzle exit (even beyond the plate electrode), resulting in O and NO densities that are much too high beyond the plate electrode. It is, however, interesting to see that the maximum NO
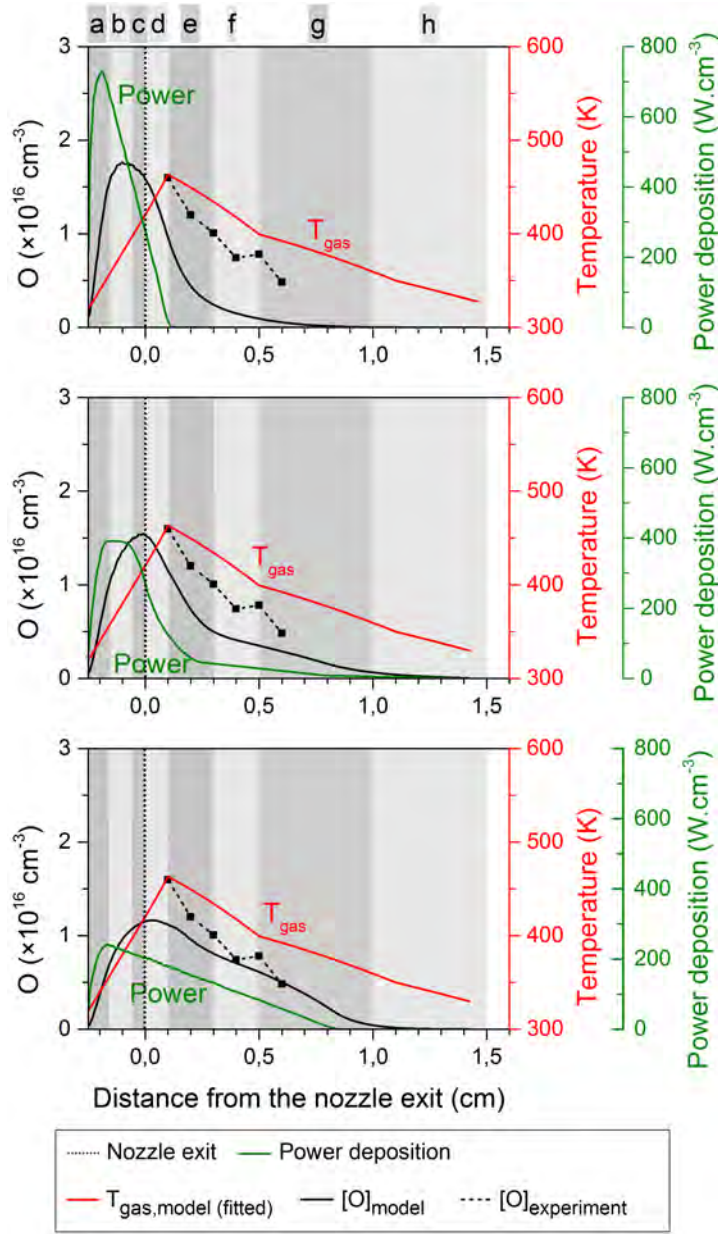
Figure 5.5: Calculated O density profiles (black solid lines, left axis) for three different power deposition profiles (green curves, right axis). Also shown are the experimental O density profile (black dashed lines), and the fitted gas temperature profile (red curves) for the ring electrode configuration.
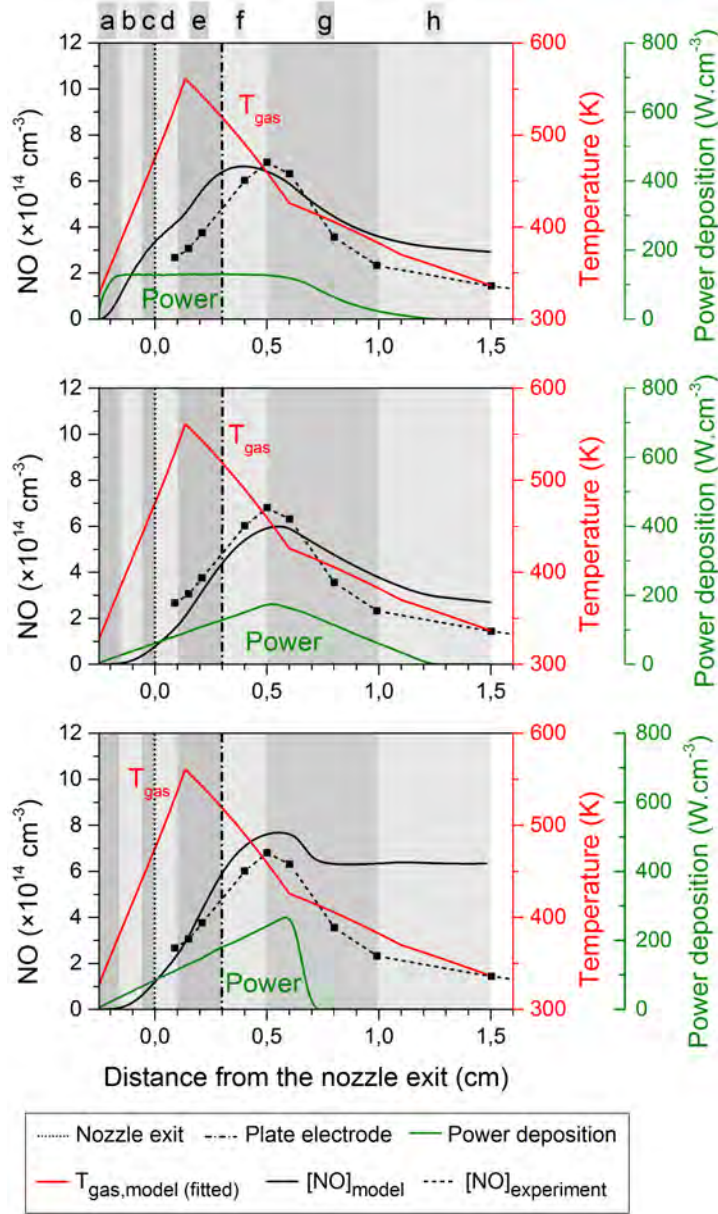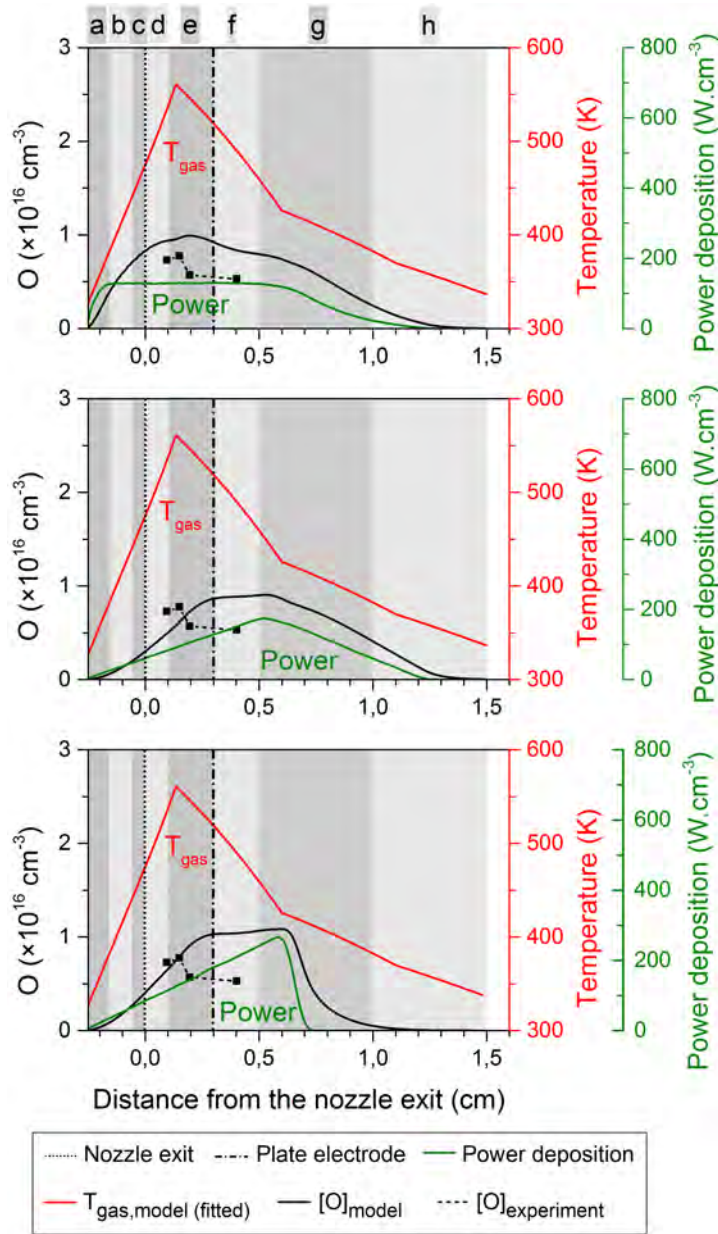
Figure 5.6: Calculated NO density profiles (black solid lines, left axis) for three different power deposition profiles (green curves, right axis). Also shown are the experimental NO density profile (black dashed lines), and the fitted gas temperature profile (red curves) for the plate electrode configuration. The vertical dash-dotted line at 3 mm from the nozzle exit denotes the position of this plate electrode.

Figure 5.7: Calculated O density profiles (black solid lines, left axis) for three different power deposition profiles (green curves, right axis). Also shown are the experimental data points for the O density (black dashed lines), and the fitted gas temperature profile (red curves) for the plate electrode configuration. The vertical dash-dotted line at 3 mm from the nozzle exit denotes the position of this plate electrode.

density is still located at about the same position, which demonstrates that it is not possible to get an NO peak even further in the effluent, not even by placing the majority of the power deposition profile further away from the nozzle exit.

To conclude, one can clearly see that the distinct power deposition profiles result in remarkably different O and NO density profiles. In general, the NO density is higher for the ring electrode configuration (with a maximum density of 9×10^{14} cm^{-3}) and it peaks closely to the nozzle exit, whereas for the plate electrode configuration the NO density is generally lower (with a maximum density of about 6×10^{14} cm^{-3}) and it peaks shortly after the jet passes through the grounded plate electrode.

The O density profile of the ring electrode configuration also exhibits a peak close to the nozzle exit, *i.e.* similar to the NO density. Its maximum density is more than an order of magnitude higher than the maximum NO density (*i.e.* 1.5×10^{16} cm^{-3}), but the density drop is steeper as a function of distance from the nozzle exit. In the effluent of the plate electrode the O density is generally lower, but the concentration of this species fluctuates around 8-9$\times 10^{15}$ cm^{-3} even up to 0.5 cm from the nozzle exit.

The validity of the chosen power deposition profiles is further confirmed by the experimental observations of the electron density profiles (and also the intensity of the light emission) for both plasma jet configurations [165]. Indeed, the experiments indicated that the plasma intensity rapidly drops in between 1 and 3 mm from the nozzle exit for the ring electrode configuration, whereas the active plasma can be found up to 8 mm from the nozzle exit for the plate electrode configuration. This corresponds well with the power deposition profiles used in our calculations which give the best fit for the O and NO density.

Although we demonstrated good correspondence between the model and experiment, we will also address here the possibility of a slightly different temperature profile within the plasma jet device. As mentioned previously, there is no experimental data available on the temperature and species densities for that area. Up to now we assumed that the ring electrode configuration is corona-like with most of the power deposited in close proximity to the needle electrode tip. However, one might argue that this configuration has some characteristics of a broader axial dielectric barrier discharge with plasma formation over the entire length of the ring electrode that surrounds the glass tube. Also, in this case it is likely that the temperature will reach its maximum value earlier than at the nozzle exit. Therefore, we performed
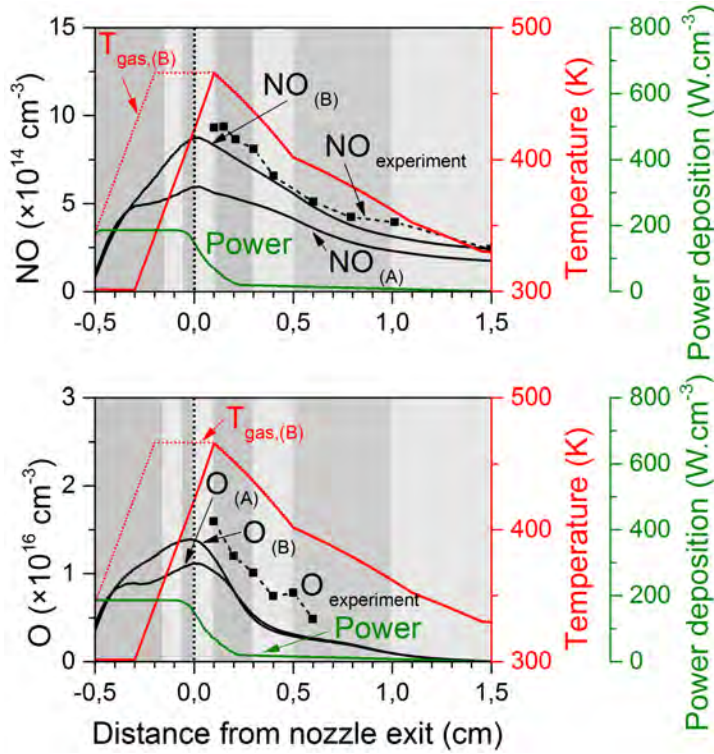
Figure 5.8: Calculated NO and O density profiles (black solid lines, upper and lower graph respectively) for the ring electrode configuration for a power deposition profile representing a more DBD-like discharge (A), in contrast to the corona-like profile used in figures 5.4-5.7. The graphs also contain NO and O density profiles for the DBD-like power deposition profile and a higher gas temperature within the plasma jet device (B). This modified gas temperature profile is indicated with the dotted red curve, the DBD-like power deposition profile is indicated with the green curve (both with axes on the right).

a simulation mimicking these characteristics and the results are plotted in figure 5.8.

By comparing figures 5.8 and 5.4, we can conclude from this simulation that the NO density profile (indicated with 'NO$_{(A)}$') is indeed affected by this different power deposition profile. However, when also the different temperature profile (indicated with 'T$_{gas,(B)}$') is applied, the NO density profile (indicated with 'NO$_{(B)}$') again becomes remarkably similar to the case of a corona-like power deposition profile as discussed above (see figure 5.4). This is because a higher temperature within the device compensates for a lower power density. Indeed, a lower power density results in a lower amount of reactive species out of which NO is created (see section 5.3.3) but the temperature dependent rate coefficients of these reactions increase.

Similarly, by comparing the two O density profile of figure 5.8 with figure 5.5 (middle graph) we can conclude that the generation of O atoms, which are created by electron impact reactions (see below) is affected differently because gas temperature variations have less influence on these reactions. Thus, a high power density at a lower temperature results in more O atoms nearby the needle electrode (see middle graph of figure 5.5), even though the area of high power deposition is smaller and the total amount of power dissipation is the same.

We acknowledge that the power distribution and temperature within the plasma device is important, but additional (experimental) research is necessary to clarify this. However, it has a limited effect on the NO and O density in the effluent and will not change the conclusions made about the effluent chemistry in this work.

The following two sections will elaborate more on the NO and O chemistry, which will help to explain the specific shape of their density profiles. In the remainder of this chapter, we will use the power deposition profile of the middle graph of figures 5.4 and 5.5 for the ring electrode configuration and the power deposition profile of the top graph of figures 5.6 and 5.7 for the plate electrode configuration, as they yield good agreement with experiment for the NO and O density profiles.
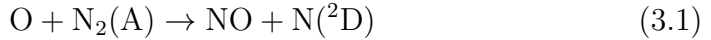
5.3.3   NO chemistry

In this section the chemical reactions for the production and loss of NO throughout the plasma jet will be analyzed for both electrode configurations. The rates of the reactions shown in figures 5.9 and 5.10 are spatial

averages for a specific region in the jet. In some regions of the plasma jet the chemistry changes more rapidly than in others and therefore the averaging is performed over different spatial lengths in the axial direction (corresponding to the letters a-h in figure 5.1). The power deposition profiles used for the ring and plate configuration are taken from the middle graph of figure 5.4 and the top graph of figure 5.6, respectively.

Figure 5.9 clearly illustrates that the predominant production and loss pathways are largely the same for both electrode configurations, although the relative contributions and the total rates can be quite different depending on the region. Indeed, both the production and loss rates are more than a factor 3 higher in the ring electrode configuration than in the plate electrode configuration. In both configurations the rates are the highest close to the nozzle exit, but for the ring electrode configuration they immediately drop drastically beyond that position whereas for the plate configuration the rates only slightly decrease throughout the effluent. This is of course directly correlated to the power deposition profiles, see figures 5.4 and 5.6. Indeed, in the ring electrode configuration, the power deposition profile is more concentrated inside the device and just after the nozzle exit, whereas in the plate electrode configuration, it extends till some distance beyond the plate electrode.

(a) Production of NO

Several processes contribute to the NO production both inside the device and in the effluent for both electrode configurations:

$$O + N_2(A) \rightarrow NO + N(^2D) \tag{3.1}$$

$$O + NO_2 \rightarrow NO + O_2 \tag{3.2}$$

$$H + NO_2 \rightarrow OH + NO \tag{3.3}$$

$$OH + N \rightarrow H + NO \tag{3.4}$$

The first three processes seem to be dominant, especially for the ring electrode setup. For more details on these reactions and species, we refer to chapter 2 .

To a lesser extent, also the reaction between O_2 and $N(^2D)$ and the three-body association reaction between O and N (with any gas molecule M as
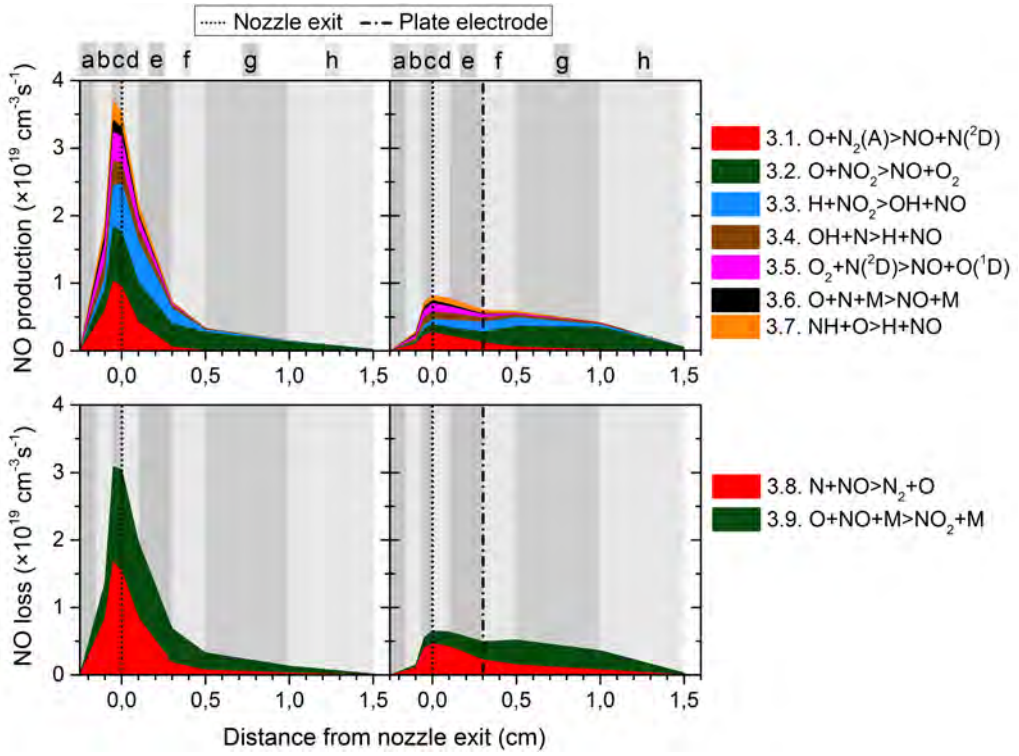
Figure 5.9: Most important chemical production and loss processes for NO throughout the plasma jet, for the ring electrode configuration (left) and plate electrode configuration (right).

third body) contribute to the NO production:

$$O_2 + N(^2D) \rightarrow NO + O(^1D) \tag{3.5}$$
$$O + N + M \rightarrow NO + M \tag{3.6}$$

Finally, also the reaction of NH with O contributes to some minor extent to the production of NO in the effluent:

$$NH + O \rightarrow H + NO \tag{3.7}$$

It should be noted that this reaction actually takes over the role of reaction (3.5) after the nozzle exit because, in the presence of water, $N(^2D)$ rather reacts with water to form NH instead of reacting with O_2. Indeed, water is present in the jet as impurity but the water fraction also rapidly rises after the nozzle exit due to the mixing with humid ambient air.

Note that reaction (3.1) was also identified by Guerra *et al* as an important production channel of NO for an $Ar/O_2/N_2$ surface microwave plasma [201]. Furthermore, reactions (3.1) and (3.5) are similar to the Zel'dovich reaction mechanism, which is well studied in the combustion community [202]. Obviously, as combustion applications occur at high temperature, three-body association reactions, such as reaction (3.6), will not be important at these conditions, because the rate coefficients drop significantly upon higher temperature. Furthermore, due to the high temperatures, a reaction between ground state molecules or atoms is possible in combustion, whereas for cold plasmas activation to electronically excited states, such as $N_2(A)$ and $N(^2D)$ in reactions (3.1) and (3.5), is necessary.

It is also important to mention that reactions (3.2) and (3.3) can be seen as the regeneration of NO because NO_2 is first created out of NO itself (in loss process (3.9); see below). Nevertheless, such regeneration processes are very important and they greatly affect the NO density profile; otherwise NO would be removed almost immediately when the power drops.

(b)   Loss of NO

As far as the loss of NO is concerned, the only two processes that play a significant role, in the entire plasma jet for both electrode configurations, are the reactions with N and O atoms:

$$N + NO \rightarrow N_2 + O \tag{3.8}$$
$$O + NO + M \rightarrow NO_2 + M \tag{3.9}$$

Note that the first process is a two-body reaction, whereas the second process is a three-body reaction involving any background gas molecule (M) as the collision partner.

(c) Explanation of the NO density profiles

After identifying the most important production and loss reactions, we can now compare the chemistry and also explain the NO density peak beyond the plate electrode for that setup.

We see that, for the plate electrode configuration, several of the production processes will decrease significantly beyond the nozzle exit, especially reactions (3.1), (3.5) and (3.6). In these reactions nitrogen species, such as $N_2(A)$, N and $N(^2D)$, are involved. The reason that the rates of these reactions decrease is that the electronically excited $N_2(A)$ state is very efficiently quenched by H_2O and that both N and $N(^2D)$ are created mainly by a dissociation of this $N_2(A)$ state, rather than from ground state N_2. Obviously the H_2O concentration rapidly rises in the effluent due to ambient air diffusion.

On the other hand, the rates of the NO regeneration reactions involving O and H atoms (*i.e.* reaction (3.2) and (3.3)) increase in the effluent of the plate electrode configuration because of increasing O_2 and H_2O levels (again due to ambient air diffusion) while the power deposition stays constant. We want to stress once more that this is thus regeneration of NO_2 into NO and not the creation of 'new' NO. This regeneration mechanism is clearly not very important for the ring configuration because the power deposition in the effluent is not sufficient to yield a large production of either O or H.

Additionally, the loss processes also play an important role in determining the NO density peak beyond the plate electrode. Recall that the gas temperature is significantly higher for the plate electrode configuration than for the ring electrode configuration (see figure 5.1). Therefore, the three-body loss reaction (3.9) is suppressed even far in the effluent of the plate electrode configuration, as this reaction type is typically slower at higher temperature. The lower gas temperature in the ring electrode configuration aids to the fact that the NO destruction becomes larger than the production already shortly beyond the nozzle exit. Nevertheless, even for the plate electrode configuration the loss will eventually become larger than the production (*i.e.* shortly after the plate electrode), although this might be difficult to see in figure 5.9 as the difference is so small.

Overall, it can be deduced from figure 5.9 that for the ring electrode configuration the absolute difference between total production and total loss rate is, depending on the region, much higher than for the plate electrode configuration (*i.e.* at the maximum the values are 3.6×10^{19} cm^{-3}s^{-1} vs. 3.0×10^{19} cm^{-3}s^{-1} for the ring electrode configuration, and about 8.0×10^{18} cm^{-3}s^{-1} vs. 7.0×10^{18} cm^{-3}s^{-1} for the plate electrode configuration). The fact that the net NO production is positive for a larger part of the effluent in the case of the plate electrode clearly cannot compensate for this because the maximum NO density is much lower for the ring electrode configuration, even though the calculations are performed for the same total deposited power in both configurations.

5.3.4   O chemistry

The dominant chemical processes for O formation and loss are displayed in figure 5.10 for both electrode configurations, in a similar way as in section 5.3.3.

The total O production rate for the ring electrode again abruptly drops after the nozzle exit following the power deposition profile which is only high inside the device and just after the nozzle exit, whereas the loss rates decrease more gradually. Therefore, the total O loss rate becomes significantly higher than the total O production rate beyond the nozzle exit (*i.e.* starting from region e).

For the plate electrode configuration, the total O production rate also drops beyond the nozzle exit, although the decrease is less steep than for the ring electrode. This is somewhat unexpected as the power deposition stays constant and the O_2 concentration keeps rising by ambient air diffusion. The total loss of O atoms, however, does not follow the decreasing trend of O production and reaches a maximum shortly after the plate electrode which is also the position where the O density decrease becomes more steep (see figure 5.7).

Finally, figure 5.10 shows that the same reactions are dominant for both configurations, although the absolute rates and the relative contributions greatly vary throughout the plasma jet. Similar to the NO chemistry, the O production and loss rates are 2-3 times larger in the case of the ring electrode compared to the plate electrode configuration.
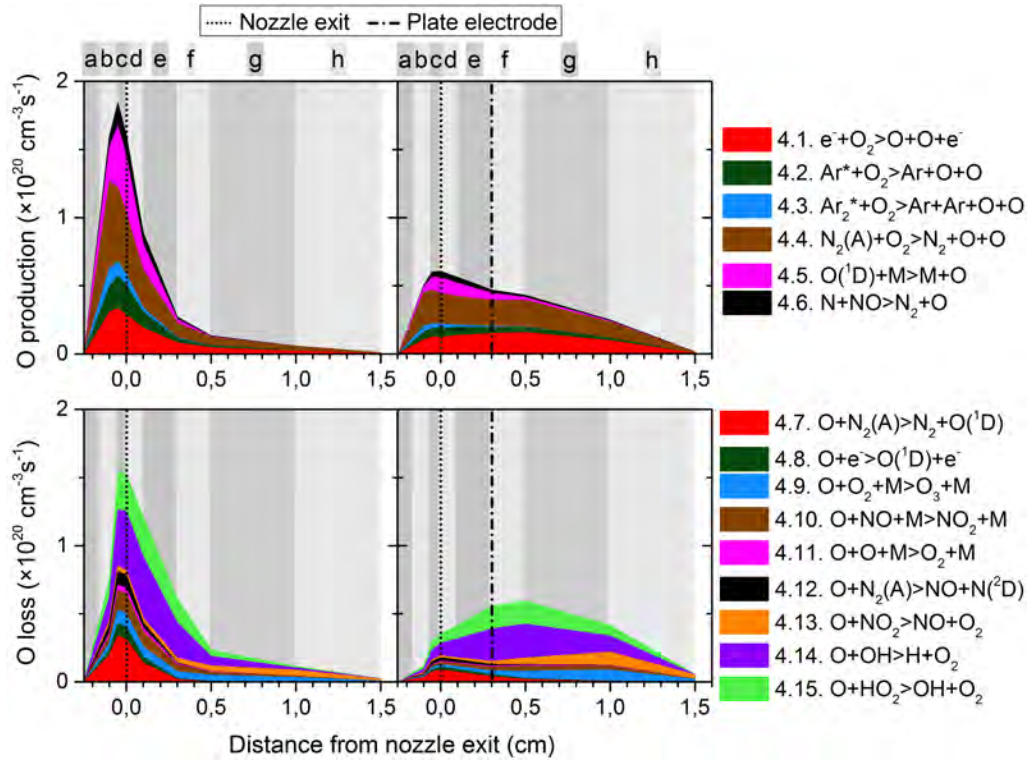
Figure 5.10: Most important chemical production and loss processes for O throughout the plasma jet, for the ring electrode configuration (left) and plate electrode configuration (right).

(a) Production of O

The O atoms are mainly generated by the dissociation of molecular oxygen through various pathways, *i.e.* by electron impact dissociation and by collisions with electronically excited argon atoms (Ar^*), argon excimers (Ar_2^*) and nitrogen metastables ($N_2(A)$), see first four production reactions in figure 5.10 (4.1–4.4).

Furthermore, the quenching of $O(^1D)$ upon collision with any gas molecule M (*i.e.* physical quenching) also contributes to a large extent to the O production (see reaction 4.5 in figure 5.10). This process is, however, not an actual production pathway because $O(^1D)$ is formed out of the O atoms by excitation.

Finally, as was the case for NO, a non-negligible amount of the O atoms is produced in a chemical regeneration reaction:

$$N + NO \rightarrow N_2 + O \tag{4.6}$$

as NO is (mainly) created from O itself (see section 5.3.3 above).

(b) Loss of O

The predominant loss processes of the O atoms, *i.e.* excitation to $O(^1D)$ upon collision with $N_2(A)$ metastable molecules or electrons (see reactions 4.7–4.8 in figure 5.10), are in fact no real destruction pathways, as this excited state is physically quenched back to the ground state O atoms (reaction 4.5 in figure 5.10 and see also chapter 3). Near the nozzle exit, the collisions of O atoms with OH and HO_2, rapidly gain importance:

$$OH + O \rightarrow H + O_2 \tag{4.14}$$
$$HO_2 + O \rightarrow OH + O_2 \tag{4.15}$$

These processes are in fact part of a cycle in which also reaction (4.16) is involved:

$$H + O_2 + M \rightarrow HO_2 + M \tag{4.16}$$

Thus, after the generation of H from H_2O, the H atoms are converted into HO_2 radicals (reaction (4.16)) which are subsequently reduced to OH (reaction (4.15)). The cycle ends with a further reduction, creating H atoms again (reaction (4.14)). Previously, this mechanism has been reported by

Komuro *et al* [203] and Verreycken and Bruggeman [204]. In these three processes there is a net loss of two O atoms and a net production of one O_2 molecule.

The other loss processes shown in figure 5.10 (producing O_3, NO_2, O_2 and NO; reactions 4.9-4.13) all contribute to about the same extent, both inside the device and in the effluent for both electrode configurations.

(c) Explanation of the O density profiles

The efficient H-cycle for the destruction of O atoms (involving loss processes (4.14) and (4.15)) can explain the observed trends in figure 5.5, where the density of the O atoms in the ring electrode configuration decreases quite drastically shortly beyond the nozzle exit (by a factor 3). Note that beyond 3 mm from the nozzle exit the drop in O density is less steep because there is still a low amount of power deposited up to 8 mm beyond the nozzle, as is clear from the middle graph of figure 5.4 and 5.5. Recall that sufficient O atoms are required to convert NO into NO_2 and thus to lower the NO concentration. The presence of O atoms, even far from the discharge tube, was previously reported by Waskoenig *et al* [205] and Reuter *et al* [142].

From the loss processes of the plate electrode configuration it becomes clear that, for a constant power deposition, this H-cycle for the destruction of O atoms becomes more and more efficient in the effluent due to (humid) ambient air diffusion. Of course H atoms can also be created from the initial water impurities in the gas feed and figure 5.10 indeed indicates that there is a considerable loss of O atoms by the H cycle even within the device.

Although it is difficult to see from figure 5.10, it can be deduced that the loss becomes greater than the production in region e for the ring electrode configuration (6.4×10^{19} cm^{-3}s^{-1} versus 3.7×10^{19} cm^{-3}s^{-1}), whereas this happens only in region f for the plate electrode configuration (6.3×10^{19} cm^{-3}s^{-1} versus 5.6×10^{19} cm^{-3}s^{-1}), thus beyond the plate electrode.

It is very clear that the H atom generation is important both inside the device and in the effluent, and plays a significant role in determining the O density profile. Recall that H was also important for NO (re-)generation (at least for the plate electrode configuration) as the H atoms reduce NO_2 (reaction (3.3)) after NO is oxidized to NO_2 (reaction (3.9), see section 5.3.3).
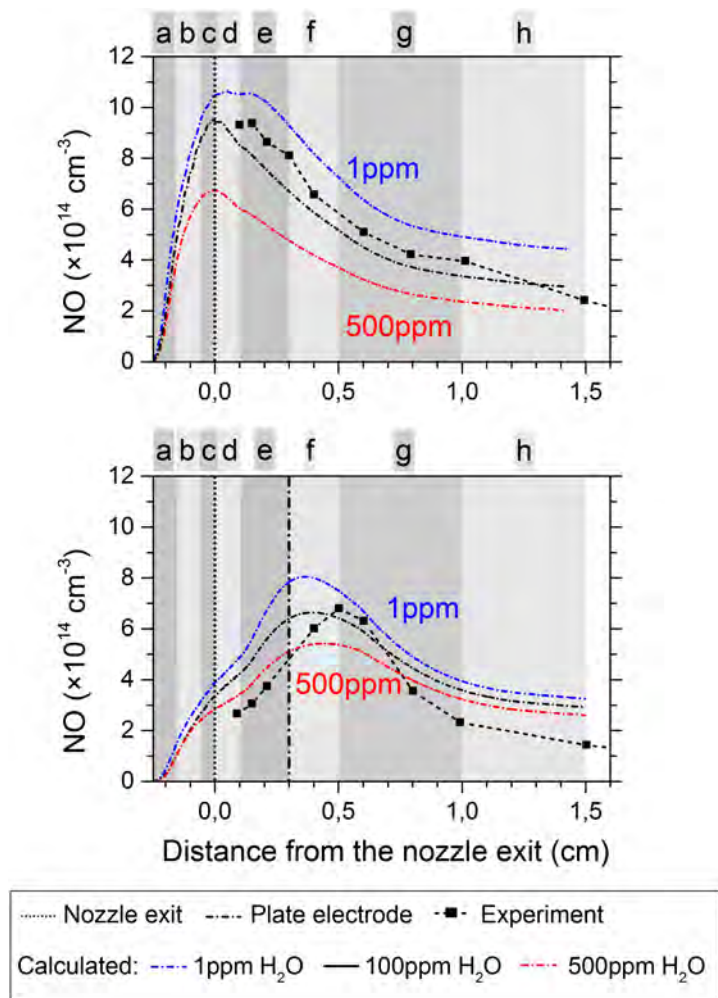
Figure 5.11: Influence of ppm water impurities on the calculated NO density profiles for both the ring and plate configurations (upper and lower graph, respectively).
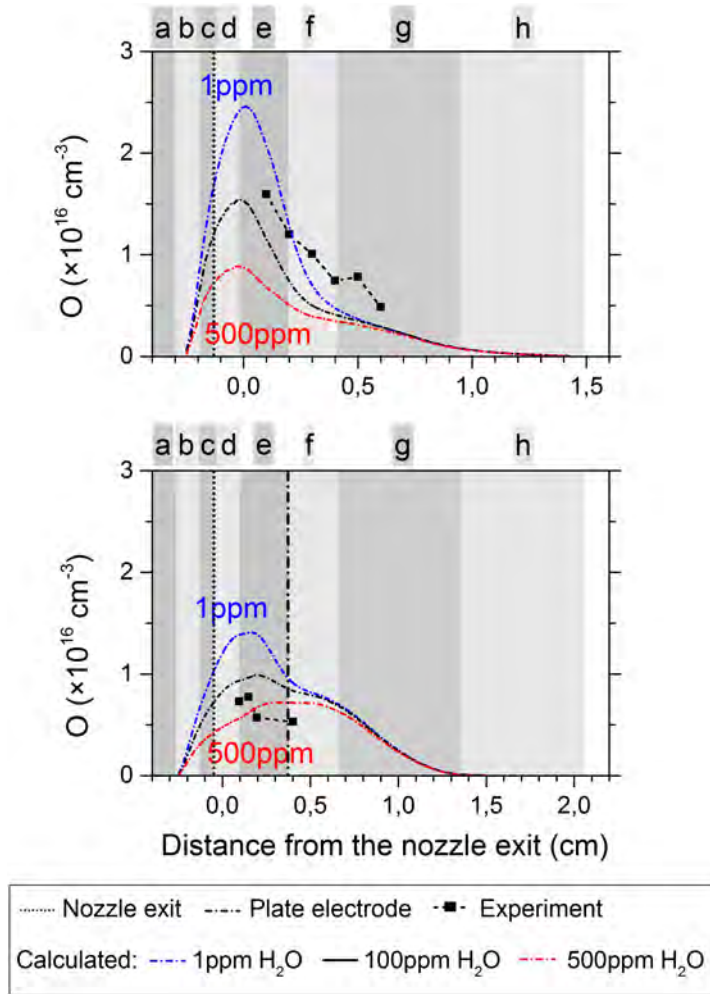
Figure 5.12: Influence of ppm water impurities on the calculated O density profiles for both the ring and plate configurations (upper and lower graph, respectively).

5.3.5 Influence of water impurities

Finally, we discuss the effect of varying the water impurity level in the initial gas feed on our calculation results, as we showed in the previous sections that the H-containing species are very important for the NO and O concentration in the plasma jet. The importance of the feed gas humidity was recently reported by Winter *et al* [163]. Note that this parameter is difficult to control in an experiment, even if the setup is flushed for several minutes or even up to hours.

Figure 5.11 displays the effect of 1 ppm, 100 ppm and 500 ppm water impurity in the Ar + 2% air feed gas on the NO density. The model indeed predicts a considerable influence of the water impurities on the maximum NO density for both electrode configurations, although the shape of the NO density profile does not change much. In general, only the relative contributions of the different loss and production reactions change (data not shown), which still leads to a total decrease of the maximum NO density of about 38% when we increase the water impurity level from 1 ppm to 500 ppm.

Although the rate of NO production processes (3.3) and (3.4) (with H and OH as reactants) should increase for a higher feed gas humidity, as both OH and H are generated in higher amounts when the feed gas humidity increases, we still see the opposite correlation for both electrode configurations.

First of all, this is caused by the efficient quenching of $N_2(A)$ by water, lowering the production of NO through reaction (3.1). Recall that N radicals are also created from $N_2(A)$, as already mentioned above, and so the reactions (3.4), (3.5) and (3.6) are inhibited (indirectly) as well.

Secondly, the NO generation will also be influenced by reactions where O atoms are involved and this concerns both the production (reactions (3.1), (3.2), (3.6) and (3.7)) and the loss (reaction (3.9)) pathways for NO. Therefore, we must first take a look at the effect of the water impurity level on the O density, and this is shown in figure 5.12. It is very clear from these graphs that the O density increases when the feed gas is more dry for both the ring electrode and the plate electrode configuration. Nevertheless, it is not evident to quantify the net effect on the NO density because O atoms will influence both the production and the loss of NO.

For the ring electrode configuration the maximum O density is 70% lower for 500 ppm water in the gas feed than for 1 ppm. For the plate electrode

configuration the decrease is only 45%. This is like expected because, for the ring electrode configuration, most of the O radicals are formed just after the nozzle exit where the humid air diffusion is not yet very large and where the feed gas humidity is thus absolutely crucial. After a few millimetres from the nozzle exit, the water concentration in the jet rises to the level of percentages, which is of course significantly higher than the amount of water that originates from water impurities in the discharge tube. This explains why the effect is less pronounced for the plate electrode configuration.

The reason for the rapidly decreasing O concentration upon increasing feed gas humidity is twofold. First, the production of O radicals is lower because $N_2(A)$ (involved in reaction 4.4 of figure 5.10) is efficiently quenched by water. Second, the destruction of O atoms will be higher at increased humidity since more H-containing species that quench O atoms (see reactions (4.14)-(4.16)) are produced at higher water concentrations.

5.4 Conclusions

In this chapter we demonstrated a good agreement between our semi–empirical 0D kinetic model and experimental observations for two distinct cold atmospheric pressure plasma jet setups. The model provides chemical information on O and NO and their reaction pathways, even for regions that are not accessible by optical diagnostics.

We observed that the power distribution in the effluent is very different in a cross field and in a linear field plasma jet (*i.e.* the setup with a grounded ring electrode and plate electrode, respectively). For the latter, the electric field is oriented in the same direction as the gas flow, which allows power dissipation much further from the nozzle exit causing a longer plasma plume (*i.e.* for the investigated plasma jet setup about 8 millimetres for 3.5 W). Moreover, the power dissipation seems to be more or less constant over the entire length of the visible plasma plume in the linear field jet. In the case of the cross field, the main power deposition is restricted up to a few millimetres from the nozzle exit (*i.e.* for the investigated plasma jet setup about 3 millimetres for 3.5 W). Hence, the power density is much higher for the ring electrode configuration as the total power deposition is equal for both setups.

As a result, the chemistry and the species concentrations in the effluent are quite different for both setups. For the ring electrode configuration the NO

density profile shows a high maximum density of almost 10^{15} cm^{-3} close to the nozzle exit, but the NO concentration then drops abruptly.

The maximum NO density for the plate electrode configuration is, however, only 6.5×10^{14} cm^{-3} and is reached a few millimetres further from the nozzle. The NO density peak is now located much further from the nozzle exit because H and O atoms are being produced in large quantities in that region due to the constant power deposition, and these two atoms are able to regenerate NO from NO_2.

We demonstrated for the ring electrode case that the O density rises to a maximum of 1.5×10^{15} cm^{-3} just beyond the nozzle exit. Beyond 2 millimetres from the nozzle exit the power drastically drops along with the O production. As a result, O is now rapidly destroyed by collisions with OH and HO_2. Note that H atoms act as a catalyst in this multi-step process that results in the conversion of two O atoms into one O_2 molecule and ends with the regeneration of the H atom.

For the plate electrode configuration, O atoms continue to be produced even beyond the plate electrode itself since the power deposition is more or less constant for that entire region. A maximum O density of only 1.0×10^{15} cm^{-3} is reached just before the plate electrode, but the maximum is much broader.

Finally, we also demonstrated that the feed gas humidity is a crucial parameter due to the importance of the hydrogen chemistry and should not be neglected in both modelling and experiments, not even at ppm impurity levels. The effect was the largest for the O atoms, for which we showed a three-fold density decrease upon rising feed gas humidity, in the range between 1 and 500 ppm.

Chapter 6

Analysis of the O$_3$ and NO$_2$ density and reaction pathways in the kinpen atmospheric pressure plasma jet: effect of nitrogen and oxygen admixtures

Preface

This chapter reports on the production of nitrogen dioxide (NO$_2$) and ozone (O$_3$), which are both identified as important RONS in plasma medicine applications.

When nitrogen oxides (NO$_x$) of the gas phase dissolve into the aqueous phase, they react further with water molecules to generate nitrite (NO$_2^-$), nitrate (NO$_3^-$), peroxynitrite ions (ONOO$^-$) and protons [70]. Although the exact ratio between the different NO$_x$ and their reactivity depends on the pH of the biological sample, they generally cause oxidative reactions and are therefore highly bactericidal. The latter is also valid for O$_3$ generated in the gas phase, which causes oxidation of organic cell components in the aqueous phase. When O$_3$ enters the liquid phase it is converted into hydroxyl radicals (OH), especially at alkali conditions since O$_3$ is slightly more stable at acidic conditions. Furthermore, O$_3$ in the liquid is also rapidly decomposed by nitrite ions, forming nitrate ions [71]. However, it should be noted that O$_3$ in fact does not dissolve efficiently into liquid water. This might be compensated by the fact that it is a long-lived species in the gas phase and that, for most operating conditions [206], it is generated in high amounts in oxygen containing plasmas [207].

Besides the bactericidal properties of the RONS, these species are also im-

---

A modified version of this chapter is submitted to New Journal of Physics as: Van Gaens W, Iséni S, Schmidt-Bleker A, Weltmann K-D, Reuter S and Bogaerts A 'Numerical analysis of the effect of nitrogen and oxygen admixtures on the chemistry of an argon plasma jet operating at atmospheric pressure.'

portant in other biological processes such as wound healing. Nitric oxide (NO) is an important signaling molecule for the wound healing process. Furthermore, nitrite ion formation can be important as it can act as storage form of NO [68]. At the right operating conditions, both NO and NO_2 can be generated in large quantities in the gas phase, as will be demonstrated in this chapter. Moreover, in the liquid phase, NO_2 is rapidly converted into nitrite ions and thus indirectly contributes to the level of NO in the biological sample.

In this study we combine the results of laser infrared absorption measurements of NO_2 and O_3 in the plasma jet effluent with numerical simulations of the gas phase chemistry. Both methods are greatly complementary because the numerical simulations offer a very detailed insight in the discharge kinetics, although the complexity of the plasma processes is simplified in the model. Details about the experimental work and the model, which are applicable to this specific chapter will be given in section 6.1.

The results of the measurements and the simulations for a range of operating conditions, *i.e.* different admixtures of O_2 and N_2 to the argon feed gas, are presented in section 6.2. Additionally, these results will be further discussed by means of a chemical analysis for O_3 and NO_2.

6.1 Experimental setup and model description

6.1.1 Plasma source: kinpen

The room temperature, non-equilibrium atmospheric-pressure argon plasma jet considered in this chapter (see also figure 1.6(c) in chapter 1) is a commercial device, the so-called kinpen (neoplas GmbH, Germany) [43, 44]. It is driven by 1 MHz radio frequency (RF) electric excitation.

Figure 6.1 depicts the basic geometrical and electrical configuration, which consists of a high-voltage (HV) needle electrode centred within a dielectric capillary of radius 1.6 mm. The electrode potential is brought from 2 kV to 6 kV and dissipates an average power ranging from 0.9 W to 2.2 W in the plasma (see also section 6.1.3).

A feed gas flow rate ranging from 0.5 slm to 3.0 slm of dry argon can be blown through the capillary and after excitation produces a visual plasma effluent outside the nozzle between 0.3 and 15 mm length. The plasma ef-

fluent length depends on the admixture type and fraction (see also below). In order to control the interaction of the effluent with the surrounding atmosphere, an external gas flux is implemented by means of a gas curtain device. More information can be found in [208]. This gas curtain can be fed with different gases, however, for the purpose of this work dry air is used, only to keep the ambient humidity out of the active region, as reported in [209]. Additionally, the gas curtain enhances the reproducibility and the stability by excluding any variation of water vapour concentration, which strongly depends on the location and time of operation. Furthermore, this gas curtain device is used to couple the plasma jet with the measurement chamber providing a similar atmosphere near the plasma effluent as in open conditions.

6.1.2   QCLAS diagnostic technique

Absolute density measurements of NO$_2$ and O$_3$ produced by the kinpen are performed by laser infrared absorption spectroscopy in the mid-infrared. The experimental setup is identical to the one reported in a previous work by Iséni *et al* and is only described briefly here [210].

The diagnostic apparatus is initially based on the Q-MACS system (neoplas control GmbH, Germany) although some optimizations were performed to allow investigations of plasma jets operating at atmospheric pressure [157, 210].

For the measurement of both species, NO$_2$ and O$_3$, a nanosecond single mode pulsed quantum cascade laser (QCL) is used as a mid-infrared source driven in intra-pulse mode [211, 212]. Unfortunately, pulsed QCLs have typically an emission range only within a few wavenumbers (about $5\,\mathrm{cm}^{-1}$ to $15\,\mathrm{cm}^{-1}$) whereas both NO$_2$ and O$_3$ have their absorption bands separated with a gap of about $600\,\mathrm{cm}^{-1}$. Consequently, two different QCLs (Alpes Lasers SA, Switzerland) are used alternatively, emitting from 1607.72 cm^{-1} to 1619.43 cm^{-1} and from $1024.5\,\mathrm{cm}^{-1}$ to $1029.9\,\mathrm{cm}^{-1}$ to match the absorption band positions of NO$_2$ and O$_3$ respectively.

As the absorption properties of each molecule in the mid-infrared as well as the expected densities are rather low [213], a $60\,\mathrm{cm}$ multipass White cell is used in order to increase the absorption length. The laser beam is focused on the entrance of the multipass cell and is then reflected several times before reaching a very fast mercury cadmium telluride detector (Q-MACS IRDM-600A, neoplas control GmbH, Germany). The number of passes through the

cell is tunable. In this work, a number of 32 passes and a total absorption length of 19.2 m is sufficient to observe a good absorption signal. The signal is acquired by a digitizer board controlled via a computer. The latter monitors the complete system by means of QMACSoft Monitor software [214]. Figure 6.1 illustrates the diagnostic bench and focuses on the coupling of the plasma source to the measurement chamber. In order to collect the reactive species produced by the plasma jet, a measurement chamber is mounted within the multipass cell. The chamber is a cylinder of 9.0 cm inner diameter and 57.5 cm length, yielding a volume of 3660 cm^3.

The coupling of the plasma jet to the measurement chamber is achieved by an opening located at the half-height of the cylinder at the centre of the multipass cell to conserve symmetry between the two exhausts. The gas curtain cap mounted on the plasma device helps to keep the connection with the chamber tightened. It also provides air around the plasma effluent to reproduce the ambient conditions and prevent the chamber to be filled with argon.

As shown in figure 6.1, the mid-IR beam is reflecting on the multipass cell mirrors and passes through the chamber without interaction with the active visual plasma effluent itself. The homogeneity of the gas mixture within the chamber has been checked in a previous work and confirmed by a numerical CFD model [210].

The absolute density measured within the chamber is determined as follows: the laser is tuned to scan a range of about 0.8 cm^{-1} yielding the absorption spectrum. The latter is fitted with a simulated spectrum based on the line strength reported in the HITRAN database [213, 215]. The procedure is automatically implemented through the QMACSoft Monitor software and allows a sample rate of 0.5 Hz in our experimental conditions. The absolute wavelength position and wavelength scale distortion during the laser tuning are corrected via a calibration procedure reported in [157]. Herein, a more detailed description of the fitting method is given.

In order to dry the pipes and the measurement chamber, the gas curtain was flushed with 5.0 slm dry air, at least 12 h before to start. Similarly, the argon pipes were flushed in advance with 0.5 slm for over 6 hours. Indeed, water is known to have many broad absorption bands in the mid-IR, which can lead to a significant disturbance and to an over-estimation of the production rates (or concentrations) of the species but also because even very low amounts of water will influence the plasma chemistry [163, 209, 216]. Moreover, this protocol enhances the repeatability and stability of the di-

agnostic.

From the measured densities n_i (cm^{-3}) of species i, the net production rates R_i:

$$R_i = n_i \times 8 \times 10^3/60 \ \ \text{molec.s}^{-1}$$

are calculated accounting for the total gas flux of 8 slm, *i.e.* combined curtain gas and argon feed gas flux.
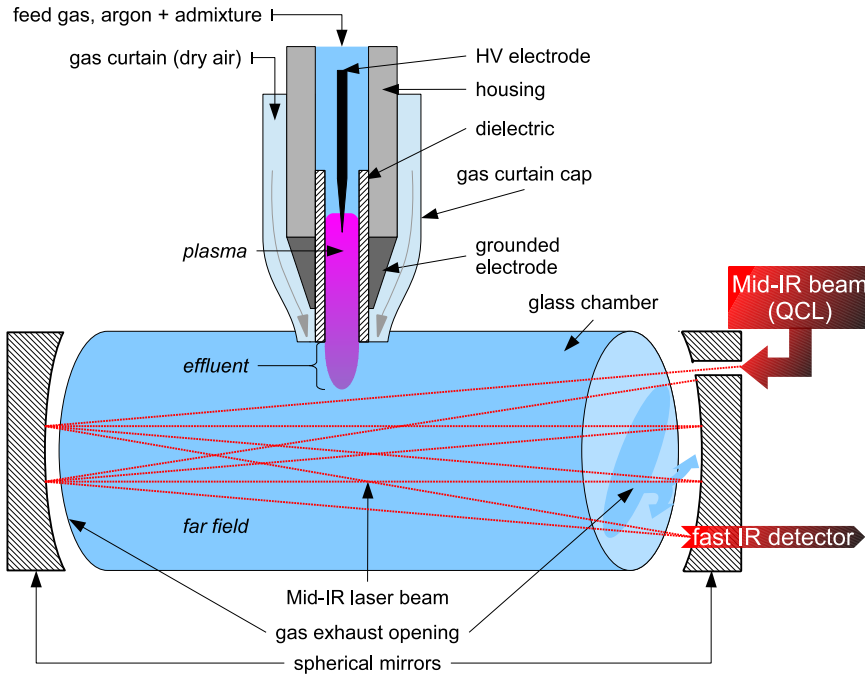
Figure 6.1: Sketch of the experimental setup illustrating the plasma source kinpen with the gas curtain cap connected with the diagnostic chamber of the QCL absorption setup located in a multipass cell.

6.1.3 Power

The power dissipated at the electrode is one of the key parameters to determine how much energy excites the electrons and it is a crucial input parameter for the simulations (see below).

In this work, the power measurement is performed in the same way as reported by Hofmann *et al* [38]. This results in a measured dissipated power

ranging from 1.4 W to 1.8 W in the case of impurity admixtures up to 1.0 %. These values of dissipated power are in agreement with the power reported by other groups using similar argon RF atmospheric pressure plasma jets, *i.e.* with similar length and gas temperature of the effluent, geometry, gas flow rate, *etc.* [42, 217].

6.1.4 Gas temperature

The gas temperature value is a crucial parameter for the application as it needs to be close to room temperature (a few millimeters from the nozzle) in order to avoid any thermal damage on the sample. Moreover, it is also important to know the evolution of the temperature throughout the effluent to be able to accurately model the reaction chemistry.

The gas temperature is measured with a non-metallic fiber-optics probe mounted on a three-axis linear table (FOTEMP1-OEM and TS3, Optocon AG, Germany). Unlike for metallic probes, there is no visible change in the emission of the plasma when the probe is brought in contact with the visible effluent. However, it is noted that with the probe merely average temperatures can be detected, while in a turbulent flow the local temperature can be expected to exhibit significant statistical fluctuations.

6.1.5 Admixture variation

The kinpen in this work is operated with 3.0 slm argon (99.999 % purity) gas feed flow rate and an additional gas curtain of 5.0 slm dry air. The gas flow is regulated by mass-flow controllers (MFC, MKS Instruments, USA). To prevent any impurities and ambient humidity from penetrating the pipes and contaminating the argon, stainless-steel and PTFE gas tubes are used [163].

In this chapter, an admixture variation of O_2 and/or N_2 is applied from 0.0 % to 1.0 % of the total feed gas flow rate (0.0 sccm to 30.0 sccm in absolute values, respectively). The purity is 99.995 % for O_2 and 99.999 % for N_2 according to the provider specifications (Air Liquide GmbH).

The mixing of either of these molecular gases with argon is performed before the gas is blown through the plasma jet in order to obtain a better homogeneity.

Additionally, an artificial mixture of both N_2 and O_2 is also used in this work besides admixing both gases separately. Obviously, this should re-

sult again in a different gas composition of the effluent. In this case, the argon/admixture ratio is fixed (Ar 99.0 % + 1.0 % admixture) but the content of the admixture fraction itself is varied from 0.0 % to 100.0 % O$_2$ with 100.0 % to 0.0 % N$_2$. Hence, a 0.2 % O$_2$/0.8 % N$_2$ ratio is equivalent to a 1.0 % dry air/99.0 % argon admixture.
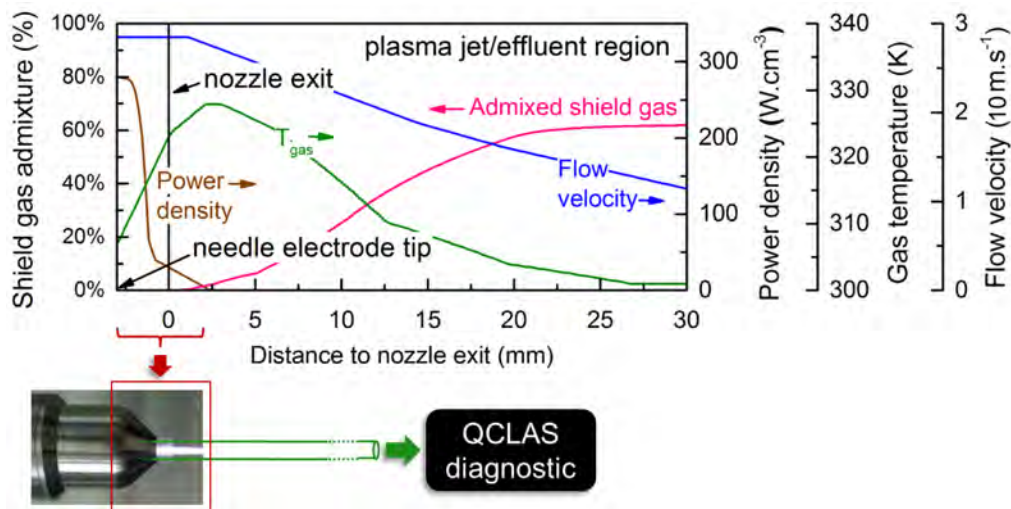
Figure 6.2: Kinpen characteristics along the axial symmetry axis of the device. These profiles of the curtain gas diffusing into the argon feed gas stream, the power density, gas temperature and gas flow velocity are the input to our chemistry model and match either the experimental measurements or the fluid flow calculations (see text). The nozzle exit is located at the axial position of 0 mm. The powered needle electrode (and thus the highest power density) is located a few millimeters before this position. After the nozzle, the plasma jet can freely propagate and eventually enters the 'effluent region' when the power density has become zero and where the temperature drops to 300K.

6.1.6   Model description

The numerical simulations are performed with the same reaction set as used in the previous chapter. The simulated area is the visual plasma jet and beyond (see figure 6.2). The gas flow velocity and the gas curtain entrainment rate follow from an external 2D computational fluid dynamics simulation of the neutral gas at room temperature using Reynolds-averaged Navier-Stokes

with a standard k-ϵ model equations to account for the turbulence [218]. The computed ambient species densities agree well with mass spectrometric measurements [218, 219].

In the far effluent region the gas will eventually become stationary and there we assume that the 3 slm argon feed gas is fully mixed with the 5 slm dry air of the gas curtain. However, it is obvious that there is also an admixture gradient of the gas curtain in the radial direction of the jet. As our model is 0D without a degree of freedom in the radial direction, we simply tested which of the admixture profiles (from different off-axis positions) resulted in the best agreement between the simulations and the measurements. Eventually, the gas curtain admixture profile at r = 0.6 mm resulted in the best correspondence between the experimental and the calculated species densities.

In reality the situation is more complex as the propagation of the ionization wave is strongly linked to the turbulent flow pattern. It was recently found that the ionization wave preferentially propagates through the channel with the highest noble gas content and thus the lowest concentration of admixtures (in the order of 1% and lower). Moreover, as the ionization wave follows the vortices occurring in the turbulent flow, it is often positioned off-axis [220].

The power deposition profile along the effluent obviously depends on the electric field generated by the electrodes and the plasma itself. It is greatly affected by the electrode setup, as was already demonstrated by this model in the previous chapter. Because the electrode configuration of the kinpen has a very similar geometry, we use the same shape for the power deposition profile (see figure 6.2) but the magnitude of the power density is scaled down to match the operating conditions of the kinpen; we set the total power deposition equal to 1.5 W (see section 6.1.3).

Important is also that our power deposition profile, shown in figure 6.2, does not explicitly take the RF excitation waveform into account. We apply this simplification since we are primarily interested in the dynamics of long-lived species and therefore neglect fluctuations on the sub-microsecond timescale. Thus, it should be sufficiently accurate that the total deposited power for the calculations is equivalent to the experimentally measured plasma power deposition, as long as the bulk chemistry does not change by neglecting the RF excitation. Our previous work showed that this assumption is sufficiently valid for argon plasma jets operating at a higher frequency of 13.56 MHz.

The experimentally measured gas temperature profile is plotted in figure 6.2 as well.

6.2   Results

In this section the spectroscopically measured and numerically simulated O_3 and NO_2 net production rates in the far effluent of the plasma jet (measurement cell) are displayed and compared. In the following three subsections, this is done for N_2, O_2 or N_2+O_2 admixtures, respectively. In each of these sections, we also present a detailed reaction kinetics analysis for both O_3 and NO_2, as obtained from the model.

In the context of the comparison of these net production rates in the measurement cell (*e.g.* the values depicted in figure 6.3), it is important to mention that the model was previously only used for simulating the plasma jet effluent for a typical timescale of milliseconds. However, as the residence time of the plasma jet effluent within the measurement cell during sampling by the QCLAS is significantly longer (calculated to be around $25\,\text{s}$), we changed the end time for our simulations to $6\,\text{s}$, in order to allow for a correct comparison with the measured net production rates. At this point there are no drastic changes in the gas densities of O_3 and NO_2 anymore.

Additionally, it needs to be stressed that the values depicted in figure 6.3 are net production rates, so the total production minus the total loss of the species. This distinction has to be made in order to avoid any confusion with some of the values of figure 6.4 (and the consecutive similar figures) where the production and loss rates are presented separately.

6.2.1   Nitrogen admixtures

Figure 6.3 (top) demonstrates a very good agreement between the experimentally measured and simulated NO_2 production rate, for the investigated range of N_2 admixtures between 0 and 1 %: the trend as a function of the N_2 admixture and the absolute values are very similar, with at maximum a factor 2 difference for 0 % N_2. Unfortunately, this is not the case for the O_3 production rate where the difference is up to a factor 3 (see figure 6.3 (bottom)). Furthermore, the model predicts a steeply increasing O_3 production rate between 0 and 0.2 % admixed N_2, whereas the experiments
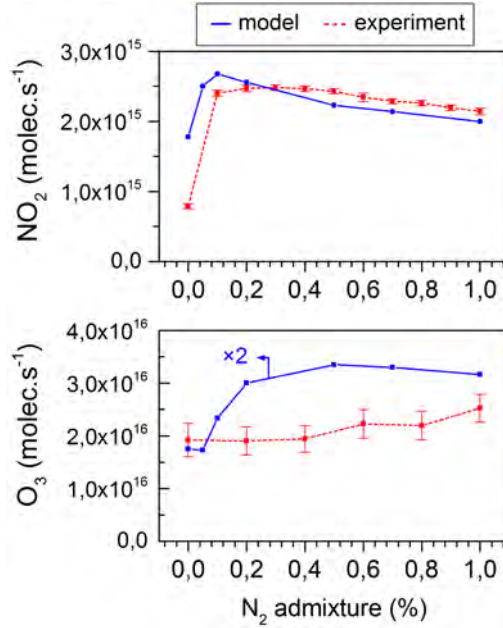
Figure 6.3: NO_2 and O_3 net production rates in the far plasma jet effluent as measured by infrared absorption spectroscopy and simulated by the 0D model, for different N_2 fractions added to the argon feed gas.

indicate only a very slight increase over the entire operating range. Note that this might be explained by the fact that these O_3 concentrations are near the detection limit of the diagnostic setup under the present experimental conditions. Moreover, experimentally, very slight differences in the jet properties, such as turbulence or impurities in the tubes, can easily occur. This determines the concentration of molecular gases in the argon and therefore indirectly affects the O_3 concentrations. Indeed, we will show in this work that the balance between production and loss rates is often very delicate and that a slight inaccuracy can have a large influence on the NO_2 and O_3 net production rate. In this context it needs to be mentioned that we chose to keep the gas curtain entrainment rate consistent for all the simulations, so for the different admixture amounts and for the different admixture gases.

We will now further clarify the production pathways of O_3 and NO_2 by means of a detailed chemical analysis, as obtained from the model, but now focussing mainly on the chemistry that occurs on the time scale of mil-

liseconds. Indeed, this is the time frame where, chemically speaking, the most interesting changes happen. Obviously, this time frame corresponds to the distance that a gas element travels within the kinpen device, the active/visual plasma jet and finally the initial effluent region (thus not the entire measurement cell). The displayed values in figures 6.4-6.9 below (*i.e.* density, the total production and loss rates, the relative contributions of the reactions and electron temperature) are averages for one of these three regions, obtained by performing an integration along the symmetry axis of the jet. Accordingly, the most important chemical phenomena can be identified for each region.

For example, the density evolution of a species, from the vicinity of the needle electrode tip until the far effluent, is thus reduced to only three data points. Indeed, this turned out to be crucial for maintaining a relatively simple overview of the changing chemistry when varying the admixture ratios and at different distances from the nozzle and the needle tip. To make this concept easier to interpret, we added the schematic of the plasma jet above the reaction kinetics data in figure 6.4.

Also important is that in each figure the production rates are displayed in the upper part of the top graph and the loss rates in the bottom part of the top graph (both with white dots, left axis). Note that the y-axis of the loss rates increases from top to bottom, hence opposite to the y-axis of the production rates, to clearly indicate their opposite effect. The same top graph also displays the contribution of the different reactions to the total production and loss rates by colour areas (right axis). We only show the reactions, which contribute more than 10% to the total loss or production of a species. Therefore, the sum of the different contributions often does not reach the full 100%. Note that we show all these contributions, for the sake of completeness, but in the text we only discuss the most important production and loss processes, which are indicated in bold in the legends at the right of the graphs. The bottom graph of these figures presents the species densities.

The short time-scale information in these plots (*e.g.* figure 6.4) is, in general, sufficient to explain the trend observed on the longer time-scale (see figure 6.3).
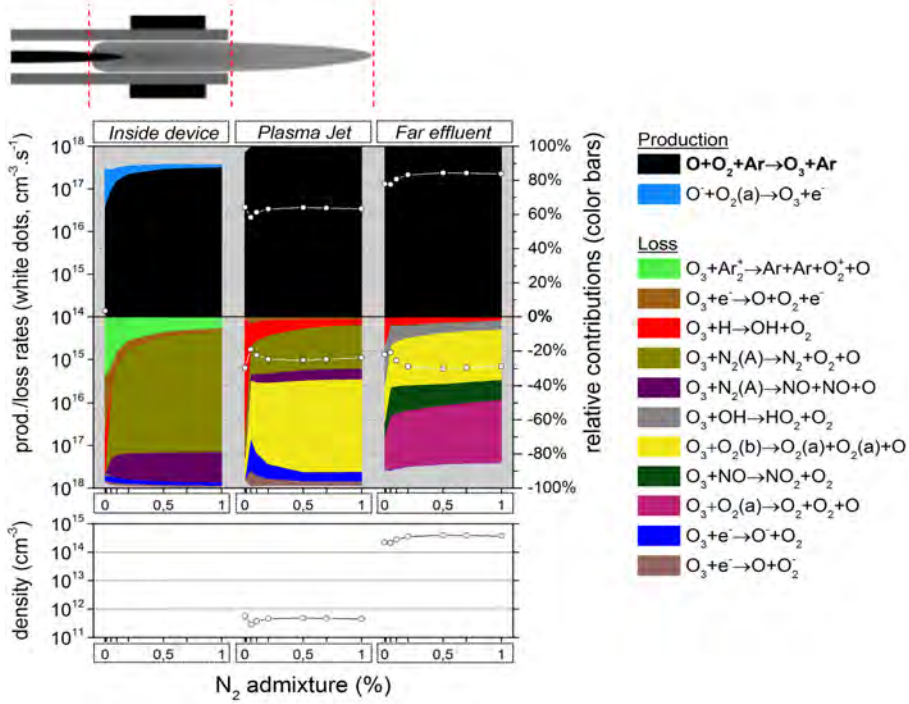
Figure 6.4: O_3 chemistry inside the device, the plasma jet and the far effluent, as a function of the N_2 admixture. Top graph: the white dots represent the total production/loss rates ($cm^{-3} \, s^{-1}$, left y-axis); the colour areas (linked to the right y-axis) represent for each region the spatially averaged relative contributions of the dominant reactions to the total production/loss. The production is plotted in the upper half and the loss in the lower half of the top graph. Note that the y-axis of the loss rates increases from top to bottom, hence opposite to the y-axis of the production rates, to clearly indicate their opposite effect. Bottom graph: spatially averaged O_3 densities in the three regions as a function of the N_2 admixture.
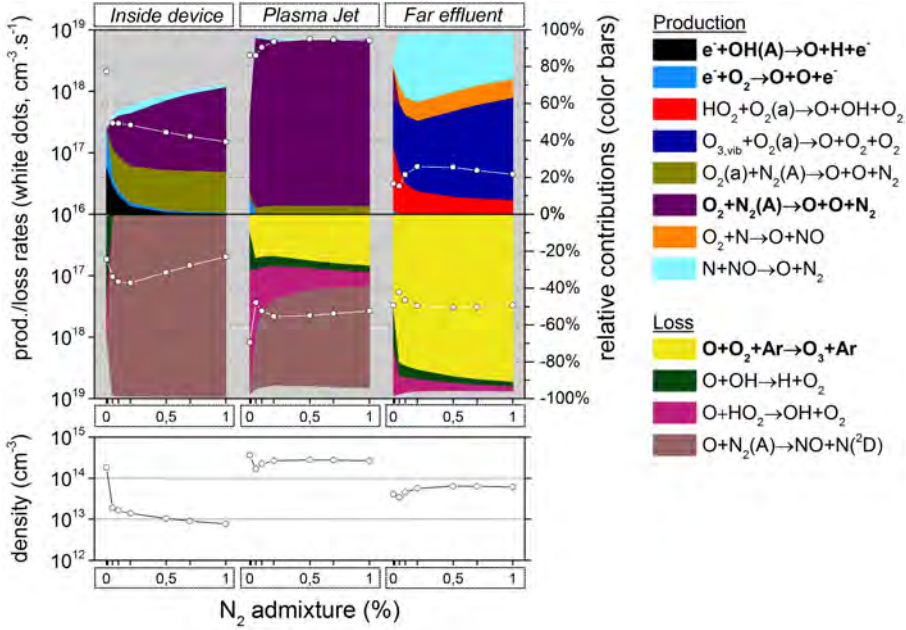
Figure 6.5: O chemistry inside the device, the plasma jet and the far effluent as a function of the N_2 admixture (see figure 6.4 for explanation about top and bottom graph).
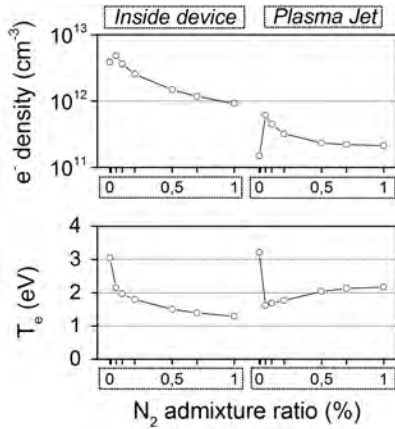
Figure 6.6: Spatially averaged electron densities (cm^{-3}) and average electron temperature (eV) inside the device and in the plasma jet, as a function of the N_2 admixture. The far effluent region is not shown, as the electrons will be negligible in this region.
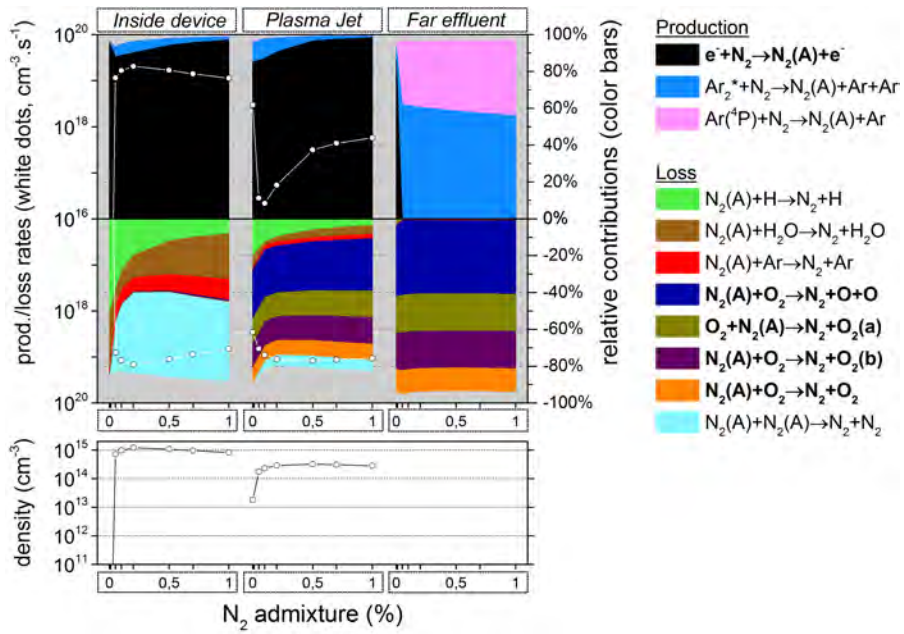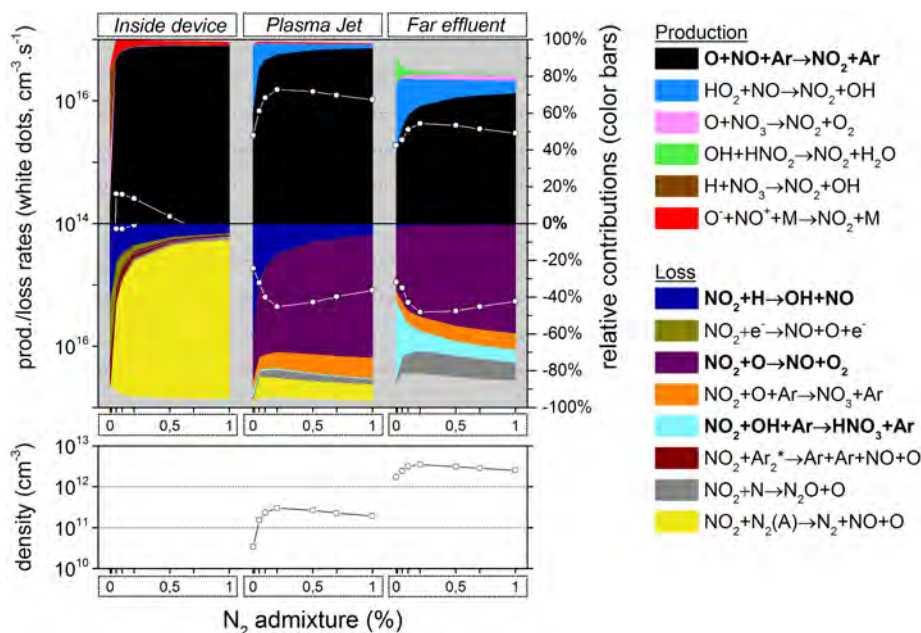
Figure 6.7: $N_2(A)$ chemistry inside the device, the plasma jet and the far effluent as a function of the N_2 admixture (see figure 6.4 for explanation about top and bottom graph).

(a) O_3 formation

Figure 6.4 illustrates that O_3 is mainly formed in the effluent region (see white dots in the top graph) for all N_2 admixtures investigated. Indeed, the formation rate in the plasma jet is about one order of magnitude lower, and there is no O_3 formation at all inside the device. The figure shows the following dominant pathway:

$$O + O_2 + Ar \rightarrow O_3 + Ar \tag{1.1}$$

It is clear from figure 6.4 that the production rate in the far effluent region is more than two orders of magnitude higher than the loss rate (*cf.* upper and lower part of the top graph). Indeed, the main species responsible for the loss of O_3 are the electronically excited states $O_2(a)$ and $O_2(b)$ (see figure 6.4 as well), but they do not reach sufficiently high concentrations. The O_3 density as a function of the N_2 admixture in the early effluent therefore corresponds to the production rate in the far effluent as predicted by the model and depicted in figure 6.3 (note the logarithmic scale in figure 6.4). Recall, however, that the agreement with the experimental result was not very good in this case.

As the O atoms are fully responsible for the O_3 production, we will now analyze the chemistry of this species.

Figure 6.5 illustrates the variation of the O density as a function of the N_2 admixture. Furthermore, it can be seen that the O atom production occurs mainly in the plasma jet region. Indeed, in this region O_2 from the gas curtain starts to diffuse into the argon jet, as shown in [142, 219, 220]. The production in this area is very similar to that of O_3.

Yet for 0% N_2 admixture, the O atom production inside the device is quite significant. Indeed, there is only some N_2 present in the form of impurities, because, as initial conditions of our simulations, we always impose a slight amount of N_2, O_2 and H_2O in the argon feed gas (1 ppm) to mimic the impurities in the gas bottles and desorbed molecules from the piping. This N_2 impurity level is insufficient to reduce the electron temperature as drastically as for cases with significant N_2 fractions (see figure 6.6), where a lot of energy is used for vibrational excitation of N_2. Fast electron impact dissociation of O_2 and electronically excited OH radicals, *i.e.* OH(A) created from H_2O, are therefore possible within the kinpen device at 0% N_2.

$$e^- + O_2 \rightarrow e^- + O + O \tag{1.2}$$
$$e^- + OH(A) \rightarrow e^- + O + H \tag{1.3}$$
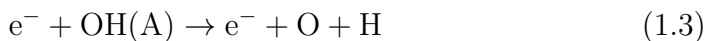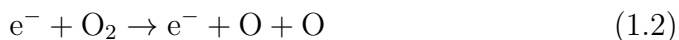
As a result, the O atom density is already significant within the kinpen device when no N_2 is admixed to the argon.

This also explains the maximum in the O atom density in the plasma jet region, at 0% N_2, and the clear drop upon addition of small N_2 admixtures. However, at larger N_2 admixtures the O atom density increases again. Here, the O atoms are mainly created from collisions of O_2 species with the nitrogen metastable $(N_2(A))$:

$$N_2(A) + O_2 \rightarrow 2\,O + N_2 \tag{1.4}$$
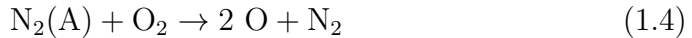
Moreover, in the plasma jet region the rates of the reactions 1.2 and 1.3 become insignificant for 0% N_2. This is because the electron density drastically drops as a result of electron attachment to oxygen species (see figure 6.6; note that the electron chemistry itself is, however, not explicitly shown in this work) since the O_2 density quickly rises due to the mixing of curtain gas with the argon.

Note that figure 6.7 illustrates that $N_2(A)$ is also significantly quenched in this region but the quenching of this state is much slower than that of the electrons. Additionally, the rising O_2 density compensates for this $N_2(A)$ quenching and still causes the rate of reaction 1.4 to be high in the plasma jet region.

Besides, figure 6.7 also illustrates that $N_2(A)$ is mainly formed inside the kinpen device, *i.e.* by electron impact excitation of ground state N_2:

$$e^- + N_2 \rightarrow e^- + N_2(A) \tag{1.5}$$

Thus one might expect a rising $N_2(A)$ density upon increasing N_2 admixture, simply because the density of one of the reactants becomes higher.

However, above 0.4% N_2 the electron density and electron temperature, plotted in figure 6.6, become quite low (due to the vibrational kinetics, as mentioned above) and this compensates for the rising N_2 density. This even causes a slight drop in the rate of reaction 1.5 above 0.4% N_2 and the same behavior is therefore seen for the $N_2(A)$ density in the bottom graph of figure 6.7. As a result the rate of reaction 1.4 (causing the dissociation of O_2 into O atoms in the plasma jet) will also first increase upon increasing N_2 fraction (after the initial drop, as explained above), but after 0.2% N_2 it will remain more or less constant (see figure 6.5). This explains the behaviour of the O atom density upon rising N_2 fraction, and because the O atoms are mainly responsible for the O_3 production, this also clarifies why

the O$_3$ production and O$_3$ density first increase upon rising N$_2$ fraction, then remains more or less constant and eventually slightly decreases for N$_2$ fractions above 0.5% (see figure 6.4 and also figure 6.3 above).

The above explains the production rates predicted by the model. We believe that we at least identified all the dominant reactions correctly, although the agreement with the experiments is not perfect. Note that deviations can easily occur since the balance between the production and loss processes of all the species involved here is delicate. A more complete model approach might be better in this case.

Figure 6.8: NO$_2$ chemistry inside the device, the plasma jet and the far effluent as a function of the N$_2$ admixture (see figure 6.4 for explanation about top and bottom graph).

(b) NO$_2$ formation

Figure 6.8 illustrates the NO$_2$ production and loss rates, as well as the relative contributions of the different processes and the NO$_2$ density, as a function of N$_2$ admixture. It is clear that NO$_2$ is mainly produced from NO,
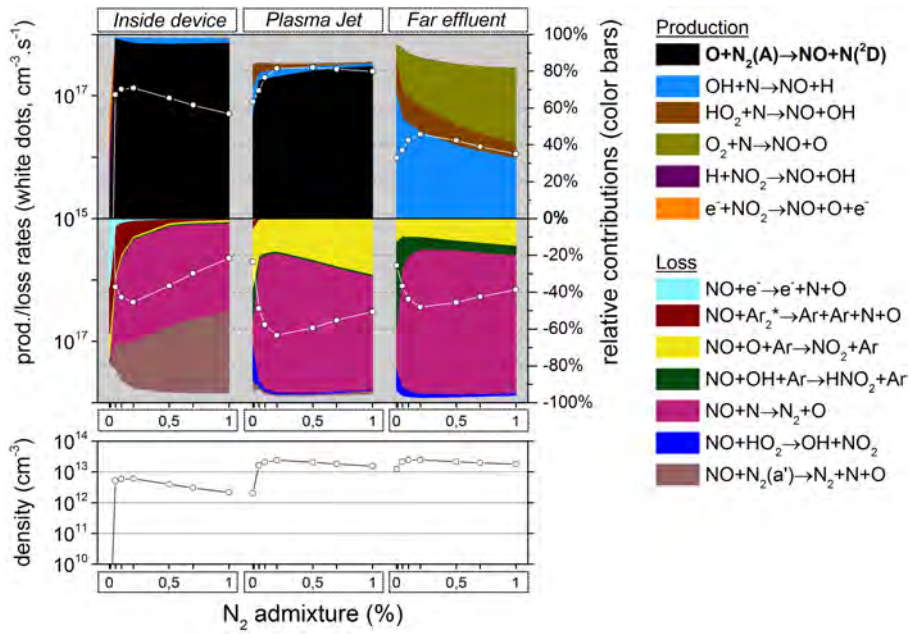
Figure 6.9: NO chemistry inside the device, the plasma jet and the far effluent as a function of the N₂ admixture (see figure 6.4 for explanation about top and bottom graph).

especially by reaction 1.6, and to a lower extent also by reaction 1.7:

$$O + NO + Ar \rightarrow NO_2 + Ar \tag{1.6}$$
$$HO_2 + NO \rightarrow OH + NO_2 \tag{1.7}$$
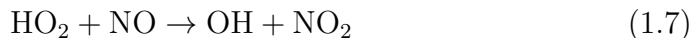
These processes are especially important in the plasma jet. Indeed, the total production rate of NO_2 is almost an order of magnitude larger than the total loss rate here. In the effluent region this production rate has already decreased by at least a factor 2, but additionally the loss rate (*i.e.* mainly the reaction $NO_2 + O \rightarrow NO + O_2$) is now of about the same magnitude. The net production rate is therefore much smaller in the effluent than in the plasma jet region.

Still, NO_2 is a rather long-lived species because there are no highly reactive species present in the effluent that are sufficiently abundant to cause considerable NO_2 loss within these time scales. Note that the O atoms are involved both in the main production and loss reactions of NO_2 and this species will eventually get depleted in the effluent region (see figure 6.5 above. The same is true for N and OH, which are involved in several other loss processes).

Important to mention is that NO_2 reaches only its maximum concentration towards the end of the plasma jet region, whereas the density practically does not change any more in the effluent region and stays continuously high here. The averaging we performed thus results in a relatively low NO_2 density in the plasma jet region, although it is mainly produced here.

Because NO is the main NO_2 precursor, we show the NO chemistry in figure 6.9. NO is produced in large amounts early in the plasma jet region, by a reaction between $N_2(A)$ and O atoms:

$$N_2(A) + O \rightarrow NO + N(^2D) \tag{1.8}$$
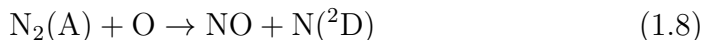
The reason for this is twofold: first, the maximum $N_2(A)$ density is located close to the needle electrode where the power density is at maximum; further in the plasma jet it is rapidly quenched by O_2, thereby creating O atoms or excited O_2 molecules (see figure 6.7). Second, the O atoms only reach a maximum density in the plasma jet region, as illustrated in figure 6.5, because of the oxygen entrainment from the ambient into the argon, which obviously only starts after the nozzle exit. The combination of these two effects explains why the maximum rate of reaction 1.8 is located in the early plasma jet, close to the nozzle exit. Nevertheless, the production of

NO by this reaction is also non-negligible inside the device, as is clear from figure 6.9.

As the excited $N_2(A)$ molecules mainly determine the NO formation, and NO is the dominant NO_2 precursor, the NO_2 production as a function of the N_2 admixture therefore largely follows the trend of the $N_2(A)$ state, which depends both on the N_2 fraction and on the electron temperature inside the kinpen device, as the latter determines the rate coefficient. Because the electron temperature (and hence the rate coefficient) drastically decreases upon increasing N_2 fraction, at least within the device (see figure 6.6 above), these two effects are opposite to each other.

Thus, the NO_2 production (and density) steeply rises immediately when small amounts of N_2 are added, but beyond 0.15% N_2 the NO_2 production (and density) drops again, because the effect of the electron temperature starts to play a more dominant role. Indeed, this explains the trend seen for the NO_2 production rate in figure 6.3 above.
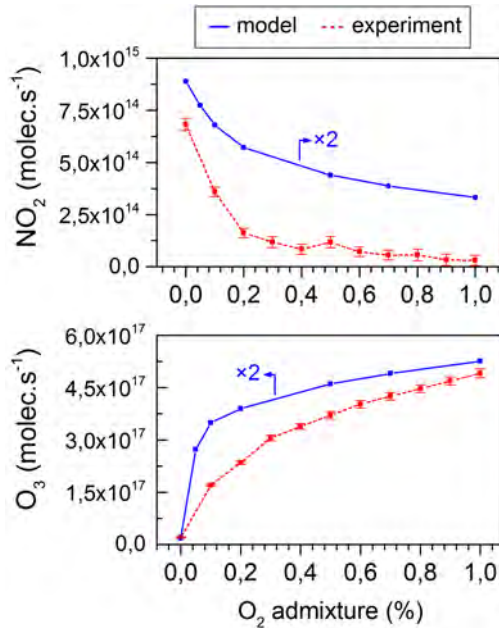
Figure 6.10: NO_2 and O_3 net production rates in the far plasma jet effluent as measured by infrared absorption spectroscopy and simulated by the 0D model, for different O_2 fractions added to the argon feed gas.

6.2.2 Oxygen admixtures

This subsection is structured in exactly the same way as the previous one for nitrogen admixtures. We first look at the longer timescale, comparing experiments with simulations and consequently we explain the observed trends on the basis of a chemical reaction analysis of the short timescale.

The trends of both the NO$_2$ and the O$_3$ production rate as a function of the O$_2$ fraction in the argon feed gas (from 0 and 1 %) are reproduced well by the model, as demonstrated in figure 6.10. The NO$_2$ production rate decays exponentially as a function of the O$_2$ fraction, while the O$_3$ trend is practically the inverse with a sharp increase between 0 and 0.2% O$_2$. The absolute values are, however, not fully comparable, although the difference is at most one order of magnitude within the investigated range of the O$_2$ fraction. As previously stated, this might be related to the inaccuracy on the amounts of curtain gas that diffuses into the jet (*i.e.* the absence of a radial gradient in the model or consequences of turbulence).
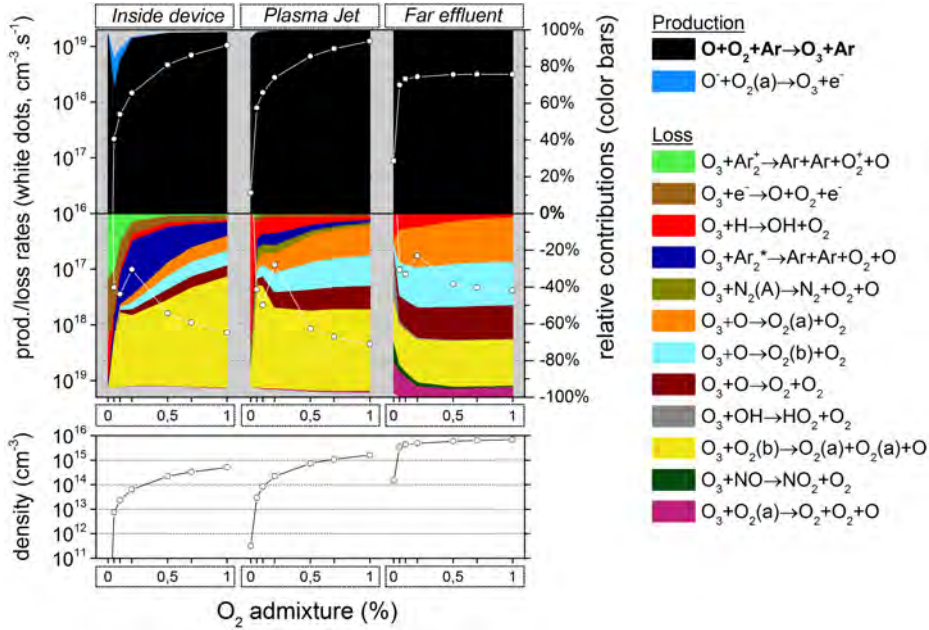
Figure 6.11: O$_3$ chemistry inside the device, the plasma jet and the far effluent as a function of the O$_2$ admixture (see figure 6.4 for explanation about top and bottom graph).
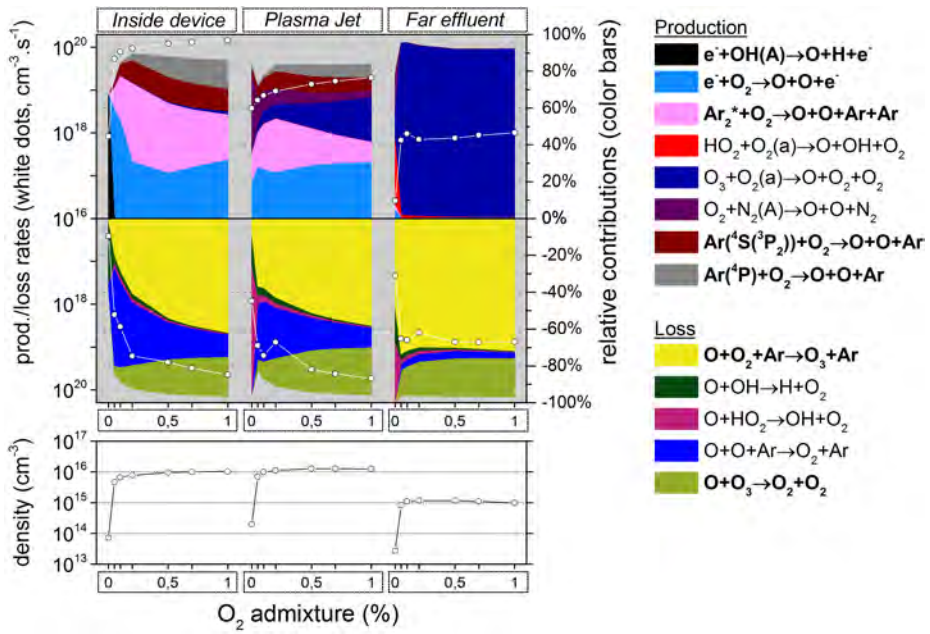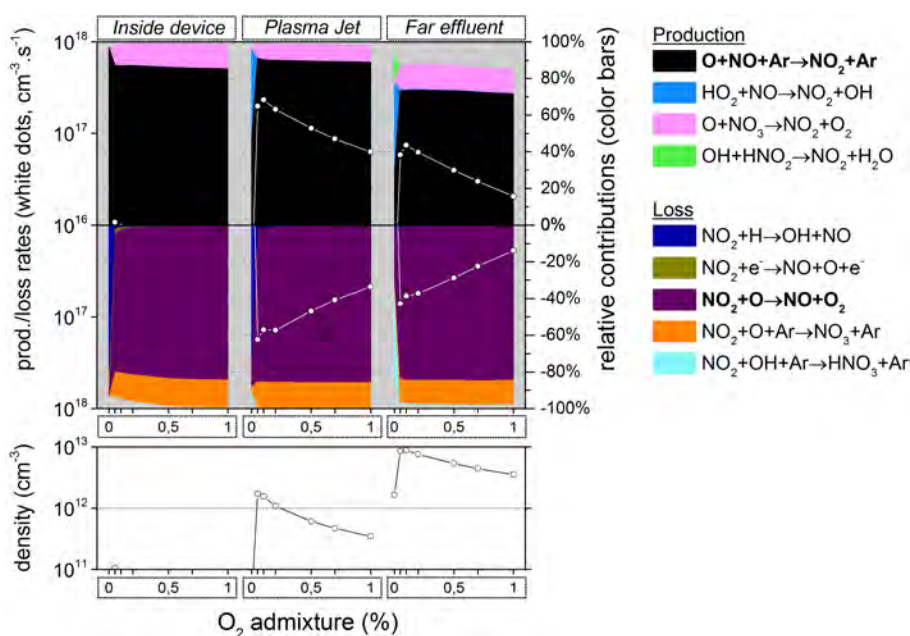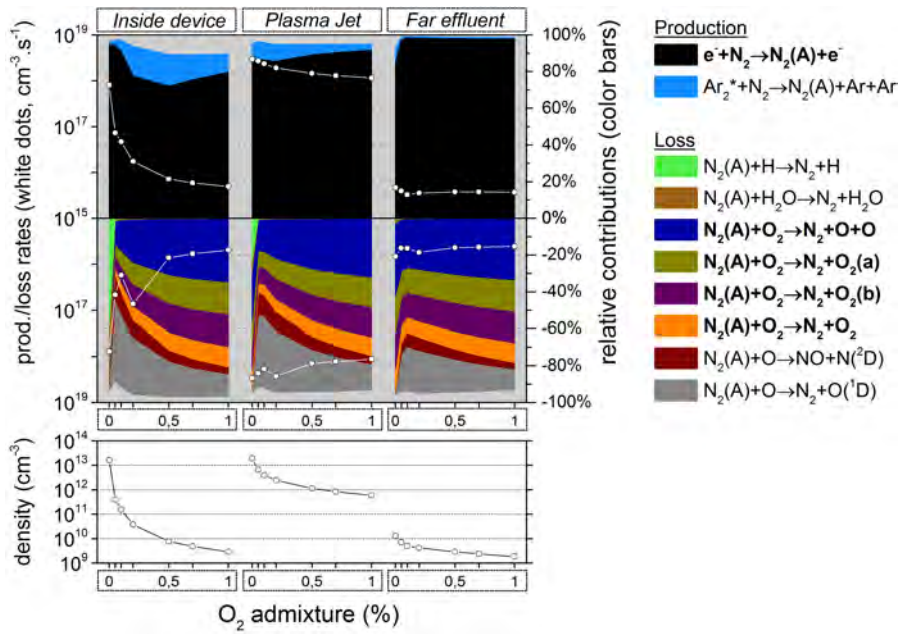
Figure 6.12: O chemistry inside the device, the plasma jet and the far effluent as a function of the O₂ admixture (see figure 6.4 for explanation about top and bottom graph).
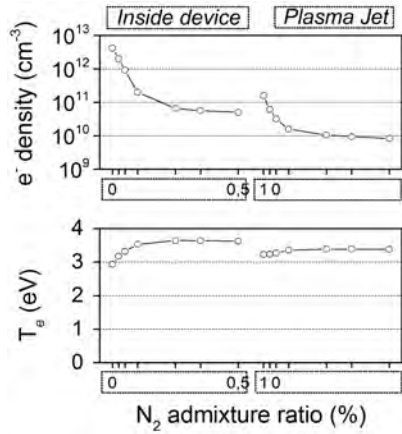
Figure 6.13: Spatially averaged electron densities (cm^{-3}) and average electron temperature (eV) inside the device and in the plasma jet, as a function of the O$_2$ admixture. The far effluent region is not shown, as the electrons will be negligible in this region.

(a) O$_3$ formation

As described in section 6.2.1(a), O$_3$ is almost exclusively produced by reaction 1.1. However, in the case of adding O$_2$, this occurs already in the plasma jet region and even inside the device, at least for O$_2$ fractions above 0.2%, as demonstrated in figure 6.11.

For lower O$_2$ levels there is clearly not yet enough O$_2$ present inside the device and in the (early) plasma jet to yield a large rate for reaction 1.1. Therefore, the production will occur in such a case mainly in the effluent region when there is enough entrainment of O$_2$ from the gas curtain.

At higher O$_2$ fractions, the production of O$_3$ is smaller in the effluent than in the plasma jet region or even inside the device. Nevertheless, since the O$_3$ loss is clearly negligible in the effluent region, the O$_3$ density is still at maximum here (see figure 6.11). The absence of a significant loss process explains why O$_3$ is a relative long-lived species.

As described in section 6.2.1(a), the O$_3$ production is mainly determined by the O atoms; therefore, the chemistry of the O atoms is displayed in figure 6.12. The O chemistry, however, is now considerably different from the case when adding N$_2$ (section 6.2.1(a)). Indeed, the O atoms are now mainly produced within the kinpen device, so mainly from the oxygen admixture itself and not from the gas curtain.

Secondly, in the absence of significant N_2 admixtures, the O atom production is now mainly due to the dissociation of O_2 by direct electron impact and by collisions with energetic argon species (*i.e.* Ar_2^* excimers, $Ar(^4S(^3P_2))$) metastables, as well as higher excited states, grouped in the model as $Ar(^4P)$, but not by collisions with $N_2(A)$. Note that the heavy particle reactions with energetic argon species are in fact also an (indirect) result of electron impact reactions, because these species are created by electron impact excitation of Ar ground state atoms, possibly followed by an association with another Ar atom to form the Ar_2^* excimers (data not shown).

A third difference is that the contribution of O_2 dissociation upon collisions with the argon species increases with rising O_2 fraction, whereas the contribution of direct electron impact dissociation drops (at least between 0 and 0.2% O_2). Indeed, the contribution of the latter process is more than 60% at very small O_2 concentrations, compared to about 30% above 0.2% O_2. This can be explained by the electron temperature evolution as a function of the O_2 admixture (see figure 6.13). Clearly, the average electron temperature rises for higher O_2 admixtures and argon excitation therefore becomes relatively more important than O_2 dissociation because its higher threshold energy is not an issue anymore and since the reaction coefficient drastically increases with the electron temperature.

Finally, note that after the initial rise in net O atom production (and thus O atom density) until 0.2% O_2, the O atom density stays relatively constant at higher O_2 admixtures (*i.e.* between 0.2% and 1.0% O_2). This is not only because the average electron temperature is rather constant in this range but also because the O atoms seem to be 'self-quenching' as the main loss pathway of the O atoms creates O_3 (see reaction 1.1) and the latter is also quite important for the loss of O atoms (see figure 6.12 again):

$$O_3 + O \rightarrow 2\ O_2 \qquad (2.1)$$

The O_3 production is therefore almost linearly dependent on the O_2 fraction between 0.2% and 1.0% (or between 0.3% and 1.0% for the experimental values), as was depicted in figure 6.10. Indeed, the rate of reaction 1.1 is practically first order because the O atom concentration does not change much in this range.

Figure 6.14: NO$_2$ chemistry inside the device, the plasma jet and the far effluent as a function of the O$_2$ admixture (see figure 6.4 for explanation about top and bottom graph).

Figure 6.15: $N_2(A)$ chemistry inside the device, the plasma jet and the far effluent as a function of the O_2 admixture (see figure 6.4 for explanation about top and bottom graph).

(b) NO_2 formation

The admixture of O_2 does not change the dominant production pathway for NO_2 compared to the admixture of N_2 (see section 6.2.1(b)). NO_2 is still mainly formed by the reaction between O and $N_2(A)$ producing NO (by reaction 1.8 above, data not shown again here), which then oxidises further by the three-body reaction with O atom and Ar as the third collision partner (see reaction 1.6 above), as depicted in figure 6.14.

The net production rate is the highest towards the end of the plasma jet region (the loss is significantly lower than the production although this is difficult to see due to the log scale). Note that some NO_2 production also occurs in the far effluent region but the loss rate is now more comparable to the production rate here. However, the NO_2 density shown in figure 6.14 is not as high in the plasma jet region as in far effluent region, again simply due to the averaging (as explained above).

The NO_2 formation once more depends indirectly on the $N_2(A)$ formation and this species is produced less upon increasing O_2 admixture (see figure 6.15). This is because $N_2(A)$ is mainly formed from electron impact excitation, as can be seen from this figure, and the density of the electrons, which are involved in this reaction, rapidly drops when increasing the O_2 content (see figure 6.13). The latter is caused by efficient electron attachment processes for O_2 species. Obviously, the reaction rate of electron impact excitation (reaction 1.5) also depends on the electron temperature, which determines the rate coefficient, but this is less important in this range of electron temperatures (3-3.5 eV). Therefore, the production of $N_2(A)$, as well as the $N_2(A)$ density, clearly drop upon increasing O_2 fraction, as shown in figure 6.15.

Secondly, the NO_2 formation also depends on the concentration of the other reactant, *i.e.* the O atoms. The density of this species drastically rises when very small amounts of O_2 are added to the feed gas, but afterwards (beyond 0.1%) the density remains more or less constant, as discussed above (see figure 6.12).

Combining the $N_2(A)$ and the O density trends upon increasing O_2 admixture indeed leads to the observed behaviour of the NO_2 density as a function of the O_2 fraction, depicted in figure 6.14: a steep rise between 0 and 0.1% O_2 to a maximum of about $10^{13} cm^{-3}$ followed by a clear drop for higher O_2 fractions.

Note, however, that the calculated and measured net NO_2 production rates

as a function of the O_2 admixture, illustrated in figure 6.10 above, do not exhibit this initial rise between 0 and 0.1% O_2, that is observed in figure 6.14 (not only for the NO_2 density, but also for the NO_2 production rate). The reason is that the calculated and measured NO_2 net production rates, shown in figure 6.10 above, apply to a much longer time scale (*i.e.* in the order of seconds; *cf.* the total residence time in the measurement cell, as described at the beginning of section 6.2), whereas the calculation results of the effluent region depicted in figure 6.14, apply to a time scale in the order of milliseconds.

Within this shorter time frame, the loss of NO_2 occurs predominantly by collision with O atoms, and these species will eventually disappear from the discharge (for example by forming O_3 as described above). Therefore, in a later stage of the effluent, O_3 will be the only available molecule able to react with NO_2 as it is the only 'reactive' species that is at least as abundant as NO_2. Note that the reaction NO_2+O_3 is not displayed in figure 6.14 because only the dominant reactions contributing more than 10% are presented, but at longer residence times, this reaction eventually becomes important. As the O_3 density is rather small for O_2 admixtures between 0 and 0.1%, the NO_2 loss at these longer time scales will also be negligible at these low O_2 admixtures. Therefore the net production of NO_2 will be for a longer time scales, eventually, the highest between 0 and 0.1%, and indeed the NO_2 net production rate will continuously drop from 0 to 1% O_2 as illustrated in figure 6.10 above.

6.2.3   Oxygen+nitrogen admixtures

An interesting combination of the two chemistries clarified in the previous sections is obtained when O_2 and N_2 are simultaneously added to the argon feed gas. Recall that in this case, a fixed 1% O_2+N_2 admixture is used, but with the $O_2/(O_2+N_2)$ ratio varied between 0% and 100%. Therefore, 0% $O_2/(O_2+N_2)$ in figures 6.17–6.21 correspond to the conditions of 1% N_2 admixture in figures 6.4–6.9, whereas 100% $O_2/(O_2+N_2)$ corresponds to the case of 1% O_2 in figures 6.11–6.15.

Figure 6.16 illustrates that the simulated evolution of the NO_2 and O_3 net production rates is also well in accordance with the measurements. For both species, the shape of the curve is quite complex. The NO_2 production rate initially drops (except for a first rise between 0 and 5% O_2 for the
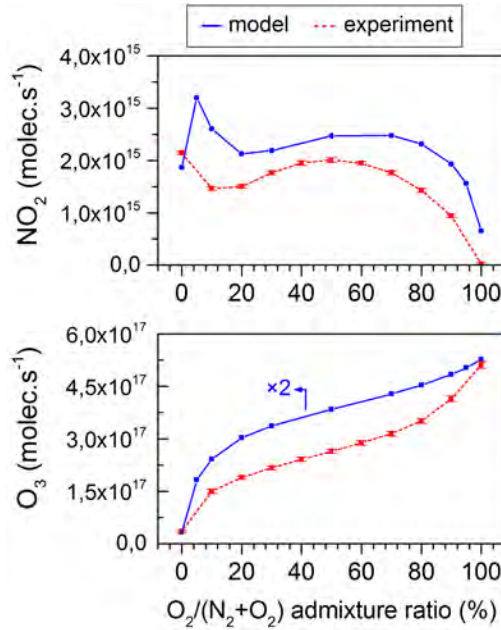
Figure 6.16: NO_2 and O_3 net production rates in the far plasma jet effluent as measured by infrared absorption spectroscopy and simulated by the 0D model, when adding 1% O_2+N_2 to the argon feed gas, in different $O_2/(O_2+N_2)$ ratios.

model results), but increases again at about 20% $O_2/(N_2+O_2)$. A second maximum is formed at about 50% $O_2/(N_2+O_2)$ before the production rate steeply drops close to 100% O_2 (thus for low N_2 levels).

The shape of the O_3 production rate as a function of the admixture composition is clearly x^3-shaped, although more pronounced in the experimental measurements. Indeed, the difference between the simulated and measured O_3 production rate is in general about a factor 2, but in the middle of the investigated range, at an O_2/N_2 ratio close to 1, this difference has increased to a factor 3.

(a) O_3 formation

The O_3 formation pathway was found to be similar for O_2 or N_2 admixtures, as demonstrated above. Therefore, figure 6.17 indicates that the same mechanisms are applicable here when admixing both gases at the same time, *i.e.* the formation is mainly due to the three-body reaction between O atoms
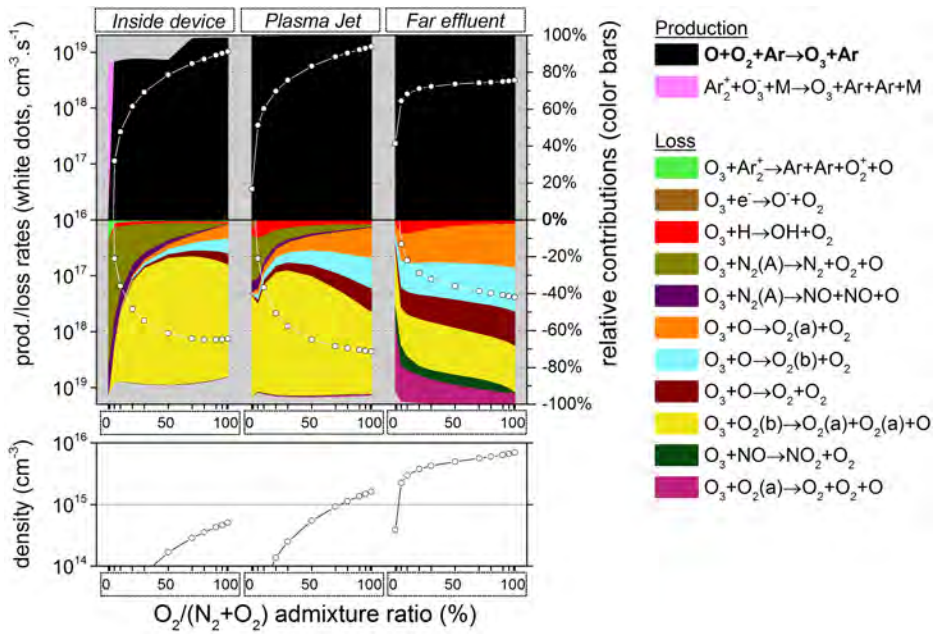
Figure 6.17: O_3 chemistry inside the device, the plasma jet and the far effluent as a function of the O_2+N_2 admixture (see figure 6.4 for explanation about top and bottom graph).
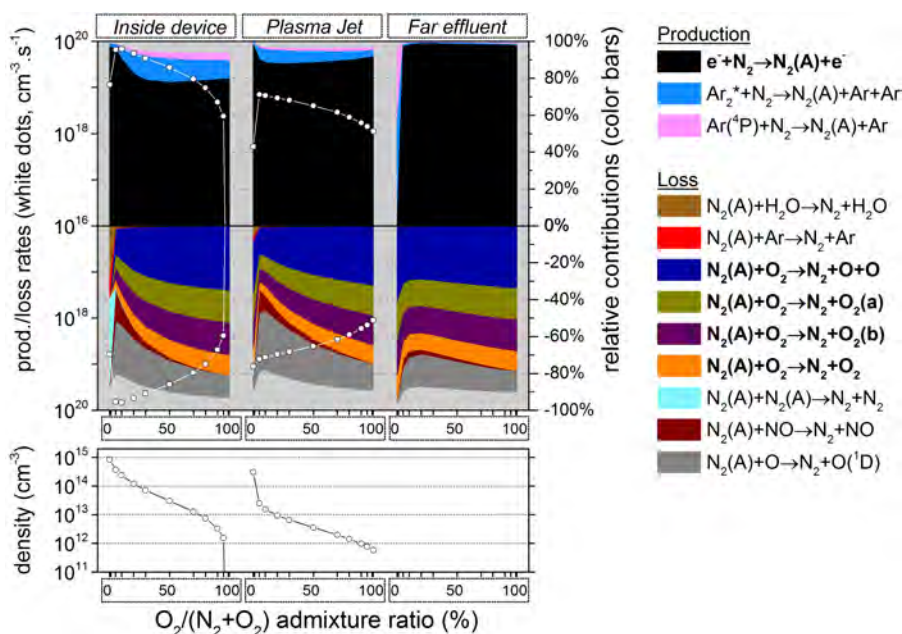
Figure 6.18: N$_2$(A) chemistry inside the device, the plasma jet and the far effluent as a function of the O$_2$+N$_2$ admixture (see figure 6.4 for explanation about top and bottom graph).
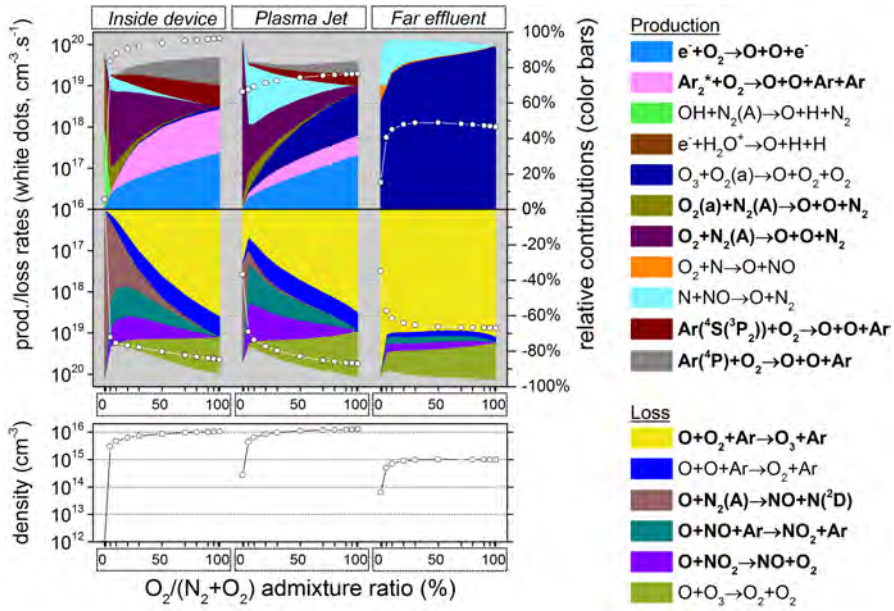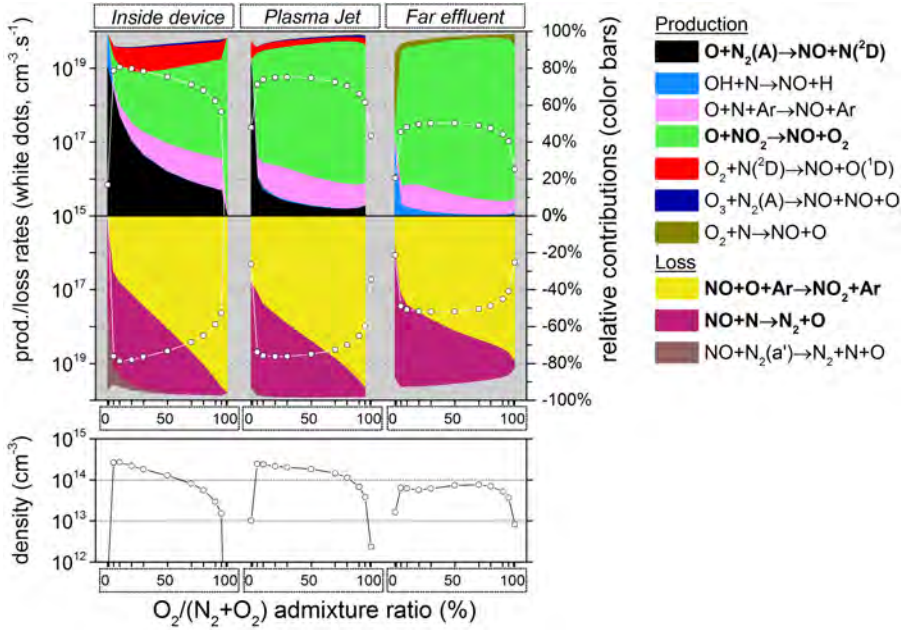
Figure 6.19: O chemistry inside the device, the plasma jet and the far effluent as a function of the O_2+N_2 admixture (see figure 6.4 for explanation about top and bottom graph).

and O_2 molecules, with Ar as third body (see reaction 1.1).

Again, like in the case of O_2 addition, the production is highest in either the plasma jet (and inside the device) or in the early effluent, depending on the O_2 content, as explained in section 6.2.2(a) above.

A dissimilarity between figures 6.10 and 6.16 concerning the net O_3 production rate as a function of the O_2 fraction is that for pure O_2 admixtures the net production rate first rapidly rises (between 0% and 0.2% O_2 in argon) but it tends to saturate at higher O_2 concentrations (see figure 6.10), whereas for O_2+N_2 admixtures (see figure 6.16) the first rise (between 0% and 0.2% in argon) is less steep and is followed by a gradual rise (between 0.2% and 0.8% O_2 in argon) and, finally, a more drastic increase between 0.8% and 1% O_2 in argon (which is more pronounced in the experimental data). The O_3 production without N_2 (for pure O_2 admixtures) is thus higher between 0% and 0.8% O_2 than with N_2 (in the case of O_2+N_2 admixtures).

Indeed, the observed effect must be explained by the role of $N_2(A)$ (which is created from the N_2 admixture molecules in reaction 1.5, see figure 6.18) in the generation of O atoms, which eventually leads to O_3 production by reaction 1.1. This O chemistry is illustrated in figure 6.19.

As demonstrated in section 6.2.1(a) above, the O atoms can easily be formed by reaction 1.4 (*i.e.* between $N_2(A)$ and O_2 molecules) when significant amounts of N_2 are present. Indeed, figure 6.19 illustrates that this reaction gains importance when the $O_2/(O_2+N_2)$ ratio drops and it takes over the role of O_2 dissociation by collision with argon species and by electron impact as the most important O atom production process.

Consequently, the $N_2(A)$ chemistry in figure 6.18 provides the final answer. The increase in $N_2(A)$ density upon decreasing O_2 fraction in the plasma jet region is not linear between 100 and 0% $O_2/(O_2+N_2)$ (looking from right to left on the x-axis). Indeed, the $N_2(A)$ density seems to be somewhat suppressed until 10% $O_2/(O_2+N_2)$, yet for even lower $O_2/(O_2+N_2)$ fractions than 10% the $N_2(A)$ density will finally increase drastically.

It is clear from the loss reactions in figure 6.18 that even small amounts of O_2 (above 0.1% $O_2/(O_2+N_2)$) efficiently quench the $N_2(A)$ molecules, not only by chemical quenching leading to O atoms and thus O_3 formation, but also by physical quenching. Thus, it can be concluded that the O_3 production is partially inhibited when significant amounts of O_2 and N_2 are added simultaneously, explaining why the rise in the net O_3 production is higher between 80 and 100% $O_2/(O_2+N_2)$ than between 20 and 80% $O_2/(O_2+N_2)$,
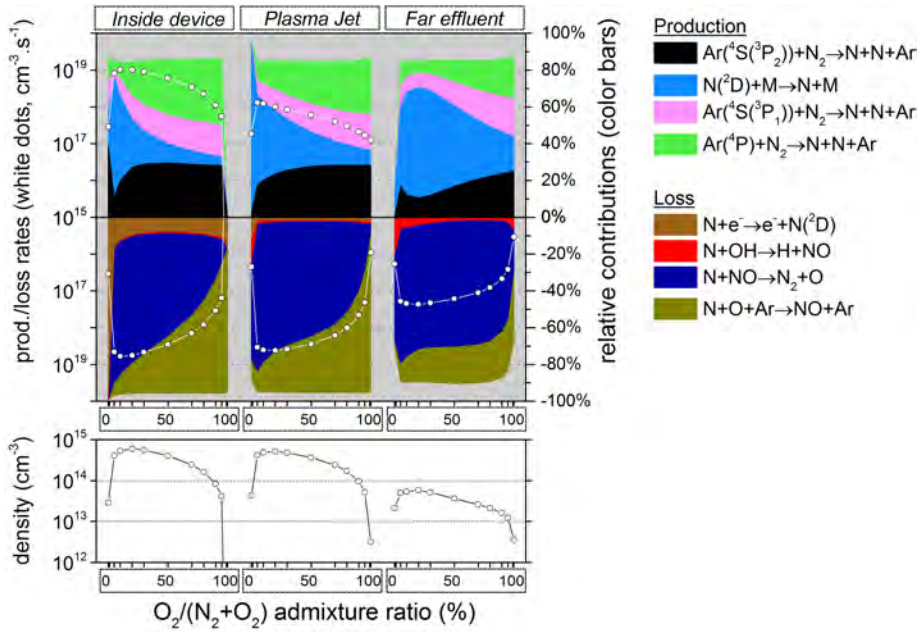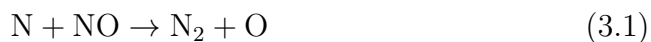
as depicted in figure 6.16 above.

Figure 6.20: NO chemistry inside the device, the plasma jet and the far effluent as a function of the O_2+N_2 admixture (see figure 6.4 for explanation about top and bottom graph).

(b) NO$_2$ formation

For the NO_2 production rate as a function of the $O_2/(O_2+N_2)$ admixture ratio one might expect the highest value for equivalent O_2 and N_2 fractions, but this does not seem to be the case (see figure 6.16 above). From the above sections, we know that NO_2 is formed from NO and this is also valid here (therefore, the NO_2 chemistry is not explicitly shown, as it does not give new information). Thus, by studying the chemistry of NO in figure 6.20 it is possible to explain the observed trend for the net NO_2 production rate displayed in figure 6.16.

In the plasma jet region the NO density is, as expected, the highest between 10% and 70% $O_2/(O_2+N_2)$ ratio. However, in the effluent region a small dip at 20% starts to develop. This is due to significant NO destruction upon

Figure 6.21: N chemistry inside the device, the plasma jet and the far effluent as a function of the O_2+N_2 admixture (see figure 6.4 for explanation about top and bottom graph).

collision with N atoms:

$$N + NO \rightarrow N_2 + O \tag{3.1}$$

Indeed, the concentration of the N atoms is at maximum at this $O_2/(O_2+N_2)$ ratio, as demonstrated by figure 6.21.

As a result, the measured and modelled net NO_2 production rate further in the measurement cell (shown in figure 6.16 above) exhibits a similar profile as the NO density in the effluent region of figure 6.20, because NO_2 is created from NO.

6.3   Conclusions

In this chapter we presented the results of both our semi-empirical numerical model, which describes the chemical kinetics within the kinpen plasma jet device (with a surrounding dry air gas curtain), and experimental measurements of the jet effluent by high resolution QCL infrared absorption spectroscopy. The net production rates of the biomedical species, O$_3$ and NO$_2$, were determined with both techniques for multiple different operating conditions.

In the first two cases either O$_2$ or N$_2$ is admixed from $0\,\%$ to $1.0\,\%$ of the total argon feed gas flow rate. Additionally, an artificial mixture of N$_2$+O$_2$ is used and in this case, the admixture fraction is fixed at 1% but its content is varied from $0\,\%$ to $100\,\%$ O$_2$ with $100\,\%$ to $0\,\%$ N$_2$.

We obtained a good qualitative agreement in all cases for the net production rates of NO$_2$ as a function of the different admixtures. Concerning O$_3$, the similarity of the results computed in the model and the experimental data is qualitatively correct for most of the investigated conditions. Nevertheless, in case of N$_2$ admixtures, a mismatch between the calculation and the measurement is observed. It is not clear whether this is caused by a possible inaccuracy in the reaction set or due to the gas curtain diffusion profile assumed in our 0D model, which is much more complex in reality [220]. In the latter case, a more sophisticated model approach might offer a solution. Quantitatively, the results of both techniques do not vary by more than a factor three at maximum within the investigated range (*i.e.* a consistent overestimation compared to the experimental measurements). The highest O$_3$ production rate was achieved at the highest investigated O$_2$ admixture of 1%, see figures 6.10 and 6.16 (*i.e.* 4.9×10^{17} molec.s^{-1} measured and 1.0×10^{18} molec.s^{-1} simulated). These figures also illustrate that the O$_3$ production initially drops steeply when O$_2$ is being replaced by N$_2$ (between 100% and 80% O$_2$/N$_2$+O$_2$) while the decrease is much more gradual between 1% and 0.3% pure O$_2$ admixtures.

For the net production rate of NO$_2$ in the case of N$_2$ and N$_2$+O$_2$ the agreement is almost perfect. It is remarkable that the calculated NO$_2$ production rate is quite comparable to the measured results within the investigated ranges of pure N$_2$ admixtures and N$_2$+O$_2$ admixtures, *i.e.* between 1×10^{15} molec.s^{-1} and 3×10^{15} molec.s^{-1}. Moreover, in both cases the NO$_2$ production rate becomes significantly lower when the N$_2$ fraction is lower than 0.1% in the argon gas, see figures 6.3 and 6.16.

Due to the complementarity of the two distinct techniques that have been used, we have acquired important insight in the reaction kinetics in all regions of the kinpen device, even in areas that are not accessible by optical diagnostics. The pathways for the formation of O_3 and NO_2 are quite complex. From the analysis of the model output, it is demonstrated that the production of NO_2 and O_3 is mostly triggered by two common species: atomic oxygen (O) as well as metastables of nitrogen ($N_2(A)$), which are both energy carriers and lead to the formation and/or destruction of NO_2 and O_3. O and $N_2(A)$, among other species like Ar metastables, can be considered as transient particles that are direct results of the electron chemistry and eventually lead to the formation of longer living molecules outside the kinpen device.

Even more important is that admixture differences, even at these relatively low levels, can significantly alter the electron density and temperature and therefore have a large impact on the chemistry. In general, it can be concluded that the production of these important biomedically active species can be manipulated by up to one order of magnitude by varying the amount of admixture or the admixture type.

Based on these results, the feed gas and also the gas curtain composition can be selected even more carefully to optimize the applications.

Summary

Atmospheric pressure plasma jets (APPJs) for plasma medicine applications are discharges produced inside a millimetre sized apparatus by applying an electric field. The plasma exits the device through an opening at the front and flows into ambient air, by means of a gas flow through the device. Note that this gas is usually mainly argon or helium. Furthermore, the APPJs are characterized by their non-equilibrium state, which means that the electron temperature is much higher than the gas temperature, making it safe for humans in terms of heat damage. However, the collisions of the background gas with energetic electrons result in a complex chemistry, in which all kinds of reactive species are produced, for example oxygen (O) and nitrogen (N) atoms, hydroxyl (OH) and nitrogen monoxide (NO) radicals and ozone (O_3). These species, combined with other plasma agents like UV photons, make this technology suitable for applications such as decontamination and wound healing. Moreover, APPJs are not only efficient, but also easy to handle (*e.g.* in a hospital by doctors) due to its relatively small size and the possibility of remote treatment.

In this thesis three different argon APPJ sources are investigated, one of which is a commercial device. In all these sources power is supplied by a radio–frequency driven needle electrode (possibly kHz modulated).

Currently, several plasma jet properties can be measured by a range of different diagnostic tools. However, not all information can be acquired, for example, because species densities might be below the detection limit and since some areas in the setup are difficult to access by diagnostics. Furthermore, experimental measurements are expensive and time consuming. Numerical simulations, on the other hand, offer a large amount of information but have the disadvantage that the complexity of the plasma processes often has to be reduced by making assumptions. Therefore, a good validation or benchmark of the model is necessary.

The goal of this thesis is therefore to provide new insights in the plasma chemistry in APPJs, so that the efficiency and safety of the technology can be improved.

This thesis starts in **chapter 1** with a general introduction on plasmas. Furthermore, the most important devices used in the field of plasma medicine are briefly described, all with their specific advantages and disadvantages. Although this thesis is not devoted to the study of the application itself,

we end this chapter with a summary of the different biological and medical applications that might benefit from our work.

In **chapter 2** the numerical model we developed is described in detail. In this work a zero-dimensional (0D) model is used to describe the reaction kinetics of argon plasma jets flowing into humid air. The model is used in a semi-empirical way because we fit several important plasma parameters (*e.g.* gas temperature and air entrainment) to experimentally measured values. We also present the argon/humid air mixture reaction chemistry set that we have built. It considers 84 different species and 1880 reactions. The model allows us to simulate the densities of the biomedical species (which are often not the main plasma components) without excessive calculation times, and at the same time to 'mimic' the experimental conditions.

A case study for the plasma jet geometry developed at the Eindhoven University of Technology is presented as well. Calculated species density profiles along the plasma jet are shown and the major chemical pathways are explained. It is demonstrated that chemically reactive H, N, O and OH radicals are formed in large quantities after the nozzle exit and $O_2(^1\Delta_g)$, O_3, H_2O_2, NO, NO_2, N_2O, HNO_2 and HNO_3 are predominantly formed further in the effluent as 'long-lived' species. The simulations show that water clustering of positive ions is very important under these conditions. The influence of vibrational excitation of nitrogen impurities on the calculated electron temperature and the electron energy distribution function proved to be quite large but only when air entrainment becomes significant or if a considerable amount of molecular gas is admixed to the argon gas feed (more than ppm impurity levels).

The gas phase production and loss pathways of the aforementioned biomedically active species are examined in more detail in **chapter 3**. We demonstrate how the pathways of the biomedically active species drastically change as a function of the position in the effluent, *i.e.* inside the discharge device, active plasma jet effluent and afterglow region far from the nozzle.

Additionally, we show how the reaction kinetics and species densities are affected by different ambient air humidities, total deposited power into the plasma and gas temperature along the jet. It follows that the pathways are readily affected by these parameters.

We conclude that the chemical pathways are more complex than usually presumed and that the different species groups (*i.e.* derivation products from either oxygen, nitrogen or water) intensively interact, under all circumstances. Thus, it turned out to be extremely important to consider all

possible reactions with all possible humid air species. Our parameter study showed that the species concentrations can easily vary by one order of magnitude, but usually not much more than that.

The thesis is continued with **chapter 4**, which contains complementary numerical work and experimental measurements on the ozone generation in the same APPJ from the Eindhoven University of Technology. Significant gas heating in the core of the plasma is found experimentally and this coincides with a depletion of the ozone density in that area. The comparison shows that the depletion of O_3 in the core of the plasma is mainly caused by an enhanced destruction of O_3 due to a large density of O and H atoms in that area. Additionally, the high temperature largely inhibits association reactions between O atoms and O_2 in which O_3 is being formed. It is found that thermal dissociation of O_3 is not causing the depletion of O_3 in the core of the plasma.

The next combinatorial study of experiments and simulations concerns two cold atmospheric pressure plasma jets (**chapter 5**), operating in Ar + 2% air, with a different electrode geometry but with the same power dissipated in the plasma. One of these APPJs from the Eindhoven University of Technology is the same as the one we studied in the previous chapters, namely with a grounded ring electrode around the dielectric tube. The other one is constructed with a grounded plate electrode in front of the device.

A good agreement between the calculated and measured data (obtained by laser diagnostics) is demonstrated. Furthermore, the most probable spatial power distribution in an RF driven plasma jet is obtained for the first time by comparing measured and calculated species density profiles. This was possible due to the strong effect of the power distribution on the NO and O density profiles.

The power dissipation seems to be more or less constant over the entire length of the visible plasma plume when a grounded plate electrode is placed in front of the nozzle, causing an NO density peak near the plate electrode and a high O density throughout the entire plume. In the case of the grounded ring electrode around the dielectric tube, the main power deposition is restricted up to a few millimetres from the nozzle exit and the NO and O density are higher than in the other configuration but also drop much more rapidly.

In addition, the dominant reaction pathways for both the NO and the O species are identified, which enables us to explain the observed phenomena. Finally, we demonstrate that water impurities in the order of 100 ppm in

the gas feed can have a significant effect on the spatial distribution of the NO and O density.

In the final **chapter 6** we study the commercial APPJ developed at the INP institute in Greifswald (GE), called kinpen, operating in Ar with different admixture fractions up to 1% pure N_2, O_2 and N_2+O_2. Moreover, the device is operating with a shield gas shower of dry air. The production of the biomedically active O_3 and NO_2 species, determined in the far effluent by infrared absorption spectroscopy, is calculated by our model. Very good qualitative and even quantitative agreement between the calculated and measured data is demonstrated.

The analysis shows that small differences in the admixture amount (even at these relatively low levels) can already significantly alter the electron density and temperature and therefore have a large impact on the chemistry. Indeed, the production of these species can be manipulated up to one order of magnitude. Based on these results, the feed gas and also the shower composition can be selected even more carefully to optimize the applications.

As a general conclusion we would like to state that the variety of configurations in the field of plasma medicine is both a blessing and a curse; each setup has its own advantages and disadvantages and the slightest modification of the geometry or the operation conditions can cause considerable differences in the plasma chemistry. This all enables many different applications but at the same time it is quite difficult to compare the different experiments performed all over the world and it prevents even faster developments.

Our outlook to the future is that the work has only just begun since modelling efforts in this research field are still rather limited due to the novelty of this application. Besides, fully self-consistent modelling of an APPJ is incredibly complex. Indeed, there are many different physical phenomena present, each occurring at different time–scales that range from nanoseconds to milliseconds. For almost every part of the physics a different modelling approach must be used and to couple them while maintaining a reasonable calculation time is a huge challenge. It is therefore evident that these issues are first handled one by one. Much endeavour was for example made to obtain more insight in the mechanism of the propagating ionisation waves within the jet. Our contribution to the unravelling of the complex argon/humid air chemistry must be be viewed in this context as well. We hope that the developers of more sophisticated models can benefit from it and build their reaction set more efficiently.

Additionally, modellers will also have to solve new issues that were more recently detected by experimentalists. First of all, most diagnostics and modelling is performed for freely developing jets but in practice the jet is in contact with a wound or object and this seems to change the plasma properties. For instance, laminar flow is generally assumed. However, the electrostatic forces in the jet seem to trigger a transition to turbulent flow in some cases, especially in contact with an object or liquid surface. A second huge obstacle is how the gas phase species are transferred to the liquid phase, both physically and chemically. In other words, can all species diffuse across the boundary layer and if they do, are they chemically stable or are they converted into new species. Moreover, what is the influence of the gas flow in this when it disturbs the liquid surface.

These issues and open research questions offer in the next few years some nice opportunities for modellers in the field of plasma medicine.

Samenvatting

Plasma jets, die gegenereerd worden bij atmosfeerdruk (APPJ's), zijn ontladingen die geproduceerd worden in apparaten met afmetingen in de orde van millimeters. Ze worden gegenereerd door een elektrisch veld aan te leggen en vinden hun toepassingen in de biomedische sector. Doorheen het toestel wordt een gasstroming aangebracht en langs een opening aan de voorzijde verlaat het plasma het apparaat. Het gebruikte gas is meestal argon of helium. Voorts worden deze APPJ's gekarakteriseerd door hun niet-thermisch evenwicht. Dit betekent dat de elektrontemperatuur vele malen groter is dan de gastemperatuur, wat de toepassing veilig maakt voor de mens in termen van thermische schade aan weefsels. Niettemin zorgen botsingen tussen het achtergrondgas en de elektronen voor een complexe chemie waarin vele verschillende reactieve deeltjessoorten worden geproduceerd, bijvoorbeeld zuurstof (O) en stikstof (N) atomen, hydroxyl (OH) en stikstofmonoxide (NO) radicalen, maar ook ozon (O_3). Deze deeltjes, gecombineerd met andere plasma agentia zoals UV straling, maken dat deze technologie onder andere ontsmettend werkt, maar de verschillende componenten kunnen ook het wondgenezingsproces doen versnellen. Bovendien zijn APPJ's niet alleen erg efficiënt in vergelijking met conventionele technieken, maar zijn ze ook handig in gebruik door de relatief kleine afmetingen (bijvoorbeeld voor dokters in een hospitaal) en de mogelijkheid om een object op afstand te behandelen (maximaal één of twee centimeter).

In deze thesis worden drie verschillende argon APPJ bronnen onderzocht, waarvan er één commercieel beschikbaar is. Bij al deze apparaten wordt het vermogen op eenzelfde manier geleverd, namelijk via een radio-frequent (RF) aangedreven naald elektrode (mogelijks kHz gepulst).

Momenteel worden verschillende plasma eigenschappen gemeten door een uitgebreid gamma aan diagnostische technieken. Desondanks is dat meestal niet voldoende om al de informatie en inzichten te verkrijgen, die nodig is om de toepassing te verbeteren. De concentratie van de deeltjes kan bijvoorbeeld onder de detectielimiet liggen en sommige regionen zijn experimenteel zeer moeilijk te bereiken. Ook zijn de metingen vaak duur en tijdrovend. Numerieke simulaties daarentegen bieden een nog veel grotere hoeveelheid informatie maar hebben als nadeel dat de complexiteit van de plasma processen moet gereduceerd worden door aannames te maken en dat daardoor een goede aftoetsing aan experimentele resultaten noodzakelijk is.

Het verkrijgen van nieuwe inzichten in de plasmachemie van APPJ's is dus het einddoel van deze thesis, en zodoende willen we een bijdrage leveren tot de verbetering van de veiligheid en efficiëntie van deze technologie.

Dit werk start in **hoofdstuk 1** met een algemene inleiding over plasma's. Daarna worden de meest gangbare toestellen kort beschreven die gebruikt worden in de biomedische toepassingen, inclusief hun specifieke voor- en nadelen. Hoewel deze thesis niet focust op het eigenlijke gebruik van de APPJ, geven we aan het einde van dit hoofdstuk een samenvatting van de verschillende biologische en medische toepassingsdomeinen waarvoor ons werk van nut kan zijn.

In **hoofdstuk 2** wordt in detail het numerieke model beschreven dat door ons ontwikkeld werd. Het betreft een nul-dimensionaal (0D) model dat gebruikt kan worden om de reactiekinetiek te bestuderen binnenin een argon APPJ die in een omgevingslucht met aanzienlijke relatieve vochtigheid propageert.

Het model wordt gebruikt op semi-empirische wijze aangezien verschillende belangrijke plasma parameters, zoals de gas temperatuur en de opname van omgevingslucht in de argon stroom, niet berekend worden maar gefit worden aan experimenteel gemeten data. Daarnaast presenteren we ook de benodigde argon/lucht reactieset die door ons werd opgebouwd. Deze brengt 84 verschillende deeltjessoorten en 1880 reacties in rekening. Het model laat ons toe om de deeltjesdichtheden van de biomedisch relevante deeltjessoorten (die overigens meestal niet bij de belangrijkste plasma componenten behoren) te bekomen binnen een aanvaardbare rekentijd en om de experimentele condities voldoende accuraat na te bootsen.

Ook wordt in dit hoofdstuk een casus beschreven voor de APPJ geometrie die ontwikkeld werd aan de Technische Universiteit Eindhoven. De berekende dichtheden voor de verschillende deeltjessoorten en de voornaamste chemische reactiepaden worden hier vermeld. Er wordt aangetoond dat H, N, O en OH radicalen in grote hoeveelheden worden gevormd vlak na de uitlaat van het toestel en dat $O_2(^1\Delta_g)$, O_3, H_2O_2, NO, NO_2, N_2O, HNO_2 en HNO_3 eerder verderop gecreëerd worden en dat deze laatste groep deeltjes 'lang levend' is, of toch binnen de gesimuleerde tijdschalen. We laten tevens zien dat de vorming van waterclusters erg belangrijk is onder deze omstandigheden. Tenslotte blijkt dat de invloed van vibrationele excitatie van stikstofonzuiverheden op de berekening van de elektrontemperatuur en de elektronenergie distributie functie aanzienlijk kan zijn, maar enkel op het moment dat er reeds veel omgevingslucht is opgenomen in de jet of wanneer

significante hoeveelheden moleculair gas wordt toegevoegd aan de initiële argon gastoevoer (meer dan ppm niveau).

De productie- en verlieskanalen voor de eerder vermelde biomedisch actieve deeltjes in de gasfase worden in meer detail onderzocht in **hoofdstuk 3** voor hetzelfde type APPJ als in **hoofdstuk 2**. Er wordt aangetoond dat de reactiepaden sterk verschillen in functie van de positie in de jet/gasstroom. Er is vooral een onderscheid te maken tussen de chemie binnen het apparaat, in het actieve plasma en in het grotendeels gerecombineerde gas nog verder van de uitlaat.

Aanvullend tonen we hoe de reactiekinetiek en de deeltjesdichtheden worden beïnvloed bij een verandering van de relatieve vochtigheid van de omgevingslucht, het totaal geleverde vermogen of de gastemperatuur doorheen de jet. Het besluit is dat de chemie veel ingewikkelder is dan meestal wordt aangenomen en dat de verschillende groepen deeltjessoorten - afkomstig van ofwel zuurstof, stikstof of water - intensief interageren onder al de onderzochte omstandigheden. Het is dus uitermate belangrijk om al de verschillende reacties en de verschillende luchtcomponenten in rekening te brengen. De parameterstudie maakt ook duidelijk dat de deeltjesconcentratie makkelijk een ordegrootte kan verschillen bij het variëren van de werkingsparameters die eerder werden vermeld, maar ook niet veel meer dan dat.

De thesis wordt verdergezet met **hoofdstuk 4**, die een combinatie bevat van berekeningen en metingen van de ozon productie voor hetzelfde type APPJ als in de vorige hoofdstukken. Een beduidende verhitting in de kern van de jet wordt experimenteel geobserveerd en dit blijkt bovendien samen te gaan met een erg lage ozon concentratie op dezelfde locatie. Aan de hand van de berekeningen wordt aangetoond dat dit hoofdzakelijk kan toegeschreven worden aan de destructie van O_3 in reacties met O en H atomen. Daarnaast zorgt de hoge temperatuur er voor dat de snelheid van de reactie tussen O atomen en O_2 - hetgeen de belangrijkste bron van ozone is - sterk afneemt. De conclusie is dus dat thermische dissociatie van O_3 niet die oorzaak is van de lage ozon concentratie in de kern van de plasma jet.

De volgende complementaire studie van experimenten en simulaties betreft twee APPJ's (**hoofdstuk 5**), beiden met Ar + 2% lucht als achtergrondgas en hetzelfde totaal geleverde vermogen maar met een verschillende elektrode geometrie. Eén van deze twee APPJ's van de Technische Universiteit Eindhoven beschikt opnieuw over dezelfde configuratie als beschreven in de eerdere hoofdstukken, namelijk die met geaarde ring elektrode rond het toestel. De andere maakt gebruikt van een een geaarde plaatelektrode net voor

het toestel.

Er is een goede overeenkomst tussen de berekende en de gemeten data (bekomen via laser diagnostiek). Een verder resultaat is dat de vermogensdepositie ook ruimtelijk kon bepaald worden door de metingen en de simulaties te vergelijken. Het is overigens de eerste maal dat dit bekomen werd voor een RF aangedreven plasma jet.

De vermogendissipatie blijkt, voor de geometrie met een geaarde plaatelektrode net voor het toestel, min of meer constant te zijn over de volledige lengte van de zichtbare plasma pluim. Dit veroorzaakt een NO dichtheidspiek vlak na de plaat en een hoge O dichtheid doorheen de volledige jet. In het geval dat een geaarde ring elektrode rond het toestel wordt gebruikt, zien we dat de vermogensdepositie beperkt is tot enkele millimeters achter de uitlaat, dat de NO en O dichtheid een hogere waarde bereiken maar dat deze wel veel sneller afnemen. De analyse van de dominante reactiepaden voor zowel NO als O maakt het mogelijk om deze fenomenen in detail te verklaren.

Uiteindelijk tonen we in dit hoodstuk ook aan dat wateronzuiverheden in de gastoevoer - van de ordegrootte van 100 ppm - een beduidende invloed hebben op de NO en O dichtheden in het plasma.

In het laatste **hoofdstuk 6** wordt de commerciële APPJ bestudeerd die werd ontwikkeld aan het INP instituut in Greifswald (GE). Het toestel met de naam 'kinpen' werkt met argon als achtergrondgas waaraan vervolgens verschillende gasfracties (N_2, O_2 of N_2+O_2) kunnen worden toegevoegd. Meer specifiek bekeken we mengsels van deze moleculaire gassen tot 1% in de configuratie waarbij een afschermende gasstroom (bestaande uit droge lucht) rondom de jet is aangebracht om meer controleerbare omstandigheden te verkrijgen. De productie van de biomedisch actieve deeltjes O_3 en NO_2, gemeten door infrarood spectrometrie ver van de uitlaat, werd gesimuleerd door het 0D model. Opnieuw werd een goede overeenkomst bekomen tussen de berekende en experimentele waarden, zowel kwalitatief als kwantitatief. De analyse wijst uit dat zelfs kleine verschillen in de toegevoegde gasfracties kunnen leiden tot een aanzienlijk verschillende elektronen kinetiek en dat dit dus een grote impact heeft op de chemie binnenin de jet. Op basis van de verkregen resultaten kan de samenstelling van de gastoevoer in de toekomst nog zorgvuldiger gekozen worden om zo de toepassing verder te optimaliseren.

Als een algemene conclusie kan gesteld worden dat de verscheidenheid aan configuraties binnen het veld van biomedische plasma toepassingen zowel

een zegen is als een vloek. Elke opstelling heeft namelijk zijn specifieke voor- en nadelen en de minste verschillen in werkingscondities kunnen leiden tot aanzienlijke verschillen in plasma samenstelling. Dit maakt de technologie interessant voor uiteenlopende toepassingen maar maakt het moeilijk om de verschillende experimenten, uitgevoerd over de hele wereld, te vergelijken en verhindert aldus een snellere ontwikkeling.

Onze conclusie is dat het modelleerwerk nog grote stappen heeft te zetten, eenvoudigweg omdat de technologie nog zo nieuw is. Bovendien is het enorm moeilijk om volledig zelf-consistente modellen te ontwikkelen door de hoge mate van complexiteit van APPJ's. Er doen zich immers verscheiden fysische verschijnselen gelijktijdig voor, die elk optreden met uiteenlopende tijdschalen (van nanoseconden tot milliseconden). Bijna voor elk aspect moet een andere numerische benadering gebruikt worden en daarom is het ook een grote uitdaging om deze met elkaar te koppelen en tegelijkertijd de rekentijd binnen de perken te houden. Het is dus evident dat de onderzoeksvragen eerst individueel worden aangepakt. Veel inspanningen zijn bevoorbeeld al geleverd om meer inzicht te krijgen in het propagatiemechanisme van de ionisatiefronten binnenin de jet. Onze bijdrage bestond dan weer uit het ontrafelen van de complexe argon/lucht chemie. We hopen dan ook dat de ontwikkelaars van meer gesofisticeerde modellen hier in de toekomst baat bij zullen hebben en hun reactieset op een efficiënte manier kunnen opbouwen.

Daarnaast werden recentelijk door experimentalisten ook nog andere zaken ontdekt die door modelleerders zullen moeten bekeken worden. Eerst en vooral blijkt dat de plasma eigenschappen plots sterk kunnen veranderen wanneer de jet in contact komt te staan met een object zoals een wonde, terwijl de meeste simulaties worden uitgevoerd voor alleenstaande jets. Het is bijvoorbeeld zo dat de elektrostatische krachten binnen het plasma voor een transitie naar een turbulent regime kunnen zorgen wanneer er contact is tussen de jet en het object, hoewel in de berekeningen meestal laminaire gasstroom wordt verondersteld. Een tweede groot obstakel is hoe de gasdeeltjes worden getransfereerd naar de vloeistoffase, zowel op fysisch als op chemisch vlak. Met andere woorden, kunnen alle deeltjes doorheen de grenslaag diffunderen en zoja, zijn ze chemisch stabiel of worden ze omgezet in andere deeltjessoorten. Bovendien, wat is de invloed van de gasstroming hierbij, indien deze zorgt voor een verstoring van het vloeistofoppervlak.

Deze onderzoeksvragen bieden in de komende jaren dus nog erg mooie opportuniteiten voor modelleergroepen in het gebied van biomedische toepas-

singen van plasma's.

Appendix A

Reaction set used in this work, with the rate constants and the corresponding references

Nr	Reaction name	A[a]	B[a]	C[a]	Set[b]	Ref.
Electron impact collisions						
(1)	$e^- + Ar \rightarrow Ar + e^-$	$\sigma(\varepsilon)$				[222]
(2)	$e^- + Ar \rightarrow Ar(^4S[^3P_2]) + e^-$	$\sigma(\varepsilon)$			A,B	[223]
(3)	$e^- + Ar \rightarrow Ar(^4S[^3P_1]) + e^-$	$\sigma(\varepsilon)$			A,B	[223]
(4)	$e^- + Ar \rightarrow Ar(^4S[^3P_0]) + e^-$	$\sigma(\varepsilon)$			A,B	[223]
(5)	$e^- + Ar \rightarrow Ar(^4S[^1P_1]) + e^-$	$\sigma(\varepsilon)$			A,B	[223]
(6)	$e^- + Ar \rightarrow Ar(^4P) + e^-$	$\sigma(\varepsilon)$			A,B	[223]
(7)	$e^- + Ar \rightarrow Ar(^4P) + e^-$	$\sigma(\varepsilon)$			A	[223]
(8)	$e^- + Ar \rightarrow Ar(^4P) + e^-$	$\sigma(\varepsilon)$			A	[223]
(9)	$e^- + Ar \rightarrow Ar(^4P) + e^-$	$\sigma(\varepsilon)$			A	[223]
(10)	$e^- + Ar \rightarrow Ar^+ + e^- + e^-$	$\sigma(\varepsilon)$			A,B	[224]
(11)	$e^- + Ar(^4S[^3P_2]) \rightarrow Ar(^4S[^3P_2]) + e^-$	$\sigma(\varepsilon)$				[177]
(12)	$e^- + Ar(^4S[^3P_2]) \rightarrow Ar + e^-$	$\sigma(\varepsilon)$				[225]
(13)	$e^- + Ar(^4S[^3P_2]) \rightarrow Ar(^4S[^3P_1]) + e^-$	$\sigma(\varepsilon)$			A,B	[225]
(14)	$e^- + Ar(^4S[^3P_2]) \rightarrow Ar(^4S[^3P_0]) + e^-$	$\sigma(\varepsilon)$				[225]
(15)	$e^- + Ar(^4S[^3P_2]) \rightarrow Ar(^4S[^1P_1]) + e^-$	$\sigma(\varepsilon)$				[225]
(16)	$e^- + Ar(^4S[^3P_2]) \rightarrow Ar(^4P) + e^-$	$\sigma(\varepsilon)$			A,B	[226]
(17)	$e^- + Ar(^4S[^3P_2]) \rightarrow Ar^+ + e^- + e^-$	$\sigma(\varepsilon)$			A,B	[227]
(18)	$e^- + Ar(^4S[^3P_1]) \rightarrow Ar(^4S[^3P_1]) + e^-$	$\sigma(\varepsilon)$				[177]
(19)	$e^- + Ar(^4S[^3P_1]) \rightarrow Ar + e^-$	$\sigma(\varepsilon)$				[225]
(20)	$e^- + Ar(^4S[^3P_1]) \rightarrow Ar(^4S[^3P_2]) + e^-$	$\sigma(\varepsilon)$			A	[225]
(21)	$e^- + Ar(^4S[^3P_1]) \rightarrow Ar(^4S[^3P_0]) + e^-$	$\sigma(\varepsilon)$				[225]
(22)	$e^- + Ar(^4S[^3P_1]) \rightarrow Ar(^4S[^1P_1]) + e^-$	$\sigma(\varepsilon)$				[225]
(23)	$e^- + Ar(^4S[^3P_1]) \rightarrow Ar(^4P) + e^-$	$\sigma(\varepsilon)$				[226]

Nr	Reaction name	A^a	B^a	C^a	Set^b	Ref.
(24)	e⁻ + Ar(^{4}S[^{3}P$_1$]) → Ar$^+$ + e⁻ + e⁻	$\sigma(\varepsilon)$			A	[227]
(25)	e⁻ + Ar(^{4}S[^{3}P$_0$]) → Ar(^{4}S[^{3}P$_0$]) + e⁻	$\sigma(\varepsilon)$				[177]
(26)	e⁻ + Ar(^{4}S[^{3}P$_0$]) → Ar + e⁻	$\sigma(\varepsilon)$				[225]
(27)	e⁻ + Ar(^{4}S[^{3}P$_0$]) → Ar(^{4}S[^{3}P$_2$]) + e⁻	$\sigma(\varepsilon)$				[225]
(28)	e⁻ + Ar(^{4}S[^{3}P$_0$]) → Ar(^{4}S[^{3}P$_1$]) + e⁻	$\sigma(\varepsilon)$				[225]
(29)	e⁻ + Ar(^{4}S[^{3}P$_0$]) → Ar(^{4}S[^{1}P$_1$]) + e⁻	$\sigma(\varepsilon)$			A	[225]
(30)	e⁻ + Ar(^{4}S[^{3}P$_0$]) → Ar(^{4}P) + e⁻	$\sigma(\varepsilon)$			A,B	[226]
(31)	e⁻ + Ar(^{4}S[^{3}P$_0$]) → Ar$^+$ + e⁻ + e⁻	$\sigma(\varepsilon)$			A	[227]
(32)	e⁻ + Ar(^{4}S[^{1}P$_1$]) → Ar(^{4}S[^{1}P$_1$]) + e⁻	$\sigma(\varepsilon)$				[177]
(33)	e⁻ + Ar(^{4}S[^{1}P$_1$]) → Ar + e⁻	$\sigma(\varepsilon)$				[225]
(34)	e⁻ + Ar(^{4}S[^{1}P$_1$]) → Ar(^{4}S[^{3}P$_2$]) + e⁻	$\sigma(\varepsilon)$				[225]
(35)	e⁻ + Ar(^{4}S[^{1}P$_1$]) → Ar(^{4}S[^{3}P$_1$]) + e⁻	$\sigma(\varepsilon)$				[225]
(36)	e⁻ + Ar(^{4}S[^{1}P$_1$]) → Ar(^{4}S[^{3}P$_0$]) + e⁻	$\sigma(\varepsilon)$				[225]
(37)	e⁻ + Ar(^{4}S[^{1}P$_1$]) → Ar(^{4}P) + e⁻	$\sigma(\varepsilon)$				[226]
(38)	e⁻ + Ar(^{4}S[^{1}P$_1$]) → Ar$^+$ + e⁻ + e⁻	$\sigma(\varepsilon)$				[227]
(39)	e⁻ + Ar(^{4}P) → Ar(^{4}P) + e⁻	$\sigma(\varepsilon)$				[177]
(40)	e⁻ + Ar(^{4}P) → Ar + e⁻	$\sigma(\varepsilon)$				[225]
(41)	e⁻ + Ar(^{4}P) → Ar(^{4}S[^{3}P$_2$]) + e⁻	$\sigma(\varepsilon)$				[225]
(42)	e⁻ + Ar(^{4}P) → Ar(^{4}S[^{3}P$_1$]) + e⁻	$\sigma(\varepsilon)$				[225]
(43)	e⁻ + Ar(^{4}P) → Ar(^{4}S[^{3}P$_0$]) + e⁻	$\sigma(\varepsilon)$			A	[225]
(44)	e⁻ + Ar(^{4}P) → Ar(^{4}S[^{1}P$_1$]) + e⁻	$\sigma(\varepsilon)$			A	[225]
(45)	e⁻ + Ar(^{4}P) → Ar$^+$ + e⁻ + e⁻	$\sigma(\varepsilon)$			A,B	[227]
(46)	e⁻ + Ar$^+$ → Ar$^+$ + e⁻	$\sigma(\varepsilon)$				[177]
(47)	e⁻ + Ar$^+$ → Ar(^{4}P)	4.00×10^{-13}	-0.5			[228]

Nr	Reaction name	A^a	B^a	C^a	Set^b	Ref.
(48)	$e^- + e^- + Ar^+ \rightarrow Ar(^4P) + e^-$	5.00×10^{-27}	-4.5			[228]
(49)	$e^- + Ar_2^* \rightarrow Ar_2^+ + e^- + e^-$	9.00×10^{-08}	0.7	3.66	A,B	[229]
(50)	$e^- + Ar_2^+ \rightarrow Ar_2^+ + e^-$	$\sigma(\varepsilon)$				[177]
(51)	$e^- + Ar_2^+ \rightarrow Ar(^4P) + Ar$	5.38×10^{-08}	-0.66		A,B	[229]
(52)	$e^- + O \rightarrow O + e^-$	$\sigma(\varepsilon)$				[230]
(53)	$e^- + O \rightarrow O(^1D) + e^-$	$\sigma(\varepsilon)$			A,B	[231]
(54)	$e^- + O \rightarrow O^+ + e^- + e^-$	$\sigma(\varepsilon)$			A,B	[231]
(55)	$e^- + O + O_2 \rightarrow O^- + O_2$					c, d
(56)	$e^- + O + N_2 \rightarrow O^- + N_2$					c, d
(57)	$e^- + O + Ar \rightarrow O^- + Ar$					c, d
(58)	$e^- + O + H_2O \rightarrow O^- + H_2O$					c, d
(59)	$e^- + O + H_2 \rightarrow O^- + H_2$					c, d
(60)	$e^- + O(^1D) \rightarrow O(^1D) + e^-$	$\sigma(\varepsilon)$				e
(61)	$e^- + O(^1D) \rightarrow O + e^-$	$\sigma(\varepsilon)$				f
(62)	$e^- + O(^1D) \rightarrow O^+ + e^- + e^-$	$\sigma(\varepsilon)$				[227]
(63)	$e^- + O^+ \rightarrow e^- + O^+$	$\sigma(\varepsilon)$				[177]
(64)	$e^- + e^- + O^+ \rightarrow e^- + O$	7.10×10^{-27}	-4.5			[105]
(65)	$e^- + O^+ + M \rightarrow O + M$	4.31×10^{-34}	-1.5			[105]
(66)	$e^- + O^- \rightarrow O^- + e^-$	$\sigma(\varepsilon)$				[177]
(67)	$e^- + O^- \rightarrow O + e^- + e^-$	$\sigma(\varepsilon)$			A	[232]
(68)	$e^- + O_2 \rightarrow O_2 + e^-$	$\sigma(\varepsilon)$				[222]
(69)	$e^- + O_2 \rightarrow O_{2,rot} + e^-$	$\sigma(\varepsilon)$			A,B	[222]
(70)	$e^- + O_2 \rightarrow O_{2,vib1} + e^-$	$\sigma(\varepsilon)$			A,B	[222]
(71)	$e^- + O_2 \rightarrow O_{2,vib2} + e^-$	$\sigma(\varepsilon)$			A	[222]

Nr	Reaction name	A^a	B^a	C^a	Set^b	Ref.
(72)	$e^- + O_2 \rightarrow O_{2,vib3} + e^-$	$\sigma(\varepsilon)$			A	[222]
(73)	$e^- + O_2 \rightarrow O_{2,vib4} + e^-$	$\sigma(\varepsilon)$				[222]
(74)	$e^- + O_2 \rightarrow O_{2,vib5} + e^-$	$\sigma(\varepsilon)$			A,B	[222]
(75)	$e^- + O_2 \rightarrow O_{2,vib6} + e^-$	$\sigma(\varepsilon)$			A	[222]
(76)	$e^- + O_2 \rightarrow O_2(a) + e^-$	$\sigma(\varepsilon)$			A,B	[222]
(77)	$e^- + O_2 \rightarrow O_2(b) + e^-$	$\sigma(\varepsilon)$			A,B	[222]
(78)	$e^- + O_2 \rightarrow O_2^+ + e^- + e^-$	$\sigma(\varepsilon)$			A,B	[222]
(79)	$e^- + O_2 \rightarrow O + O + e^-$	$\sigma(\varepsilon)$			A,B	[222]
(80)	$e^- + O_2 \rightarrow O + O + e^-$	$\sigma(\varepsilon)$			A,B	[222, 233]
(81)	$e^- + O_2 \rightarrow O^+ + O + e^- + e^-$	$\sigma(\varepsilon)$			A,B	[234]
(82)	$e^- + O_2 \rightarrow O^- + O$	$\sigma(\varepsilon)$			A,B	[222, 235]
(83)	$e^- + O_2 + O_2 \rightarrow O_2^- + O_2$				A	[105] [c]
(84)	$e^- + O_2 + N_2 \rightarrow O_2^- + N_2$				A,B	[105] [c]
(85)	$e^- + O_2 + Ar \rightarrow O_2^- + Ar$				A,B	c, g
(86)	$e^- + O_2 + H_2O \rightarrow O_2^- + H_2O$					c, g
(87)	$e^- + O_2 + H_2 \rightarrow O_2^- + H_2$					c, g
(88)	$e^- + O_{2,vib} \rightarrow O_{2,vib} + e^-$	$\sigma(\varepsilon)$				e
(89)	$e^- + O_{2,vib} \rightarrow O_{2,rot} + e^-$	$\sigma(\varepsilon)$				e
(90)	$e^- + O_{2,vib} \rightarrow O_2 + e^-$	$\sigma(\varepsilon)$				f
(91)	$e^- + O_{2,vib} \rightarrow O_2(a) + e^-$	$\sigma(\varepsilon)$				h
(92)	$e^- + O_{2,vib} \rightarrow O_2(b) + e^-$	$\sigma(\varepsilon)$				h
(93)	$e^- + O_{2,vib} \rightarrow O + O + e^-$	$\sigma(\varepsilon)$				h
(94)	$e^- + O_{2,vib} \rightarrow O + O + e^-$	$\sigma(\varepsilon)$				h
(95)	$e^- + O_{2,vib} \rightarrow O_2^+ + e^- + e^-$	$\sigma(\varepsilon)$				h

Nr	Reaction name	A^a	B^a	C^a	Set^b	Ref.
(96)	$e^- + O_{2,vib} \rightarrow O^+ + O + e^- + e^-$	$\sigma(\varepsilon)$				h
(97)	$e^- + O_2(a) \rightarrow O_2(a) + e^-$	$\sigma(\varepsilon)$				[177]
(98)	$e^- + O_2(a) \rightarrow O + O + e^-$	$\sigma(\varepsilon)$			A	h
(99)	$e^- + O_2(a) \rightarrow O + O + e^-$	$\sigma(\varepsilon)$			A	h
(100)	$e^- + O_2(a) \rightarrow O^+ + O + e^- + e^-$	$\sigma(\varepsilon)$				h
(101)	$e^- + O_2(a) \rightarrow O^+ + O$	$\sigma(\varepsilon)$			A,B	[236]
(102)	$e^- + O_2(a) \rightarrow O_2 + e^-$	$\sigma(\varepsilon)$			A	f
(103)	$e^- + O_2(a) \rightarrow O_2(b) + e^-$	$\sigma(\varepsilon)$			A,B	[237]
(104)	$e^- + O_2(a) \rightarrow O_2^+ + e^- + e^-$	$\sigma(\varepsilon)$			A	h
(105)	$e^- + O_2(a) + O_2 \rightarrow O_2^- + O_2$					c, d
(106)	$e^- + O_2(a) + N_2 \rightarrow O_2^- + N_2$					c, d
(107)	$e^- + O_2(a) + Ar \rightarrow O_2^- + Ar$				A	c, d
(108)	$e^- + O_2(a) + H_2O \rightarrow O_2^- + H_2O$					c, d
(109)	$e^- + O_2(a) + H_2 \rightarrow O_2^- + H_2$					c, d
(110)	$e^- + O_2(b) \rightarrow O_2(b) + e^-$	$\sigma(\varepsilon)$				[177]
(111)	$e^- + O_2(b) \rightarrow O + O + e^-$	$\sigma(\varepsilon)$			A,B	h
(112)	$e^- + O_2(b) \rightarrow O + O + e^-$	$\sigma(\varepsilon)$			A	h
(113)	$e^- + O_2(b) \rightarrow O^+ + O + e^- + e^-$	$\sigma(\varepsilon)$				h
(114)	$e^- + O_2(b) \rightarrow O^- + O$	$\sigma(\varepsilon)$			A	i
(115)	$e^- + O_2(b) \rightarrow O_2(a) + e^-$	$\sigma(\varepsilon)$			A,B	f
(116)	$e^- + O_2(b) \rightarrow O_2 + e^-$	$\sigma(\varepsilon)$				f
(117)	$e^- + O_2(b) \rightarrow O_2^+ + e^- + e^-$	$\sigma(\varepsilon)$				h
(118)	$e^- + O_2(b) + O_2 \rightarrow O_2^- + O_2$					c, d
(119)	$e^- + O_2(b) + N_2 \rightarrow O_2^- + N_2$					c, d

Nr	Reaction name	A^a	B^a	C^a	Set^b	Ref.
(120)	$e^- + O_2(b) + Ar \rightarrow O_2^- + Ar$					c, d
(121)	$e^- + O_2(b) + H_2O \rightarrow O_2^- + H_2O$					c, d
(122)	$e^- + O_2(b) + H_2 \rightarrow O_2^- + H_2$					c, d
(123)	$e^- + O_2^+ \rightarrow e^- + O_2^+$	$\sigma(\varepsilon)$				[177]
(124)	$e^- + O_2^+ \rightarrow O + O$	$\sigma(\varepsilon)$			A,B	[178]
(125)	$e^- + O_2^+ + M \rightarrow O_2 + M$	4.31×10^{-34}	-1.5			[105]
(126)	$e^- + e^- + O_2^+ \rightarrow e^- + O_2$	7.18×10^{-27}	-4.5			[105]
(127)	$e^- + O_2^- \rightarrow O_2 + e^-$	$\sigma(\varepsilon)$				[177]
(128)	$e^- + O_2^- \rightarrow O_2 + e^- + e^-$	$\sigma(\varepsilon)$				[232]
(129)	$e^- + O_3 \rightarrow e^- + O_3$	$\sigma(\varepsilon)$				[177]
(130)	$e^- + O_3 \rightarrow O + O_2 + e^-$	$\sigma(\varepsilon)$			A,B	[238]
(131)	$e^- + O_3 \rightarrow O + O_2^+ + e^- + e^-$	$\sigma(\varepsilon)$				[104]
(132)	$e^- + O_3 \rightarrow O^+ + O^- + O + e^-$	$\sigma(\varepsilon)$				[104]
(133)	$e^- + O_3 \rightarrow O^- + O_2$	$\sigma(\varepsilon)$			A,B	[239]
(134)	$e^- + O_3 \rightarrow O + O_2^-$	$\sigma(\varepsilon)$			A,B	[104]
(135)	$e^- + O_3^- \rightarrow O_3 + e^-$	$\sigma(\varepsilon)$				[177]
(136)	$e^- + O_4^+ \rightarrow O_2 + O_2$	7.12×10^{-08}	-0.5			[105]
(137)	$e^- + N \rightarrow e^- + N$	$\sigma(\varepsilon)$				[240]
(138)	$e^- + N \rightarrow e^- + N(^2D)$	$\sigma(\varepsilon)$			A,B	[241]
(139)	$e^- + N \rightarrow e^- + N^+ + e^-$	$\sigma(\varepsilon)$				[242]
(140)	$e^- + N(^2D) \rightarrow e^- + N(^2D)$	$\sigma(\varepsilon)$				e
(141)	$e^- + N(^2D) \rightarrow e^- + N$	$\sigma(\varepsilon)$			A,B	f
(142)	$e^- + N(^2D) \rightarrow e^- + N^+ + e^-$	$\sigma(\varepsilon)$				[227]
(143)	$e^- + N^+ \rightarrow e^- + N^+$	$\sigma(\varepsilon)$				[177]

Nr	Reaction name	A[a]	B[a]	C[a]	Set[b]	Ref.
(144)	$e^- + N^+ \rightarrow N$	$\sigma(\varepsilon)$				[177]
(145)	$e^- + N^+ + e^- \rightarrow N + e^-$	5.40×10^{-24}	-4.5			[171]
(146)	$e^- + N^+ + M \rightarrow N + M$	2.49×10^{-29}	-1.5			[171]
(147)	$e^- + N_2 \rightarrow e^- + N_2$	$\sigma(\varepsilon)$				[243]
(148)	$e^- + N_2 \rightarrow e^- + N_{2,rot}$	$\sigma(\varepsilon)$			A,B	[222]
(149)	$e^- + N_2 \rightarrow N_{2,vib1} + e^-$	$\sigma(\varepsilon)$			A,B	[222]
(150)	$e^- + N_2 \rightarrow N_{2,vib2} + e^-$	$\sigma(\varepsilon)$			A	[222]
(151)	$e^- + N_2 \rightarrow N_{2,vib3} + e^-$	$\sigma(\varepsilon)$			A	[222]
(152)	$e^- + N_2 \rightarrow N_{2,vib4} + e^-$	$\sigma(\varepsilon)$			A	[222]
(153)	$e^- + N_2 \rightarrow N_{2,vib5} + e^-$	$\sigma(\varepsilon)$			A	[222]
(154)	$e^- + N_2 \rightarrow N_{2,vib6} + e^-$	$\sigma(\varepsilon)$			A	[222]
(155)	$e^- + N_2 \rightarrow N_{2,vib7} + e^-$	$\sigma(\varepsilon)$			A	[222]
(156)	$e^- + N_2 \rightarrow N_{2,vib8} + e^-$	$\sigma(\varepsilon)$			A	[222]
(157)	$e^- + N_2 \rightarrow e^- + N_2(A)$	$\sigma(\varepsilon)$			A,B	[222]
(158)	$e^- + N_2 \rightarrow e^- + N_2(a')$	$\sigma(\varepsilon)$			A,B	[222]
(159)	$e^- + N_2 \rightarrow e^- + N + N$	$\sigma(\varepsilon)$			A,B	[222]
(160)	$e^- + N_2 \rightarrow e^- + N^+ + N + e^-$	$\sigma(\varepsilon)$			A,B	[244]
(161)	$e^- + N_2 \rightarrow e^- + e^- + N_2^+$	$\sigma(\varepsilon)$			A,B	[243]
(162)	$e^- + N_{2,vib} \rightarrow N_{2,vib} + e^-$	$\sigma(\varepsilon)$				e
(163)	$e^- + N_{2,vib} \rightarrow N_2 + e^-$	$\sigma(\varepsilon)$				f
(164)	$e^- + N_{2,vib} \rightarrow N_2(A) + e^-$	$\sigma(\varepsilon)$			A,B	i
(165)	$e^- + N_{2,vib} \rightarrow N_2^+ + e^- + e^-$	$\sigma(\varepsilon)$				j
(166)	$e^- + N_2(A) \rightarrow e^- + N_2(A)$	$\sigma(\varepsilon)$				e
(167)	$e^- + N_2(A) \rightarrow e^- + N_2$	$\sigma(\varepsilon)$			A,B	f

Nr	Reaction name	A^a	B^a	C^a	Set^b	Ref.
(168)	$e^- + N_2(A) \rightarrow N_{2,vib} + e^-$	$\sigma(\varepsilon)$			A,B	f
(169)	$e^- + N_2(A) \rightarrow e^- + N_2^+ + e^-$	$\sigma(\varepsilon)$			A,B	[227]
(170)	$e^- + N_2(a') \rightarrow N_2(a') + e^-$	$\sigma(\varepsilon)$				e
(171)	$e^- + N_2(a') \rightarrow e^- + N_2$	$\sigma(\varepsilon)$			A,B	f
(172)	$e^- + N_2(a') \rightarrow N_2^+ + e^- + e^-$	$\sigma(\varepsilon)$				[245]
(173)	$e^- + N_2^+ \rightarrow e^- + N_2^+$	$\sigma(\varepsilon)$				[177]
(174)	$e^- + N_2^+ \rightarrow N + N$	$\sigma(\varepsilon)$			A,B	[178]
(175)	$e^- + e^- + N_2^+ \rightarrow N_2 + e^-$	7.18×10^{-27}	-4.5			[105]
(176)	$e^- + M + N_2^+ \rightarrow N_2 + M$	4.31×10^{-34}	-4.5			[105]
(177)	$e^- + N_3^+ \rightarrow e^- + N_3^+$	$\sigma(\varepsilon)$				[177]
(178)	$e^- + N_3^+ \rightarrow N + N + N_2$	3.22×10^{-08}	-0.5			[171]
(179)	$e^- + N_4^+ \rightarrow e^- + N_4^+$	$\sigma(\varepsilon)$				[177]
(180)	$e^- + N_4^+ \rightarrow N_2 + N_2$	3.21×10^{-07}	-0.5			[183]
(181)	$e^- + N_4^+ \rightarrow N_2 + N + N$	3.13×10^{-07}	-0.41			[183]
(182)	$e^- + NO \rightarrow e^- + NO$	$\sigma(\varepsilon)$				[246]
(183)	$e^- + NO \rightarrow e^- + N + O$	$\sigma(\varepsilon)$			A,B	[246]
(184)	$e^- + NO \rightarrow N + O^-$	$\sigma(\varepsilon)$			A,B	[247]
(185)	$e^- + NO \rightarrow e^- + e^- + N^+ + O$	$\sigma(\varepsilon)$				[248]
(186)	$e^- + NO \rightarrow e^- + e^- + N + O^+$	$\sigma(\varepsilon)$				[248]
(187)	$e^- + NO \rightarrow e^- + e^- + NO^+$	$\sigma(\varepsilon)$			A,B	[248]
(188)	$e^- + NO^+ \rightarrow e^- + NO^+$	$\sigma(\varepsilon)$				[177]
(189)	$e^- + NO^+ \rightarrow N + O$	$\sigma(\varepsilon)$			A,B	[178] k
(190)	$e^- + NO^+ \rightarrow N(^2D) + O$	7.76×10^{-09}	-1		A,B	[105]
(191)	$e^- + NO^+ + e^- \rightarrow NO + e^-$	7.18×10^{-27}	-4.5		A,B	[105]

Nr	Reaction name	A[a]	B[a]	C[a]	Set[b]	Ref.
(192)	$e^- + NO^+ + M \rightarrow NO + M$	2.52×10^{-29}	-1.5			[105]
(193)	$e^- + NO_2 \rightarrow e^- + NO_2$	$\sigma(\varepsilon)$				[249]
(194)	$e^- + NO_2 \rightarrow e^- + e^- + NO^+ + O$	$\sigma(\varepsilon)$				[248]
(195)	$e^- + NO_2 \rightarrow e^- + e^- + NO_2^+$	$\sigma(\varepsilon)$			A,B	[248]
(196)	$e^- + NO_2 \rightarrow NO + O + e^-$	5.60×10^{-09}		3.11	A,B	[183]
(197)	$e^- + NO_2^+ \rightarrow NO + O$	2.00×10^{-07}	-0.5		A,B	[179]
(198)	$e^- + NO_2^+ \rightarrow NO + O(^1D)$	2.00×10^{-07}	-0.5		A,B	[179]
(199)	$e^- + N_2O \rightarrow N_2O + e^-$	$\sigma(\varepsilon)$				[250]
(200)	$e^- + N_2O \rightarrow N_2O_{vib1} + e^-$	$\sigma(\varepsilon)$			A,B	[250]
(201)	$e^- + N_2O \rightarrow N_2O_{vib2} + e^-$	$\sigma(\varepsilon)$			A	[250]
(202)	$e^- + N_2O \rightarrow N_2O_{vib3} + e^-$	$\sigma(\varepsilon)$			A,B	[250]
(203)	$e^- + N_2O \rightarrow N_2 + O^-$	$\sigma(\varepsilon)$				[250]
(204)	$e^- + N_2O \rightarrow NO^+ + N + e^- + e^-$	$\sigma(\varepsilon)$				[177]
(205)	$e^- + N_2O \rightarrow O^+ + N_2 + e^- + e^-$	$\sigma(\varepsilon)$				[177]
(206)	$e^- + N_2O \rightarrow N_2^+ + O + e^- + e^-$	$\sigma(\varepsilon)$				[177]
(207)	$e^- + N_2O \rightarrow N^+ + NO + e^- + e^-$	$\sigma(\varepsilon)$				[177]
(208)	$e^- + N_2O \rightarrow N_2 + O + e^-$	1.40×10^{-09}		1.67		[183]
(209)	$e^- + N_2O \rightarrow N_2 + O(^1D) + e^-$	1.20×10^{-09}		3.64		[183]
(210)	$e^- + N_2O \rightarrow NO + N + e^-$	1.00×10^{-10}		4.93		[183]
(211)	$e^- + H \rightarrow e^- + H$	$\sigma(\varepsilon)$				[251, 252]
(212)	$e^- + H \rightarrow H^* + e^-$	$\sigma(\varepsilon)$			A,B	[226]
(213)	$e^- + H \rightarrow H^* + e^-$	$\sigma(\varepsilon)$			A,B	[226]
(214)	$e^- + H \rightarrow H^* + e^-$	$\sigma(\varepsilon)$			A,B	[226]
(215)	$e^- + H \rightarrow e^- + H^+ + e^-$	$\sigma(\varepsilon)$			A,B	[226]

Nr	Reaction name	A^a	B^a	C^a	Set^b	Ref.
(216)	$e^- + H^* \rightarrow H^* + e^-$	$\sigma(\varepsilon)$				e
(217)	$e^- + H^* \rightarrow H + e^-$	$\sigma(\varepsilon)$			A	f
(218)	$e^- + H^* \rightarrow H^+ + e^- + e^-$	$\sigma(\varepsilon)$			A,B	[227]
(219)	$e^- + H^+ \rightarrow e^- + H^+$	$\sigma(\varepsilon)$				[177]
(220)	$e^- + H^+ \rightarrow H$	$\sigma(\varepsilon)$				[177]
(221)	$e^- + H^+ + e^- \rightarrow e^- + H$	8.80×10^{-27}	-4.5			[121]
(222)	$e^- + H^- \rightarrow e^- + H^-$	$\sigma(\varepsilon)$				[177]
(223)	$e^- + H^- \rightarrow e^- + e^- + H$	$\sigma(\varepsilon)$			A,B	[253]
(224)	$e^- + H_2 \rightarrow e^- + H_2$	$\sigma(\varepsilon)$				[254]
(225)	$e^- + H_2 \rightarrow H_{2,rot(0-2)} + e^-$	$\sigma(\varepsilon)$			A,B	[254]
(226)	$e^- + H_2 \rightarrow H_{2,rot(1-3)} + e^-$	$\sigma(\varepsilon)$			A,B	[254]
(227)	$e^- + H_2 \rightarrow H_{2,vib1} + e^-$	$\sigma(\varepsilon)$			A,B	[254]
(228)	$e^- + H_2 \rightarrow H_{2,vib2} + e^-$	$\sigma(\varepsilon)$				[254]
(229)	$e^- + H_2 \rightarrow H_2^* + e^-$	$\sigma(\varepsilon)$			A,B	[254]
(230)	$e^- + H_2 \rightarrow H_2^* + e^-$	$\sigma(\varepsilon)$			A,B	[254]
(231)	$e^- + H_2 \rightarrow e^- + H + H$	$\sigma(\varepsilon)$				[255]
(232)	$e^- + H_2 \rightarrow e^- + e^- + H_2^+$	$\sigma(\varepsilon)$			A,B	[254]
(233)	$e^- + H_2^* \rightarrow H_2^* + e^-$	$\sigma(\varepsilon)$				e
(234)	$e^- + H_2^* \rightarrow H_2 + e^-$	$\sigma(\varepsilon)$			A	f
(235)	$e^- + H_2^* \rightarrow H_2^+ + e^- + e^-$	$\sigma(\varepsilon)$			A,B	[227]
(236)	$e^- + H_2^+ \rightarrow e^- + H_2^+$	$\sigma(\varepsilon)$				[177]
(237)	$e^- + H_2^+ \rightarrow H + H$	$\sigma(\varepsilon)$				[256]
(238)	$e^- + H_2^+ \rightarrow e^- + H^+ + H$	$\sigma(\varepsilon)$			A,B	[256]
(239)	$e^- + H_2^+ \rightarrow H^+ + H^-$	$\sigma(\varepsilon)$				[257]

Nr	Reaction name	A^a	B^a	C^a	Set[b]	Ref.
(240)	$e^- + H_3^+ \rightarrow H_3^+ + e^-$	$\sigma(\varepsilon)$				[177]
(241)	$e^- + H_3^+ \rightarrow H_2 + H$	$\sigma(\varepsilon)$				[257]
(242)	$e^- + H_3^+ \rightarrow e^- + H_2 + H^+$	$\sigma(\varepsilon)$				[256]
(243)	$e^- + H_3^+ \rightarrow H + H + H$	$\sigma(\varepsilon)$				[257]
(244)	$e^- + H_3^+ \rightarrow e^- + H + H + H^+$	$\sigma(\varepsilon)$				[257]
(245)	$e^- + OH \rightarrow e^- + OH$	$\sigma(\varepsilon)$				[258][1]
(246)	$e^- + OH \rightarrow e^- + O + H$	2.08×10^{-07}	-0.76	6.9	A,B	[259]
(247)	$e^- + OH \rightarrow e^- + OH(A)$	1.52×10^{-06}	0.52	3.85	A,B	[259]
(248)	$e^- + OH \rightarrow e^- + e^- + OH^+$	$\sigma(\varepsilon)$			A,B	[259]
(249)	$e^- + OH(A) \rightarrow e^- + OH^+ + e^-$	3.02×10^{-11}	2.61	10.58	A,B	[258]
(250)	$e^- + OH(A) \rightarrow e^- + O + H$	1.54×10^{-07}	-0.75	3.9	A,B	[258]
(251)	$e^- + OH^+ \rightarrow O + H$	6.03×10^{-09}	-0.5		A,B	[121]
(252)	$e^- + OH^- \rightarrow OH^- + e^-$	$\sigma(\varepsilon)$				[260]
(253)	$e^- + OH^- \rightarrow OH + e^- + e^-$	$\sigma(\varepsilon)$			A	[260]
(254)	$e^- + OH^- \rightarrow O + H + e^- + e^-$	9.67×10^{-06}	-1.89	12.1		[259]
(255)	$e^- + H_2O \rightarrow e^- + H_2O$	$\sigma(\varepsilon)$				[172]
(256)	$e^- + H_2O \rightarrow e^- + H_2O_{vib(100)}$	$\sigma(\varepsilon)$			A,B	[172]
(257)	$e^- + H_2O \rightarrow e^- + H_2O_{vib(010)}$	$\sigma(\varepsilon)$			A,B	[172]
(258)	$e^- + H_2O \rightarrow e^- + H_2O_{vib(001)}$	$\sigma(\varepsilon)$			A,B	[172]
(259)	$e^- + H_2O \rightarrow O^- + H_2$	$\sigma(\varepsilon)$			A,B	[172]
(260)	$e^- + H_2O \rightarrow OH + H^-$	$\sigma(\varepsilon)$			A,B	[172]
(261)	$e^- + H_2O \rightarrow OH^- + H$	$\sigma(\varepsilon)$			A,B	[172]
(262)	$e^- + H_2O \rightarrow e^- + OH + H$	$\sigma(\varepsilon)$			A	[172]
(263)	$e^- + H_2O \rightarrow e^- + O + H + H$	$\sigma(\varepsilon)$			A,B	[172]

Nr	Reaction name	A^a	B^a	C^a	Set^b	Ref.
(264)	$e^- + H_2O \rightarrow e^- + e^- + H_2O^+$	$\sigma(\varepsilon)$			A,B	[172]
(265)	$e^- + H_2O^+ \rightarrow e^- + H_2O^+$	$\sigma(\varepsilon)$				[177]
(266)	$e^- + H_2O^+ \rightarrow O + H_2$	6.27×10^{-09}	-0.5		A,B	[180] [m]
(267)	$e^- + H_2O^+ \rightarrow O + H + H$	4.90×10^{-08}	-0.5		A,B	[180] [m]
(268)	$e^- + H_2O^+ \rightarrow OH + H$	1.38×10^{-08}	-0.5		A	[180] [m]
(269)	$e^- + H_3O^+ \rightarrow H + H + OH$	6.00×10^{-08}	-0.7		A,B	[105] [n]
(270)	$e^- + H_3O^+ \rightarrow H_2O + H$	2.50×10^{-08}	-0.7		A	[105] [n]
(271)	$e^- + H_3O^+ \rightarrow H_2 + OH$	1.40×10^{-08}	-0.7		A	[105] [n]
(272)	$e^- + H_3O^+ \rightarrow H_2 + O + H$	1.30×10^{-09}	-0.7			[105] [n]
(273)	$e^- + H_2O_2 \rightarrow H_2O + O^-$	$\sigma(\varepsilon)$			A,B	[261]
(274)	$e^- + H_2O_2 \rightarrow OH + OH^-$	$\sigma(\varepsilon)$			A,B	[261]
(275)	$e^- + NH \rightarrow NH + e^-$	$\sigma(\varepsilon)$				[262] [o]
(276)	$e^- + NH \rightarrow N + H + e^-$	$\sigma(\varepsilon)$			A,B	[262]
(277)	$e^- + NH \rightarrow N^+ + H + e^- + e^-$	$\sigma(\varepsilon)$				[263]
(278)	$e^- + ArH^+ \rightarrow e^- + ArH^+$	$\sigma(\varepsilon)$				[177]
(279)	$e^- + ArH^+ \rightarrow Ar + H$	$\sigma(\varepsilon)$				[178] [k]
	Argon heavy particle collisions					
(280)	$Ar(^4S[^3P_2]) + Ar(^4S[^3P_2]) \rightarrow Ar^+ + Ar + e^-$	6.40×10^{-10}	0	0		[264]
(281)	$Ar(^4S[^3P_2]) + Ar(^4S[^3P_1]) \rightarrow Ar^+ + Ar + e^-$	2.10×10^{-09}	0	0		[264]
(282)	$Ar(^4S[^3P_2]) + Ar(^4S[^3P_0]) \rightarrow Ar^+ + Ar + e^-$	6.40×10^{-10}	0	0		[264]
(283)	$Ar(^4S[^3P_2]) + Ar(^4S[^1P_1]) \rightarrow Ar^+ + Ar + e^-$	2.10×10^{-09}	0	0		[264]
(284)	$Ar(^4S[^3P_1]) + Ar(^4S[^3P_1]) \rightarrow Ar^+ + Ar + e^-$	2.10×10^{-09}	0	0		[264]
(285)	$Ar(^4S[^3P_1]) + Ar(^4S[^3P_0]) \rightarrow Ar^+ + Ar + e^-$	2.10×10^{-09}	0	0		[264]
(286)	$Ar(^4S[^3P_1]) + Ar(^4S[^1P_1]) \rightarrow Ar^+ + Ar + e^-$	2.10×10^{-09}	0	0		[264]

Nr	Reaction name	A^a	B^a	C^a	Set^b	Ref.
(287)	$Ar(^4S[^3P_0]) + Ar(^4S[^3P_0]) \rightarrow Ar^+ + Ar + e^-$	6.40×10^{-10}	0	0		[264]
(288)	$Ar(^4S[^3P_0]) + Ar(^4S[^1P_1]) \rightarrow Ar^+ + Ar + e^-$	2.10×10^{-09}	0	0		[264]
(289)	$Ar(^4S[^1P_1]) + Ar(^4S[^1P_1]) \rightarrow Ar^+ + Ar + e^-$	2.10×10^{-09}	0	0		[264]
(290)	$Ar(^4S[^3P_2]) + Ar(^4P) \rightarrow Ar^+ + Ar + e^-$	5.00×10^{-10}	0	0		[264]
(291)	$Ar(^4S[^3P_1]) + Ar(^4P) \rightarrow Ar^+ + Ar + e^-$	5.00×10^{-10}	0	0		[264]
(292)	$Ar(^4S[^3P_0]) + Ar(^4P) \rightarrow Ar^+ + Ar + e^-$	5.00×10^{-10}	0	0		[264]
(293)	$Ar(^4S[^1P_1]) + Ar(^4P) \rightarrow Ar^+ + Ar + e^-$	5.00×10^{-10}	0	0		[264]
(294)	$Ar(^4P) + Ar(^4P) \rightarrow Ar^+ + Ar + e^-$	5.00×10^{-10}	0	0		[264]
(295)	$Ar(^4S[^3P_2]) + Ar_2^* \rightarrow Ar^+ + Ar + Ar + e^-$	5.00×10^{-10}	0	0	A	[265] p
(296)	$Ar(^4S[^3P_1]) + Ar_2^* \rightarrow Ar^+ + Ar + Ar + e^-$	5.00×10^{-10}	0	0		[265] p
(297)	$Ar(^4S[^3P_0]) + Ar_2^* \rightarrow Ar^+ + Ar + Ar + e^-$	5.00×10^{-10}	0	0		[265] p
(298)	$Ar(^4S[^1P_1]) + Ar_2^* \rightarrow Ar^+ + Ar + Ar + e^-$	5.00×10^{-10}	0	0		[265] p
(299)	$Ar(^4P) + Ar_2^* \rightarrow Ar^+ + Ar + Ar + e^-$	5.00×10^{-10}	0	0		[265] p
(300)	$Ar(^4S[^3P_2]) + Ar_2^* \rightarrow Ar_2^+ + Ar + e^-$	5.00×10^{-10}	0	0		[265] p
(301)	$Ar(^4S[^3P_1]) + Ar_2^* \rightarrow Ar_2^+ + Ar + e^-$	5.00×10^{-10}	0	0		[265] p
(302)	$Ar(^4S[^3P_0]) + Ar_2^* \rightarrow Ar_2^+ + Ar + e^-$	5.00×10^{-10}	0	0		[265] p
(303)	$Ar(^4S[^1P_1]) + Ar_2^* \rightarrow Ar_2^+ + Ar + e^-$	5.00×10^{-10}	0	0		[265] p
(304)	$Ar(^4P) + Ar_2^* \rightarrow Ar_2^+ + Ar + e^-$	5.00×10^{-10}	0	0		[265] p
(305)	$Ar(^4S[^3P_2]) + Ar \rightarrow Ar + Ar$	2.09×10^{-15}	0	0		[266]
(306)	$Ar(^4S[^3P_1]) + Ar \rightarrow Ar + Ar$	2.09×10^{-15}	0	0		[266] q
(307)	$Ar(^4S[^3P_0]) + Ar \rightarrow Ar + Ar$	5.30×10^{-15}	0	0		[266]
(308)	$Ar(^4S[^1P_1]) + Ar \rightarrow Ar + Ar$	5.30×10^{-15}	0	0		[266] q
(309)	$Ar(^4S[^3P_2]) + Ar + M \rightarrow Ar_2^* + M$	3.30×10^{-32}	0	0	A,B	[267]
(310)	$Ar(^4S[^3P_1]) + Ar + M \rightarrow Ar_2^* + M$	3.30×10^{-32}	0	0	A,B	[267]

Nr	Reaction name	A^a	B^a	C^a	Set^b	Ref.
(311)	$Ar(^4S[^3P_0]) + Ar + M \rightarrow Ar_2^* + M$	3.30×10^{-32}	0	0	A,B	[267]
(312)	$Ar(^4S[^1P_1]) + Ar + M \rightarrow Ar_2^* + M$	3.30×10^{-32}	0	0	A	[267]
(313)	$Ar(^4P) + Ar + M \rightarrow Ar_2^* + M$	1.00×10^{-31}	0	0	A,B	[267]
(314)	$Ar^+ + Ar + M \rightarrow Ar_2^+ + M$	2.50×10^{-31}	0	0	A,B	[267]
(315)	$Ar_2^* + Ar_2^* \rightarrow Ar_2^+ + Ar + Ar + e^-$	5.00×10^{-10}	0	0	A	[267]
(316)	$Ar_2^* + M \rightarrow Ar + Ar + M$	5.00×10^{-15}	0	0	A	[266]
(317)	$Ar_2^* + M \rightarrow Ar(^4S[^3P_2]) + Ar + M$	5.00×10^{-15}	0	0	A,B	[266]
(318)	$Ar_2^* + M \rightarrow Ar(^4S[^3P_1]) + Ar + M$	5.00×10^{-15}	0	0	A	[266]
(319)	$Ar_2^* + M \rightarrow Ar(^4S[^3P_0]) + Ar + M$	5.00×10^{-15}	0	0	A,B	[266]
(320)	$Ar_2^* + M \rightarrow Ar(^4S[^1P_1]) + Ar + M$	5.00×10^{-15}	0	0	A,B	[266]

Argon - dry air heavy particle collisions

Nr	Reaction name	A^a	B^a	C^a	Set^b	Ref.
(321)	$Ar(^4S[^3P_2]) + O_2 \rightarrow Ar + O + O$	2.10×10^{-10}	0	0	A,B	[183, 268]
(322)	$Ar(^4S[^3P_2]) + O_2(a) \rightarrow Ar + O + O$	2.10×10^{-10}	0	0	A	r
(323)	$Ar(^4S[^3P_2]) + O_2(b) \rightarrow Ar + O + O$	2.10×10^{-10}	0	0		r
(324)	$Ar(^4S[^3P_2]) + O_3 \rightarrow Ar + O_2 + O(^1D)$	2.10×10^{-10}	0	0		[187, 268]
(325)	$Ar(^4S[^3P_2]) + N \rightarrow Ar + N(^2D)$	1.00×10^{-12}	0	0		[269]
(326)	$Ar(^4S[^3P_2]) + N(^2D) \rightarrow Ar + N^+ + e^-$	5.00×10^{-10}	0	0	A,B	[269]
(327)	$Ar(^4S[^3P_2]) + N_2 \rightarrow Ar + N_2(A)$	3.60×10^{-11}	0	0	A,B	[183, 266] s
(328)	$Ar(^4S[^3P_2]) + N_2 \rightarrow Ar + N + N$	3.60×10^{-11}	0	0	A,B	[183]
(329)	$Ar(^4S[^3P_2]) + N_2(A) \rightarrow Ar + N_2^+ + e^-$	5.00×10^{-10}	0	0	A,B	[269]
(330)	$Ar(^4S[^3P_2]) + N_2(A) \rightarrow Ar + N + N$	3.60×10^{-11}	0	0		t
(331)	$Ar(^4S[^3P_2]) + N_2(a') \rightarrow Ar + N_2^+ + e^-$	5.00×10^{-10}	0	0		u
(332)	$Ar(^4S[^3P_2]) + N_2(a') \rightarrow Ar + N + N$	3.60×10^{-11}	0	0		t
(333)	$Ar(^4S[^3P_2]) + NO \rightarrow Ar + N + O$	2.39×10^{-10}	0	0		[183]

Nr	Reaction name	A^a	B^a	C^a	Set^b	Ref.
(334)	$Ar(^4S[^3P_2]) + NO_2 \rightarrow Ar + NO + O$	6.49×10^{-10}	0	0		[266]
(335)	$Ar(^4S[^3P_2]) + N_2O \rightarrow Ar + NO + N$	4.40×10^{-10}	0	0		[183]
(336)	$Ar(^4S[^3P_2]) + N_2O \rightarrow Ar + N_2(A) + O$	4.40×10^{-10}	0	0		[183, 266] s
(337)	$Ar(^4S[^3P_1]) + O_2 \rightarrow Ar + O + O$	2.10×10^{-10}	0	0	A,B	v
(338)	$Ar(^4S[^3P_1]) + O_2(a) \rightarrow Ar + O + O$	2.10×10^{-10}	0	0		v
(339)	$Ar(^4S[^3P_1]) + O_2(b) \rightarrow Ar + O + O$	2.10×10^{-10}	0	0		v
(340)	$Ar(^4S[^3P_1]) + O_3 \rightarrow Ar + O_2 + O(^1D)$	2.10×10^{-10}	0	0		v
(341)	$Ar(^4S[^3P_1]) + N \rightarrow Ar + N(^2D)$	1.00×10^{-12}	0	0		v
(342)	$Ar(^4S[^3P_1]) + N(^2D) \rightarrow Ar + N^+ + e^-$	1.00×10^{-11}	0	0		v
(343)	$Ar(^4S[^3P_1]) + N_2 \rightarrow Ar + N_2(A)$	3.60×10^{-11}	0	0	A	v
(344)	$Ar(^4S[^3P_1]) + N_2 \rightarrow Ar + N + N$	3.60×10^{-11}	0	0	A	v
(345)	$Ar(^4S[^3P_1]) + N_2(A) \rightarrow Ar + N_2^+ + e^-$	5.00×10^{-10}	0	0	A	v
(346)	$Ar(^4S[^3P_1]) + N_2(A) \rightarrow Ar + N + N$	3.60×10^{-11}	0	0		v
(347)	$Ar(^4S[^3P_1]) + N_2(a') \rightarrow Ar + N_2^+ + e^-$	5.00×10^{-10}	0	0		v
(348)	$Ar(^4S[^3P_1]) + N_2(a') \rightarrow Ar + N + N$	3.60×10^{-11}	0	0		v
(349)	$Ar(^4S[^3P_1]) + NO \rightarrow Ar + N + O$	2.39×10^{-10}	0	0		v
(350)	$Ar(^4S[^3P_1]) + NO_2 \rightarrow Ar + NO + O$	6.49×10^{-10}	0	0		v
(351)	$Ar(^4S[^3P_1]) + N_2O \rightarrow Ar + NO + N$	4.40×10^{-10}	0	0		v
(352)	$Ar(^4S[^3P_1]) + N_2O \rightarrow Ar + N_2(A) + O$	4.40×10^{-10}	0	0		v
(353)	$Ar(^4S[^3P_0]) + O_2 \rightarrow Ar + O + O$	2.10×10^{-10}	0	0	A,B	v
(354)	$Ar(^4S[^3P_0]) + O_2(a) \rightarrow Ar + O + O$	2.10×10^{-10}	0	0		v
(355)	$Ar(^4S[^3P_0]) + O_2(b) \rightarrow Ar + O + O$	2.10×10^{-10}	0	0		v
(356)	$Ar(^4S[^3P_0]) + O_3 \rightarrow Ar + O_2 + O(^1D)$	2.10×10^{-10}	0	0		v
(357)	$Ar(^4S[^3P_0]) + N \rightarrow Ar + N(^2D)$	1.00×10^{-12}	0	0		v

Nr	Reaction name	A[a]	B[a]	C[a]	Set[b]	Ref.
(358)	$Ar(^4S[^3P_0]) + N(^2D) \rightarrow Ar + N^+ + e^-$	1.00×10^{-11}	0	0		v
(359)	$Ar(^4S[^3P_0]) + N_2 \rightarrow Ar + N_2(A)$	3.60×10^{-11}	0	0	A,B	v
(360)	$Ar(^4S[^3P_0]) + N_2 \rightarrow Ar + N + N$	3.60×10^{-11}	0	0	A,B	v
(361)	$Ar(^4S[^3P_0]) + N_2(A) \rightarrow Ar + N_2^+ + e^-$	5.00×10^{-10}	0	0	A	v
(362)	$Ar(^4S[^3P_0]) + N_2(A) \rightarrow Ar + N + N$	3.60×10^{-11}	0	0		v
(363)	$Ar(^4S[^3P_0]) + N_2(a') \rightarrow Ar + N_2^+ + e^-$	5.00×10^{-10}	0	0		v
(364)	$Ar(^4S[^3P_0]) + N_2(a') \rightarrow Ar + N + N$	3.60×10^{-11}	0	0		v
(365)	$Ar(^4S[^3P_0]) + NO \rightarrow Ar + N + O$	2.39×10^{-10}	0	0		v
(366)	$Ar(^4S[^3P_0]) + NO_2 \rightarrow Ar + NO + O$	6.49×10^{-10}	0	0		v
(367)	$Ar(^4S[^3P_0]) + N_2O \rightarrow Ar + NO + N$	4.40×10^{-10}	0	0		v
(368)	$Ar(^4S[^3P_0]) + N_2O \rightarrow Ar + N_2(A) + O$	4.40×10^{-10}	0	0		v
(369)	$Ar(^4S[^1P_1]) + O_2 \rightarrow Ar + O + O$	2.10×10^{-10}	0	0	A,B	v
(370)	$Ar(^4S[^1P_1]) + O_2(a) \rightarrow Ar + O + O$	2.10×10^{-10}	0	0		v
(371)	$Ar(^4S[^1P_1]) + O_2(b) \rightarrow Ar + O + O$	2.10×10^{-10}	0	0		v
(372)	$Ar(^4S[^1P_1]) + O_3 \rightarrow Ar + O_2 + O(^1D)$	2.10×10^{-10}	0	0		v
(373)	$Ar(^4S[^1P_1]) + N \rightarrow Ar + N(^2D)$	1.00×10^{-12}	0	0		v
(374)	$Ar(^4S[^1P_1]) + N(^2D) \rightarrow Ar + N^+ + e^-$	1.00×10^{-11}	0	0		v
(375)	$Ar(^4S[^1P_1]) + N_2 \rightarrow Ar + N_2(A)$	3.60×10^{-11}	0	0	A	v
(376)	$Ar(^4S[^1P_1]) + N_2 \rightarrow Ar + N + N$	3.60×10^{-11}	0	0	A	v
(377)	$Ar(^4S[^1P_1]) + N_2(A) \rightarrow Ar + N_2^+ + e^-$	5.00×10^{-10}	0	0		v
(378)	$Ar(^4S[^1P_1]) + N_2(A) \rightarrow Ar + N + N$	3.60×10^{-11}	0	0		v
(379)	$Ar(^4S[^1P_1]) + N_2(a') \rightarrow Ar + N_2^+ + e^-$	5.00×10^{-10}	0	0		v
(380)	$Ar(^4S[^1P_1]) + N_2(a') \rightarrow Ar + N + N$	3.60×10^{-11}	0	0		v
(381)	$Ar(^4S[^1P_1]) + NO \rightarrow Ar + N + O$	2.39×10^{-10}	0	0		v

Nr	Reaction name	A^a	B^a	C^a	Set^b	Ref.
(382)	$Ar(^4S[^1P_1]) + NO_2 \rightarrow Ar + NO + O$	6.49×10^{-10}	0	0		v
(383)	$Ar(^4S[^1P_1]) + N_2O \rightarrow Ar + NO + N$	4.40×10^{-10}	0	0		v
(384)	$Ar(^4S[^1P_1]) + N_2O \rightarrow Ar + N_2(A) + O$	4.40×10^{-10}	0	0		v
(385)	$Ar(^4P) + O_2 \rightarrow Ar + O + O$	2.10×10^{-10}	0	0	A,B	v
(386)	$Ar(^4P) + O_2(a) \rightarrow Ar + O + O$	2.10×10^{-10}	0	0	A	v
(387)	$Ar(^4P) + O_2(b) \rightarrow Ar + O + O$	2.10×10^{-10}	0	0		v
(388)	$Ar(^4P) + O_3 \rightarrow Ar + O_2 + O(^1D)$	2.10×10^{-10}	0	0		v
(389)	$Ar(^4P) + N \rightarrow Ar + N(^2D)$	1.00×10^{-12}	0	0		v
(390)	$Ar(^4P) + N(^2D) \rightarrow Ar + N^+ + e^-$	1.00×10^{-11}	0	0		v
(391)	$Ar(^4P) + N_2 \rightarrow Ar + N_2(A)$	3.60×10^{-11}	0	0	A,B	v
(392)	$Ar(^4P) + N_2 \rightarrow Ar + N + N$	3.60×10^{-11}	0	0	A,B	v
(393)	$Ar(^4P) + N_2(A) \rightarrow Ar + N_2^+ + e^-$	5.00×10^{-10}	0	0	A	v
(394)	$Ar(^4P) + N_2(A) \rightarrow Ar + N + N$	3.60×10^{-11}	0	0		v
(395)	$Ar(^4P) + N_2(a') \rightarrow Ar + N_2^+ + e^-$	5.00×10^{-10}	0	0		v
(396)	$Ar(^4P) + N_2(a') \rightarrow Ar + N + N$	3.60×10^{-11}	0	0		v
(397)	$Ar(^4P) + NO \rightarrow Ar + N + O$	2.39×10^{-10}	0	0	A	v
(398)	$Ar(^4P) + NO_2 \rightarrow Ar + NO + O$	6.49×10^{-10}	0	0		v
(399)	$Ar(^4P) + N_2O \rightarrow Ar + NO + N$	4.40×10^{-10}	0	0	A	v
(400)	$Ar(^4P) + N_2O \rightarrow Ar + N_2(A) + O$	4.40×10^{-10}	0	0	A	v
(401)	$Ar^+ + O \rightarrow Ar + O^+$	6.40×10^{-12}	0	0	A,B	[170]
(402)	$Ar^+ + O(^1D) \rightarrow Ar + O^+$	6.40×10^{-12}	0	0		w
(403)	$Ar^+ + O^- \rightarrow Ar + O$	2.00×10^{-07}	-0.5	0		[105,170]
(404)	$Ar^+ + O^- + M \rightarrow Ar + O + M$	2.00×10^{-25}	-2.5	0		[105]
(405)	$Ar^+ + O_2 \rightarrow Ar + O_2^+$	5.00×10^{-11}	0	0	A	[170,186]

Nr	Reaction name	A^a	B^a	C^a	Set^b	Ref.
(406)	$Ar^+ + O_2(a) \rightarrow Ar + O_2^+$	5.00×10^{-11}	0	0		[170]
(407)	$Ar^+ + O_2(b) \rightarrow Ar + O_2^+$	5.00×10^{-11}	0	0		[170]
(408)	$Ar^+ + O_2^- \rightarrow Ar + O_2$	2.00×10^{-07}	-0.5	0		[105]
(409)	$Ar^+ + O_2 \rightarrow Ar + O + O$	1.00×10^{-07}	0	0		[105]
(410)	$Ar^+ + O_2^- + M \rightarrow Ar + O_2 + M$	2.00×10^{-25}	-2.5	0		[105]
(411)	$Ar^+ + O_3 \rightarrow Ar + O_2^+ + O$	4.00×10^{-11}	0	0		[187, 268]
(412)	$Ar^+ + N \rightarrow Ar + N^+$	1.00×10^{-11}	0	0		[269]
(413)	$Ar^+ + N(^2D) \rightarrow Ar + N^+$	1.00×10^{-11}	0	0		[269]
(414)	$Ar^+ + N_2 \rightarrow Ar + N_2^+$	7.00×10^{-10}	0	0	A,B	[186]
(415)	$Ar^+ + N_2 \rightarrow Ar + N^+ + N$	5.00×10^{-12}	0	0	A,B	[265]
(416)	$Ar^+ + N_2(A) \rightarrow Ar + N_2^+$	1.00×10^{-11}	0	0		[269]
(417)	$Ar^+ + N_2(a') \rightarrow Ar + N_2^+$	1.00×10^{-11}	0	0		x
(418)	$Ar^+ + NO \rightarrow Ar + NO^+$	2.70×10^{-10}	0	0		[190]
(419)	$Ar^+ + NO_2 \rightarrow Ar + NO^+ + O$	4.32×10^{-10}	0	0		[271]
(420)	$Ar^+ + NO_2 \rightarrow Ar + NO_2^+$	2.76×10^{-11}	0	0		[271]
(421)	$Ar^+ + NO_2^- \rightarrow Ar + NO_2$	2.00×10^{-07}	-0.5	0		[170]
(422)	$Ar^+ + NO_2^- \rightarrow Ar + NO + O$	1.00×10^{-07}	0	0		[170]
(423)	$Ar^+ + NO_2^- + M \rightarrow Ar + NO_2 + M$	2.00×10^{-25}	-2.5	0		[170]
(424)	$Ar^+ + NO_3^- \rightarrow Ar + NO_3$	2.00×10^{-07}	-0.5	0		[170]
(425)	$Ar^+ + NO_3^- \rightarrow Ar + NO_2 + O$	1.00×10^{-07}	0	0		[170]
(426)	$Ar^+ + NO_3^- + M \rightarrow Ar + NO_3 + M$	2.00×10^{-25}	-2.5	0		[170]
(427)	$Ar_2^* + O_2 \rightarrow Ar + Ar + O + O$	4.60×10^{-11}	0	0	A,B	[272] y
(428)	$Ar_2^* + O_3 \rightarrow Ar + Ar + O_2 + O$	2.10×10^{-10}	0	0	A,B	v
(429)	$Ar_2^* + N_2 \rightarrow Ar + Ar + N_2(A)$	1.20×10^{-11}	0	0	A,B	[266] s

Nr	Reaction name	A^a	B^a	C^a	Set^b	Ref.
(430)	$Ar_2^* + NO \rightarrow Ar + Ar + N + O$	3.10×10^{-10}	0	0	A,B	[266]
(431)	$Ar_2^* + NO_2 \rightarrow Ar + Ar + NO + O$	8.44×10^{-10}	0	0	A,B	[266]
(432)	$Ar_2^* + N_2O \rightarrow Ar + Ar + N_2 + O$	5.50×10^{-10}	0	0	A,B	[266]
(433)	$Ar_2^+ + O^- \rightarrow Ar + Ar + O$	1.00×10^{-07}	0	0	A,B	[105,187]
(434)	$Ar_2^+ + O_2 \rightarrow Ar + Ar + O_2^+$	1.00×10^{-10}	0	0	A,B	[187,268]
(435)	$Ar_2^+ + O_2^- \rightarrow Ar + Ar + O_2$	1.00×10^{-07}	0	0	A,B	[105]
(436)	$Ar_2^+ + O_2^- \rightarrow Ar + Ar + O + O$	1.00×10^{-07}	0	0	A,B	[105]
(437)	$Ar_2^+ + O_3 \rightarrow Ar + Ar + O_2^+ + O$	5.00×10^{-09}	0	0	A,B	[272] z
(438)	$Ar_2^+ + NO \rightarrow Ar + Ar + NO^+$	4.40×10^{-11}	0	0	A	[190,271]
(439)	$Ar_2^+ + NO_2 \rightarrow Ar + Ar + NO^+ + O$	7.82×10^{-10}	0	0	A	[271]
(440)	$Ar_2^+ + NO_2 \rightarrow Ar + Ar + NO_2^+$	1.38×10^{-10}	0	0	A,B	[271]
(441)	$Ar_2^+ + NO_2^- \rightarrow Ar + Ar + NO_2$	1.00×10^{-07}	0	0	A,B	[105]
(442)	$Ar_2^+ + NO_2^- \rightarrow Ar + Ar + NO + O$	1.00×10^{-07}	0	0	A,B	[105]
(443)	$Ar_2^+ + NO_3^- \rightarrow Ar + Ar + NO_3$	1.00×10^{-07}	0	0	A,B	[105]
(444)	$Ar_2^+ + NO_3^- \rightarrow Ar + Ar + NO_2 + O$	1.00×10^{-07}	0	0	A,B	[105]
Oxygen heavy particle collisions						
(445)	$O + O + Ar \rightarrow O_2 + Ar$	5.21×10^{-35}	0	-900	A	g
(446)	$O + O + N_2 \rightarrow O_2 + N_2$	5.21×10^{-35}	0	-900		[112]
(447)	$O + O + O_2 \rightarrow O_2 + O_2$	5.21×10^{-35}	0	-900		g
(448)	$O + O + H_2 \rightarrow O_2 + H_2$	1.30×10^{-34}	0	-900		g
(449)	$O + O + O_3 \rightarrow O_2 + O_3$	1.30×10^{-34}	0	-900		g
(450)	$O + O + H_2O \rightarrow O_2 + H_2O$	2.60×10^{-34}	0	-900		g
(451)	$O + O + M \rightarrow O_2(a) + M$	6.93×10^{-35}	-0.63	0	A,B	[140,185]
(452)	$O + O + M \rightarrow O_2(b) + M$	6.93×10^{-35}	-0.63	0	A,B	aa

Nr	Reaction name	A^a	B^a	C^a	Set^b	Ref.
(453)	$O + O(^1D) + M \rightarrow O_2 + M$	9.90×10^{-33}	0	0		[184,274]
(454)	$O + O^+ + M \rightarrow O_2^+ + M$	1.00×10^{-29}	0	0	A,B	[140,170]
(455)	$O + O^- \rightarrow O_2 + e^-$	1.50×10^{-10}	0	0	A,B	[186,275]
(456)	$O + O_2 + Ar \rightarrow O_3 + Ar$	6.40×10^{-35}	0	-663	A,B	g
(457)	$O + O_2 + O_2 \rightarrow O_3 + O_2$	6.40×10^{-35}	0	-663	A	[170]
(458)	$O + O_2 + N_2 \rightarrow O_3 + N_2$	6.40×10^{-35}	0	-663	A,B	g
(459)	$O + O_2 + H_2 \rightarrow O_3 + H_2$	1.30×10^{-34}	0	-663		g
(460)	$O + O_2 + O_3 \rightarrow O_3 + O_3$	1.30×10^{-34}	0	-663		g
(461)	$O + O_2 + H_2O \rightarrow O_3 + H_2O$	3.20×10^{-34}	0	-663		g
(462)	$O + O_2^- \rightarrow O_2 + O^-$	1.50×10^{-10}	0.5	0	A,B	[140,185]
(463)	$O + O_2^- \rightarrow O_3 + e^-$	1.50×10^{-10}	0	0	A,B	[105,183]
(464)	$O + O_3 \rightarrow O_2 + O_2$	8.00×10^{-12}	0	2060	A,B	[112,280]
(465)	$O + O_3^- \rightarrow O_2^- + O_2$	3.20×10^{-10}	0	0	A,B	[105]
(466)	$O + O_3^- \rightarrow O_2 + O_2 + e^-$	3.00×10^{-10}	0	0	A,B	[105]
(467)	$O + O_4^+ \rightarrow O_3 + O_2^+$	3.00×10^{-10}	0	0	A,B	[105]
(468)	$O(^1D) + O_2 \rightarrow O_2(a) + O$	2.60×10^{-11}	0	-67	A,B	[274]
(469)	$O(^1D) + O_2 \rightarrow O_2(b) + O$	2.56×10^{-11}	0	-67	A,B	[140,170]
(470)	$O(^1D) + O_2^+ \rightarrow O_2(a) + O^+$	1.00×10^{-12}	-0.5	0		[121]
(471)	$O(^1D) + O_3 \rightarrow O_2 + O + O$	1.20×10^{-10}	0	0		[112,170]
(472)	$O(^1D) + O_3 \rightarrow O_2 + O_2$	2.40×10^{-10}	0	0		[170,280]
(473)	$O(^1D) + O_3 \rightarrow O_2(a) + O_2$	2.65×10^{-10}	0	0	A	[274]
(474)	$O(^1D) + O_3 \rightarrow O_2(b) + O_2$	7.20×10^{-12}	0	0		[270]
(475)	$O(^1D) + M \rightarrow M + O$	5.00×10^{-12}	0	0	A,B	[170,185]
(476)	$O^+ + O^- \rightarrow O + O$	2.70×10^{-07}	-0.5	0	A	[170]

223

Nr	Reaction name	A^a	B^a	C^a	Set^b	Ref.
(477)	$O^+ + O^- + M \rightarrow O + O + M$	2.00×10^{-25}	-2.5	0	A	[105,140]
(478)	$O^+ + O_2 \rightarrow O + O_2^+$	2.10×10^{-11}	0	0	A,B	[170,180]
(479)	$O^+ + O_2(a) \rightarrow O + O_2^+$	2.10×10^{-11}	0	0		[170]
(480)	$O^+ + O_2(b) \rightarrow O + O_2^+$	2.10×10^{-11}	0	0		[170]
(481)	$O^+ + O_2^- \rightarrow O + O_2$	2.70×10^{-07}	-0.5	0		[121,183]
(482)	$O^+ + O_2^- \rightarrow O + O + O$	1.00×10^{-07}	0	0		[105]
(483)	$O^+ + O_2^- + M \rightarrow O + O + O_2 + M$	2.00×10^{-25}	-2.5	0		[105,270]
(484)	$O^+ + O_2^- + M \rightarrow O + O_3 + M$	2.00×10^{-25}	-2.5	0		[105]
(485)	$O^+ + O_3 \rightarrow O_2 + O_2^+$	1.00×10^{-10}	0	0		[170,191]
(486)	$O^+ + O_3^- \rightarrow O_3 + O$	2.00×10^{-07}	-0.5	0		[105]
(487)	$O^+ + O_3^- \rightarrow O_2 + O + O$	1.00×10^{-07}	0	0		[105]
(488)	$O^+ + O_3^- + M \rightarrow O_3 + O + M$	2.00×10^{-25}	-2.5	0	A	[105]
(489)	$O^- + O_2 \rightarrow O_3 + e^-$	5.00×10^{-15}	0	0		[170,183]
(490)	$O^- + O_2 \rightarrow O_2^- + O$	1.00×10^{-10}	0	0	A,B	[184]
(491)	$O^- + O_2 + M \rightarrow O_3^- + M$	1.10×10^{-30}	-1	0	A,B	[105]
(492)	$O^- + O_2(a) \rightarrow O_3 + e^-$	3.00×10^{-10}	0	0	A,B	[170,183]
(493)	$O^- + O_2(a) \rightarrow O_2^- + O$	1.00×10^{-10}	0	0	A	[105,183]
(494)	$O^- + O_2(b) \rightarrow O_2 + e^- + O$	6.90×10^{-10}	0	0		[140,170]
(495)	$O^- + O_2^+ \rightarrow O + O_2$	1.50×10^{-07}	-0.5	0	A	[170,184]
(496)	$O^- + O_2^+ \rightarrow O + O + O$	1.00×10^{-07}	0	0	A	[105,140]
(497)	$O^- + O_2^+ + M \rightarrow O + O_2 + M$	2.00×10^{-25}	-2.5	0	A,B	[105,270]
(498)	$O^- + O_3 \rightarrow O_2 + O_2 + e^-$	5.30×10^{-10}	0	0		[183]
(499)	$O^- + O_3 \rightarrow O_2 + O_2^-$	1.00×10^{-10}	0.5	0		[185,273]
(500)	$O^- + O_3 \rightarrow O + O_3^-$	5.30×10^{-10}	0	0	A	[105]

Nr	Reaction name	A^a	B^a	C^a	Set^b	Ref.
(501)	$O^- + O_4^+ \rightarrow O + O_2 + O_2$	1.00×10^{-07}	0	0		[105]
(502)	$O^- + O_4^+ + M \rightarrow O + O_2 + O_2 + M$	2.00×10^{-25}	-2.5	0		[105]
(503)	$O_2 + O_2(a) \rightarrow O_3 + O$	3.00×10^{-21}	0	0		[121,140]
(504)	$O_2 + O_2^+ + M \rightarrow O_4^+ + M$	2.40×10^{-30}	-3.2	0	A,B	[105]
(505)	$O_{2,vib} + N_2 \rightarrow O_2 + N_2$	1.00×10^{-13}	0	0	A,B	ab
(506)	$O_{2,vib} + O_2 \rightarrow O_2 + O_2$	1.00×10^{-13}	0	0	A	ab
(507)	$O_{2,vib} + O_3 \rightarrow O_2 + O_3$	1.00×10^{-13}	0	0		ab
(508)	$O_{2,vib} + Ar \rightarrow O_2 + Ar$	1.00×10^{-13}	0	0	A,B	ab
(509)	$O_{2,vib} + H_2 \rightarrow O_2 + H_2$	1.00×10^{-13}	0	0		ab
(510)	$O_{2,vib} + O_3 \rightarrow O_2 + O_3$	1.00×10^{-13}	0	0		ab
(511)	$O_{2,vib} + H_2O \rightarrow O_2 + H_2O$	1.00×10^{-13}	0	0		ab
(512)	$O_{2,rot} + N_2 \rightarrow O_2 + N_2$	1.00×10^{-13}	0	0	A,B	ab
(513)	$O_{2,rot} + O_2 \rightarrow O_2 + O_2$	1.00×10^{-13}	0	0	A	ab
(514)	$O_{2,rot} + O_3 \rightarrow O_2 + O_3$	1.00×10^{-13}	0	0		ab
(515)	$O_{2,rot} + Ar \rightarrow O_2 + Ar$	1.00×10^{-13}	0	0	A,B	ab
(516)	$O_{2,rot} + H_2 \rightarrow O_2 + H_2$	1.00×10^{-13}	0	0		ab
(517)	$O_{2,rot} + O_3 \rightarrow O_2 + O_3$	1.00×10^{-13}	0	0		ab
(518)	$O_{2,rot} + H_2O \rightarrow O_2 + H_2O$	1.00×10^{-13}	0	0		ab
(519)	$O_2(a) + O_2(a) \rightarrow O_2 + O_2$	9.00×10^{-17}	0	560		[140,185]
(520)	$O_2(a) + O_2(a) \rightarrow O_2(b) + O_2$	1.80×10^{-19}	3.8	-700	A,B	[170]
(521)	$O_2(a) + O_2^- \rightarrow O_2 + O_2 + e^-$	2.00×10^{-10}	0	0	A,B	[105,121]
(522)	$O_2(a) + O_3 \rightarrow O_2 + O_2 + O$	1.00×10^{-14}	0	0	A,B	[274]
(523)	$O_2(a) + O_4^+ \rightarrow O_2 + O_2^+ + O_2$	1.00×10^{-10}	0	0		[105]
(524)	$O_2(a) + O_2 \rightarrow O_2 + O_2$	3.00×10^{-18}	0	200		[112,188]

Nr	Reaction name	A^a	B^a	C^a	Set[b]	Ref.
(525)	$O_2(a) + Ar \rightarrow O_2 + Ar$	3.00×10^{-18}	0	200	A,B	g
(526)	$O_2(a) + N_2 \rightarrow O_2 + N_2$	3.00×10^{-18}	0	200	A	g
(527)	$O_2(a) + H_2 \rightarrow O_2 + H_2$	6.00×10^{-18}	0	200		g
(528)	$O_2(a) + H_2O \rightarrow O_2 + H_2O$	1.50×10^{-17}	0	200		g
(529)	$O_2(a) + O_3 \rightarrow O_2 + O_3$	6.00×10^{-18}	0	200		g
(530)	$O_2(b) + O_2(b) \rightarrow O_2(a) + O_2$	3.60×10^{-17}	0.5	0		[140,185]
(531)	$O_2(b) + O_2^- \rightarrow O_2 + O_2 + e^-$	3.60×10^{-10}	0	0		[105,121]
(532)	$O_2(b) + O_3 \rightarrow O_2(a) + O_2 + O$	1.00×10^{-14}	0	0		[274]
(533)	$O_2(b) + O_4^+ \rightarrow O_2 + O_2^+ + O_2$	1.00×10^{-10}	0	0		[105]
(534)	$O_2(b) + O_2 \rightarrow O_2 + O_2$	3.79×10^{-16}	2.4	241		[274]
(535)	$O_2(b) + O \rightarrow O_2 + O$	8.00×10^{-15}	0.5	0		[140,185]
(536)	$O_2(b) + H \rightarrow O_2 + H$	8.00×10^{-15}	0.5	0		ac
(537)	$O_2(b) + N_2 \rightarrow O_2 + N_2$	4.90×10^{-15}	0	253		[274]
(538)	$O_2(b) + H_2O \rightarrow O_2 + H_2O$	2.30×10^{-12}	0	0	A,B	[112,188]
(539)	$O_2(b) + H_2 \rightarrow O_2 + H_2$	4.90×10^{-15}	0	253		ad
(540)	$O_2(b) + O_3 \rightarrow O_2 + O_3$	2.20×10^{-11}	0	0	A,B	[112,188]
(541)	$O_2(b) + Ar \rightarrow O_2 + Ar$	1.00×10^{-16}	0	0	A	[170]
(542)	$O_2(b) + O_2 \rightarrow O_2(a) + O_2$	3.73×10^{-16}	2.4	241		[183]
(543)	$O_2(b) + O \rightarrow O_2(a) + O$	7.20×10^{-14}	0.5	0		[140,185]
(544)	$O_2(b) + H \rightarrow O_2(a) + H$	7.20×10^{-14}	0.5	0		[140,185]
(545)	$O_2(b) + N_2 \rightarrow O_2(a) + N_2$	4.90×10^{-15}	0	253		[183,277]
(546)	$O_2(b) + H_2O \rightarrow O_2(a) + H_2O$	2.30×10^{-12}	0	0	A,B	[112,277]
(547)	$O_2(b) + H_2 \rightarrow O_2(a) + H_2$	4.90×10^{-15}	0	253		ae
(548)	$O_2(b) + O_3 \rightarrow O_2(a) + O_3$	2.20×10^{-11}	0	0	A,B	[112,277]

Nr	Reaction name	A^a	B^a	C^a	Set^b	Ref.
(549)	$O_2(b) + NO \rightarrow O_2(a) + NO$	4.00×10^{-14}	0	0		[183]
(550)	$O_2(b) + Ar \rightarrow O_2(a) + Ar$	6.00×10^{-16}	0	0	A,B	[170]
(551)	$O_2^+ + O_2^- \rightarrow O_2 + O_2$	1.00×10^{-07}	-0.5	0		[105,183]
(552)	$O_2^+ + O_2^- \rightarrow O_2 + O + O$	1.00×10^{-07}	0	0		[105,140]
(553)	$O_2^+ + O_2^- \rightarrow O + O + O + O$	1.00×10^{-07}	0	0		[105]
(554)	$O_2^+ + O_2^- + M \rightarrow O_2 + O_2 + M$	1.00×10^{-24}	-2.5	0	A,B	[105,270]
(555)	$O_2^+ + O_3^- \rightarrow O_3 + O_2$	2.00×10^{-07}	-0.5	0	A	[105]
(556)	$O_2^+ + O_3^- \rightarrow O_2 + O + O_2$	1.00×10^{-07}	0	0	A	[105]
(557)	$O_2^+ + O_3^- \rightarrow O_2 + O + O + O$	1.00×10^{-07}	0	0	A	[105]
(558)	$O_2^+ + O_3^- + M \rightarrow O_3 + O_2 + M$	2.00×10^{-25}	-2.5	0	A,B	[105]
(559)	$O_2^- + O_3 \rightarrow O_2 + O_3^-$	4.00×10^{-10}	0	0	A,B	[105]
(560)	$O_2^- + O_4^+ \rightarrow O_2 + O_2 + O_2$	1.00×10^{-07}	0	0		[105]
(561)	$O_2^- + O_4^+ \rightarrow O + O + O_2 + O_2$	1.00×10^{-07}	0	0		[105]
(562)	$O_2^- + O_4^+ + M \rightarrow O_2 + O_2 + O_2 + M$	2.00×10^{-25}	-2.5	0		[105]
(563)	$O_2^- + M \rightarrow O_2 + e^- + M$	2.70×10^{-10}	0.5	5590	A,B	[105,183]
(564)	$O_3 + O_3 \rightarrow O_2 + O_2 + O_2$	7.47×10^{-12}	0	9310		[283]
(565)	$O_3 + Ar \rightarrow O + O_2 + Ar$	7.30×10^{-10}	0	11400	A	[170]
(566)	$O_3 + N_2 \rightarrow O + O_2 + N_2$	7.30×10^{-10}	0	11400	A,B	[170]
(567)	$O_3 + O_2 \rightarrow O + O_2 + O_2$	7.30×10^{-10}	0	11400	A	g
(568)	$O_3 + O_3 \rightarrow O + O_2 + O_3$	1.40×10^{-09}	0	11400		g
(569)	$O_3 + H_2 \rightarrow O + O_2 + H_2$	1.40×10^{-09}	0	11400		g
(570)	$O_3 + H_2O \rightarrow O + O_2 + H_2O$	4.00×10^{-09}	0	11400		g
(571)	$O_3^- + O_4^+ \rightarrow O_3 + O_2 + O_2$	1.00×10^{-07}	0	0		[105]
(572)	$O_3^- + O_4^+ \rightarrow O + O_2 + O_2 + O_2$	1.00×10^{-07}	0	0		[105]

Nr	Reaction name	A^a	B^a	C^a	Set^b	Ref.
(573)	$O_3^- + O_4^+ + M \rightarrow O_2^- + O_2 + O_2 + O + M$	2.00×10^{-25}	-2.5	0		[105]
(574)	$O_4^+ + M \rightarrow O_2^+ + O_2 + M$	3.30×10^{-06}	-2.5	2650	A,B	[105]
	Nitrogen heavy particle collisions					
(575)	$N + N + Ar \rightarrow N_2 + Ar$	1.38×10^{-34}	0	-500		g
(576)	$N + N + N_2 \rightarrow N_2 + N_2$	1.38×10^{-34}	0	-500		[284]
(577)	$N + N + O_2 \rightarrow N_2 + O_2$	1.38×10^{-34}	0	-500		[284]
(578)	$N + N + H_2O \rightarrow N_2 + H_2O$	6.50×10^{-34}	0	-500		g
(579)	$N + N + H_2 \rightarrow N_2 + H_2$	2.50×10^{-34}	0	-500		g
(580)	$N + N + O_3 \rightarrow N_2 + O_3$	2.50×10^{-34}	0	-500		g
(581)	$N + N^+ + M \rightarrow N_2^+ + M$	1.00×10^{-29}	0	0		[105,171]
(582)	$N + N_2^+ \rightarrow N_2 + N^+$	7.20×10^{-13}	1	0		[105,171]
(583)	$N + N_2^+ + M \rightarrow M + N_3^+$	9.00×10^{-30}	1	-400	A,B	[171]
(584)	$N + N_3^+ \rightarrow N_2^+ + N_2$	6.60×10^{-11}	0	0		[171]
(585)	$N + N_4^+ \rightarrow N_2 + N_2 + N^+$	1.00×10^{-11}	0	0		[171,270]
(586)	$N(^2D) + N_2^+ \rightarrow N^+ + N_2$	1.00×10^{-10}	0	0		[269]
(587)	$N(^2D) + M \rightarrow N + M$	2.40×10^{-14}	0	0	A,B	[111,179]
(588)	$N^+ + N_2 \rightarrow N + N_2^+$	4.45×10^{-10}	0	0	A,B	[171]
(589)	$N^+ + N_2 + M \rightarrow N_3^+ + M$	9.00×10^{-30}	0	-400	A,B	[171]
(590)	$N_2 + N_2^+ + M \rightarrow N_4^+ + M$	6.80×10^{-29}	-1.64	0	A,B	[171,185]
(591)	$N_{2,rot} + N_2 \rightarrow N_2 + N_2$	1.00×10^{-13}	0	0	A,B	ab
(592)	$N_{2,rot} + N \rightarrow N_2 + N$	1.00×10^{-13}	0	0		ab
(593)	$N_{2,rot} + O_2 \rightarrow N_2 + O_2$	1.00×10^{-13}	0	0	A	ab
(594)	$N_{2,rot} + O_3 \rightarrow N_2 + O_3$	1.00×10^{-13}	0	0		ab
(595)	$N_{2,rot} + O \rightarrow N_2 + O$	1.00×10^{-13}	0	0		ab

Nr	Reaction name	A^a	B^a	C^a	Set^b	Ref.
(596)	$N_{2,rot} + H_2O \rightarrow N_2 + H_2O$	1.00×10^{-13}	0	0		ab
(597)	$N_{2,rot} + H_2 \rightarrow N_2 + H_2$	1.00×10^{-13}	0	0		ab
(598)	$N_{2,rot} + Ar \rightarrow N_2 + Ar$	1.00×10^{-13}	0	0	A,B	ab
(599)	$N_{2,vib} + N_2 \rightarrow N_2 + N_2$	1.00×10^{-13}	0	0	A,B	ab
(600)	$N_{2,vib} + N \rightarrow N_2 + N$	1.00×10^{-13}	0	0		ab
(601)	$N_{2,vib} + O_2 \rightarrow N_2 + O_2$	1.00×10^{-13}	0	0	A	ab
(602)	$N_{2,vib} + O_3 \rightarrow N_2 + O_3$	1.00×10^{-13}	0	0		ab
(603)	$N_{2,vib} + O \rightarrow N_2 + O$	1.00×10^{-13}	0	0		ab
(604)	$N_{2,vib} + H_2O \rightarrow N_2 + H_2O$	1.00×10^{-13}	0	0		ab
(605)	$N_{2,vib} + H_2 \rightarrow N_2 + H_2$	1.00×10^{-13}	0	0		ab
(606)	$N_{2,vib} + Ar \rightarrow N_2 + Ar$	1.00×10^{-13}	0	0	A,B	ab
(607)	$N_2(A) + N_2(a') \rightarrow N_4^+ + e^-$	9.00×10^{-12}	0	0	A,B	[171]
(608)	$N_2(A) + N_2(a') \rightarrow N_2^+ + N_2 + e^-$	1.00×10^{-12}	0	0		[171]
(609)	$N_2(A) + Ar \rightarrow N_2 + Ar$	4.00×10^{-17}	0	0		[285]
(610)	$N_2(A) + N_2 \rightarrow N_2 + N_2$	3.70×10^{-16}	0	0		[179, 184]
(611)	$N_2(A) + O_2 \rightarrow N_2 + O_2$	8.10×10^{-13}	0	0	A	[179]
(612)	$N_2(A) + O_2(a) \rightarrow N_2 + O_2 + O_2(a)$	8.10×10^{-13}	0	0		af
(613)	$N_2(A) + O \rightarrow N_2 + O$	2.70×10^{-11}	0	0	A,B	[184, 191]
(614)	$N_2(A) + NO \rightarrow N_2 + NO$	1.50×10^{-10}	0	0	A	[279]
(615)	$N_2(A) + H \rightarrow N_2 + H$	2.10×10^{-10}	0	0	A	[110]
(616)	$N_2(A) + N_2O \rightarrow N_2 + N_2O$	1.70×10^{-10}	0	0		[187, 279]
(617)	$N_2(A) + H_2 \rightarrow N_2 + H_2$	2.10×10^{-10}	0	0		[110]
(618)	$N_2(A) + H_2O \rightarrow N_2 + H_2O$	2.10×10^{-10}	0	0	A,B	[110]
(619)	$N_2(A) + N \rightarrow N_2 + N$	2.00×10^{-11}	0	0		[183]

Nr	Reaction name	A^a	B^a	C^a	Set^b	Ref.
(620)	$N_2(A) + N_2(A) \rightarrow N_2 + N_2(A)$	2.00×10^{-12}	0	0		[184]
(621)	$N_2(a') + N_2(a') \rightarrow N_4^+ + e^-$	1.00×10^{-11}	0	0		[183]
(622)	$N_2(a') + N_2(a') \rightarrow N_2^+ + N_2 + e^-$	5.00×10^{-13}	0	0		[171]
(623)	$N_2(a') + Ar \rightarrow N_2 + Ar$	4.00×10^{-17}	0	0		ag
(624)	$N_2(a') + N_2 \rightarrow N_2 + N_2$	3.70×10^{-16}	0	0		ag
(625)	$N_2(a') + O_2 \rightarrow N_2 + O_2$	8.10×10^{-13}	0	0		ag
(626)	$N_2(a') + O_2(a) \rightarrow N_2 + O_2 + O_2(a)$	8.10×10^{-13}	0	0		ag
(627)	$N_2(a') + O \rightarrow N_2 + O$	2.70×10^{-11}	0	0	A	ag
(628)	$N_2(a') + NO \rightarrow N_2 + NO$	1.50×10^{-10}	0	0		ag
(629)	$N_2(a') + H \rightarrow N_2 + H$	2.10×10^{-10}	0	0	A	ag
(630)	$N_2(a') + N_2O \rightarrow N_2 + N_2O$	1.70×10^{-10}	0	0		ag
(631)	$N_2(a') + H_2 \rightarrow N_2 + H_2$	2.10×10^{-10}	0	0		ag
(632)	$N_2(a') + H_2O \rightarrow N_2 + H_2O$	2.10×10^{-10}	0	0	A,B	ag
(633)	$N_2(a') + N \rightarrow N_2 + N$	2.00×10^{-11}	0	0		ag
(634)	$N_2(a') + N_2(a') \rightarrow N_2 + N_2(a')$	2.00×10^{-12}	0	0		ag
(635)	$N_3^+ + M \rightarrow M + N + N_2^+$	6.60×10^{-11}	0	0	A,B	[171]
(636)	$N_4^+ + M \rightarrow N_2^+ + M + N_2$	2.50×10^{-15}	0	0		[105]
(637)	$N_4^+ + Ar \rightarrow Ar^+ + N_2 + N_2$	1.00×10^{-11}	0	0	A,B	[171]
Dry air heavy particle collisions						
(638)	$O + N + Ar \rightarrow NO + Ar$	1.02×10^{-32}	-0.5	0	A	g
(639)	$O + N + N_2 \rightarrow NO + N_2$	1.02×10^{-32}	-0.5	0		[183]
(640)	$O + N + O_2 \rightarrow NO + O_2$	1.02×10^{-32}	-0.5	0		[183]
(641)	$O + N + H_2 \rightarrow NO + H_2$	2.02×10^{-32}	-0.5	0		g
(642)	$O + N + H_2O \rightarrow NO + H_2O$	5.02×10^{-32}	-0.5	0		g

Nr	Reaction name	A^a	B^a	C^a	Set^b	Ref.
(643)	$O + N + O_3 \rightarrow NO + O_3$	2.02×10^{-32}	-0.5	0		g
(644)	$O + N(^2D) \rightarrow N + O(^1D)$	2.80×10^{-13}	0	0		[110]
(645)	$O + N^+ \rightarrow N + O^+$	1.08×10^{-12}	0	0		[105, 191]
(646)	$O + N^+ + M \rightarrow NO^+ + M$	1.00×10^{-29}	0	0	A	[105, 191]
(647)	$O + N_2(A) \rightarrow NO + N$	7.00×10^{-12}	0	0	A,B	[105, 191]
(648)	$O + N_2(A) \rightarrow NO + N(^2D)$	1.00×10^{-12}	0	0	A,B	[105]
(649)	$O + N_2(a') \rightarrow NO + N$	7.00×10^{-12}	0	0		ah
(650)	$O + N_2(a') \rightarrow NO + N(^2D)$	1.00×10^{-12}	0	0	A,B	ai
(651)	$O + N_2^+ \rightarrow N + NO^+$	1.30×10^{-10}	-0.5	0	A,B	[105, 186]
(652)	$O + N_2^+ \rightarrow N_2 + O^+$	1.00×10^{-11}	-0.2	0	A,B	[105, 276]
(653)	$O + N_4^+ \rightarrow N_2 + N_2 + O^+$	2.50×10^{-10}	0	0	A,B	[183]
(654)	$O + NO \rightarrow N + O_2$	9.00×10^{-13}	1	19500		[274]
(655)	$O + NO + Ar \rightarrow NO_2 + Ar$	1.00×10^{-31}	-1.6	0	A,B	g
(656)	$O + NO + N_2 \rightarrow NO_2 + N_2$	1.00×10^{-31}	-1.6	0	A	[183]
(657)	$O + NO + O_2 \rightarrow NO_2 + O_2$	1.00×10^{-31}	-1.6	0		[183]
(658)	$O + NO + H_2 \rightarrow NO_2 + H_2$	2.00×10^{-31}	-1.6	0		g
(659)	$O + NO + H_2O \rightarrow NO_2 + H_2O$	5.00×10^{-31}	-1.6	0		g
(660)	$O + NO + O_3 \rightarrow NO_2 + O_3$	2.00×10^{-31}	-1.6	0		g
(661)	$O + NO_2 \rightarrow NO + O_2$	6.50×10^{-12}	0	-120	A,B	[180, 280]
(662)	$O + NO_2 + Ar \rightarrow NO_3 + Ar$	9.00×10^{-32}	-2	0	A,B	g
(663)	$O + NO_2 + N_2 \rightarrow NO_3 + N_2$	9.00×10^{-32}	-2	0	A,B	[183]
(664)	$O + NO_2 + O_2 \rightarrow NO_3 + O_2$	9.00×10^{-32}	-2	0	A	[183]
(665)	$O + NO_2 + H_2 \rightarrow NO_3 + H_2$	2.00×10^{-31}	-2	0		g
(666)	$O + NO_2 + H_2O \rightarrow NO_3 + H_2O$	5.00×10^{-31}	-2	0		g

231

Nr	Reaction name	A^a	B^a	C^a	Set^b	Ref.
(667)	$O + NO_2 + O_3 \rightarrow NO_3 + O_3$	2.00×10^{-31}	-2	0		g
(668)	$O + NO_2^+ \rightarrow NO^+ + O_2$	8.00×10^{-12}	0	0	A,B	[186]
(669)	$O + NO_2^- \rightarrow NO_3 + e^-$	1.00×10^{-11}	0	0	A,B	[276]
(670)	$O + N_2O \rightarrow N_2 + O_2$	1.66×10^{-10}	0	14100		[180]
(671)	$O + N_2O \rightarrow NO + NO$	1.15×10^{-10}	0	13400		[180]
(672)	$O + NO_3 \rightarrow NO_2 + O_2$	1.70×10^{-11}	0	0	A,B	[111, 112]
(673)	$O + NO_3^- \rightarrow NO_2 + O_2^-$	2.50×10^{-12}	0	0	A,B	[186, 276] aj
(674)	$O + NO_3^- \rightarrow NO_2^- + O_2$	2.50×10^{-12}	0	0	A,B	[186, 276] aj
(675)	$O + NO_3^- \rightarrow NO_2 + O_2 + e^-$	2.50×10^{-12}	0	0	A,B	[186, 276] aj
(676)	$O + N_2O_5 \rightarrow N_2 + O_2 + O_2 + O_2 + O_2$	3.00×10^{-16}	0.5	0		[183, 277]
(677)	$O(^1D) + N_2 + Ar \rightarrow N_2O + Ar$	2.80×10^{-36}	0	0		g
(678)	$O(^1D) + N_2 + N_2 \rightarrow N_2O + N_2$	2.80×10^{-36}	0	0		[188]
(679)	$O(^1D) + N_2 + O_2 \rightarrow N_2O + O_2$	2.80×10^{-36}	0	0		g
(680)	$O(^1D) + N_2 + H_2 \rightarrow N_2O + H_2$	5.00×10^{-36}	0	0		g
(681)	$O(^1D) + N_2 + H_2O \rightarrow N_2O + H_2O$	1.00×10^{-35}	0	0		g
(682)	$O(^1D) + N_2 + O_3 \rightarrow N_2O + O_3$	5.00×10^{-36}	0	0		g
(683)	$O(^1D) + NO \rightarrow O_2 + N$	1.70×10^{-10}	0	0	A,B	[105, 184]
(684)	$O(^1D) + NO_2 \rightarrow O_2 + NO$	3.00×10^{-10}	0	0		[187, 278]
(685)	$O(^1D) + N_2O \rightarrow NO + NO$	8.22×10^{-11}	0	0		[280, 292]
(686)	$O(^1D) + N_2O \rightarrow O_2 + N_2$	4.93×10^{-11}	0	0		[277, 292]
(687)	$O(^1D) + N_2O \rightarrow O + N_2O$	5.48×10^{-12}	0	0		[292]
(688)	$O^+ + N + M \rightarrow NO^+ + M$	1.00×10^{-29}	0	0		[105]
(689)	$O^+ + N(^2D) \rightarrow N^+ + O$	1.30×10^{-10}	0	0	A	[105]
(690)	$O^+ + N_2 \rightarrow NO^+ + N$	3.00×10^{-12}	0	0.0031		[105, 191]

Nr	Reaction name	A^a	B^a	C^a	Set^b	Ref.
(691)	$O^+ + N_2 + M \rightarrow NO^+ + N + M$	6.00×10^{-29}	-2	0	A,B	[105,186]
(692)	$O^+ + NO \rightarrow O_2^+ + N$	3.00×10^{-12}	0	0		[105,183]
(693)	$O^+ + NO \rightarrow NO^+ + O$	2.40×10^{-11}	0	0		[105,183]
(694)	$O^+ + NO_2 \rightarrow NO_2^+ + O$	1.60×10^{-09}	0	0	A	[105,183]
(695)	$O^+ + NO_2 \rightarrow NO^+ + O_2$	5.00×10^{-10}	0	0		[191]
(696)	$O^+ + NO_2^- \rightarrow NO_2 + O$	2.00×10^{-07}	-0.5	0		[105]
(697)	$O^+ + NO_2^- \rightarrow NO + O + O$	1.00×10^{-07}	0	0		[105]
(698)	$O^+ + NO_2^- + M \rightarrow NO_2 + O + M$	2.00×10^{-25}	-2.5	0		[105]
(699)	$O^+ + NO_2^- + M \rightarrow NO_3 + M$	2.00×10^{-25}	-2.5	0	A	[105]
(700)	$O^+ + N_2O \rightarrow NO^+ + NO$	2.30×10^{-10}	0	0		[105,186]
(701)	$O^+ + N_2O \rightarrow O_2^+ + N_2$	2.00×10^{-11}	0	0		[105,183]
(702)	$O^+ + NO_3^- \rightarrow NO_3 + O$	2.00×10^{-07}	-0.5	0		[177]
(703)	$O^+ + NO_3^- \rightarrow NO_2 + O + O$	1.00×10^{-07}	0	0		[105]
(704)	$O^+ + NO_3^- + M \rightarrow NO_3 + O + M$	2.00×10^{-25}	-2.5	0		[105]
(705)	$O^- + N \rightarrow NO + e^-$	2.60×10^{-10}	0	0		[105,180]
(706)	$O^- + N^+ \rightarrow N + O$	2.00×10^{-07}	-0.5	0		[105]
(707)	$O^- + N^+ + M \rightarrow NO + M$	2.00×10^{-25}	-2.5	0	A	[105]
(708)	$O^- + N^+ + M \rightarrow N + O + M$	2.00×10^{-25}	-2.5	0	A	[105]
(709)	$O^- + N_2 \rightarrow N_2O + e^-$	1.00×10^{-12}	0	0	A,B	[105,186]
(710)	$O^- + N_2(A) \rightarrow N_2 + O + e^-$	2.20×10^{-09}	0	0	A,B	[105,183]
(711)	$O^- + N_2(a') \rightarrow N_2 + O + e^-$	1.90×10^{-09}	0	0		[105]
(712)	$O^- + N_2^+ \rightarrow N_2 + O$	2.00×10^{-07}	-0.5	0		[105]
(713)	$O^- + N_2^+ \rightarrow N + N + O$	1.00×10^{-07}	0	0		[105]
(714)	$O^- + N_2^+ + M \rightarrow N_2 + O + M$	2.00×10^{-25}	-2.5	0	A	[105]

Nr	Reaction name	A^a	B^a	C^a	Set^b	Ref.
(715)	$O^- + N_2^+ + M \rightarrow N_2O + M$	2.00×10^{-25}	-2.5	0	A,B	[105]
(716)	$O^- + N_3^+ \rightarrow N + N_2 + O$	1.00×10^{-07}	0	0		[105]
(717)	$O^- + N_4^+ \rightarrow N_2 + N_2 + O$	1.00×10^{-07}	0	0		[105]
(718)	$O^- + NO \rightarrow NO_2 + e^-$	2.60×10^{-10}	0	0	A,B	[105,180]
(719)	$O^- + NO + M \rightarrow NO_2^- + M$	1.00×10^{-29}	0	0	A,B	[105]
(720)	$O^- + NO^+ \rightarrow O + NO$	2.00×10^{-07}	-0.5	0	A	[105,184]
(721)	$O^- + NO^+ \rightarrow N + O + O$	1.00×10^{-07}	0	0		[105]
(722)	$O^- + NO^+ + M \rightarrow O + NO + M$	2.00×10^{-25}	-2.5	0	A,B	[105]
(723)	$O^- + NO^+ + M \rightarrow NO_2 + M$	2.00×10^{-25}	-2.5	0	A,B	[105,183]
(724)	$O^- + NO_2 \rightarrow NO_2^- + O$	1.20×10^{-09}	0	0	A,B	[105,186]
(725)	$O^- + NO_2^+ \rightarrow NO_2 + O$	2.00×10^{-07}	-0.5	0		[105]
(726)	$O^- + NO_2^+ \rightarrow NO + O + O$	1.00×10^{-07}	0	0		[105]
(727)	$O^- + NO_2^+ + M \rightarrow O + NO_2 + M$	2.00×10^{-25}	-2.5	0	A,B	[105]
(728)	$O^- + NO_2^+ + M \rightarrow NO_3 + M$	2.00×10^{-25}	-2.5	0	A,B	[105]
(729)	$O_2 + N \rightarrow NO + O$	3.30×10^{-12}	1	3150	A,B	[105,180]
(730)	$O_2 + N(^2D) \rightarrow NO + O$	1.50×10^{-12}	0.5	0	A	[105,183]
(731)	$O_2 + N(^2D) \rightarrow NO + O(^1D)$	6.00×10^{-12}	0.5	0	A,B	[105]
(732)	$O_2 + N^+ \rightarrow N + O_2^+$	2.80×10^{-10}	0	0	A,B	[105,180]
(733)	$O_2 + N^+ \rightarrow NO^+ + O$	2.50×10^{-10}	0	0	A,B	[105,180]
(734)	$O_2 + N^+ \rightarrow NO + O^+$	2.80×10^{-11}	0	0	A,B	[105,186]
(735)	$O_2 + N_2 \rightarrow N_2O + O$	1.00×10^{-10}	0	55200		[180]
(736)	$O_2 + N_2(A) \rightarrow N_2 + O + O$	2.54×10^{-12}	0	0	A,B	[105,111]
(737)	$O_2 + N_2(A) \rightarrow N_2 + O_2(a)$	1.29×10^{-12}	0	0	A,B	[105,184]
(738)	$O_2 + N_2(A) \rightarrow N_2 + O_2(b)$	1.29×10^{-12}	0	0	A,B	[105,277]

Nr	Reaction name	A^a	B^a	C^a	Set^b	Ref.
(739)	$O_2 + N_2(A) \rightarrow N_2O + O$	7.80×10^{-14}	0	0	A,B	[105,183]
(740)	$O_2 + N_2(A) \rightarrow N_2O + O(^1D)$	3.00×10^{-14}	0	0	A,B	[279]
(741)	$O_2 + N_2(a') \rightarrow N_2 + O + O$	2.80×10^{-11}	0	0	A,B	[105,191]
(742)	$O_2 + N_2^+ \rightarrow N_2 + O_2^+$	6.00×10^{-11}	-0.5	0	A,B	[105,186]
(743)	$O_2 + N_2^+ \rightarrow NO + NO^+$	1.00×10^{-17}	0	0		[191,276]
(744)	$O_2 + N_3^+ \rightarrow NO^+ + N_2O$	3.60×10^{-11}	0	0	A	[179]
(745)	$O_2 + N_3^+ \rightarrow NO_2^+ + N_2$	1.50×10^{-11}	0	0	A,B	[179]
(746)	$O_2 + N_4^+ \rightarrow N_2 + N_2 + O_2^+$	2.50×10^{-10}	0	0	A,B	[105,113]
(747)	$O_2 + NO \rightarrow NO_2 + O$	2.80×10^{-12}	0	23400		[180]
(748)	$O_2 + NO + NO \rightarrow NO_2 + NO_2$	1.40×10^{-38}	0	0		[179,280]
(749)	$O_2 + NO_3 \rightarrow NO_2 + O_3$	1.00×10^{-17}	0	0	A,B	[112]
(750)	$O_2(a) + N \rightarrow O + NO$	2.00×10^{-14}	0	600	A,B	[105,183]
(751)	$O_2(a) + N_2(A) \rightarrow N_2 + O + O$	2.00×10^{-11}	0	0	A,B	[110,111]
(752)	$O_2(a) + NO \rightarrow O + NO_2$	4.88×10^{-18}	0	0		[283]
(753)	$O_2(b) + N \rightarrow O + NO$	2.00×10^{-14}	0	600		ak
(754)	$O_2(b) + N_2(A) \rightarrow N_2 + O + O$	2.00×10^{-11}	0	0	A,B	al
(755)	$O_2(b) + NO \rightarrow O + NO_2$	4.88×10^{-18}	0	0		am
(756)	$O_2^+ + N \rightarrow NO^+ + O$	1.20×10^{-10}	0	0	A,B	[105,186]
(757)	$O_2^+ + N_2 \rightarrow NO^+ + NO$	1.00×10^{-17}	0	0		[105,186]
(758)	$O_2^+ + NO \rightarrow NO^+ + O_2$	4.40×10^{-10}	0	0	A,B	[105,180]
(759)	$O_2^+ + NO_2 \rightarrow NO_2^+ + O_2$	6.60×10^{-10}	0	0	A,B	[105,191]
(760)	$O_2^+ + NO_2 \rightarrow O_3 + NO^+$	1.00×10^{-11}	0	0	A,B	[105,184]
(761)	$O_2^+ + NO_2 \rightarrow NO_2 + O_2$	2.00×10^{-07}	-0.5	0	A	[105]
(762)	$O_2^+ + NO_2 \rightarrow NO_2 + O + O$	1.00×10^{-07}	0	0	A	[105]

Nr	Reaction name	A^a	B^a	C^a	Set^b	Ref.
(763)	$O_2^+ + NO_2^- \rightarrow NO + O + O_2$	1.00×10^{-07}	0	0	A	[105]
(764)	$O_2^+ + NO_2^- \rightarrow NO + O + O + O$	1.00×10^{-07}	0	0	A	[105]
(765)	$O_2^+ + NO_2^- + M \rightarrow NO_2 + O_2 + M$	2.00×10^{-25}	-2.5	0	A,B	[105]
(766)	$O_2^+ + NO_3^- \rightarrow NO_3 + O_2$	2.00×10^{-07}	-0.5	0	A	[105]
(767)	$O_2^+ + NO_3^- \rightarrow NO_3 + O + O$	1.00×10^{-07}	0	0	A	[105]
(768)	$O_2^+ + NO_3^- \rightarrow NO_2 + O + O_2$	1.00×10^{-07}	0	0	A	[105]
(769)	$O_2^+ + NO_3^- \rightarrow NO_2 + O + O + O$	1.00×10^{-07}	0	0	A	[105, 183]
(770)	$O_2^+ + NO_3^- + M \rightarrow NO_3 + O_2 + M$	2.00×10^{-25}	-2.5	0	A,B	[105]
(771)	$O_2^+ + N_2O_5 \rightarrow NO_2^+ + NO_3 + O_2$	8.80×10^{-10}	0	0	A,B	[105, 191]
(772)	$O_2 + N \rightarrow NO_2 + e^-$	5.00×10^{-10}	0	0	A,B	[105, 183]
(773)	$O_2 + N^+ \rightarrow O_2 + N$	2.00×10^{-07}	-0.5	0	A	[105]
(774)	$O_2 + N^+ \rightarrow O + O + N$	1.00×10^{-07}	0	0	A	[105]
(775)	$O_2 + N^+ + M \rightarrow O_2 + N + M$	2.00×10^{-25}	-2.5	0	A	[105]
(776)	$O_2 + N^+ + M \rightarrow NO_2 + M$	2.00×10^{-25}	-2.5	0	A	[105]
(777)	$O_2 + N_2(A) \rightarrow O_2 + N_2 + e^-$	2.10×10^{-09}	0	0	A,B	[105, 183]
(778)	$O_2 + N_2(a') \rightarrow O_2 + N_2 + e^-$	2.50×10^{-09}	0	0		[105, 183] s
(779)	$O_2 + N_2^+ \rightarrow N_2 + O_2$	2.00×10^{-07}	-0.5	0		[105]
(780)	$O_2 + N_2^+ \rightarrow N + N + O_2$	1.00×10^{-07}	0	0		[105]
(781)	$O_2 + N_2^+ \rightarrow N_2 + O + O$	1.00×10^{-07}	0	0		[105]
(782)	$O_2 + N_2^+ \rightarrow N + N + O + O$	1.00×10^{-07}	0	0		[105]
(783)	$O_2 + N_2^+ + M \rightarrow O_2 + N_2 + M$	2.00×10^{-25}	-2.5	0		[105]
(784)	$O_2 + N_3^+ \rightarrow N + N_2 + O_2$	1.00×10^{-07}	0	0		[105]
(785)	$O_2 + N_3^+ \rightarrow N + N_2 + O + O$	1.00×10^{-07}	0	0		[105]
(786)	$O_2 + N_4^+ \rightarrow N_2 + N_2 + O_2$	1.00×10^{-07}	0	0		[105]

Nr	Reaction name	A^a	B^a	C^a	Set^b	Ref.
(787)	$O_2^- + N_4^+ \rightarrow N_2 + N_2 + O + O$	1.00×10^{-07}	0	0		[105]
(788)	$O_2^- + NO^+ \rightarrow O_2 + NO$	2.00×10^{-07}	-0.5	0		[105,184]
(789)	$O_2^- + NO^+ \rightarrow N + O + O_2$	1.00×10^{-07}	0	0		[105,183]
(790)	$O_2^- + NO^+ \rightarrow N + O + O + O$	1.00×10^{-07}	0	0		[105]
(791)	$O_2^- + NO^+ + M \rightarrow NO_3 + M$	2.00×10^{-25}	-2.5	0	A,B	[105]
(792)	$O_2^- + NO^+ + M \rightarrow O_2 + NO + M$	2.00×10^{-25}	-2.5	0	A	[105,183]
(793)	$O_2^- + NO_2 \rightarrow NO_2^- + O_2$	8.00×10^{-10}	0	0	A,B	[105,186]
(794)	$O_2^- + NO_2^+ \rightarrow O_2 + NO_2$	2.00×10^{-07}	-0.5	0	A	[105]
(795)	$O_2^- + NO_2^+ \rightarrow NO + O + O_2$	1.00×10^{-07}	0	0		[105]
(796)	$O_2^- + NO_2^+ \rightarrow NO + O + O + O$	1.00×10^{-07}	0	0		[105]
(797)	$O_2^- + NO_2^+ + M \rightarrow O_2 + NO_2 + M$	2.00×10^{-25}	-2.5	0	A,B	[105]
(798)	$O_2^- + N_2O \rightarrow N_2 + O_3^-$	9.00×10^{-13}	0	0		[105]
(799)	$O_2^- + N_2O \rightarrow NO_2^- + NO$	1.00×10^{-14}	0	0		[190] an
(800)	$O_2^- + NO_3 \rightarrow NO_3^- + O_2$	5.00×10^{-10}	0	0	A,B	[105]
(801)	$O_3 + N \rightarrow NO + O_2$	5.00×10^{-16}	0	0		[179,191]
(802)	$O_3 + N(^2D) \rightarrow NO + O_2$	1.00×10^{-10}	0	0		[112]
(803)	$O_3 + N^+ \rightarrow NO^+ + O_2$	5.00×10^{-10}	0	0		[105,191]
(804)	$O_3 + N_2(A) \rightarrow N_2 + O_2 + O$	3.36×10^{-11}	0	0	A,B	[110,111]
(805)	$O_3 + N_2(A) \rightarrow NO + NO + O$	8.40×10^{-12}	0	0	A	[110,111]
(806)	$O_3 + N_2(a') \rightarrow N_2 + O_2 + O$	3.36×10^{-11}	0	0		ao
(807)	$O_3 + N_2(a') \rightarrow NO + NO + O$	8.40×10^{-12}	0	0		ap
(808)	$O_3 + N_2^+ \rightarrow N_2 + O_2^+ + O$	1.00×10^{-10}	0	0		[105,191]
(809)	$O_3 + NO \rightarrow NO_2 + O_2$	4.30×10^{-12}	0	1560	A,B	[105,183]
(810)	$O_3 + NO^+ \rightarrow O_2 + NO_2^+$	1.00×10^{-15}	0	0		[105]

Nr	Reaction name	A^a	B^a	C^a	Set^b	Ref.
(811)	$O_3 + NO_2 \rightarrow NO_3 + O_2$	1.40×10^{-13}	0	2470	A,B	[111,112]
(812)	$O_3 + NO_2 \rightarrow NO + O_2 + O_2$	1.00×10^{-18}	0	0	A,B	[187,280]
(813)	$O_3 + NO_2^- \rightarrow NO_3^- + O_2$	1.80×10^{-11}	0	0	A,B	[105,276]
(814)	$O_3 + NO_3 \rightarrow NO_2 + O_2 + O_2$	1.00×10^{-17}	0	0		[283]
(815)	$O_3 + NO_3^- \rightarrow NO_2^- + O_2 + O_2$	1.00×10^{-13}	0	0	A,B	[186]
(816)	$O_3^- + N^+ \rightarrow O_3 + N$	2.00×10^{-07}	-0.5	0		[105]
(817)	$O_3^- + N^+ \rightarrow O_2 + O + N$	1.00×10^{-07}	0	0		[105]
(818)	$O_3^- + N^+ + M \rightarrow O_3 + N + M$	2.00×10^{-25}	-2.5	0		[105]
(819)	$O_3^- + N_2^+ \rightarrow O_3 + N_2$	2.00×10^{-07}	-0.5	0		[105]
(820)	$O_3^- + N_2^+ \rightarrow O_2 + O + N_2$	1.00×10^{-07}	0	0		[105]
(821)	$O_3^- + N_2^+ \rightarrow O_3 + N + N$	1.00×10^{-07}	0	0		[105]
(822)	$O_3^- + N_2^+ \rightarrow O_2 + O + N + N$	1.00×10^{-07}	0	0		[105]
(823)	$O_3^- + N_2^+ + M \rightarrow O_3 + N_2 + M$	2.00×10^{-25}	-2.5	0	A	[105]
(824)	$O_3^- + N_3^+ \rightarrow N + N_2 + O_3$	1.00×10^{-07}	0	0		[105]
(825)	$O_3^- + N_3^+ \rightarrow N + N_2 + O_2 + O$	1.00×10^{-07}	0	0		[105]
(826)	$O_3^- + N_4^+ \rightarrow O_3 + N_2 + N_2$	1.00×10^{-07}	0	0		[105]
(827)	$O_3^- + NO \rightarrow NO_3^- + O$	1.00×10^{-11}	0	0	A,B	[105]
(828)	$O_3^- + NO \rightarrow NO_2^- + O_2$	2.60×10^{-12}	0	0		[105]
(829)	$O_3^- + NO^+ \rightarrow O_3 + NO$	2.00×10^{-07}	-0.5	0		[105]
(830)	$O_3^- + NO^+ \rightarrow O_2 + O + NO$	1.00×10^{-07}	0	0		[105]
(831)	$O_3^- + NO^+ \rightarrow O_3 + N + O$	1.00×10^{-07}	0	0		[105]
(832)	$O_3^- + NO^+ \rightarrow O_2 + O + N + O$	1.00×10^{-07}	0	0		[105]
(833)	$O_3^- + NO^+ + M \rightarrow O_3 + NO + M$	2.00×10^{-25}	-2.5	0	A	[105]
(834)	$O_3^- + NO_2 \rightarrow NO_2^- + O_3$	7.00×10^{-10}	0	0	A,B	[105]

Nr	Reaction name	A^a	B^a	C^a	Set^b	Ref.
(835)	$O_3^- + NO_2 \rightarrow NO_3^- + O_2$	2.00×10^{-11}	0	0		[105]
(836)	$O_3^- + NO_2^+ \rightarrow O_3 + NO_2$	2.00×10^{-07}	-0.5	0		[105]
(837)	$O_3^- + NO_2^+ \rightarrow O_2 + O + NO_2$	1.00×10^{-07}	0	0		[105]
(838)	$O_3^- + NO_2^+ \rightarrow O_3 + NO + O$	1.00×10^{-07}	0	0		[105]
(839)	$O_3^- + NO_2^+ \rightarrow O_2 + O + NO + O$	1.00×10^{-07}	0	0		[105]
(840)	$O_3^- + NO_2^+ + M \rightarrow O_3 + NO_2 + M$	2.00×10^{-25}	-2.5	0	A,B	[105]
(841)	$O_3^- + NO_3 \rightarrow NO_3^- + O_3$	5.00×10^{-10}	0	0	A,B	[105]
(842)	$O_4^+ + NO \rightarrow NO^+ + O_2 + O_2$	1.00×10^{-10}	0	0		[105]
(843)	$O_4^+ + NO_2^- \rightarrow NO_2 + O_2 + O_2$	1.00×10^{-07}	0	0		[105]
(844)	$O_4^+ + NO_2^- \rightarrow NO + O + O_2 + O_2$	1.00×10^{-07}	0	0		[105]
(845)	$O_4^+ + NO_2 + M \rightarrow NO_2 + O_2 + O_2 + M$	2.00×10^{-25}	-2.5	0		[105]
(846)	$O_4^+ + NO_3^- \rightarrow NO_3 + O_2 + O_2$	1.00×10^{-07}	0	0		[105]
(847)	$O_4^+ + NO_3^- \rightarrow NO_2 + O + O_2 + O_2$	1.00×10^{-07}	0	0		[105]
(848)	$O_4^+ + NO_3^- + M \rightarrow NO_3 + O_2 + O_2 + M$	2.00×10^{-25}	-2.5	0		[105]
(849)	$N + NO \rightarrow N_2 + O$	8.20×10^{-11}	0	410	A,B	[283]
(850)	$N + NO_2 \rightarrow N_2 + O_2$	3.99×10^{-13}	0	-220		[291]
(851)	$N + NO_2 \rightarrow NO + NO$	1.33×10^{-12}	0	-220	A,B	[291]
(852)	$N + NO_2 \rightarrow N_2O + O$	1.66×10^{-12}	0	-220	A,B	[291]
(853)	$N + NO_2^+ \rightarrow NO^+ + NO$	8.00×10^{-12}	0	0		[186]
(854)	$N + NO_3 \rightarrow NO_2 + NO$	3.00×10^{-12}	0	0	A,B	[112]
(855)	$N + NO_3^- \rightarrow NO_2^- + NO$	5.00×10^{-12}	0	0	A,B	[186, 276] aq
(856)	$N(^2D) + NO \rightarrow N_2O$	6.00×10^{-11}	0	0	A,B	[105, 110]
(857)	$N(^2D) + NO \rightarrow N_2 + O$	4.50×10^{-11}	0	0		[112, 179]
(858)	$N(^2D) + NO \rightarrow N_2 + O(^1D)$	4.50×10^{-11}	0	0		[112]

Nr	Reaction name	A^a	B^a	C^a	Set^b	Ref.
(859)	$N(^2D) + N_2O \rightarrow NO + N_2$	1.50×10^{-11}	0	570		[110,112]
(860)	$N(^2D) + NO_2 \rightarrow N_2O + O$	1.50×10^{-12}	0	570		[179,187]
(861)	$N(^2D) + NO_2 \rightarrow NO + NO$	1.50×10^{-12}	0	570		[179,187]
(862)	$N^+ + NO \rightarrow N + NO^+$	8.00×10^{-10}	0	0		[105,186]
(863)	$N^+ + NO \rightarrow N_2^+ + O$	3.00×10^{-12}	0	0		[105]
(864)	$N^+ + NO \rightarrow N_2 + O^+$	1.00×10^{-12}	0	0		[105]
(865)	$N^+ + NO_2 \rightarrow NO^+ + NO$	5.00×10^{-10}	0	0		[191]
(866)	$N^+ + NO_2 \rightarrow NO_2^+ + N$	3.00×10^{-10}	0	0		[191]
(867)	$N^+ + NO_2^- \rightarrow NO_2 + N$	2.00×10^{-07}	-0.5	0		[105]
(868)	$N^+ + NO_2^- \rightarrow NO + O + N$	1.00×10^{-07}	0	0		[105]
(869)	$N^+ + NO_2^- + M \rightarrow NO_2 + N + M$	2.00×10^{-25}	-2.5	0		[105]
(870)	$N^+ + N_2O \rightarrow N_2 + NO^+$	5.50×10^{-10}	0	0		[105]
(871)	$N^+ + NO_3^- \rightarrow NO_3 + N$	2.00×10^{-07}	-0.5	0		[105]
(872)	$N^+ + NO_3^- \rightarrow NO_2 + O + N$	1.00×10^{-07}	0	0		[105]
(873)	$N^+ + NO_3^- + M \rightarrow NO_3 + N + M$	2.00×10^{-25}	-2.5	0		[105]
(874)	$N_2(A) + NO_2 \rightarrow N_2 + NO + O$	1.30×10^{-11}	0	0	A,B	[110,112]
(875)	$N_2(A) + N_2O \rightarrow N_2 + N_2 + O$	9.30×10^{-12}	0	-120	A	[112,179]
(876)	$N_2(A) + N_2O \rightarrow N_2 + N + NO$	1.00×10^{-11}	0	0	A	[105,290]
(877)	$N_2(a') + NO \rightarrow N_2 + N + O$	3.60×10^{-10}	0	0	A,B	[105,191]
(878)	$N_2^+ + NO \rightarrow N_2 + NO^+$	3.30×10^{-10}	0	0		[105,186]
(879)	$N_2^+ + NO_2 \rightarrow N_2 + NO_2^+$	3.00×10^{-10}	0	0		[179,187]
(880)	$N_2^+ + NO_2 \rightarrow N_2O + NO^+$	5.00×10^{-11}	0	0		[179,187]
(881)	$N_2^+ + NO_2 \rightarrow NO_2 + N_2$	2.00×10^{-07}	-0.5	0		[105]
(882)	$N_2^+ + NO_2 \rightarrow NO_2 + N + N$	1.00×10^{-07}	0	0		[105]

Nr	Reaction name	A^a	B^a	C^a	Set^b	Ref.
(883)	$N_2^+ + NO_2^- \rightarrow NO + O + N_2$	1.00×10^{-07}	0	0		[105]
(884)	$N_2^+ + NO_2^- \rightarrow NO + O + N + N$	1.00×10^{-07}	0	0		[105]
(885)	$N_2^+ + NO_2^- + M \rightarrow NO_2 + N_2 + M$	2.00×10^{-25}	-2.5	0		[105]
(886)	$N_2^+ + N_2O \rightarrow N_2 + NO^+ + N$	4.00×10^{-10}	0	0		[105, 183]
(887)	$N_2^+ + NO_3^- \rightarrow NO_3 + N_2$	2.00×10^{-07}	-0.5	0		[105]
(888)	$N_2^+ + NO_3^- \rightarrow NO_3 + N + N$	1.00×10^{-07}	0	0		[105]
(889)	$N_2^+ + NO_3^- \rightarrow NO_2 + O + N_2$	1.00×10^{-07}	0	0		[105]
(890)	$N_2^+ + NO_3^- \rightarrow NO_2 + O + N + N$	1.00×10^{-07}	0	0		[105]
(891)	$N_2^+ + NO_3^- + M \rightarrow NO_3 + N_2 + M$	2.00×10^{-25}	-2.5	0		[105]
(892)	$N_3^+ + NO \rightarrow N + N_2 + NO^+$	1.40×10^{-10}	0	0		[187]
(893)	$N_3^+ + NO_2 \rightarrow NO + N_2 + NO^+$	7.00×10^{-11}	0	0		[187]
(894)	$N_3^+ + NO_2 \rightarrow N + N_2 + NO_2^+$	7.00×10^{-11}	0	0		[187]
(895)	$N_3^+ + N_2O \rightarrow N_2 + N_2 + NO^+$	5.00×10^{-11}	0	0		[187]
(896)	$N_3^+ + NO_2^- \rightarrow NO_2 + N_2 + N$	1.00×10^{-07}	0	0		[105]
(897)	$N_3^+ + NO_2^- \rightarrow NO + O + N_2 + N$	1.00×10^{-07}	0	0		[105]
(898)	$N_3^+ + NO_3^- \rightarrow NO_3 + N_2 + N$	1.00×10^{-07}	0	0		[105]
(899)	$N_3^+ + NO_3^- \rightarrow NO_2 + O + N_2 + N$	1.00×10^{-07}	0	0		[105]
(900)	$N_4^+ + NO \rightarrow N_2 + N_2 + NO^+$	4.00×10^{-10}	0	0		[105, 113]
(901)	$N_4^+ + NO_2 \rightarrow NO_2^+ + N_2 + N_2$	2.50×10^{-10}	0	0		[179, 187]
(902)	$N_4^+ + NO_2 \rightarrow NO^+ + N_2O + N_2$	5.00×10^{-11}	0	0		[179, 187]
(903)	$N_4^+ + NO_2^- \rightarrow NO_2 + N_2 + N_2$	1.00×10^{-07}	0	0		[105]
(904)	$N_4^+ + NO_2^- \rightarrow NO + O + N_2 + N_2$	1.00×10^{-07}	0	0		[105]
(905)	$N_4^+ + NO_3^- \rightarrow NO_3 + N_2 + N_2$	1.00×10^{-07}	0	0		[105]
(906)	$N_4^+ + NO_3^- \rightarrow NO_2 + O + N_2 + N_2$	1.00×10^{-07}	0	0		[105]

Nr	Reaction name	A^a	B^a	C^a	Set^b	Ref.
(907)	$NO + NO \rightarrow N_2O + O$	7.22×10^{-12}	0	33155		[180]
(908)	$NO + NO \rightarrow N_2 + O_2$	2.51×10^{-11}	0	30653		[180]
(909)	$NO + NO + O_2 \rightarrow NO_2 + NO_2$	3.30×10^{-39}	0	-530		[188, 191]
(910)	$NO + NO_2 \rightarrow N_2O_3$	7.90×10^{-12}	1.4	0	A,B	[189]
(911)	$NO + NO_2 + Ar \rightarrow N_2O_3 + Ar$	3.10×10^{-34}	-7.7	0		g
(912)	$NO + NO_2 + N_2 \rightarrow N_2O_3 + N_2$	3.10×10^{-34}	-7.7	0		[188]
(913)	$NO + NO_2 + O_2 \rightarrow N_2O_3 + O_2$	3.10×10^{-34}	-7.7	0		g
(914)	$NO + NO_2 + H_2 \rightarrow N_2O_3 + H_2$	6.10×10^{-34}	-7.7	0		g
(915)	$NO + NO_2 + H_2O \rightarrow N_2O_3 + H_2O$	9.10×10^{-34}	-7.7	0		g
(916)	$NO + NO_2 + O_3 \rightarrow N_2O_3 + O_3$	6.10×10^{-34}	-7.7	0		g
(917)	$NO + NO_2^+ \rightarrow NO_2 + NO^+$	2.90×10^{-10}	0	0	A,B	[105, 183]
(918)	$NO + N_2O \rightarrow NO_2 + N_2$	2.92×10^{-13}	2.23	23292		[180]
(919)	$NO + NO_3 \rightarrow NO_2 + NO_2$	1.80×10^{-11}	0	-110	A,B	[111, 188]
(920)	$NO + NO_3 \rightarrow NO + NO + O_2$	7.30×10^{-12}	-0.23	947		[110, 191]
(921)	$NO + NO_3 \rightarrow NO_2 + NO_2$	3.00×10^{-15}	0	0		[105, 276]
(922)	$NO^+ + NO_2 \rightarrow NO + NO_2$	2.00×10^{-07}	-0.5	0		[105]
(923)	$NO^+ + NO_2^- \rightarrow NO_2 + N + O$	1.00×10^{-07}	0	0		[105]
(924)	$NO^+ + NO_2^- \rightarrow NO + O + NO$	1.00×10^{-07}	0	0		[105]
(925)	$NO^+ + NO_2^- \rightarrow NO + O + N + O$	1.00×10^{-07}	0	0		[105]
(926)	$NO^+ + NO_2^- + M \rightarrow NO + NO_2 + M$	2.00×10^{-25}	-2.5	0	A	[105]
(927)	$NO^+ + NO_3^- \rightarrow NO + NO_3$	2.00×10^{-07}	-0.5	0		[105]
(928)	$NO^+ + NO_3^- \rightarrow NO_3 + N + O$	1.00×10^{-07}	0	0	A,B	[105]
(929)	$NO^+ + NO_3^- \rightarrow NO_2 + O + NO$	1.00×10^{-07}	0	0		[105]
(930)	$NO^+ + NO_3^- \rightarrow NO_2 + O + N + O$	1.00×10^{-07}	0	0	A,B	[105, 183]

Nr	Reaction name	A^a	B^a	C^a	Set^b	Ref.
(931)	$NO^+ + NO_3^- + M \rightarrow NO + NO_3 + M$	2.00×10^{-25}	-2.5	0	A	[105]
(932)	$NO^+ + N_2O_5 \rightarrow NO_2 + NO_2 + NO_2^+$	5.90×10^{-10}	0	0	A,B	[105,191]
(933)	$NO_2 + NO_2 \rightarrow NO + NO + O_2$	7.49×10^{-12}	0	13898.1		[115,189]
(934)	$NO_2 + NO_2 \rightarrow NO_3 + NO$	1.03×10^{-12}	0.73	10524.3		[115,189]
(935)	$NO_2 + NO_2 + Ar \rightarrow N_2O_4 + Ar$	1.40×10^{-33}	-3.8	0	A,B	g
(936)	$NO_2 + NO_2 + N_2 \rightarrow N_2O_4 + N_2$	1.40×10^{-33}	-3.8	0	A,B	[112]
(937)	$NO_2 + NO_2 + O_2 \rightarrow N_2O_4 + O_2$	1.40×10^{-33}	-3.8	0	A	g
(938)	$NO_2 + NO_2 + H_2 \rightarrow N_2O_4 + H_2$	3.00×10^{-33}	-3.8	0		g
(939)	$NO_2 + NO_2 + H_2O \rightarrow N_2O_4 + H_2O$	8.00×10^{-33}	-3.8	0		g
(940)	$NO_2 + NO_2 + O_3 \rightarrow N_2O_4 + O_3$	3.00×10^{-33}	-3.8	0		g
(941)	$NO_2 + NO_2^- \rightarrow NO_3^- + NO$	4.00×10^{-12}	0	0		[105,276]
(942)	$NO_2 + NO_3 \rightarrow NO + NO_2 + O_2$	4.50×10^{-14}	0	1260		[112,277]
(943)	$NO_2 + NO_3 + Ar \rightarrow N_2O_5 + Ar$	2.80×10^{-30}	-3.5	0	A,B	g
(944)	$NO_2 + NO_3 + O_2 \rightarrow N_2O_5 + O_2$	2.80×10^{-30}	-3.5	0	A	g
(945)	$NO_2 + NO_3 + N_2 \rightarrow N_2O_5 + N_2$	2.80×10^{-30}	-3.5	0	A,B	[112]
(946)	$NO_2 + NO_3 + H_2 \rightarrow N_2O_5 + H_2$	6.00×10^{-30}	-3.5	0		g
(947)	$NO_2 + NO_3 + H_2O \rightarrow N_2O_5 + H_2O$	1.50×10^{-30}	-3.5	0		g
(948)	$NO_2 + NO_3 + O_3 \rightarrow N_2O_5 + O_3$	6.00×10^{-30}	-3.5	0		g
(949)	$NO_2^+ + NO_2^- \rightarrow NO_2 + NO_2$	2.00×10^{-07}	-0.5	0		[105]
(950)	$NO_2^+ + NO_2^- \rightarrow NO_2 + NO + O$	1.00×10^{-07}	0	0		[105]
(951)	$NO_2^+ + NO_2^- \rightarrow NO + O + NO + O$	1.00×10^{-07}	0	0		[105]
(952)	$NO_2^+ + NO_2^- + M \rightarrow NO_2 + NO_2 + M$	2.00×10^{-25}	-2.5	0		[105]
(953)	$NO_2^+ + NO_3^- \rightarrow NO_2 + NO_3$	2.00×10^{-07}	-0.5	0		[105]
(954)	$NO_2^+ + NO_3 \rightarrow NO_2 + NO_2 + O$	1.00×10^{-07}	0	0		[105]

Nr	Reaction name	A^a	B^a	C^a	Set^b	Ref.
(955)	$NO_2^+ + NO_3^- \rightarrow NO + O + NO_3$	1.00×10^{-07}	0	0		[105]
(956)	$NO_2^+ + NO_3^- \rightarrow NO + O + NO_2 + O$	1.00×10^{-07}	0	0		[105]
(957)	$NO_2^+ + NO_3^- + M \rightarrow N_2O_5 + M$	2.00×10^{-25}	-0.5	0	A,B	[105]
(958)	$NO_2^+ + NO_3^- + M \rightarrow NO_2 + NO_3 + M$	2.00×10^{-25}	-0.5	0	A	[105]
(959)	$NO_2^- + N_2O \rightarrow NO_3^- + N_2$	5.00×10^{-13}	0	0	A,B	[179,187]
(960)	$NO_2^- + NO_3 \rightarrow NO_3^- + NO_2$	5.00×10^{-10}	0	0	A	[105,183]
(961)	$NO_2^- + N_2O_5 \rightarrow NO_3^- + NO_3 + NO$	7.00×10^{-10}	0	0	A,B	[105,186]
(962)	$N_2O_{vib} + N_2 \rightarrow N_2O + N_2$	1.00×10^{-13}	0	0	A,B	ab
(963)	$N_2O_{vib} + N \rightarrow N_2O + N$	1.00×10^{-13}	0	0		ab
(964)	$N_2O_{vib} + O_2 \rightarrow N_2O + O_2$	1.00×10^{-13}	0	0	A	ab
(965)	$N_2O_{vib} + O_3 \rightarrow N_2O + O_3$	1.00×10^{-13}	0	0		ab
(966)	$N_2O_{vib} + O \rightarrow N_2O + O$	1.00×10^{-13}	0	0		ab
(967)	$N_2O_{vib} + H_2O \rightarrow N_2O + H_2O$	1.00×10^{-13}	0	0		ab
(968)	$N_2O_{vib} + H_2 \rightarrow N_2O + H_2$	1.00×10^{-13}	0	0		ab
(969)	$N_2O_{vib} + Ar \rightarrow N_2O + Ar$	1.00×10^{-13}	0	0	A,B	ab
(970)	$NO_3 + NO_3 \rightarrow NO_2 + NO_2 + O_2$	5.00×10^{-12}	0	3000		[105,279]
(971)	$N_2O_3 + M \rightarrow NO + NO_2 + M$	1.91×10^{-07}	-8.7	4882	A,B	[107,283]
(972)	$N_2O_4 + M \rightarrow NO_2 + NO_2 + M$	1.30×10^{-05}	-3.5	6403	A,B	[107,283]
(973)	$N_2O_5 + M \rightarrow NO_2 + NO_3 + M$	1.33×10^{-03}	-3.5	11000	A,B	[112,283]
Argon - humid air heavy particle collisions						
(974)	$Ar(^4S[^3P_2]) + H_2 \rightarrow Ar + H + H$	6.60×10^{-11}	0	0		[295]
(975)	$Ar(^4S[^3P_2]) + OH \rightarrow Ar + O + H$	6.60×10^{-11}	0	0		ar
(976)	$Ar(^4S[^3P_2]) + OH \rightarrow Ar + OH(A)$	6.60×10^{-11}	0	0	A,B	ar
(977)	$Ar(^4S[^3P_2]) + H_2O \rightarrow Ar + OH + H$	2.10×10^{-10}	0	0	A,B	[187,281]

Nr	Reaction name	A^a	B^a	C^a	Set^b	Ref.
(978)	$Ar(^4S[^3P_1]) + H_2 \rightarrow Ar + H + H$	6.60×10^{-11}	0	0		[295]
(979)	$Ar(^4S[^3P_1]) + OH \rightarrow Ar + O + H$	6.60×10^{-11}	0	0		ar
(980)	$Ar(^4S[^3P_1]) + OH \rightarrow Ar + OH(A)$	6.60×10^{-11}	0	0		ar
(981)	$Ar(^4S[^3P_1]) + H_2O \rightarrow Ar + OH + H$	2.10×10^{-10}	0	0	A	[187, 281]
(982)	$Ar(^4S[^3P_0]) + H_2 \rightarrow Ar + H + H$	6.60×10^{-11}	0	0		[295]
(983)	$Ar(^4S[^3P_0]) + OH \rightarrow Ar + O + H$	6.60×10^{-11}	0	0		ar
(984)	$Ar(^4S[^3P_0]) + OH \rightarrow Ar + OH(A)$	6.60×10^{-11}	0	0		ar
(985)	$Ar(^4S[^3P_0]) + H_2O \rightarrow Ar + OH + H$	2.10×10^{-10}	0	0	A,B	[187, 281]
(986)	$Ar(^4S[^1P_1]) + H_2 \rightarrow Ar + H + H$	6.60×10^{-11}	0	0		[295]
(987)	$Ar(^4S[^1P_1]) + OH \rightarrow Ar + O + H$	6.60×10^{-11}	0	0		ar
(988)	$Ar(^4S[^1P_1]) + OH \rightarrow Ar + OH(A)$	6.60×10^{-11}	0	0		ar
(989)	$Ar(^4S[^1P_1]) + H_2O \rightarrow Ar + OH + H$	2.10×10^{-10}	0	0		[187, 281]
(990)	$Ar(^4P) + H_2 \rightarrow Ar + H + H$	4.00×10^{-10}	0	0	A	[296]
(991)	$Ar(^4P) + OH \rightarrow Ar + O + H$	2.10×10^{-10}	0	0		as
(992)	$Ar(^4P) + H_2O \rightarrow Ar + OH + H$	2.10×10^{-10}	0	0	A,B	[187, 281]
(993)	$Ar^+ + H \rightarrow Ar + H^+$	1.00×10^{-10}	0	0	A,B	[273]
(994)	$Ar^+ + H^- \rightarrow Ar + H$	2.00×10^{-07}	-0.5	0		[105]
(995)	$Ar^+ + H^- + M \rightarrow Ar + H + M$	2.00×10^{-25}	-2.5	0		[105]
(996)	$Ar^+ + H_2 \rightarrow ArH^+ + H$	1.10×10^{-09}	0	0	A	[187, 271]
(997)	$Ar^+ + H_2 \rightarrow Ar + H_2^+$	1.10×10^{-09}	0	0	A,B	[271, 281]
(998)	$Ar^+ + OH^- \rightarrow Ar + OH$	2.00×10^{-07}	-0.5	0		[105]
(999)	$Ar^+ + OH^- \rightarrow Ar + O + H$	1.00×10^{-07}	0	0		[105]
(1000)	$Ar^+ + OH^- + M \rightarrow Ar + OH + M$	2.00×10^{-25}	-2.5	0		[105]
(1001)	$Ar^+ + H_2O \rightarrow Ar + H_2O^+$	7.00×10^{-10}	0	0	A,B	[186, 271]

Nr	Reaction name	A^a	B^a	C^a	Set^b	Ref.
(1002)	$Ar^+ + H_2O \rightarrow ArH^+ + OH$	3.00×10^{-10}	0	0	A,B	[186, 271]
(1003)	$Ar_2^* + H_2 \rightarrow Ar + Ar + H + H$	6.60×10^{-11}	0	0		ar
(1004)	$Ar_2^* + OH \rightarrow Ar + Ar + O + H$	6.60×10^{-11}	0	0		ar
(1005)	$Ar_2^* + H_2O \rightarrow Ar + Ar + OH + H$	1.00×10^{-10}	0	0	A,B	ar
(1006)	$Ar_2^+ + H \rightarrow Ar + Ar + H^+$	5.00×10^{-11}	0	0	A,B	[273]
(1007)	$Ar_2^+ + H^- \rightarrow Ar + Ar + H$	1.00×10^{-07}	0	0	A	[105]
(1008)	$Ar_2^+ + H_2O \rightarrow Ar + Ar + H_2O^+$	1.60×10^{-09}	0	0	A,B	[186, 271]
(1009)	$Ar_2^+ + H_2O \rightarrow ArH^+ + Ar + OH$	4.00×10^{-10}	0	0	A,B	at
(1010)	$Ar_2^+ + OH^- \rightarrow Ar + Ar + OH$	1.00×10^{-07}	0	0	A,B	[105]
(1011)	$Ar_2^+ + OH^- \rightarrow Ar + Ar + O + H$	1.00×10^{-07}	0	0	A,B	[105]
Humid air heavy particle collisions						
(1012)	$H + O + Ar \rightarrow OH + Ar$	1.50×10^{-32}	-1	0	A	[121] g
(1013)	$H + O + N_2 \rightarrow OH + N_2$	1.50×10^{-32}	-1	0		[121] g
(1014)	$H + O + O_2 \rightarrow OH + O_2$	1.50×10^{-32}	-1	0		[121] g
(1015)	$H + O + H_2 \rightarrow OH + H_2$	3.00×10^{-32}	-1	0		[121] g
(1016)	$H + O + O_3 \rightarrow OH + O_3$	3.00×10^{-32}	-1	0		[121] g
(1017)	$H + O + H_2O \rightarrow OH + H_2O$	7.50×10^{-32}	-1	0		[121] g
(1018)	$H + O^+ \rightarrow H^+ + O$	5.66×10^{-10}	0.36	-8.6	A,B	[180]
(1019)	$H + O^- \rightarrow OH + e^-$	5.00×10^{-10}	0	0	A,B	[121, 180]
(1020)	$H + O_2 \rightarrow OH + O$	1.62×10^{-10}	0	7470		[121, 283]
(1021)	$H + O_2 \rightarrow O + H + O$	6.00×10^{-09}	0	52300		[180]
(1022)	$H + O_2 + Ar \rightarrow HO_2 + Ar$	6.09×10^{-32}	-0.8	0	A,B	[283]
(1023)	$H + O_2 + N_2 \rightarrow HO_2 + N_2$	6.09×10^{-32}	-0.8	0	A,B	g
(1024)	$H + O_2 + O_2 \rightarrow HO_2 + O_2$	6.09×10^{-32}	-0.8	0	A	g

Nr	Reaction name	A^a	B^a	C^a	Set^b	Ref.
(1025)	$H + O_2 + H_2O \rightarrow HO_2 + H_2O$	3.05×10^{-31}	-0.8	0		g
(1026)	$H + O_2 + H_2 \rightarrow HO_2 + H_2$	1.53×10^{-31}	-0.8	0		g
(1027)	$H + O_2 + O_3 \rightarrow HO_2 + O_3$	1.53×10^{-31}	-0.8	0		g
(1028)	$H + O_2(a) \rightarrow OH + O$	1.83×10^{-13}	0	1550		[121,191]
(1029)	$H + O_2^- \rightarrow H\text{-} + O_2$	7.00×10^{-10}	0	0	A,B	[186,276] an
(1030)	$H + O_2^- \rightarrow HO_2 + e^-$	7.00×10^{-10}	0	0	A,B	[186,276] an
(1031)	$H + O_3 \rightarrow OH + O_2$	2.71×10^{-11}	0.75	0	A,B	[121,283]
(1032)	$H + O_3 \rightarrow HO_2 + O$	7.51×10^{-13}	0	0		[121,283]
(1033)	$H + N + Ar \rightarrow NH + Ar$	5.00×10^{-32}	0	0	A,B	g
(1034)	$H + N + N_2 \rightarrow NH + N_2$	5.00×10^{-32}	0	0	A	g
(1035)	$H + N + O_2 \rightarrow NH + O_2$	5.00×10^{-32}	0	0		g
(1036)	$H + N + H_2 \rightarrow NH + H_2$	1.00×10^{-31}	0	0		g
(1037)	$H + N + H_2O \rightarrow NH + H_2O$	2.00×10^{-31}	0	0		g
(1038)	$H + N + O_3 \rightarrow NH + O_3$	1.00×10^{-31}	0	0		g
(1039)	$H + N^+ \rightarrow N + H^+$	2.00×10^{-09}	0	0	A,B	[185,273]
(1040)	$H + NO + Ar \rightarrow HNO + Ar$	1.22×10^{-31}	-1.17	212	A,B	g
(1041)	$H + NO + O_2 \rightarrow HNO + O_2$	1.22×10^{-31}	-1.17	212		g
(1042)	$H + NO + N_2 \rightarrow HNO + N_2$	1.22×10^{-31}	-1.17	212	A,B	g
(1043)	$H + NO + H_2 \rightarrow HNO + H_2$	3.05×10^{-31}	-1.17	212		[109]
(1044)	$H + NO + H_2O \rightarrow HNO + H_2O$	6.10×10^{-31}	-1.17	212		g
(1045)	$H + NO + O_3 \rightarrow HNO + O_3$	3.05×10^{-31}	-1.17	212		g
(1046)	$H + NO \rightarrow OH + N$	3.60×10^{-10}	0	24910		[180]
(1047)	$H + NO \rightarrow NH + O$	9.29×10^{-10}	-0.1	35220		[180]
(1048)	$H + NO_2 \rightarrow OH + NO$	4.00×10^{-10}	0	340	A,B	[112,277]

Nr	Reaction name	A^a	B^a	C^a	Set^b	Ref.
(1049)	$H + NO_2 + Ar \rightarrow HNO_2 + Ar$	7.43×10^{-34}	-1.5	453		[291]
(1050)	$H + NO_2 + N_2 \rightarrow HNO_2 + N_2$	7.43×10^{-34}	-1.5	453		g
(1051)	$H + NO_2 + O_2 \rightarrow HNO_2 + O_2$	7.43×10^{-34}	-1.5	453		g
(1052)	$H + NO_2 + H_2 \rightarrow HNO_2 + H_2$	1.53×10^{-33}	-1.5	453		g
(1053)	$H + NO_2 + H_2O \rightarrow HNO_2 + H_2O$	3.43×10^{-33}	-1.5	453		g
(1054)	$H + NO_2 + O_3 \rightarrow HNO_2 + O_3$	1.53×10^{-33}	-1.5	453		g
(1055)	$H + NO_2^+ \rightarrow OH + NO^+$	1.90×10^{-10}	0	0	A,B	[180]
(1056)	$H + NO_2^- \rightarrow HNO_2 + e^-$	3.70×10^{-10}	0	0	A,B	[186, 276]
(1057)	$H + NO_2^- \rightarrow OH^- + NO$	1.85×10^{-10}	0	0	A,B	[190]
(1058)	$H + N_2O \rightarrow NO + NH$	4.96×10^{-07}	-2.16	18700		[180]
(1059)	$H + N_2O \rightarrow OH + N_2$	5.13×10^{-14}	3.15	3603		[180]
(1060)	$H + NO_3 \rightarrow OH + NO_2$	5.80×10^{-10}	0	750	A,B	[183]
(1061)	$H + NO_3^- \rightarrow OH^- + NO_2$	1.66×10^{-11}	0	0	A	[186] au
(1062)	$H + NO_3^- \rightarrow HNO_3 + e^-$	1.66×10^{-11}	0	0	A	[186] au
(1063)	$H + NO_3^- \rightarrow NO_2^- + OH$	1.66×10^{-11}	0	0	A,B	[186] au
(1064)	$H + H + Ar \rightarrow H_2 + Ar$	2.00×10^{-32}	-1	0	A,B	g
(1065)	$H + H + O_2 \rightarrow H_2 + O_2$	2.00×10^{-32}	-1	0		g
(1066)	$H + H + N_2 \rightarrow H_2 + N_2$	2.00×10^{-32}	-1	0		g
(1067)	$H + H + H_2 \rightarrow H_2 + H_2$	4.00×10^{-32}	-1	0		g
(1068)	$H + H + H_2O \rightarrow H_2 + H_2O$	9.20×10^{-32}	-1	0		[288]
(1069)	$H + H + O_3 \rightarrow H_2 + O_3$	4.00×10^{-32}	-1	0		g
(1070)	$H + H^+ + M \rightarrow H_2^+ + M$	1.00×10^{-34}	0	0		[121]
(1071)	$H + H^- \rightarrow H_2 + e^-$	1.30×10^{-09}	0	0		[121, 273]
(1072)	$H + H_2 \rightarrow H + H + H$	4.67×10^{-07}	-1	55000		[180]

Nr	Reaction name	A^a	B^a	C^a	Set^b	Ref.
(1073)	$H + H_2^+ \rightarrow H_2 + H^+$	6.39×10^{-10}	0	0	A,B	[121,180]
(1074)	$H + OH \rightarrow H + H + O$	6.00×10^{-09}	0	50900		[180]
(1075)	$H + OH \rightarrow H_2 + O$	7.00×10^{-14}	2.8	1950		[183,274]
(1076)	$H + OH + Ar \rightarrow H_2O + Ar$	8.00×10^{-31}	-2.6	0	A,B	g
(1077)	$H + OH + O_2 \rightarrow H_2O + O_2$	8.00×10^{-31}	-2.6	0		g
(1078)	$H + OH + N_2 \rightarrow H_2O + N_2$	8.00×10^{-31}	-2.6	0		g
(1079)	$H + OH + H_2 \rightarrow H_2O + H_2$	1.80×10^{-30}	-2.6	0		g
(1080)	$H + OH + H_2O \rightarrow H_2O + H_2O$	3.99×10^{-30}	-2.6	0		[291]
(1081)	$H + OH + O_3 \rightarrow H_2O + O_3$	1.80×10^{-30}	-2.6	0		g
(1082)	$H + OH^- \rightarrow H_2O + e^-$	1.80×10^{-09}	0	0	A,B	[121]
(1083)	$H + HO_2 \rightarrow H_2 + O_2$	2.06×10^{-11}	0.84	277	A,B	[180]
(1084)	$H + HO_2 \rightarrow OH + OH$	1.66×10^{-10}	0	413	A,B	[180]
(1085)	$H + HO_2 \rightarrow H_2O + O$	5.00×10^{-11}	0	866	A	[287,288]
(1086)	$H + HO_2 \rightarrow H_2O + O(^1D)$	2.32×10^{-12}	1.55	-80.85	A,B	[121,283]
(1087)	$H + H_2O \rightarrow OH + H + H$	5.80×10^{-09}	0	52900		[180]
(1088)	$H + H_2O \rightarrow OH + H_2$	6.89×10^{-12}	1.6	9720		[187,286]
(1089)	$H + H_2O_2 \rightarrow HO_2 + H_2$	8.00×10^{-11}	0	4000	A	[121,183]
(1090)	$H + H_2O_2 \rightarrow H_2O + OH$	4.00×10^{-11}	0	2000	A,B	[121,183]
(1091)	$H + NH \rightarrow H_2 + N$	1.70×10^{-11}	0	0	A,B	[111,112]
(1092)	$H + HNO \rightarrow H_2 + NO$	3.00×10^{-11}	0	500	A,B	[112,115]
(1093)	$H + HNO \rightarrow OH + NH$	2.40×10^{-09}	-0.5	9010		[180]
(1094)	$H + HNO_2 \rightarrow H_2 + NO_2$	2.00×10^{-11}	0	3700	A,B	[112,115]
(1095)	$H + HNO_2 \rightarrow HNO + OH$	1.26×10^{-11}	0.86	2501	A	[288,291]
(1096)	$H + HNO_2 \rightarrow H_2O + NO$	6.50×10^{-13}	1.89	1932		[288,291]

Nr	Reaction name	A^a	B^a	C^a	Set^b	Ref.
(1097)	$H + HNO_3 \rightarrow HNO_2 + OH$	3.16×10^{-13}	2.3	3512.8	A	[189, 288]
(1098)	$H + HNO_3 \rightarrow H_2O + NO_2$	1.51×10^{-14}	3.3	3164.8		[189, 288]
(1099)	$H + HNO_3 \rightarrow H_2 + NO_3$	4.80×10^{-12}	1.5	8258.3		[189, 288]
(1100)	$H + HNO_4 \rightarrow HO_2 + HNO_2$	2.46×10^{-14}	0	0	A,B	[298] z
(1101)	$H + ArH^+ \rightarrow H_2^+ + Ar$	9.10×10^{-10}	0	0	A,B	av
(1102)	$H^* + N_2 \rightarrow H + N_2$	1.00×10^{-13}	0	0	A,B	ab
(1103)	$H^* + N \rightarrow H + N$	1.00×10^{-13}	0	0		ab
(1104)	$H^* + O_2 \rightarrow H + O_2$	1.00×10^{-13}	0	0	A	ab
(1105)	$H^* + O_3 \rightarrow H + O_3$	1.00×10^{-13}	0	0		ab
(1106)	$H^* + O \rightarrow H + O$	1.00×10^{-13}	0	0		ab
(1107)	$H^* + H_2O \rightarrow H + H_2O$	1.00×10^{-13}	0	0		ab
(1108)	$H^* + H_2 \rightarrow H + H_2$	1.00×10^{-13}	0	0		ab
(1109)	$H^* + Ar \rightarrow H + Ar$	1.00×10^{-13}	0	0	A,B	ab
(1110)	$H^+ + O \rightarrow H + O^+$	3.04×10^{-10}	0.47	-11.5	A,B	[121, 180]
(1111)	$H^+ + O^{\cdot} \rightarrow H + O$	2.00×10^{-07}	-0.5	0		[105]
(1112)	$H^+ + O^{\cdot} + M \rightarrow H + O + M$	2.00×10^{-25}	-2.5	0	A	[105]
(1113)	$H^+ + O^{\cdot} + M \rightarrow OH + M$	2.00×10^{-25}	-2.5	0	A	[105]
(1114)	$H^+ + O_2 \rightarrow H + O_2^+$	2.00×10^{-09}	0	0	A,B	[121, 180]
(1115)	$H^+ + O_2^- \rightarrow H + O_2$	2.00×10^{-07}	-0.5	0		[105]
(1116)	$H^+ + O_2^- \rightarrow H + O + O$	1.00×10^{-07}	0	0		[105]
(1117)	$H^+ + O_2^- + M \rightarrow H + O_2 + M$	2.00×10^{-25}	-2.5	0		[105]
(1118)	$H^+ + O_2^- + M \rightarrow HO_2 + M$	2.00×10^{-25}	-2.5	0		[105]
(1119)	$H^+ + O_3^- \rightarrow H + O_3$	2.00×10^{-07}	-0.5	0		[105]
(1120)	$H^+ + O_3^- \rightarrow H + O_2 + O$	1.00×10^{-07}	0	0		[105]

Nr	Reaction name	A^a	B^a	C^a	Set^b	Ref.
(1121)	$H^+ + O_3^- + M \rightarrow H + O_3 + M$	2.00×10^{-25}	-2.5	0	A	[105]
(1122)	$H^+ + N \rightarrow N^+ + H$	5.00×10^{-11}	0	0	A	[265]
(1123)	$H^+ + NO \rightarrow NO^+ + H$	2.90×10^{-09}	0	0	A	[180]
(1124)	$H^+ + NO_2 \rightarrow NO^+ + OH$	1.90×10^{-09}	0	0		[180]
(1125)	$H^+ + NO_2^- \rightarrow NO_2 + H$	2.00×10^{-07}	-0.5	0		[105]
(1126)	$H^+ + NO_2^- \rightarrow H + NO + O$	1.00×10^{-07}	0	0		[105]
(1127)	$H^+ + NO_2 + M \rightarrow H + NO_2 + M$	2.00×10^{-25}	-2.5	0		[105]
(1128)	$H^+ + NO_2 + M \rightarrow HNO_2 + M$	2.00×10^{-25}	-2.5	0		[105]
(1129)	$H^+ + NO_3^- \rightarrow NO_3 + H$	2.00×10^{-07}	-0.5	0		[105]
(1130)	$H^+ + NO_3^- \rightarrow H + NO_2 + O$	1.00×10^{-07}	0	0		[105]
(1131)	$H^+ + NO_3^- + M \rightarrow H + NO_3 + M$	2.00×10^{-25}	-2.5	0		[105]
(1132)	$H^+ + NO_3^- + M \rightarrow HNO_3 + M$	2.00×10^{-25}	-2.5	0	A,B	[105]
(1133)	$H^+ + HNO \rightarrow NO^+ + H_2$	4.00×10^{-09}	0	0		[180]
(1134)	$H^+ + H^- \rightarrow H + H$	2.00×10^{-07}	-0.5	0		[105,185]
(1135)	$H^+ + H^- + M \rightarrow H + H + M$	2.00×10^{-25}	-2.5	0		[105]
(1136)	$H^+ + H + M \rightarrow H_2^+ + M$	1.00×10^{-34}	0	0		[121]
(1137)	$H^+ + H_2 + M \rightarrow H_3^+ + M$	1.50×10^{-29}	0	0	A	[121]
(1138)	$H^+ + OH \rightarrow H + OH^+$	2.10×10^{-09}	0	0	A,B	[121,180]
(1139)	$H^+ + OH^- \rightarrow OH + H$	2.00×10^{-07}	-0.5	0		[105]
(1140)	$H^+ + OH^- \rightarrow H + O + H$	1.00×10^{-07}	0	0		[105]
(1141)	$H^+ + OH^- + M \rightarrow H + OH + M$	2.00×10^{-25}	-2.5	0		[105]
(1142)	$H^+ + OH^- + M \rightarrow H_2O + M$	2.00×10^{-25}	-2.5	0		[105]
(1143)	$H^+ + H_2O \rightarrow H + H_2O^+$	6.90×10^{-09}	0	0	A,B	[121,180]
(1144)	$H^- + O \rightarrow OH + e^-$	1.00×10^{-09}	0	0	A	[121,180]

Nr	Reaction name	A^a	B^a	C^a	Set^b	Ref.
(1145)	$H^- + O^+ \rightarrow H + O$	2.30×10^{-07}	-0.5	0		[121, 180]
(1146)	$H^- + O^+ + M \rightarrow O + H + M$	2.00×10^{-25}	-2.5	0		[105]
(1147)	$H^- + O^+ + M \rightarrow OH + M$	2.00×10^{-25}	-2.5	0		[105]
(1148)	$H^- + O_2 \rightarrow HO_2 + e^-$	1.20×10^{-09}	0	0	A,B	[121, 299]
(1149)	$H^- + O_2^+ \rightarrow O_2 + H$	2.00×10^{-07}	-0.5	0		[105, 184]
(1150)	$H^- + O_2^+ \rightarrow O + O + H$	1.00×10^{-07}	0	0		[105]
(1151)	$H^- + O_2^+ + M \rightarrow H + O_2 + M$	2.00×10^{-25}	-2.5	0	A	[105]
(1152)	$H^- + O_2^+ + M \rightarrow HO_2 + M$	2.00×10^{-25}	-2.5	0	A,B	[105, 281]
(1153)	$H^- + O_4^+ \rightarrow O_2 + O_2 + H$	1.00×10^{-07}	0	0		[105]
(1154)	$H^- + O_4^+ + M \rightarrow H + O_2 + O_2 + M$	2.00×10^{-25}	-2.5	0		[105]
(1155)	$H^- + N \rightarrow NH + e^-$	1.00×10^{-09}	0	0		[180]
(1156)	$H^- + N^+ \rightarrow N + H$	2.00×10^{-07}	-0.5	0		[105, 180]
(1157)	$H^- + N^+ + M \rightarrow NH + M$	2.00×10^{-25}	-2.5	0		[105]
(1158)	$H^- + N_2^+ \rightarrow N_2 + H$	2.00×10^{-07}	-0.5	0		[105, 177]
(1159)	$H^- + N_2^+ \rightarrow N + N + H$	1.00×10^{-07}	0	0		[105]
(1160)	$H^- + N_2^+ + M \rightarrow N_2 + H + M$	2.00×10^{-25}	-2.5	0		[105]
(1161)	$H^- + N_3^+ \rightarrow N + N_2 + H$	1.00×10^{-07}	0	0		[105]
(1162)	$H^- + N_4^+ \rightarrow N_2 + N_2 + H$	1.00×10^{-07}	0	0		[105]
(1163)	$H^- + NO \rightarrow HNO + e^-$	4.60×10^{-10}	0	0		[276, 299]
(1164)	$H^- + NO^+ \rightarrow NO + H$	2.00×10^{-07}	-0.5	0		[105]
(1165)	$H^- + NO^+ \rightarrow N + O + H$	1.00×10^{-07}	0	0		[105]
(1166)	$H^- + NO^+ + M \rightarrow HNO + M$	2.00×10^{-25}	-2.5	0	A,B	[105]
(1167)	$H^- + NO^+ + M \rightarrow H + NO + M$	2.00×10^{-25}	-2.5	0		[105]
(1168)	$H^- + N_2O \rightarrow OH^- + N_2$	1.10×10^{-09}	0	0		[186, 299]

Nr	Reaction name	A^a	B^a	C^a	Set^b	Ref.
(1169)	$H^- + NO_2 \rightarrow NO_2^- + H$	2.90×10^{-09}	0	0	A	[276]
(1170)	$H^- + NO_2^+ \rightarrow NO_2 + H$	2.00×10^{-07}	-0.5	0		[105]
(1171)	$H^- + NO_2^+ \rightarrow NO + O + H$	1.00×10^{-07}	0	0		[105]
(1172)	$H^- + NO_2^+ + M \rightarrow H + NO_2 + M$	2.00×10^{-25}	-2.5	0		[105]
(1173)	$H^- + NO_2^+ + M \rightarrow HNO_2 + M$	2.00×10^{-25}	-2.5	0	A,B	[105, 187]
(1174)	$H^- + H_2^+ \rightarrow H + H_2$	2.00×10^{-07}	-0.5	0		[121, 177]
(1175)	$H^- + H_2^+ \rightarrow H + H + H$	1.00×10^{-07}	0	0		[105]
(1176)	$H^- + H_2^+ + M \rightarrow H + H_2 + M$	2.00×10^{-25}	-2.5	0		[105]
(1177)	$H^- + H_3^+ \rightarrow H_2 + H + H$	1.00×10^{-07}	0	0		[105, 273]
(1178)	$H^- + OH \rightarrow H_2O + e^-$	1.00×10^{-10}	0	0		[121, 180]
(1179)	$H^- + OH^+ \rightarrow H + OH$	2.00×10^{-07}	-0.5	0		[105]
(1180)	$H^- + OH^+ \rightarrow H + OH$	1.00×10^{-07}	0	0		[105]
(1181)	$H^- + OH^+ + M \rightarrow H + OH + M$	2.00×10^{-25}	-2.5	0		[105]
(1182)	$H^- + OH^+ + M \rightarrow H_2O + M$	2.00×10^{-25}	-2.5	0		[105]
(1183)	$H^- + H_2O \rightarrow OH^- + H_2$	3.80×10^{-09}	0	0	A,B	[121, 180]
(1184)	$H^- + H_2O^+ \rightarrow H_2O + H$	2.00×10^{-07}	-0.5	0		[105]
(1185)	$H^- + H_2O^+ \rightarrow H + H + OH$	1.00×10^{-07}	0	0		[105]
(1186)	$H^- + H_2O^+ + M \rightarrow H + H_2O + M$	2.00×10^{-25}	-2.5	0	A	[105]
(1187)	$H^- + H_3O^+ \rightarrow H_2 + H_2O$	2.30×10^{-07}	-0.5	0		[121, 180]
(1188)	$H^- + H_3O^+ \rightarrow H + H_2 + OH$	2.30×10^{-07}	-0.5	0		[121, 180]
(1189)	$H^- + H_3O^+ + M \rightarrow H_2 + H_2O + M$	2.00×10^{-25}	-2.5	0		[105]
(1190)	$H^- + H_3O^+ + M \rightarrow H + H_2 + OH + M$	2.00×10^{-25}	-2.5	0		e
(1191)	$H^- + M \rightarrow H + e^- + M$	2.70×10^{-10}	0.5	5590	A,B	aw
(1192)	$H^- + ArH^+ \rightarrow H_2 + Ar$	5.00×10^{-06}	0	0	A,B	[300]

Nr	Reaction name	A^a	B^a	C^a	Set^b	Ref.
(1193)	$H^- + ArH^+ \rightarrow H + H + Ar$	1.00×10^{-07}	0	0		[105]
(1194)	$H_2 + O \rightarrow OH + H$	1.60×10^{-11}	0	4570	A,B	[275,297]
(1195)	$H_2 + O(^1D) \rightarrow OH + H$	1.10×10^{-10}	0	0		[112,188]
(1196)	$H_2 + O^+ \rightarrow OH^+ + H$	1.62×10^{-09}	0	0	A,B	[183,186]
(1197)	$H_2 + O^- \rightarrow H_2O + e^-$	6.72×10^{-10}	0	0	A	[180,183]
(1198)	$H_2 + O^- \rightarrow OH^- + H$	2.80×10^{-11}	0	0	A	[121,180]
(1199)	$H_2 + O_2 \rightarrow H + HO_2$	2.40×10^{-10}	0	28500		[187,278]
(1200)	$H_2 + O_2 \rightarrow O + O + H_2$	6.00×10^{-09}	0	52300		[180]
(1201)	$H_2 + O_2 \rightarrow OH + OH$	3.16×10^{-10}	0	21890		[180]
(1202)	$H_2 + O_2^- \rightarrow OH^- + OH$	5.00×10^{-13}	0	0		[186,276] ^{aq}
(1203)	$H_2 + O_2^- \rightarrow H^- + HO_2$	5.00×10^{-13}	0	0	A,B	[186,276] ^{aq}
(1204)	$H_2 + N \rightarrow NH + H$	1.69×10^{-09}	0	18095		[180]
(1205)	$H_2 + N(^2D) \rightarrow NH + H$	4.60×10^{-11}	0	880	A	[110,112]
(1206)	$H_2 + N_2(A) \rightarrow N_2 + H + H$	3.80×10^{-10}	0	3500		[112,284]
(1207)	$H_2 + N_2(a') \rightarrow N_2 + H + H$	2.60×10^{-11}	0	0		[284]
(1208)	$H_2 + NO_2 \rightarrow HNO_2 + H$	1.48×10^{-13}	2.76	14991	A,B	[189,287]
(1209)	$H_2 + NO_2^+ \rightarrow NO^+ + H_2O$	1.50×10^{-10}	0	0	A,B	[180]
(1210)	$H_2 + H_2^+ \rightarrow H_2 + H^+ + H$	1.00×10^{-08}	0	84100		[180]
(1211)	$H_2 + H_2^+ \rightarrow H_3^+ + H$	2.10×10^{-09}	0	0		[180,276]
(1212)	$H_2 + OH \rightarrow H_2O + H$	9.54×10^{-13}	2	1490	A,B	[114]
(1213)	$H_2 + OH \rightarrow H_2 + O + H$	6.00×10^{-09}	0	50900		[180]
(1214)	$H_2 + OH^+ \rightarrow H_2O^+ + H$	1.30×10^{-09}	0	0		[121,180]
(1215)	$H_2 + OH^- \rightarrow H_2O + H^-$	5.00×10^{-12}	0	0	A,B	[186]
(1216)	$H_2 + HO_2 \rightarrow H_2O_2 + H$	4.38×10^{-12}	0	10751		[180]

Nr	Reaction name	A^a	B^a	C^a	Set^b	Ref.
(1217)	$H_2 + H_2O \rightarrow OH + H_2 + H$	5.80×10^{-09}	0	52900		[180]
(1218)	$H_2 + H_2O^+ \rightarrow H_3O^+ + H$	1.40×10^{-09}	0	0	A	[121, 275]
(1219)	$H_2 + H_3O^+ \rightarrow H_2O + H_3^+$	5.00×10^{-10}	0	0	A,B	[186]
(1220)	$H_2 + ArH^+ \rightarrow H_3^+ + Ar$	5.00×10^{-10}	0	0	A,B	[186, 273]
(1221)	$H_{2,vib} + N_2 \rightarrow H_2 + N_2$	1.00×10^{-13}	0	0	A,B	ab
(1222)	$H_{2,vib} + N \rightarrow H_2 + N$	1.00×10^{-13}	0	0		ab
(1223)	$H_{2,vib} + O_2 \rightarrow H_2 + O_2$	1.00×10^{-13}	0	0	A	ab
(1224)	$H_{2,vib} + O_3 \rightarrow H_2 + O_3$	1.00×10^{-13}	0	0		ab
(1225)	$H_{2,vib} + O \rightarrow H_2 + O$	1.00×10^{-13}	0	0		ab
(1226)	$H_{2,vib} + H_2O \rightarrow H_2 + H_2O$	1.00×10^{-13}	0	0		ab
(1227)	$H_{2,vib} + H_2 \rightarrow H_2 + H_2$	1.00×10^{-13}	0	0		ab
(1228)	$H_{2,vib} + Ar \rightarrow H_2 + Ar$	1.00×10^{-13}	0	0	A,B	ab
(1229)	$H_{2,rot} + N_2 \rightarrow H_2 + N_2$	1.00×10^{-13}	0	0	A,B	ab
(1230)	$H_{2,rot} + N \rightarrow H_2 + N$	1.00×10^{-13}	0	0		ab
(1231)	$H_{2,rot} + O_2 \rightarrow H_2 + O_2$	1.00×10^{-13}	0	0	A	ab
(1232)	$H_{2,rot} + O_3 \rightarrow H_2 + O_3$	1.00×10^{-13}	0	0		ab
(1233)	$H_{2,rot} + O \rightarrow H_2 + O$	1.00×10^{-13}	0	0		ab
(1234)	$H_{2,rot} + H_2O \rightarrow H_2 + H_2O$	1.00×10^{-13}	0	0		ab
(1235)	$H_{2,rot} + H_2 \rightarrow H_2 + H_2$	1.00×10^{-13}	0	0		ab
(1236)	$H_{2,rot} + Ar \rightarrow H_2 + Ar$	1.00×10^{-13}	0	0	A,B	ab
(1237)	$H_2^* + N_2 \rightarrow H_2 + N_2$	1.00×10^{-13}	0	0	A,B	ab
(1238)	$H_2^* + N \rightarrow H_2 + N$	1.00×10^{-13}	0	0		ab
(1239)	$H_2^* + O_2 \rightarrow H_2 + O_2$	1.00×10^{-13}	0	0	A	ab
(1240)	$H_2^* + O_3 \rightarrow H_2 + O_3$	1.00×10^{-13}	0	0		ab

Nr	Reaction name	A^a	B^a	C^a	Set^b	Ref.
(1241)	$H_2^* + O \rightarrow H_2 + O$	1.00×10^{-13}	0	0		ab
(1242)	$H_2^* + H_2O \rightarrow H_2 + H_2O$	1.00×10^{-13}	0	0		ab
(1243)	$H_2^* + H_2 \rightarrow H_2 + H_2$	1.00×10^{-13}	0	0		ab
(1244)	$H_2^* + Ar \rightarrow H_2 + Ar$	1.00×10^{-13}	0	0	A,B	ab
(1245)	$H_2^+ + O \rightarrow H + OH^+$	1.50×10^{-09}	0	0		[121,180]
(1246)	$H_2^+ + O^- \rightarrow H_2 + O$	2.00×10^{-07}	-0.5	0		[105]
(1247)	$H_2^+ + O^- \rightarrow H + H + O$	1.00×10^{-07}	0	0		[105]
(1248)	$H_2^+ + O^- + M \rightarrow H_2O + M$	2.00×10^{-25}	-2.5	0		[105]
(1249)	$H_2^+ + O^- + M \rightarrow H_2 + O + M$	2.00×10^{-25}	-2.5	0		[105]
(1250)	$H_2^+ + O_2 \rightarrow H_2 + O_2^+$	8.00×10^{-10}	0	0	A,B	[121,180]
(1251)	$H_2^+ + O_2^- \rightarrow H_2 + O_2$	2.00×10^{-07}	-0.5	0		[105,177]
(1252)	$H_2^+ + O_2^- \rightarrow H + H + O_2$	1.00×10^{-07}	0	0		[105]
(1253)	$H_2^+ + O_2^- \rightarrow H_2 + O + O$	1.00×10^{-07}	0	0		[105]
(1254)	$H_2^+ + O_2^- \rightarrow H + H + O + O$	1.00×10^{-07}	0	0		[105]
(1255)	$H_2^+ + O_2^- + M \rightarrow H_2O_2 + M$	2.00×10^{-25}	-2.5	0		[105]
(1256)	$H_2^+ + O_2^- + M \rightarrow H_2 + O_2 + M$	2.00×10^{-25}	-2.5	0		[105]
(1257)	$H_2^+ + O_3^- \rightarrow H_2 + O_3$	2.00×10^{-07}	-0.5	0		[105]
(1258)	$H_2^+ + O_3^- \rightarrow H + H + O_3$	1.00×10^{-07}	0	0		[105]
(1259)	$H_2^+ + O_3^- \rightarrow H_2 + O_2 + O$	1.00×10^{-07}	0	0		[105]
(1260)	$H_2^+ + O_3^- \rightarrow H + H + O_2 + O$	1.00×10^{-07}	0	0		[105]
(1261)	$H_2^+ + O_3^- + M \rightarrow H_2 + O_3 + M$	2.00×10^{-25}	-2.5	0		[105]
(1262)	$H_2^+ + N \rightarrow N^+ + H_2$	5.00×10^{-10}	0	0		[185,273]
(1263)	$H_2^+ + NO \rightarrow NO^+ + H_2$	1.10×10^{-09}	0	0		[180]
(1264)	$H_2^+ + NO_2^- \rightarrow NO_2 + H_2$	2.00×10^{-07}	-0.5	0		[105,177]

Nr	Reaction name	A[a]	B[a]	C[a]	Set[b]	Ref.
(1265)	$H_2^+ + NO_2^- \rightarrow NO_2 + H + H$	1.00×10^{-07}	-0.5	0		[105]
(1266)	$H_2^+ + NO_2^- \rightarrow NO + O + H_2$	1.00×10^{-07}	-0.5	0		[105]
(1267)	$H_2^+ + NO_2^- \rightarrow NO + O + H + H$	1.00×10^{-07}	-0.5	0		[105]
(1268)	$H_2^+ + NO_2^- + M \rightarrow H_2 + NO_2 + M$	2.00×10^{-25}	-2.5	0		[105]
(1269)	$H_2^+ + NO_3^- \rightarrow NO_3 + H_2$	2.00×10^{-07}	-0.5	0		[105,177]
(1270)	$H_2^+ + NO_3^- \rightarrow NO_3 + H + H$	1.00×10^{-07}	-0.5	0		[105]
(1271)	$H_2^+ + NO_3^- \rightarrow NO_2 + O + H_2$	1.00×10^{-07}	-0.5	0		[105]
(1272)	$H_2^+ + NO_3^- \rightarrow NO_2 + O + H + H$	1.00×10^{-07}	-0.5	0		[105]
(1273)	$H_2^+ + NO_3^- + M \rightarrow H_2 + NO_3 + M$	2.00×10^{-25}	-2.5	0		[105]
(1274)	$H_2^+ + OH \rightarrow H_2 + OH^+$	7.60×10^{-10}	0	0		[121,180]
(1275)	$H_2^+ + OH \rightarrow H_2O^+ + H$	7.60×10^{-10}	0	0		[121,180]
(1276)	$H_2^+ + OH^- \rightarrow H_2 + OH$	2.00×10^{-07}	-0.5	0		[105,177]
(1277)	$H_2^+ + OH^- \rightarrow OH + H + H$	1.00×10^{-07}	0	0		[105]
(1278)	$H_2^+ + OH^- + M \rightarrow H_2 + OH + M$	2.00×10^{-25}	-2.5	0		[105]
(1279)	$H_2^+ + OH^- \rightarrow O + H + H_2$	1.00×10^{-07}	0	0		[105]
(1280)	$H_2^+ + OH^- \rightarrow O + H + H + H$	1.00×10^{-07}	0	0		[105]
(1281)	$H_2^+ + OH^- + M \rightarrow H_2 + OH + M$	2.00×10^{-25}	-2.5	0		[105]
(1282)	$H_2^+ + H_2O \rightarrow H_2 + H_2O^+$	3.90×10^{-09}	0	0	A	[121,180]
(1283)	$H_2^+ + H_2O \rightarrow H_3O^+ + H$	3.40×10^{-09}	0	0	A	[121,180]
(1284)	$H_2^+ + Ar \rightarrow ArH^+ + H$	2.30×10^{-09}	0	0	A,B	[300,301]
(1285)	$H_2^+ + Ar \rightarrow Ar^+ + H_2$	2.20×10^{-10}	0	0	A,B	[300]
(1286)	$H_3^+ + O \rightarrow H_2O^+ + H$	3.60×10^{-10}	0	0	A,B	[180,186]
(1287)	$H_3^+ + O \rightarrow OH^+ + H_2$	8.40×10^{-10}	0	0	A,B	[180,186]
(1288)	$H_3^+ + O^- \rightarrow O + H_2 + H$	1.00×10^{-07}	0	0		[105]

Nr	Reaction name	A^a	B^a	C^a	Set^b	Ref.
(1289)	$H_3^+ + O_2^- \rightarrow O_2 + H_2 + H$	1.00×10^{-07}	0	0		[105]
(1290)	$H_3^+ + O_3^- \rightarrow H_2 + H + O_3$	1.00×10^{-07}	0	0		[105]
(1291)	$H_3^+ + O_3^- \rightarrow H_2 + H + O_2 + O$	1.00×10^{-07}	0	0		[105]
(1292)	$H_3^+ + O_3^- + M \rightarrow H_2 + H + O_3 + M$	2.00×10^{-25}	-2.5	0		[105]
(1293)	$H_3^+ + NO_2^- \rightarrow NO^+ + OH + H_2$	1.10×10^{-09}	0	0	A	[180, 276]
(1294)	$H_3^+ + NO_2^- \rightarrow H_2 + H + NO_2$	1.00×10^{-07}	0	0		[105]
(1295)	$H_3^+ + NO_2^- \rightarrow H_2 + H + NO + O$	1.00×10^{-07}	0	0		[105]
(1296)	$H_3^+ + NO_3^- \rightarrow H_2 + H + NO_3$	1.00×10^{-07}	0	0		[105]
(1297)	$H_3^+ + NO_3^- \rightarrow H_2 + H + NO_2 + O$	1.00×10^{-07}	0	0		[105]
(1298)	$H_3^+ + OH^- \rightarrow H_2O^+ + H_2$	1.30×10^{-09}	0	0	A	[121, 180]
(1299)	$H_3^+ + OH^- \rightarrow OH + H + H_2$	1.00×10^{-07}	0	0		[105, 177]
(1300)	$H_3^+ + OH^- \rightarrow O + H + H + H_2$	1.00×10^{-07}	0	0		[105, 177]
(1301)	$H_3^+ + H_2O \rightarrow H_3O^+ + H_2$	5.90×10^{-09}	0	0	A,B	[121, 180]
(1302)	$H_3^+ + Ar \rightarrow ArH^+ + H_2$	1.00×10^{-11}	0	0	A,B	[186, 300]
(1303)	$OH + O \rightarrow H + O_2$	1.81×10^{-11}	-0.31	-177	A,B	[283]
(1304)	$OH + O(^1D) \rightarrow H + O_2$	2.08×10^{-11}	-0.186	154	A,B	[121]
(1305)	$OH + O^+ \rightarrow OH^+ + O$	3.60×10^{-10}	0	0	A	[121, 180]
(1306)	$OH + O^+ \rightarrow O_2^+ + H$	3.60×10^{-10}	0	0		[121, 180]
(1307)	$OH + O_2^- \rightarrow OH^- + O_2$	1.00×10^{-10}	0	0	A,B	[121]
(1308)	$OH + O_3 \rightarrow HO_2 + O_2$	1.69×10^{-12}	0	941	A,B	[121, 283]
(1309)	$OH + N \rightarrow H + NO$	4.70×10^{-11}	0	0	A,B	[111, 112]
(1310)	$OH + N \rightarrow NH + O$	1.88×10^{-11}	0.1	10700		[180]
(1311)	$OH + N^+ \rightarrow N + OH^+$	3.70×10^{-11}	0	0		[180]
(1312)	$OH + N^+ \rightarrow NO^+ + H$	3.40×10^{-11}	0	0		[191]

Nr	Reaction name	A^a	B^a	C^a	Set^b	Ref.
(1313)	$OH + N_2(A) \rightarrow OH(A) + N_2$	1.00×10^{-10}	0	0	A,B	[110, 302]
(1314)	$OH + N_2(A) \rightarrow O + H + N_2$	1.00×10^{-11}	0	0		[302]
(1315)	$OH + N_2(a') \rightarrow OH(A) + N_2$	1.00×10^{-10}	0	0	A,B	ax
(1316)	$OH + N_2(a') \rightarrow O + H + N_2$	1.00×10^{-11}	0	0		ay
(1317)	$OH + N_2^+ \rightarrow OH^+ + N_2$	6.30×10^{-10}	0	0	A,B	[180]
(1318)	$OH + NO \rightarrow H + NO_2$	5.20×10^{-12}	0	15100		[180]
(1319)	$OH + NO + Ar \rightarrow HNO_2 + Ar$	7.40×10^{-31}	-2.4	0	A,B	g
(1320)	$OH + NO + N_2 \rightarrow HNO_2 + N_2$	7.40×10^{-31}	-2.4	0	A,B	[109]
(1321)	$OH + NO + O_2 \rightarrow HNO_2 + O_2$	7.40×10^{-31}	-2.4	0	A	[109]
(1322)	$OH + NO + H_2 \rightarrow HNO_2 + H_2$	1.50×10^{-30}	-2.4	0		g
(1323)	$OH + NO + H_2O \rightarrow HNO_2 + H_2O$	3.50×10^{-30}	-2.4	0		g
(1324)	$OH + NO + O_3 \rightarrow HNO_2 + O_3$	1.50×10^{-30}	-2.4	0		g
(1325)	$OH + NO_2 \rightarrow HO_2 + NO$	3.00×10^{-11}	0	3360		[115, 291]
(1326)	$OH + NO_2 + Ar \rightarrow HNO_3 + Ar$	4.60×10^{-29}	-5.49	1180	A,B	g
(1327)	$OH + NO_2 + O_2 \rightarrow HNO_3 + O_2$	4.60×10^{-29}	-5.49	1180	A	g
(1328)	$OH + NO_2 + N_2 \rightarrow HNO_3 + N_2$	4.60×10^{-29}	-5.49	1180	A,B	[283]
(1329)	$OH + NO_2 + H_2 \rightarrow HNO_3 + H_2$	9.20×10^{-29}	-5.49	1180		g
(1330)	$OH + NO_2 + H_2O \rightarrow HNO_3 + H_2O$	2.30×10^{-28}	-5.49	1180		g
(1331)	$OH + NO_2 + O_3 \rightarrow HNO_3 + O_3$	9.20×10^{-29}	-5.49	1180		g
(1332)	$OH + N_2O \rightarrow HNO + NO$	3.80×10^{-17}	0	0	A,B	[179, 187]
(1333)	$OH + N_2O \rightarrow HO_2 + N_2$	3.69×10^{-13}	0	2740	A,B	[180, 183]
(1334)	$OH + NO_3 \rightarrow HO_2 + NO_2$	2.00×10^{-11}	0	0	A	[112, 188]
(1335)	$OH + N_2O_5 \rightarrow HNO_3 + NO_3$	2.85×10^{-15}	0	0		[112, 303]
(1336)	$OH + N_2O_5 \rightarrow HO_2 + NO_2 + NO_2$	2.85×10^{-15}	0	0		[112, 303]

Nr	Reaction name	A^a	B^a	C^a	Set^b	Ref.
(1337)	$OH + OH \rightarrow H_2O + O$	5.49×10^{-14}	2.42	-970	A,B	[109]
(1338)	$OH + OH + Ar \rightarrow H_2O_2 + Ar$	8.00×10^{-31}	-0.8	0	A,B	g
(1339)	$OH + OH + N_2 \rightarrow H_2O_2 + N_2$	8.00×10^{-31}	-0.9	0	A,B	[283]
(1340)	$OH + OH + O_2 \rightarrow H_2O_2 + O_2$	8.00×10^{-31}	-0.9	0	A	g
(1341)	$OH + OH + H_2 \rightarrow H_2O_2 + H_2$	1.60×10^{-30}	-0.9	0		g
(1342)	$OH + OH + H_2O \rightarrow H_2O_2 + H_2O$	4.00×10^{-30}	-0.9	0		g
(1343)	$OH + OH + O_3 \rightarrow H_2O_2 + O_3$	1.60×10^{-30}	-0.9	0		g
(1344)	$OH + OH(A) \rightarrow H_2O + O$	1.50×10^{-11}	-0.37	0		[121]
(1345)	$OH + OH^+ \rightarrow H_2O^+ + O$	7.00×10^{-10}	0	0		[121,180]
(1346)	$OH + HO_2 \rightarrow H_2O + O_2$	4.80×10^{-11}	0	-250	A,B	[112,280]
(1347)	$OH + H_2O^+ \rightarrow H_3O^+ + O$	6.90×10^{-10}	0	0		[121,180]
(1348)	$OH + H_2O_2 \rightarrow H_2O + HO_2$	4.53×10^{-12}	0	288.9	A,B	[121,183]
(1349)	$OH + NH \rightarrow N + H_2O$	3.12×10^{-12}	1.2	0	A	[288,291]
(1350)	$OH + NH \rightarrow H_2 + NO$	4.00×10^{-11}	0	0	A,B	[109,288] an
(1351)	$OH + NH \rightarrow HNO + H$	4.00×10^{-11}	0	0	A,B	[109,293] an
(1352)	$OH + HNO \rightarrow H_2O + NO$	8.00×10^{-11}	0	500	A,B	[110,115]
(1353)	$OH + HNO_2 \rightarrow H_2O + NO_2$	2.70×10^{-12}	0	-260	A,B	[111,112]
(1354)	$OH + HNO_3 \rightarrow H_2O + NO_3$	1.50×10^{-13}	0	0	A,B	[188,191]
(1355)	$OH + HNO_4 \rightarrow H_2O_2 + NO_3$	1.90×10^{-13}	0	-270	A,B	[188] az
(1356)	$OH + HNO_4 \rightarrow H_2O + NO_2 + O_2$	1.71×10^{-12}	0	-270	A,B	[188] az
(1357)	$OH(A) + H_2O_2 \rightarrow HO_2 + H_2O$	1.47×10^{-10}	0	0	A,B	[121,304]
(1358)	$OH(A) + Ar \rightarrow OH + Ar$	1.44×10^{-15}	-0.5	0		[192]
(1359)	$OH(A) + O_2 \rightarrow OH + O_2$	2.49×10^{-13}	-0.5	0	A	[192]
(1360)	$OH(A) + N_2 \rightarrow OH + N_2$	2.49×10^{-14}	-0.5	0	A	a

Nr	Reaction name	A^a	B^a	C^a	Set^b	Ref.
(1361)	$OH(A) + H_2O \rightarrow OH + H_2O$	7.61×10^{-10}	-0.5	0	A,B	[306]
(1362)	$OH(A) + H_2 \rightarrow OH + H_2$	7.10×10^{-11}	0	0		[305]
(1363)	$OH^+ + O \rightarrow O_2^+ + H$	7.10×10^{-10}	0	0	A,B	[121, 180]
(1364)	$OH^+ + O^- \rightarrow O + OH$	2.00×10^{-07}	-0.5	0		[105]
(1365)	$OH^+ + O^- \rightarrow O + H + O$	1.00×10^{-07}	0	0		[105]
(1366)	$OH^+ + O^- + M \rightarrow OH + O + M$	2.00×10^{-25}	-2.5	0	A	[105]
(1367)	$OH^+ + O^- + M \rightarrow HO_2 + M$	2.00×10^{-25}	-2.5	0	A	[105]
(1368)	$OH^+ + O_3^- \rightarrow OH + O_3$	2.00×10^{-07}	-0.5	0		[105]
(1369)	$OH^+ + O_3^- \rightarrow O + H + O_3$	1.00×10^{-07}	0	0		[105]
(1370)	$OH^+ + O_3^- \rightarrow OH + O_2 + O$	1.00×10^{-07}	0	0		[105]
(1371)	$OH^+ + O_3^- \rightarrow O + H + O_2 + O$	1.00×10^{-07}	0	0		[105]
(1372)	$OH^+ + O_3^- + M \rightarrow OH + O_3 + M$	2.00×10^{-25}	-2.5	0		[105]
(1373)	$OH^+ + O_2 \rightarrow OH + O_2^+$	3.80×10^{-10}	0	0	A,B	[121, 183]
(1374)	$OH^+ + O_2^- \rightarrow OH + O_2$	2.00×10^{-07}	-0.5	0		[121]
(1375)	$OH^+ + O_2^- \rightarrow O + H + O_2$	1.00×10^{-07}	0	0		[105]
(1376)	$OH^+ + O_2^- \rightarrow OH + O + O$	1.00×10^{-07}	0	0		[105]
(1377)	$OH^+ + O_2^- \rightarrow O + H + O + O$	1.00×10^{-07}	0	0		[105]
(1378)	$OH^+ + O_2^- + M \rightarrow OH + O_2 + M$	2.00×10^{-25}	-2.5	0		[105]
(1379)	$OH^+ + N \rightarrow NO^+ + H$	8.90×10^{-10}	0	0	A,B	[180]
(1380)	$OH^+ + NO \rightarrow NO^+ + OH$	6.70×10^{-10}	0	0		[307]
(1381)	$OH^+ + NO_2 \rightarrow NO_2^+ + OH$	3.00×10^{-10}	0	0		[191]
(1382)	$OH^+ + NO_2^- \rightarrow NO_2 + OH$	2.00×10^{-07}	-0.5	0		[105, 177]
(1383)	$OH^+ + NO_2^- \rightarrow NO_2 + O + H$	1.00×10^{-07}	0	0		[105]
(1384)	$OH^+ + NO_2^- \rightarrow NO + O + OH$	1.00×10^{-07}	0	0		[105]

Nr	Reaction name	A^a	B^a	C^a	Set^b	Ref.
(1385)	$OH^+ + NO_2^- \rightarrow NO + O + O + H$	1.00×10^{-07}	0	0		[105]
(1386)	$OH^+ + NO_2^- + M \rightarrow OH + NO_2 + M$	2.00×10^{-25}	-2.5	0		[105]
(1387)	$OH^+ + NO_2^- + M \rightarrow HNO_3 + M$	2.00×10^{-25}	-2.5	0	A	[105]
(1388)	$OH^+ + N_2O \rightarrow NO^+ + HNO$	1.72×10^{-10}	0	0		[308]
(1389)	$OH^+ + NO_3^- \rightarrow NO_3 + OH$	2.00×10^{-07}	-0.5	0		[105, 177]
(1390)	$OH^+ + NO_3^- \rightarrow NO_3 + O + H$	1.00×10^{-07}	0	0		[105]
(1391)	$OH^+ + NO_3^- \rightarrow NO_2 + O + OH$	1.00×10^{-07}	0	0		[105]
(1392)	$OH^+ + NO_3^- \rightarrow NO_2 + O + O + H$	1.00×10^{-07}	0	0		[105]
(1393)	$OH^+ + NO_3^- + M \rightarrow OH + NO_3 + M$	2.00×10^{-25}	-2.5	0		[105]
(1394)	$OH^+ + NO_3^- + M \rightarrow HNO_4 + M$	2.00×10^{-25}	-2.5	0	A,B	[105]
(1395)	$OH^+ + OH^- \rightarrow OH + OH$	2.00×10^{-07}	-0.5	0		[105, 177]
(1396)	$OH^+ + OH^- \rightarrow OH + O + H$	1.00×10^{-07}	0	0		[105]
(1397)	$OH^+ + OH^- \rightarrow O + H + O + H$	1.00×10^{-07}	0	0		[105]
(1398)	$OH^+ + OH^- + M \rightarrow OH + OH + M$	2.00×10^{-25}	-2.5	0		[105]
(1399)	$OH^+ + OH^- + M \rightarrow H_2O_2 + M$	2.00×10^{-25}	-2.5	0	A,B	[105]
(1400)	$OH^+ + H_2O \rightarrow H_2O^+ + OH$	1.60×10^{-09}	0	0	A,B	[180, 191]
(1401)	$OH^+ + H_2O \rightarrow H_3O^+ + O$	1.30×10^{-09}	0	0	A,B	[180]
(1402)	$OH^- + O \rightarrow HO_2 + e^-$	4.00×10^{-10}	0.5	0	A,B	[183]
(1403)	$OH^- + O^+ \rightarrow OH + O$	2.00×10^{-07}	-0.5	0		[105, 177]
(1404)	$OH^- + O^+ \rightarrow O + H + O$	1.00×10^{-07}	0	0		[105]
(1405)	$OH^- + O^+ + M \rightarrow OH + O + M$	2.00×10^{-25}	-2.5	0		[105]
(1406)	$OH^- + O^+ + M \rightarrow HO_2 + M$	2.00×10^{-25}	-2.5	0	A,B	[105]
(1407)	$OH^- + O_2^+ \rightarrow OH + O_2$	2.00×10^{-07}	-0.5	0	A	[105, 177]
(1408)	$OH^- + O_2^+ \rightarrow O + H + O_2$	1.00×10^{-07}	0	0		[105]

Nr	Reaction name	A^a	B^a	C^a	Set^b	Ref.
(1409)	$OH^- + O_2^+ \rightarrow OH + O + O$	1.00×10^{-07}	0	0		[105]
(1410)	$OH^- + O_2^+ \rightarrow O + H + O + O$	1.00×10^{-07}	0	0		[105]
(1411)	$OH^- + O_2^+ + M \rightarrow OH + O_2 + M$	2.00×10^{-25}	-2.5	0	A,B	[105]
(1412)	$OH^- + O_3 \rightarrow O_2 + HO_2$	1.08×10^{-11}	0	0	A,B	[190]
(1413)	$OH^- + O_4^+ \rightarrow OH + O_2 + O_2$	1.00×10^{-07}	0	0		[105]
(1414)	$OH^- + O_4^+ \rightarrow O + H + O_2 + O_2$	1.00×10^{-07}	0	0		[105]
(1415)	$OH^- + O_4^+ + M \rightarrow OH + O_2 + O_2 + M$	2.00×10^{-25}	-2.5	0		[105]
(1416)	$OH^- + N \rightarrow HNO + e^-$	1.00×10^{-11}	-0.5	0	A,B	[186, 276]
(1417)	$OH^- + N^+ \rightarrow OH + N$	2.00×10^{-07}	-0.5	0		[105, 177]
(1418)	$OH^- + N^+ \rightarrow O + H + N$	1.00×10^{-07}	0	0		[105]
(1419)	$OH^- + N^+ + M \rightarrow OH + N + M$	2.00×10^{-25}	-2.5	0		[105]
(1420)	$OH^- + N^+ + M \rightarrow HNO + M$	2.00×10^{-25}	-2.5	0		[105]
(1421)	$OH^- + N_2^+ \rightarrow OH + N_2$	2.00×10^{-07}	-0.5	0		[105, 177]
(1422)	$OH^- + N_2^+ \rightarrow O + H + N_2$	1.00×10^{-07}	0	0		[105]
(1423)	$OH^- + N_2^+ \rightarrow OH + N + N$	1.00×10^{-07}	0	0		[105]
(1424)	$OH^- + N_2^+ \rightarrow O + H + N + N$	1.00×10^{-07}	0	0		[105]
(1425)	$OH^- + N_2^+ + M \rightarrow OH + N_2 + M$	2.00×10^{-25}	-2.5	0		[105]
(1426)	$OH^- + N_3^+ \rightarrow OH + N + N_2$	1.00×10^{-07}	0	0		[105]
(1427)	$OH^- + N_3^+ \rightarrow O + H + N + N_2$	1.00×10^{-07}	0	0		[105]
(1428)	$OH^- + N_4^+ \rightarrow OH + N_2 + N_2$	1.00×10^{-07}	0	0		[105]
(1429)	$OH^- + N_4^+ \rightarrow O + H + N_2 + N_2$	1.00×10^{-07}	0	0		[105]
(1430)	$OH^- + NO^+ \rightarrow OH + NO$	2.00×10^{-07}	-0.5	0		[105, 177]
(1431)	$OH^- + NO^+ \rightarrow O + H + NO$	1.00×10^{-07}	0	0		[105]
(1432)	$OH^- + NO^+ \rightarrow OH + N + O$	1.00×10^{-07}	0	0		[105]

Nr	Reaction name	A^a	B^a	C^a	Set^b	Ref.
(1433)	$OH^- + NO^+ \rightarrow O + H + N + O$	1.00×10^{-07}	0	0		[105]
(1434)	$OH^- + NO^+ + M \rightarrow OH + NO + M$	2.00×10^{-25}	-2.5	0	A	[105]
(1435)	$OH^- + NO^+ + M \rightarrow HNO_2 + M$	2.00×10^{-25}	-2.5	0	A,B	[105]
(1436)	$OH^- + NO_2 \rightarrow NO_2^- + OH$	1.10×10^{-09}	-0.5	0	A,B	[186]
(1437)	$OH^- + NO_2^+ \rightarrow OH + NO_2$	2.00×10^{-07}	-0.5	0		[105, 177]
(1438)	$OH^- + NO_2^+ \rightarrow O + H + NO_2$	1.00×10^{-07}	0	0		[105]
(1439)	$OH^- + NO_2^+ \rightarrow OH + NO + O$	1.00×10^{-07}	0	0		[105]
(1440)	$OH^- + NO_2^+ \rightarrow O + H + NO + O$	1.00×10^{-07}	0	0		[105]
(1441)	$OH^- + NO_2^+ + M \rightarrow OH + NO_2 + M$	2.00×10^{-25}	-2.5	0	A	[105]
(1442)	$OH^- + NO_2^+ + M \rightarrow HNO_3 + M$	2.00×10^{-25}	-2.5	0	A,B	[105]
(1443)	$OH^- + H_2O^+ \rightarrow OH + H_2O$	2.00×10^{-07}	-0.5	0		[105, 177]
(1444)	$OH^- + H_2O^+ \rightarrow O + H + H_2O$	1.00×10^{-07}	0	0		[105]
(1445)	$OH^- + H_2O^+ \rightarrow OH + OH + H$	1.00×10^{-07}	0	0		[105]
(1446)	$OH^- + H_2O^+ \rightarrow O + H + OH + H$	1.00×10^{-07}	0	0		[105]
(1447)	$OH^- + H_2O^+ + M \rightarrow OH + H_2O + M$	2.00×10^{-25}	-2.5	0	A,B	[105]
(1448)	$OH^- + H_3O^+ \rightarrow OH + H_2O + H$	1.00×10^{-07}	0	0		[105]
(1449)	$OH^- + H_3O^+ \rightarrow O + H + H_2O + H$	1.00×10^{-07}	0	0		[105]
(1450)	$OH^- + ArH^+ \rightarrow Ar + H + OH$	1.00×10^{-07}	0	0		[105]
(1451)	$OH^- + ArH^+ \rightarrow Ar + H + O + H$	1.00×10^{-07}	0	0		[105]
(1452)	$HO_2 + O \rightarrow OH + O_2$	2.71×10^{-11}	0	-224	A,B	[112, 291]
(1453)	$HO_2 + O(^1D) \rightarrow OH + O_2$	2.70×10^{-11}	0	-224		[121, 297]
(1454)	$HO_2 + O_2(a) \rightarrow OH + O_2 + O$	1.66×10^{-11}	0	0	A,B	[121, 191]
(1455)	$HO_2 + O_2(b) \rightarrow OH + O_2 + O$	1.66×10^{-11}	0	0		ba
(1456)	$HO_2 + O_3 \rightarrow OH + O_2 + O_2$	1.40×10^{-14}	0	600	A,B	[112, 297]

Nr	Reaction name	A^a	B^a	C^a	Set^b	Ref.
(1457)	$HO_2 + N \rightarrow OH + NO$	2.20×10^{-11}	0	0	A,B	[111, 112]
(1458)	$HO_2 + N \rightarrow NH + O_2$	1.70×10^{-13}	0	0	A,B	[180]
(1459)	$HO_2 + NO \rightarrow HNO + O_2$	9.10×10^{-19}	0	-2819	A,B	[183, 280]
(1460)	$HO_2 + NO + Ar \rightarrow HNO_3 + Ar$	5.60×10^{-33}	0	0	A,B	g
(1461)	$HO_2 + NO + N_2 \rightarrow HNO_3 + N_2$	5.60×10^{-33}	0	0	A	[274]
(1462)	$HO_2 + NO + O_2 \rightarrow HNO_3 + O_2$	5.60×10^{-33}	0	0		g
(1463)	$HO_2 + NO + H_2 \rightarrow HNO_3 + H_2$	1.20×10^{-32}	0	0		g
(1464)	$HO_2 + NO + H_2O \rightarrow HNO_3 + H_2O$	2.60×10^{-32}	0	0		g
(1465)	$HO_2 + NO + O_3 \rightarrow HNO_3 + O_3$	1.20×10^{-32}	0	0		g
(1466)	$HO_2 + NO_2 \rightarrow HNO_2 + O_2$	1.20×10^{-13}	0	0		[183, 278]
(1467)	$HO_2 + NO_2 + Ar \rightarrow HNO_2 + O_2 + Ar$	1.80×10^{-31}	-3.2	0		g
(1468)	$HO_2 + NO_2 + N_2 \rightarrow HNO_2 + O_2 + N_2$	1.80×10^{-31}	-3.2	0	A,B	[112]
(1469)	$HO_2 + NO_2 + O_2 \rightarrow HNO_2 + O_2 + O_2$	1.80×10^{-31}	-3.2	0	A	g
(1470)	$HO_2 + NO_2 + H_2 \rightarrow HNO_2 + O_2 + H_2$	4.00×10^{-31}	-3.2	0		g
(1471)	$HO_2 + NO_2 + H_2O \rightarrow HNO_2 + O_2 + H_2O$	1.00×10^{-30}	-3.55	635		g
(1472)	$HO_2 + NO_2 + O_3 \rightarrow HNO_2 + O_2 + O_3$	4.00×10^{-31}	-3.2	0		g
(1473)	$HO_2 + NO_2 + Ar \rightarrow HNO_4 + Ar$	2.20×10^{-31}	-4.6	0	A,B	g
(1474)	$HO_2 + NO_2 + N_2 \rightarrow HNO_4 + N_2$	2.20×10^{-31}	-4.6	0	A,B	[109]
(1475)	$HO_2 + NO_2 + O_2 \rightarrow HNO_4 + O_2$	2.20×10^{-31}	-4.6	0	A	[109]
(1476)	$HO_2 + NO_2 + H_2 \rightarrow HNO_4 + H_2$	4.40×10^{-31}	-4.6	0		g
(1477)	$HO_2 + NO_2 + H_2O \rightarrow HNO_4 + H_2O$	1.00×10^{-30}	-4.6	0		g
(1478)	$HO_2 + NO_2 + O_3 \rightarrow HNO_4 + O_3$	4.40×10^{-31}	-4.6	0		g
(1479)	$HO_2 + NO_3 \rightarrow HNO_3 + O_2$	2.30×10^{-12}	0	-170		[277, 309]
(1480)	$HO_2 + NO_3 \rightarrow OH + NO_2 + O_2$	4.00×10^{-12}	0	0		[111, 112]

Nr	Reaction name	A^a	B^a	C^a	Set^b	Ref.
(1481)	$HO_2 + HO_2 \rightarrow H_2O_2 + O_2$	2.20×10^{-13}	0	-600		[188, 280]
(1482)	$HO_2 + HO_2 + Ar \rightarrow H_2O_2 + O_2 + Ar$	1.90×10^{-33}	0	-980		g
(1483)	$HO_2 + HO_2 + O_2 \rightarrow H_2O_2 + O_2 + O_2$	1.90×10^{-33}	0	-980		[274]
(1484)	$HO_2 + HO_2 + N_2 \rightarrow H_2O_2 + O_2 + N_2$	1.90×10^{-33}	0	-980		[274]
(1485)	$HO_2 + HO_2 + H_2 \rightarrow H_2O_2 + O_2 + H_2$	4.00×10^{-33}	0	-980		g
(1486)	$HO_2 + HO_2 + H_2O \rightarrow H_2O_2 + O_2 + H_2O$	1.00×10^{-32}	0	-980		g
(1487)	$HO_2 + HO_2 + O_3 \rightarrow H_2O_2 + O_2 + O_3$	4.00×10^{-33}	0	-980		g
(1488)	$HO_2 + H_2O \rightarrow H_2O_2 + OH$	4.65×10^{-11}	0	16500		[180]
(1489)	$HO_2 + H_2O_2 \rightarrow OH + H_2O + O_2$	1.00×10^{-16}	0	0		[283]
(1490)	$HO_2 + NH \rightarrow HNO + OH$	2.50×10^{-14}	0	0		[112] z
(1491)	$H_2O + O \rightarrow OH + OH$	1.67×10^{-11}	1.14	8680		[180, 274]
(1492)	$H_2O + O(^1D) \rightarrow H_2 + O_2$	2.20×10^{-12}	0	0	A	[121, 188]
(1493)	$H_2O + O^+ \rightarrow H_2O^+ + O$	2.60×10^{-09}	0	0	A,B	[121, 183]
(1494)	$H_2O + O^- \rightarrow H_2O_2 + e^-$	6.00×10^{-13}	0	0	A,B	[121, 186]
(1495)	$H_2O + O_2^- \rightarrow H_2O + O_2 + e^-$	5.00×10^{-09}	0	5000	A	[121, 183]
(1496)	$H_2O + N(^2D) \rightarrow OH + NH$	2.50×10^{-10}	0	0	A,B	[111, 112]
(1497)	$H_2O + N^+ \rightarrow H_2O^+ + N$	2.90×10^{-09}	-0.52	0	A,B	[113, 186]
(1498)	$H_2O + N^+ \rightarrow NO^+ + H_2$	4.00×10^{-10}	0.52	0	A	[191]
(1499)	$H_2O + N_2(A) \rightarrow OH + N_2 + H$	6.00×10^{-14}	0	0		[111, 297]
(1500)	$H_2O + N_2(a') \rightarrow OH + N_2 + H$	5.00×10^{-14}	0	0		[183]
(1501)	$H_2O + N_2^+ \rightarrow H_2O^+ + N_2$	1.80×10^{-09}	0	0	A,B	[113, 186]
(1502)	$H_2O + N_4^+ \rightarrow H_2O^+ + N_2 + N_2$	2.80×10^{-09}	0	0	A,B	[113, 186]
(1503)	$H_2O + NO + NO_2 \rightarrow HNO_2 + HNO_2$	4.41×10^{-40}	0	0		[310]
(1504)	$H_2O + N_2O_3 \rightarrow HNO_2 + HNO_2$	6.29×10^{-11}	0	4471	A,B	[283]

Nr	Reaction name	A^a	B^a	C^a	Set^b	Ref.
(1505)	$H_2O + N_2O_4 \rightarrow HNO_3 + HNO_2$	4.18×10^{-10}	0	5830		[283]
(1506)	$H_2O + N_2O_5 \rightarrow HNO_3 + HNO_3$	2.50×10^{-22}	0	0	A	[179, 294]
(1507)	$H_2O + H_2O^+ \rightarrow H_3O^+ + OH$	1.86×10^{-09}	0	0	A,B	[121, 183]
(1508)	$H_2O + NH \rightarrow HNO + H_2$	3.32×10^{-11}	0	6974.2		[288, 293]
(1509)	$H_2O + ArH^+ \rightarrow H_3O^+ + Ar$	2.00×10^{-09}	0	0	A,B	[190]
(1510)	$H_2O_{vib} + N_2 \rightarrow H_2O + N_2$	1.00×10^{-13}	0	0	A,B	ab
(1511)	$H_2O_{vib} + N \rightarrow H_2O + N$	1.00×10^{-13}	0	0		ab
(1512)	$H_2O_{vib} + O_2 \rightarrow H_2O + O_2$	1.00×10^{-13}	0	0	A	ab
(1513)	$H_2O_{vib} + O_3 \rightarrow H_2O + O_3$	1.00×10^{-13}	0	0		ab
(1514)	$H_2O_{vib} + O \rightarrow H_2O + O$	1.00×10^{-13}	0	0		ab
(1515)	$H_2O_{vib} + H_2O \rightarrow H_2O + H_2O$	1.00×10^{-13}	0	0		ab
(1516)	$H_2O_{vib} + H_2 \rightarrow H_2O + H_2$	1.00×10^{-13}	0	0		ab
(1517)	$H_2O_{vib} + Ar \rightarrow H_2O + Ar$	1.00×10^{-13}	0	0	A,B	ab
(1518)	$H_2O^+ + O \rightarrow H_2 + O_2^+$	5.50×10^{-11}	0	0		[121, 191]
(1519)	$H_2O^+ + O^- \rightarrow H_2O + O$	2.00×10^{-07}	-0.5	0		[105]
(1520)	$H_2O^+ + O^- \rightarrow OH + H + O$	1.00×10^{-07}	0	0		[105, 185]
(1521)	$H_2O^+ + O^- + M \rightarrow H_2O + O + M$	2.00×10^{-25}	-2.5	0	A	[105]
(1522)	$H_2O^+ + O^- + M \rightarrow H_2O_2 + M$	2.00×10^{-25}	-2.5	0	A,B	[105]
(1523)	$H_2O^+ + O_2 \rightarrow H_2O + O_2^+$	3.30×10^{-10}	0	0	A,B	[121, 183]
(1524)	$H_2O^+ + O_2^- \rightarrow H_2O + O_2$	2.00×10^{-07}	-0.5	0		[105]
(1525)	$H_2O^+ + O_2^- \rightarrow OH + H + O_2$	1.00×10^{-07}	0	0		[105, 185]
(1526)	$H_2O^+ + O_2^- \rightarrow H_2O + O + O$	1.00×10^{-07}	0	0		[105]
(1527)	$H_2O^+ + O_2^- \rightarrow H + OH + O + O$	1.00×10^{-07}	0	0		[105]
(1528)	$H_2O^+ + O_2^- + M \rightarrow H_2O + O_2 + M$	2.00×10^{-25}	-2.5	0	A	[105]

Nr	Reaction name	A^a	B^a	C^a	Set^b	Ref.
(1529)	$H_2O^+ + O_3^- \rightarrow H_2O + O_3$	2.00×10^{-07}	-0.5	0	A	[105]
(1530)	$H_2O^+ + O_3^- \rightarrow OH + H + O_3$	1.00×10^{-07}	0	0		[105]
(1531)	$H_2O^+ + O_3^- \rightarrow H_2O + O_2 + O$	1.00×10^{-07}	0	0		[105]
(1532)	$H_2O^+ + O_3^- \rightarrow OH + H + O_2 + O$	1.00×10^{-07}	0	0		[105]
(1533)	$H_2O^+ + O_3^- + M \rightarrow H_2O + O_3 + M$	2.00×10^{-25}	-2.5	0	A,B	[105]
(1534)	$H_2O^+ + N \rightarrow NO^+ + H_2$	2.80×10^{-11}	0	0	A	[180]
(1535)	$H_2O^+ + NO \rightarrow NO^+ + H_2O$	2.70×10^{-10}	0	0		[180]
(1536)	$H_2O^+ + NO_2 \rightarrow NO_2^+ + H_2O$	1.20×10^{-09}	0	0	A,B	[183]
(1537)	$H_2O^+ + NO_2^- \rightarrow H_2O + NO_2$	2.00×10^{-07}	-0.5	0		[105]
(1538)	$H_2O^+ + NO_2^- \rightarrow OH + H + NO_2$	1.00×10^{-07}	0	0		[105]
(1539)	$H_2O^+ + NO_2^- \rightarrow H_2O + NO + O$	1.00×10^{-07}	0	0		[105]
(1540)	$H_2O^+ + NO_2^- \rightarrow H + OH + NO + O$	1.00×10^{-07}	0	0		[105]
(1541)	$H_2O^+ + NO_2^- + M \rightarrow H_2O + NO_2 + M$	2.00×10^{-25}	-2.5	0	A	[105]
(1542)	$H_2O^+ + NO_3^- \rightarrow H_2O + NO_3$	2.00×10^{-07}	-0.5	0		[105]
(1543)	$H_2O^+ + NO_3^- \rightarrow OH + H + NO_3$	1.00×10^{-07}	0	0		[105]
(1544)	$H_2O^+ + NO_3^- \rightarrow H_2O + NO_2 + O$	1.00×10^{-07}	0	0		[105]
(1545)	$H_2O^+ + NO_3^- \rightarrow OH + H + NO_2 + O$	1.00×10^{-07}	0	0		[105]
(1546)	$H_2O^+ + NO_3^- + M \rightarrow H_2O + NO_3 + M$	2.00×10^{-25}	-2.5	0	A,B	[105]
(1547)	$H_2O^+ + NH \rightarrow H_3O^+ + N$	7.10×10^{-10}	0	0		[180]
(1548)	$H_3O^+ + O^- \rightarrow H_2O + H + O$	1.00×10^{-07}	0	0	A	[105]
(1549)	$H_3O^+ + O_2^- \rightarrow H_2O + H + O_2$	1.00×10^{-07}	0	0	A,B	[105]
(1550)	$H_3O^+ + O_2^- \rightarrow H_2O + H + O + O$	1.00×10^{-07}	0	0	A,B	[105]
(1551)	$H_3O^+ + O_3^- \rightarrow H_2O + H + O_3$	1.00×10^{-07}	0	0		[105]
(1552)	$H_3O^+ + O_3^- \rightarrow H_2O + H + O_2 + O$	1.00×10^{-07}	0	0		[105]

Nr	Reaction name	A^a	B^a	C^a	Set^b	Ref.
(1553)	$H_3O^+ + NO \rightarrow H_2O + H + NO^+$	1.50×10^{-12}	0	0	A,B	[113]
(1554)	$H_3O^+ + NO_2^- \rightarrow H_2O + H + NO_2$	1.00×10^{-07}	0	0		[105]
(1555)	$H_3O^+ + NO_2^- \rightarrow H_2O + H + NO + O$	1.00×10^{-07}	0	0		[105]
(1556)	$H_3O^+ + NO_3^- \rightarrow H_2O + H + NO_3$	1.00×10^{-07}	0	0		[105]
(1557)	$H_3O^+ + NO_3^- \rightarrow H_2O + H + NO_2 + O$	1.00×10^{-07}	0	0		[105]
(1558)	$H_2O_2 + O \rightarrow HO_2 + OH$	1.79×10^{-13}	2.92	1394	A,B	[121, 183]
(1559)	$H_2O_2 + O \rightarrow H_2O + O_2$	1.45×10^{-15}	0	0	A,B	[280, 282]
(1560)	$H_2O_2 + O(^1D) \rightarrow H_2O + O_2$	5.20×10^{-10}	0	0		[121, 183]
(1561)	$H_2O_2 + O_2 \rightarrow HO_2 + HO_2$	9.00×10^{-11}	0	20000		[187, 278]
(1562)	$H_2O_2 + N_2(A) \rightarrow OH + OH + N_2$	5.00×10^{-14}	0	0		[297]
(1563)	$H_2O_2 + N_2(a') \rightarrow OH + OH + N_2$	3.00×10^{-10}	0	0	A,B	[297]
(1564)	$H_2O_2 + NO_3 \rightarrow HO_2 + HNO_3$	4.10×10^{-16}	0	0	A,B	[183]
(1565)	$NH + O \rightarrow H + NO$	1.16×10^{-10}	0	0	A,B	[288, 291]
(1566)	$NH + O \rightarrow OH + N$	1.16×10^{-11}	0	0	A,B	[288, 291]
(1567)	$NH + O^+ \rightarrow H + NO^+$	3.60×10^{-10}	0	0		[180]
(1568)	$NH + O_2 \rightarrow OH + NO$	9.80×10^{-15}	0	0		[111, 112]
(1569)	$NH + O_2 \rightarrow HNO + O$	2.30×10^{-13}	0	0.1	A,B	[179, 187]
(1570)	$NH + O_2^+ \rightarrow NO_2^+ + H$	3.20×10^{-10}	0	0	A,B	[180]
(1571)	$NH + N \rightarrow H + N_2$	2.50×10^{-11}	0	0	A,B	[111, 112]
(1572)	$NH + N^+ \rightarrow H + N_2^+$	3.70×10^{-10}	0	0		[180]
(1573)	$NH + NO \rightarrow H + N_2O$	3.12×10^{-11}	0	0	A	[187, 311]
(1574)	$NH + NO \rightarrow OH + N_2$	1.44×10^{-11}	0	0		[293, 311]
(1575)	$NH + NO \rightarrow O + H + N_2$	5.00×10^{-11}	0	0	A	[180]
(1576)	$NH + NO_2 \rightarrow OH + N_2O$	3.50×10^{-13}	0	-1140		[112, 277]

Nr	Reaction name	A^a	B^a	C^a	Set^b	Ref.
(1577)	$NH + NO_2 \rightarrow HO_2 + N_2$	3.50×10^{-13}	0	-1140		[110]
(1578)	$NH + NO_2 \rightarrow HNO + NO$	3.50×10^{-13}	0	-1140		[110]
(1579)	$NH + N_2O \rightarrow HNO + N_2$	3.32×10^{-12}	0	3019		[288, 291]
(1580)	$NH + NO_3 \rightarrow HNO + NO_2$	2.49×10^{-11}	0	0		[287]
(1581)	$NH + NO_3 \rightarrow HNO_3 + N$	1.66×10^{-12}	0	2516		[287]
(1582)	$NH + NH \rightarrow N_2 + H + H$	1.20×10^{-09}	0	0	A	[185, 312]
(1583)	$NH + NH \rightarrow N_2 + H_2$	1.70×10^{-11}	0	0		[180]
(1584)	$HNO + O \rightarrow OH + NO$	6.00×10^{-11}	0	0	A,B	[112, 293]
(1585)	$HNO + O \rightarrow NO_2 + H$	8.30×10^{-14}	0	1006		[288, 291]
(1586)	$HNO + O \rightarrow O_2 + NH$	2.94×10^{-12}	0.5	3500	A,B	[180]
(1587)	$HNO + O_2 \rightarrow HO_2 + NO$	5.25×10^{-12}	0	1510	A,B	[274, 280]
(1588)	$HNO + N \rightarrow NH + NO$	2.94×10^{-12}	0.5	1000	A	[180, 288]
(1589)	$HNO + N \rightarrow H + N_2O$	1.44×10^{-12}	0.5	1510		[180, 288]
(1590)	$HNO + NO \rightarrow OH + N_2O$	4.90×10^{-19}	0	0		[112]
(1591)	$HNO + NO_2 \rightarrow HNO_2 + NO$	1.00×10^{-12}	0	200		[112]
(1592)	$HNO + HNO \rightarrow H_2O + N_2O$	4.36×10^{-17}	3.98	599		[288, 291]
(1593)	$HNO_2 + O \rightarrow OH + NO_2$	2.00×10^{-11}	0	3000	A,B	[112, 115]
(1594)	$HNO_2 + NO_2 \rightarrow HNO_3 + NO$	3.32×10^{-13}	0	16466.3		[189]
(1595)	$HNO_2 + NO_3 \rightarrow NO_2 + HNO_3$	2.00×10^{-15}	0	0	A,B	[183]
(1596)	$HNO_2 + HNO_2 \rightarrow NO + NO_2 + H_2O$	6.02×10^{-16}	3.64	6113.2		[189, 287]
(1597)	$HNO_2 + HNO_3 \rightarrow NO_2 + NO_2 + H_2O$	1.55×10^{-17}	0	3000		[310]
(1598)	$HNO_3 + O \rightarrow OH + NO_3$	3.00×10^{-17}	0	0	A,B	[277, 280]
(1599)	$HNO_3 + O^- \rightarrow HNO_4 + e^-$	1.50×10^{-09}	0	0	A,B	[186] aq
(1600)	$HNO_3 + O^- \rightarrow HNO_2 + O_2$	1.50×10^{-09}	0	0	A,B	[186] aq

Nr	Reaction name	A^a	B^a	C^a	Set[b]	Ref.
(1601)	$HNO_3 + O_2^- \rightarrow NO_3^- + HO_2$	2.90×10^{-09}	0	0	A,B	[183,186]
(1602)	$HNO_3 + NO \rightarrow NO_2 + HNO_2$	1.20×10^{-12}	2	5535		[187,287]
(1603)	$HNO_3 + NO_2^- \rightarrow NO_3^- + HNO_2$	1.60×10^{-09}	0	0	A,B	[179,186]
(1604)	$HNO_4 + O \rightarrow HO_2 + NO_3$	7.80×10^{-11}	0	3400	A	[277,280] [z]
(1605)	$HNO_4 + M \rightarrow HO_2 + NO_2 + M$	5.00×10^{-06}	0	10000	A,B	[187,280]
(1606)	$ArH^+ + O^- \rightarrow Ar + O + H$	1.00×10^{-07}	0	0	A	[105]
(1607)	$ArH^+ + O^- + M \rightarrow Ar + O + H + M$	2.00×10^{-25}	-2.5	0	A,B	[105]
(1608)	$ArH^+ + O_2 \rightarrow Ar + O_2 + H$	1.00×10^{-07}	0	0	A	[105]
(1609)	$ArH^+ + O_2^- \rightarrow Ar + O + O + H$	1.00×10^{-07}	0	0	A	[105]
(1610)	$ArH^+ + O_2^- + M \rightarrow Ar + O_2 + H + M$	2.00×10^{-25}	-2.5	0	A,B	[105]
(1611)	$ArH^+ + O_3^- \rightarrow Ar + H + O_3$	1.00×10^{-07}	0	0		[105]
(1612)	$ArH^+ + O_3^- \rightarrow Ar + H + O_2 + O$	1.00×10^{-07}	0	0		[105]
(1613)	$ArH^+ + O_3^- + M \rightarrow Ar + H + O_3 + M$	2.00×10^{-25}	-2.5	0	A,B	[105]
(1614)	$ArH^+ + NO_2^- \rightarrow Ar + NO + O + H$	1.00×10^{-07}	0	0		[105]
(1615)	$ArH^+ + NO_2^- \rightarrow Ar + NO_2 + H$	1.00×10^{-07}	0	0		[105]
(1616)	$ArH^+ + NO_2^- + M \rightarrow Ar + NO_2 + H + M$	2.00×10^{-25}	-2.5	0	A	[105]
(1617)	$ArH^+ + NO_3^- \rightarrow Ar + NO_2 + O + H$	1.00×10^{-07}	0	0		[105]
(1618)	$ArH^+ + NO_3^- \rightarrow Ar + NO_3 + H$	1.00×10^{-07}	0	0		[105]
(1619)	$ArH^+ + NO_3^- + M \rightarrow Ar + NO_3 + H + M$	2.00×10^{-25}	-2.5	0	A	[105]
Radiation						
(1620)	$Ar(^4P) \rightarrow Ar(^4S[^3P_2])$	$2.00\times10^{+06}$	0	0	A,B	[265]
(1621)	$Ar(^4P) \rightarrow Ar(^4S[^3P_1])$	$2.00\times10^{+06}$	0	0	A,B	[265]
(1622)	$Ar(^4P) \rightarrow Ar(^4S[^3P_0])$	$2.00\times10^{+06}$	0	0	A,B	[265]
(1623)	$Ar(^4P) \rightarrow Ar(^4S[^1P_1])$	$2.00\times10^{+06}$	0	0	A,B	[265]

Nr	Reaction name	A^a	B^a	C^a	Set^b	Ref.
(1624)	Ar(^{4}S[^{3}P$_2$]) → Ar	2.00×10^{-02}	0	0		[266]
(1625)	Ar(^{4}S[^{3}P$_1$]) → Ar	$1.00 \times 10^{+08}$	0	0	A,B	[266]
(1626)	Ar(^{4}S[^{3}P$_0$]) → Ar	2.00×10^{-02}	0	0		[266]
(1627)	Ar(^{4}S[^{1}P$_1$]) → Ar	$4.00 \times 10^{+08}$	0	0	A,B	[266]
(1628)	Ar$_2$* → Ar + Ar	$3.17 \times 10^{+05}$	0	0	A,B	[266]
(1629)	O$_2$(a) → O$_2$	2.70×10^{-04}	0	0		[121]
(1630)	O$_2$(b) → O$_2$	8.30×10^{-02}	0	0		[121]
(1631)	OH(A) → OH	$1.25 \times 10^{+06}$	0	0	A,B	[289]
NO$_x$ water cluster ion collisions						
(1632)	H$_2$NO$_2^+$ + e⁻ → H$_2$O + NO	2.00×10^{-07}	-0.5	0	A,B	[105]
(1633)	H$_4$NO$_3^+$ + e⁻ → 2 H$_2$O + NO	2.00×10^{-07}	-0.5	0	A,B	[105]
(1634)	H$_6$NO$_4^+$ + e⁻ → NO + 3 H$_2$O	2.00×10^{-07}	-0.5	0	A,B	[105]
(1635)	NO⁺ + H$_2$O → H$_2$NO$_2^+$				A,B	[113] [c]
(1636)	H$_2$NO$_2^+$ → NO⁺ + H$_2$O				A,B	[113] [c]
(1637)	H$_2$NO$_2^+$ + H$_2$O → H$_4$NO$_3^+$				A,B	[113] [c]
(1638)	H$_2$NO$_2^+$ + O → NO$_2^+$ + H$_2$O	1.00×10^{-11}	0	0	A,B	[186]
(1639)	H$_2$NO$_2^+$ + H → H$_3$O⁺ + NO	7.00×10^{-12}	0	0		[186]
(1640)	H$_2$NO$_2^+$ + OH → H$_3$O⁺ + NO$_2$	1.00×10^{-10}	0	0	A,B	[186]
(1641)	H$_4$NO$_3^+$ → H$_2$O + H$_2$NO$_2^+$				A,B	[113] [c]
(1642)	H$_4$NO$_3^+$ + H$_2$O → H$_6$NO$_4^+$				A,B	[113] [c]
(1643)	H$_6$NO$_4^+$ → H$_4$NO$_3^+$ + H$_2$O				A,B	[113] [c]
(1644)	H$_6$NO$_4^+$ + H$_2$O → H$_7$O$_3^+$ + HNO$_2$	8.00×10^{-11}	0	0	A,B	[187]
(1645)	H$_2$NO$_2^+$ + O⁻ → NO + H$_2$O + O	1.00×10^{-07}	0	0		[105]
(1646)	H$_2$NO$_2^+$ + O⁻ + M → NO$_2$ + H$_2$O + M	2.00×10^{-25}	-2.5	0	A	[105]

Nr	Reaction name	A^a	B^a	C^a	Set^b	Ref.
(1647)	$H_2NO_2^+ + O_2^- \rightarrow NO + H_2O + O_2$	1.00×10^{-07}	0	0		[105]
(1648)	$H_2NO_2^+ + O_2^- \rightarrow NO + H_2O + O + O$	1.00×10^{-07}	0	0		[105]
(1649)	$H_2NO_2^+ + O_2^- + M \rightarrow NO_3 + H_2O + M$	2.00×10^{-25}	-2.5	0	A	[105]
(1650)	$H_2NO_2^+ + O_3^- \rightarrow NO + H_2O + O_2$	1.00×10^{-07}	0	0		[105]
(1651)	$H_2NO_2^+ + O_3^- \rightarrow NO + H_2O + O_2 + O$	1.00×10^{-07}	0	0		[105]
(1652)	$H_2NO_2^+ + O_3^- + M \rightarrow NO_2 + O_2 + H_2O + M$	2.00×10^{-25}	-2.5	0		[105]
(1653)	$H_2NO_2^+ + NO_2^- \rightarrow NO + H_2O + NO_2$	1.00×10^{-07}	0	0		[105]
(1654)	$H_2NO_2^+ + NO_2^- \rightarrow NO + H_2O + NO + O$	1.00×10^{-07}	0	0		[105]
(1655)	$H_2NO_2^+ + NO_2^- + M \rightarrow NO + NO_2 + H_2O + M$	2.00×10^{-25}	-2.5	0		[105]
(1656)	$H_2NO_2^+ + NO_3^- \rightarrow NO + H_2O + NO_3$	1.00×10^{-07}	0	0		[105]
(1657)	$H_2NO_2^+ + NO_3^- \rightarrow NO + H_2O + NO_2 + O$	1.00×10^{-07}	0	0		[105]
(1658)	$H_2NO_2^+ + NO_3^- + M \rightarrow NO_2 + NO_2 + H_2O + M$	2.00×10^{-25}	-2.5	0	A	[105]
(1659)	$H_2NO_2^+ + H^- \rightarrow NO + H_2O + H$	1.00×10^{-07}	0	0		[105]
(1660)	$H_2NO_2^+ + H^- + M \rightarrow HNO + H_2O + M$	2.00×10^{-25}	-2.5	0	A,B	[105]
(1661)	$H_2NO_2^+ + OH^- \rightarrow NO + H_2O + OH$	1.00×10^{-07}	0	0		[105]
(1662)	$H_2NO_2^+ + OH^- \rightarrow NO + H_2O + O + H$	1.00×10^{-07}	0	0		[105]
(1663)	$H_2NO_2^+ + OH^- + M \rightarrow HNO_2 + H_2O + M$	2.00×10^{-25}	-2.5	0	A	[105]
(1664)	$H_4NO_3^+ + O^- \rightarrow NO + 2\,H_2O + O$	1.00×10^{-07}	0	0		[105]
(1665)	$H_4NO_3^+ + O^- + M \rightarrow NO_2 + 2\,H_2O + M$	2.00×10^{-25}	-2.5	0	A	[105]
(1666)	$H_4NO_3^+ + O_2^- \rightarrow NO + 2\,H_2O + O_2$	1.00×10^{-07}	0	0		[105]
(1667)	$H_4NO_3^+ + O_2^- \rightarrow NO + 2\,H_2O + O + O$	1.00×10^{-07}	0	0		[105]
(1668)	$H_4NO_3^+ + O_2^- + M \rightarrow NO_3 + 2\,H_2O + M$	2.00×10^{-25}	-2.5	0		[105]
(1669)	$H_4NO_3^+ + O_3^- \rightarrow NO + 2\,H_2O + O_2$	1.00×10^{-07}	0	0		[105]
(1670)	$H_4NO_3^+ + O_3^- \rightarrow NO + 2\,H_2O + O_2 + O$	1.00×10^{-07}	0	0		[105]

Nr	Reaction name	A^a	B^a	C^a	Set^b	Ref.
(1671)	$H_4NO_3^+ + O_3^- + M \rightarrow NO_2 + O_2 + 2\,H_2O + M$	2.00×10^{-25}	-2.5	0		[105]
(1672)	$H_4NO_3^+ + NO_2^- \rightarrow NO + 2\,H_2O + NO_2$	1.00×10^{-07}	0	0		[105]
(1673)	$H_4NO_3^+ + NO_2^- \rightarrow NO + 2\,H_2O + NO + O$	1.00×10^{-07}	0	0		[105]
(1674)	$H_4NO_3^+ + NO_2^- + M \rightarrow NO + NO_2 + 2\,H_2O + M$	2.00×10^{-25}	-2.5	0		[105]
(1675)	$H_4NO_3^+ + NO_3^- \rightarrow NO + 2\,H_2O + NO_3$	1.00×10^{-07}	0	0		[105]
(1676)	$H_4NO_3^+ + NO_3^- \rightarrow NO + 2\,H_2O + NO_2 + O$	1.00×10^{-07}	0	0		[105]
(1677)	$H_4NO_3^+ + NO_3^- + M \rightarrow NO_2 + NO_2 + 2\,H_2O + M$	2.00×10^{-25}	-2.5	0		[105]
(1678)	$H_4NO_3^+ + H^- \rightarrow NO + 2\,H_2O + H$	1.00×10^{-07}	0	0		[105]
(1679)	$H_4NO_3^+ + H^- + M \rightarrow HNO + 2\,H_2O + M$	2.00×10^{-25}	-2.5	0	A,B	[105]
(1680)	$H_4NO_3^+ + OH^- \rightarrow NO + 2\,H_2O + OH$	1.00×10^{-07}	0	0		[105]
(1681)	$H_4NO_3^+ + OH^- \rightarrow NO + 2\,H_2O + O + H$	1.00×10^{-07}	0	0		[105]
(1682)	$H_4NO_3^+ + OH^- + M \rightarrow HNO_2 + 2\,H_2O + M$	2.00×10^{-25}	-2.5	0	A	[105]
(1683)	$H_4NO_3^+ + O^- \rightarrow NO + 3\,H_2O + O$	1.00×10^{-07}	0	0		[105]
(1684)	$H_6NO_4^+ + O^- + M \rightarrow NO_2 + 3\,H_2O + M$	2.00×10^{-25}	-2.5	0	A,B	[105]
(1685)	$H_6NO_4^+ + O_2^- \rightarrow NO + 3\,H_2O + O_2$	1.00×10^{-07}	0	0		[105]
(1686)	$H_6NO_4^+ + O_2^- \rightarrow NO + 3\,H_2O + O + O$	1.00×10^{-07}	0	0		[105]
(1687)	$H_6NO_4^+ + O_2^- + M \rightarrow NO_3 + 3\,H_2O + M$	2.00×10^{-25}	-2.5	0	A	[105]
(1688)	$H_6NO_4^+ + O_3^- \rightarrow NO + 3\,H_2O + O_2$	1.00×10^{-07}	0	0		[105]
(1689)	$H_6NO_4^+ + O_3^- \rightarrow NO + 3\,H_2O + O_2 + O$	1.00×10^{-07}	0	0		[105]
(1690)	$H_6NO_4^+ + O_3^- + M \rightarrow NO_2 + O_2 + 3\,H_2O + M$	2.00×10^{-25}	-2.5	0		[105]
(1691)	$H_6NO_4^+ + NO_2^- \rightarrow NO + 3\,H_2O + NO_2$	1.00×10^{-07}	0	0		[105]
(1692)	$H_6NO_4^+ + NO_2^- \rightarrow NO + 3\,H_2O + NO + O$	1.00×10^{-07}	0	0		[105]
(1693)	$H_6NO_4^+ + NO_2^- + M \rightarrow NO + NO_2 + 3\,H_2O + M$	2.00×10^{-25}	-2.5	0		[105]
(1694)	$H_6NO_4^+ + NO_3^- \rightarrow NO + 3\,H_2O + NO_3$	1.00×10^{-07}	0	0		[105]

Nr	Reaction name	A^a	B^a	C^a	Set^b	Ref.
(1695)	$H_6NO_4^+ + NO_3^- \rightarrow NO + 3\ H_2O + NO_2 + O$	1.00×10^{-07}	0	0		[105]
(1696)	$H_6NO_4^+ + NO_3^- + M \rightarrow NO_2 + NO_2 + 3\ H_2O + M$	2.00×10^{-25}	-2.5	0		[105]
(1697)	$H_6NO_4^+ + H^- \rightarrow NO + 3\ H_2O + H$	1.00×10^{-07}	0	0		[105]
(1698)	$H_6NO_4^+ + H^- + M \rightarrow HNO + 3\ H_2O + M$	2.00×10^{-25}	-2.5	0	A	[105]
(1699)	$H_6NO_4^+ + OH^- \rightarrow NO + 3\ H_2O + OH$	1.00×10^{-07}	0	0		[105]
(1700)	$H_6NO_4^+ + OH^- \rightarrow NO + 3\ H_2O + O + H$	1.00×10^{-07}	0	0		[105]
(1701)	$H_6NO_4^+ + OH^- + M \rightarrow HNO_2 + 3\ H_2O + M$	2.00×10^{-25}	-2.5	0		[105]
	Water cluster ion collisions					
(1702)	$H_4O_2^+ + e^- \rightarrow H_2O + H + OH$	9.60×10^{-07}	-0.2	0	A,B	[121]
(1703)	$H_2O_3^+ + e^- \rightarrow H + OH + O_2$	7.22×10^{-07}	-0.2	0	A,B	[121]
(1704)	$H_5O_2^+ + e^- \rightarrow H_2O + H + H + OH$	2.00×10^{-07}	-0.5	0	A,B	[105]
(1705)	$H_7O_3^+ + e^- \rightarrow 2\ H_2O + H + H + OH$	2.00×10^{-07}	-0.5	0	A,B	[105]
(1706)	$H_9O_4^+ + e^- \rightarrow 3\ H_2O + H + H + OH$	2.00×10^{-07}	-0.5	0	A,B	[105]
(1707)	$H_{11}O_5^+ + e^- \rightarrow 4\ H_2O + H + H + OH$	2.00×10^{-07}	-0.5	0	A	[105]
(1708)	$H_{13}O_6^+ + e^- \rightarrow 5\ H_2O + H + H + OH$	2.00×10^{-07}	-0.5	0		[105]
(1709)	$H_{15}O_7^+ + e^- \rightarrow 6\ H_2O + H + H + OH$	2.00×10^{-07}	-0.5	0	A	[105]
(1710)	$O_2^+ + H_2O \rightarrow H_2O_3^+$				A,B	[113] [c]
(1711)	$O_4^+ + H_2O \rightarrow H_2O_3^+ + O_2$	1.70×10^{-09}	0	0		[113]
(1712)	$H_2O_3^+ \rightarrow O_2^+ + H_2O$				A,B	[113] [c]
(1713)	$H_2O_3^+ + H_2O \rightarrow H_3O^+ + OH + O_2$	1.30×10^{-09}	0	0	A,B	[113]
(1714)	$H_2O_3^+ + H_2O \rightarrow H_4O_2^+ + O_2$	1.00×10^{-09}	0	0	A,B	[121]
(1715)	$H_2O_3^+ + NO \rightarrow NO^+ + H_2O + O_2$	5.30×10^{-10}	0	0	A,B	[113]
(1716)	$H_4O_2^+ + H_2O \rightarrow H_5O_2^+ + OH$	1.40×10^{-09}	0	0	A,B	[121]
(1717)	$H_3O^+ + H_2O \rightarrow H_5O_2^+$				A,B	[113] [c]

Nr	Reaction name	A^a	B^a	C^a	Set^b	Ref.
(1718)	$H_5O_2^+ \rightarrow H_3O^+ + H_2O$				A,B	[113]^c
(1719)	$H_5O_2^+ + H_2O \rightarrow H_7O_3^+$				A,B	[113]^c
(1720)	$H_7O_3^+ \rightarrow H_5O_2^+ + H_2O$				A,B	[113]^c
(1721)	$H_7O_3^+ + H_2O \rightarrow H_9O_4^+$				A,B	[113]^c
(1722)	$H_9O_4^+ \rightarrow H_7O_3^+ + H_2O$				A,B	[113]^c
(1723)	$H_9O_4^+ + H_2O \rightarrow H_{11}O_5^+$				A,B	[113]^c
(1724)	$H_{11}O_5^+ \rightarrow H_9O_4^+ + H_2O$				A,B	[113]^c
(1725)	$H_{11}O_5^+ + H_2O \rightarrow H_{13}O_6^+$				A,B	[113]^c
(1726)	$H_{13}O_6^+ \rightarrow H_{11}O_5^+ + H_2O$				A,B	[113]^c
(1727)	$H_{13}O_6^+ + H_2O \rightarrow H_{15}O_7^+$				A,B	[113]^c
(1728)	$H_{15}O_7^+ \rightarrow H_{13}O_6^+ + H_2O$				A,B	[113]^c
(1729)	$H_2O_3^+ + O^- \rightarrow O_2 + O + H_2O$	1.00×10^{-07}	0	0		[105]
(1730)	$H_2O_3^+ + O^- + M \rightarrow O_2 + O + H_2O + M$	2.00×10^{-25}	-2.5	0	A	[105]
(1731)	$H_2O_3^+ + O_2^- \rightarrow O_2 + O_2 + H_2O$	1.00×10^{-07}	0	0		[105]
(1732)	$H_2O_3^+ + O_2^- \rightarrow H_2O + O_2 + O + O$	1.00×10^{-07}	0	0		[105]
(1733)	$H_2O_3^+ + O_2^- + M \rightarrow O_2 + O_2 + H_2O + M$	2.00×10^{-25}	-2.5	0		[105]
(1734)	$H_2O_3^+ + O_3^- \rightarrow O_3 + O_2 + H_2O$	1.00×10^{-07}	0	0		[105]
(1735)	$H_2O_3^+ + O_3^- \rightarrow O_2 + H_2O + O_2 + O$	1.00×10^{-07}	0	0		[105]
(1736)	$H_2O_3^+ + O_3^- + M \rightarrow H_2O + O + O_2 + O_2 + O_2 + M$	2.00×10^{-25}	-2.5	0		[105]
(1737)	$H_2O_3^+ + NO_2^- \rightarrow O_2 + H_2O + NO_2$	1.00×10^{-07}	0	0		[105]
(1738)	$H_2O_3^+ + NO_2^- \rightarrow O_2 + H_2O + NO + O$	1.00×10^{-07}	0	0		[105]
(1739)	$H_2O_3^+ + NO_2^- + M \rightarrow O_2 + H_2O + NO_2 + M$	2.00×10^{-25}	-2.5	0		[105]
(1740)	$H_2O_3^+ + NO_3^- \rightarrow O_2 + H_2O + NO_3$	1.00×10^{-07}	0	0		[105]
(1741)	$H_2O_3^+ + NO_3^- \rightarrow O_2 + H_2O + NO_2 + O$	1.00×10^{-07}	0	0		[105]

Nr	Reaction name	A^a	B^a	C^a	Set^b	Ref.
(1742)	$H_2O_3^+ + NO_3^- + M \rightarrow O_2 + H_2O + NO_3 + M$	2.00×10^{-25}	-2.5	0		[105]
(1743)	$H_2O_3^+ + H^- \rightarrow O_2 + H_2O + H$	1.00×10^{-07}	0	0		[105]
(1744)	$H_2O_3^+ + H^- + M \rightarrow H_2O + H + O_2 + M$	2.00×10^{-25}	-2.5	0		[105]
(1745)	$H_2O_3^+ + OH^- \rightarrow H_2O + OH + O_2$	1.00×10^{-07}	0	0		[105]
(1746)	$H_2O_3^+ + OH^- \rightarrow H_2O + O + H + O_2$	1.00×10^{-07}	0	0		[105]
(1747)	$H_2O_3^+ + OH^- + M \rightarrow H_2O + OH + O_2 + M$	2.00×10^{-25}	-2.5	0		[105]
(1748)	$H_4O_2^+ + O^- \rightarrow O + 2\,H_2O$	1.00×10^{-07}	0	0		[105]
(1749)	$H_4O_2^+ + O^- + M \rightarrow O + 2\,H_2O + M$	2.00×10^{-25}	-2.5	0	A	[105]
(1750)	$H_4O_2^+ + O_2^- \rightarrow O_2 + 2\,H_2O$	1.00×10^{-07}	0	0		[105]
(1751)	$H_4O_2^+ + O_2^- \rightarrow O + O + 2\,H_2O$	1.00×10^{-07}	0	0		[105]
(1752)	$H_4O_2^+ + O_2^- + M \rightarrow O_2 + 2\,H_2O + M$	2.00×10^{-25}	-2.5	0	A,B	[105]
(1753)	$H_4O_2^+ + O_3^- \rightarrow O_3 + 2\,H_2O$	1.00×10^{-07}	0	0		[105]
(1754)	$H_4O_2^+ + O_3^- \rightarrow O_2 + O + 2\,H_2O$	1.00×10^{-07}	0	0		[105]
(1755)	$H_4O_2^+ + O_3^- + M \rightarrow O_3 + 2\,H_2O + M$	2.00×10^{-25}	-2.5	0	A	[105]
(1756)	$H_4O_2^+ + NO_2^- \rightarrow NO_2 + 2\,H_2O$	1.00×10^{-07}	0	0		[105]
(1757)	$H_4O_2^+ + NO_2^- \rightarrow NO + O + 2\,H_2O$	1.00×10^{-07}	0	0		[105]
(1758)	$H_4O_2^+ + NO_2^- + M \rightarrow NO_2 + 2\,H_2O + M$	2.00×10^{-25}	-2.5	0	A	[105]
(1759)	$H_4O_2^+ + NO_3^- \rightarrow NO_3 + 2\,H_2O$	1.00×10^{-07}	0	0		[105]
(1760)	$H_4O_2^+ + NO_3^- \rightarrow NO_2 + O + 2\,H_2O$	1.00×10^{-07}	0	0		[105]
(1761)	$H_4O_2^+ + NO_3^- + M \rightarrow NO_3 + 2\,H_2O + M$	2.00×10^{-25}	-2.5	0	A	[105]
(1762)	$H_4O_2^+ + H^- \rightarrow H + 2\,H_2O$	1.00×10^{-07}	0	0		[105]
(1763)	$H_4O_2^+ + H^- + M \rightarrow H + 2\,H_2O + M$	2.00×10^{-25}	-2.5	0		[105]
(1764)	$H_4O_2^+ + OH^- \rightarrow OH + 2\,H_2O$	1.00×10^{-07}	0	0		[105]
(1765)	$H_4O_2^+ + OH^- \rightarrow O + H + 2\,H_2O$	1.00×10^{-07}	0	0		[105]

Nr	Reaction name	A^a	B^a	C^a	Set^b	Ref.
(1766)	$H_4O_2^+ + OH^- + M \rightarrow OH + 2\,H_2O + M$	2.00×10^{-25}	-2.5	0		[105]
(1767)	$H_5O_2^+ + O^- \rightarrow O + H + 2\,H_2O$	1.00×10^{-07}	0	0		[105]
(1768)	$H_5O_2^+ + O^- + M \rightarrow O + H + 2\,H_2O + M$	2.00×10^{-25}	-2.5	0	A,B	[105]
(1769)	$H_5O_2^+ + O_2^- \rightarrow H + O_2 + 2\,H_2O$	1.00×10^{-07}	0	0	A	[105]
(1770)	$H_5O_2^+ + O_2^- \rightarrow O + O + 2\,H_2O + H$	1.00×10^{-07}	0	0	A	[105]
(1771)	$H_5O_2^+ + O_2^- + M \rightarrow H + O_2 + 2\,H_2O + M$	2.00×10^{-25}	-2.5	0	A,B	[105]
(1772)	$H_5O_2^+ + O_3^- \rightarrow O_3 + 2\,H_2O + H$	1.00×10^{-07}	0	0	A	[105]
(1773)	$H_5O_2^+ + O_3^- \rightarrow O_2 + O + 2\,H_2O + H$	1.00×10^{-07}	0	0		[105]
(1774)	$H_5O_2^+ + O_3^- + M \rightarrow O_3 + 2\,H_2O + H + M$	2.00×10^{-25}	-2.5	0	A,B	[105]
(1775)	$H_5O_2^+ + NO_2^- \rightarrow NO_2 + 2\,H_2O + H$	1.00×10^{-07}	0	0		[105]
(1776)	$H_5O_2^+ + NO_2^- \rightarrow NO + O + 2\,H_2O + H$	1.00×10^{-07}	0	0		[105]
(1777)	$H_5O_2^+ + NO_2^- + M \rightarrow NO_2 + 2\,H_2O + H + M$	2.00×10^{-25}	-2.5	0	A,B	[105]
(1778)	$H_5O_2^+ + NO_3^- \rightarrow NO_3 + 2\,H_2O + H$	1.00×10^{-07}	0	0	A	[105]
(1779)	$H_5O_2^+ + NO_3^- \rightarrow NO_2 + O + 2\,H_2O + H$	1.00×10^{-07}	0	0		[105]
(1780)	$H_5O_2^+ + NO_3^- + M \rightarrow NO_3 + 2\,H_2O + H + M$	2.00×10^{-25}	-2.5	0	A,B	[105]
(1781)	$H_5O_2^+ + H^- \rightarrow H + H + 2\,H_2O$	1.00×10^{-07}	0	0		[105]
(1782)	$H_5O_2^+ + H^- + M \rightarrow H + H + 2\,H_2O + M$	2.00×10^{-25}	-2.5	0		[105]
(1783)	$H_5O_2^+ + OH^- \rightarrow 2\,H_2O + H + OH$	1.00×10^{-07}	0	0		[105]
(1784)	$H_5O_2^+ + OH^- \rightarrow 2\,H_2O + H + O + H$	1.00×10^{-07}	0	0	A	[105]
(1785)	$H_5O_2^+ + OH^- + M \rightarrow 2\,H_2O + H + OH + M$	2.00×10^{-25}	-2.5	0	A	[105]
(1786)	$H_7O_3^+ + O^- \rightarrow 3\,H_2O + O + H$	1.00×10^{-07}	0	0		[105]
(1787)	$H_7O_3^+ + O^- + M \rightarrow 3\,H_2O + O + H + M$	2.00×10^{-25}	-2.5	0	A	[105]
(1788)	$H_7O_3^+ + O_2^- \rightarrow 3\,H_2O + H + O_2$	1.00×10^{-07}	0	0		[105]
(1789)	$H_7O_3^+ + O_2^- \rightarrow 3\,H_2O + O + O + H$	1.00×10^{-07}	0	0		[105]

Nr	Reaction name	A^a	B^a	C^a	Set^b	Ref.
(1790)	$H_7O_3^+ + O_2^- + M \rightarrow 3\ H_2O + H + O_2 + M$	2.00×10^{-25}	-2.5	0	A	[105]
(1791)	$H_7O_3^+ + O_3^- \rightarrow 3\ H_2O + O_3 + H$	1.00×10^{-07}	0	0		[105]
(1792)	$H_7O_3^+ + O_3^- \rightarrow 3\ H_2O + O_2 + O + H$	1.00×10^{-07}	0	0		[105]
(1793)	$H_7O_3^+ + O_3^- + M \rightarrow 3\ H_2O + O_3 + H + M$	2.00×10^{-25}	-2.5	0	A,B	[105]
(1794)	$H_7O_3^+ + NO_2^- \rightarrow 3\ H_2O + NO_2 + H$	1.00×10^{-07}	0	0		[105]
(1795)	$H_7O_3^+ + NO_2^- \rightarrow 3\ H_2O + NO + O + H$	1.00×10^{-07}	0	0		[105]
(1796)	$H_7O_3^+ + NO_2^- + M \rightarrow 3\ H_2O + NO_2 + H + M$	2.00×10^{-25}	-2.5	0	A,B	[105]
(1797)	$H_7O_3^+ + NO_3^- \rightarrow 3\ H_2O + NO_3 + H$	1.00×10^{-07}	0	0		[105]
(1798)	$H_7O_3^+ + NO_3^- \rightarrow 3\ H_2O + NO_2 + O + H$	1.00×10^{-07}	0	0		[105]
(1799)	$H_7O_3^+ + NO_3^- + M \rightarrow 3\ H_2O + NO_3 + H + M$	2.00×10^{-25}	-2.5	0	A,B	[105]
(1800)	$H_7O_3^+ + H^- \rightarrow 3\ H_2O + H + H$	1.00×10^{-07}	0	0		[105]
(1801)	$H_7O_3^+ + H^- + M \rightarrow 3\ H_2O + H + H + M$	2.00×10^{-25}	-2.5	0		[105]
(1802)	$H_7O_3^+ + OH^- \rightarrow 3\ H_2O + H + OH$	1.00×10^{-07}	0	0		[105]
(1803)	$H_7O_3^+ + OH^- \rightarrow 3\ H_2O + H + O + H$	1.00×10^{-07}	0	0		[105]
(1804)	$H_7O_3^+ + OH^- + M \rightarrow 3\ H_2O + H + OH + M$	2.00×10^{-25}	-2.5	0	A	[105]
(1805)	$H_9O_4^+ + O^- \rightarrow 4\ H_2O + O + H$	1.00×10^{-07}	0	0		[105]
(1806)	$H_9O_4^+ + O^- + M \rightarrow 4\ H_2O + O + H + M$	2.00×10^{-25}	-2.5	0	A	[105]
(1807)	$H_9O_4^+ + O_2^- \rightarrow 4\ H_2O + H + O_2$	1.00×10^{-07}	0	0		[105]
(1808)	$H_9O_4^+ + O_2^- \rightarrow 4\ H_2O + O + O + H$	1.00×10^{-07}	0	0		[105]
(1809)	$H_9O_4^+ + O_2^- + M \rightarrow 4\ H_2O + H + O_2 + M$	2.00×10^{-25}	-2.5	0	A	[105]
(1810)	$H_9O_4^+ + O_3^- \rightarrow 4\ H_2O + O_3 + H$	1.00×10^{-07}	0	0		[105]
(1811)	$H_9O_4^+ + O_3^- \rightarrow 4\ H_2O + O_2 + O + H$	1.00×10^{-07}	0	0		[105]
(1812)	$H_9O_4^+ + O_3^- + M \rightarrow 4\ H_2O + O_3 + H + M$	2.00×10^{-25}	-2.5	0	A	[105]
(1813)	$H_9O_4^+ + NO_2^- \rightarrow 4\ H_2O + NO_2 + H$	1.00×10^{-07}	0	0		[105]

Nr	Reaction name	A^a	B^a	C^a	Set^b	Ref.
(1814)	$H_9O_4^+ + NO_2^- \rightarrow 4\,H_2O + NO + O + H$	1.00×10^{-07}	0	0		[105]
(1815)	$H_9O_4^+ + NO_2^- + M \rightarrow 4\,H_2O + NO_2 + H + M$	2.00×10^{-25}	-2.5	0	A,B	[105]
(1816)	$H_9O_4^+ + NO_3^- \rightarrow 4\,H_2O + NO_3 + H$	1.00×10^{-07}	0	0		[105]
(1817)	$H_9O_4^+ + NO_3^- \rightarrow 4\,H_2O + NO_2 + O + H$	1.00×10^{-07}	0	0		[105]
(1818)	$H_9O_4^+ + NO_3^- + M \rightarrow 4\,H_2O + NO_3 + H + M$	2.00×10^{-25}	-2.5	0	A,B	[105]
(1819)	$H_9O_4^+ + H^- \rightarrow 4\,H_2O + H + H$	1.00×10^{-07}	0	0		[105]
(1820)	$H_9O_4^+ + H^- + M \rightarrow 4\,H_2O + H + H + M$	2.00×10^{-25}	-2.5	0		[105]
(1821)	$H_9O_4^+ + OH^- \rightarrow 4\,H_2O + H + OH$	1.00×10^{-07}	0	0		[105]
(1822)	$H_9O_4^+ + OH^- \rightarrow 4\,H_2O + H + O + H$	1.00×10^{-07}	0	0		[105]
(1823)	$H_9O_4^+ + OH^- + M \rightarrow 4\,H_2O + H + OH + M$	2.00×10^{-25}	-2.5	0	A	[105]
(1824)	$H_{11}O_5^+ + O^- \rightarrow 5\,H_2O + O + H$	1.00×10^{-07}	0	0		[105]
(1825)	$H_{11}O_5^+ + O^- + M \rightarrow 5\,H_2O + O + H + M$	2.00×10^{-25}	-2.5	0	A	[105]
(1826)	$H_{11}O_5^+ + O_2^- \rightarrow 5\,H_2O + H + O_2$	1.00×10^{-07}	0	0		[105]
(1827)	$H_{11}O_5^+ + O_2^- \rightarrow 5\,H_2O + O + O + H$	1.00×10^{-07}	0	0		[105]
(1828)	$H_{11}O_5^+ + O_2^- + M \rightarrow 5\,H_2O + H + O_2 + M$	2.00×10^{-25}	-2.5	0	A	[105]
(1829)	$H_{11}O_5^+ + O_3^- \rightarrow 5\,H_2O + O_3 + H$	1.00×10^{-07}	0	0		[105]
(1830)	$H_{11}O_5^+ + O_3^- \rightarrow 5\,H_2O + O_2 + O + H$	1.00×10^{-07}	0	0		[105]
(1831)	$H_{11}O_5^+ + O_3^- + M \rightarrow 5\,H_2O + O_3 + H + M$	2.00×10^{-25}	-2.5	0	A	[105]
(1832)	$H_{11}O_5^+ + NO_2^- \rightarrow 5\,H_2O + NO_2 + H$	1.00×10^{-07}	0	0		[105]
(1833)	$H_{11}O_5^+ + NO_2^- \rightarrow 5\,H_2O + NO + O + H$	1.00×10^{-07}	0	0		[105]
(1834)	$H_{11}O_5^+ + NO_2^- + M \rightarrow 5\,H_2O + NO_2 + H + M$	2.00×10^{-25}	-2.5	0	A,B	[105]
(1835)	$H_{11}O_5^+ + NO_3^- \rightarrow 5\,H_2O + NO_3 + H$	1.00×10^{-07}	0	0		[105]
(1836)	$H_{11}O_5^+ + NO_3^- \rightarrow 5\,H_2O + NO_2 + O + H$	1.00×10^{-07}	0	0		[105]
(1837)	$H_{11}O_5^+ + NO_3^- + M \rightarrow 5\,H_2O + NO_3 + H + M$	2.00×10^{-25}	-2.5	0	A,B	[105]

Nr	Reaction name	A^a	B^a	C^a	Set^b	Ref.
(1838)	$H_{11}O_5^+ + H^- \rightarrow 5\ H_2O + H + H + 2\ H_2O$	1.00×10^{-07}	0	0		[105]
(1839)	$H_{11}O_5^+ + H^- + M \rightarrow 5\ H_2O + H + H + M$	2.00×10^{-25}	-2.5	0		[105]
(1840)	$H_{11}O_5^+ + OH^- \rightarrow 5\ H_2O + H + OH$	1.00×10^{-07}	0	0		[105]
(1841)	$H_{11}O_5^+ + OH^- \rightarrow 5\ H_2O + H + O + H$	1.00×10^{-07}	0	0		[105]
(1842)	$H_{11}O_5^+ + OH^- + M \rightarrow 5\ H_2O + H + OH + M$	2.00×10^{-25}	-2.5	0	A	[105]
(1843)	$H_{13}O_6^+ + O^- \rightarrow 6\ H_2O + O + H$	1.00×10^{-07}	0	0		[105]
(1844)	$H_{13}O_6^+ + O^- + M \rightarrow 6\ H_2O + O + H + M$	2.00×10^{-25}	-2.5	0		[105]
(1845)	$H_{13}O_6^+ + O_2^- \rightarrow 6\ H_2O + H + O_2 + 2\ H_2O$	1.00×10^{-07}	0	0		[105]
(1846)	$H_{13}O_6^+ + O_2^- \rightarrow 6\ H_2O + O + O + H$	1.00×10^{-07}	0	0		[105]
(1847)	$H_{13}O_6^+ + O_2^- + M \rightarrow 6\ H_2O + H + O_2 + M$	2.00×10^{-25}	-2.5	0		[105]
(1848)	$H_{13}O_6^+ + O_3^- \rightarrow 6\ H_2O + O_3 + H$	1.00×10^{-07}	0	0		[105]
(1849)	$H_{13}O_6^+ + O_3^- \rightarrow 6\ H_2O + O_2 + O + H$	1.00×10^{-07}	0	0		[105]
(1850)	$H_{13}O_6^+ + O_3^- + M \rightarrow 6\ H_2O + O_3 + H + M$	2.00×10^{-25}	-2.5	0	A	[105]
(1851)	$H_{13}O_6^+ + NO_2^- \rightarrow 6\ H_2O + NO_2 + H$	1.00×10^{-07}	0	0		[105]
(1852)	$H_{13}O_6^+ + NO_2^- \rightarrow 6\ H_2O + NO + O + H$	1.00×10^{-07}	0	0		[105]
(1853)	$H_{13}O_6^+ + NO_2^- + M \rightarrow 6\ H_2O + NO_2 + H + M$	2.00×10^{-25}	-2.5	0	A	[105]
(1854)	$H_{13}O_6^+ + NO_3^- \rightarrow 6\ H_2O + NO_3 + H$	1.00×10^{-07}	0	0		[105]
(1855)	$H_{13}O_6^+ + NO_3^- \rightarrow 6\ H_2O + NO_2 + O + H$	1.00×10^{-07}	0	0		[105]
(1856)	$H_{13}O_6^+ + NO_3^- + M \rightarrow 6\ H_2O + NO_3 + H + M$	2.00×10^{-25}	-2.5	0	A,B	[105]
(1857)	$H_{13}O_6^+ + H^- \rightarrow 6\ H_2O + H + H + 2\ H_2O$	1.00×10^{-07}	0	0		[105]
(1858)	$H_{13}O_6^+ + H^- + M \rightarrow 6\ H_2O + H + H + M$	2.00×10^{-25}	-2.5	0		[105]
(1859)	$H_{13}O_6^+ + OH^- \rightarrow 6\ H_2O + H + OH$	1.00×10^{-07}	0	0		[105]
(1860)	$H_{13}O_6^+ + OH^- \rightarrow 6\ H_2O + H + O + H$	1.00×10^{-07}	0	0		[105]
(1861)	$H_{13}O_6^+ + OH^- + M \rightarrow 6\ H_2O + H + OH + M$	2.00×10^{-25}	-2.5	0	A	[105]

Nr	Reaction name	A^a	B^a	C^a	Set^b	Ref.
(1862)	$H_{15}O_7^+ + O^- \rightarrow 7\ H_2O + O + H$	1.00×10^{-07}	0	0		[105]
(1863)	$H_{15}O_7^+ + O^- + M \rightarrow 7\ H_2O + O + H + M$	2.00×10^{-25}	-2.5	0		[105]
(1864)	$H_{15}O_7^+ + O_2^- \rightarrow 7\ H_2O + H + O_2 + 2\ H_2O$	1.00×10^{-07}	0	0		[105]
(1865)	$H_{15}O_7^+ + O_2^- \rightarrow 7\ H_2O + O + O + H$	1.00×10^{-07}	0	0		[105]
(1866)	$H_{15}O_7^+ + O_2^- + M \rightarrow 7\ H_2O + H + O_2 + M$	2.00×10^{-25}	-2.5	0		[105]
(1867)	$H_{15}O_7^+ + O_3^- \rightarrow 7\ H_2O + O_3 + H$	1.00×10^{-07}	0	0		[105]
(1868)	$H_{15}O_7^+ + O_3^- \rightarrow 7\ H_2O + O_2 + O + H$	1.00×10^{-07}	0	0		[105]
(1869)	$H_{15}O_7^+ + O_3^- + M \rightarrow 7\ H_2O + O_3 + H + M$	2.00×10^{-25}	-2.5	0	A,B	[105]
(1870)	$H_{15}O_7^+ + NO_2^- \rightarrow 7\ H_2O + NO_2 + H$	1.00×10^{-07}	0	0		[105]
(1871)	$H_{15}O_7^+ + NO_2^- \rightarrow 7\ H_2O + NO + O + H$	1.00×10^{-07}	0	0		[105]
(1872)	$H_{15}O_7^+ + NO_2^- + M \rightarrow 7\ H_2O + NO_2 + H + M$	2.00×10^{-25}	-2.5	0	A,B	[105]
(1873)	$H_{15}O_7^+ + NO_3^- \rightarrow 7\ H_2O + NO_3 + H$	1.00×10^{-07}	0	0		[105]
(1874)	$H_{15}O_7^+ + NO_3^- \rightarrow 7\ H_2O + NO_2 + O + H$	1.00×10^{-07}	0	0		[105]
(1875)	$H_{15}O_7^+ + NO_3^- + M \rightarrow 7\ H_2O + NO_3 + H + M$	2.00×10^{-25}	-2.5	0	A,B	[105]
(1876)	$H_{15}O_7^+ + H^- \rightarrow 7\ H_2O + H + H$	1.00×10^{-07}	0	0		[105]
(1877)	$H_{15}O_7^+ + H^- + M \rightarrow 7\ H_2O + H + H + M$	2.00×10^{-25}	-2.5	0		[105]
(1878)	$H_{15}O_7^+ + OH^- \rightarrow 7\ H_2O + H + OH$	1.00×10^{-07}	0	0		[105]
(1879)	$H_{15}O_7^+ + OH^- \rightarrow 7\ H_2O + H + O + H$	1.00×10^{-07}	0	0		[105]
(1880)	$H_{15}O_7^+ + OH^- + M \rightarrow 7\ H_2O + H + OH + M$	2.00×10^{-25}	-2.5	0	A,B	[105]

^a Reaction rate coefficients are usually in the Arrhenius form, for heavy particle collisions: $k=A\times(T_g/300)^B\times\exp(-C/T_g)$, for electron impact collisions: $k=A\times(T_e)^B\times\exp(-C/T_e)$. The unit of A is (s^{-1}), $(cm^3.s^{-1})$ or $(cm^6.s^{-1})$ for first, second or third order reactions. The unit of C is K, except for electron impact reactions where the unit is eV. Thus, the units of T_g and T_e are also K and eV, respectively In the case that reaction rate coefficients are calculated by the Boltzmann solver with cross sectional data this is indicated by $\sigma(\varepsilon)$ where ε is the mean electron energy.

^b This column indicates whether the reaction is included in the reduced reaction list (see text): 'A' stands for the exclusion of a reaction when a relative contribution of less than 10% is taken as a criteria (both for the loss or gain of a species). In the case of 'B', 30% relative contribution is taken as the criteria. This results in 744 and 519 reactions, respectively.

^c The rate coefficient is more complex than the Arrhenius expression, so not given explicitly. See reference [105] for detailed information.

^d Based on $e^- + O_2 + M \longrightarrow O_2^- + M$.

^e This rate coefficient/cross section is based on the reaction with the ground species.

^f Super elastic collision rate coefficients, calculated by detailed balance.

^g Estimated (*cf.* [288]): if $M=N_2$, O_2, Ar $\rightarrow$ coefficient $\times$ 1.0, if $M=H_2$, O_3, O, N $\rightarrow$ coefficient $\times$ 2.5, if $M=H_2O \rightarrow$ coefficient $\times$ 5.0.

^h Estimated: threshold shifted and scaled from reaction with ground species.

ⁱ Estimated: threshold shifted and scaled from excitation of ground species to the first four electronically excited states of N_2.

^j Estimated: threshold shifted and scaled from ionization of ground species.

^k Cross section based on $e^- + N_2^+ \longrightarrow N + N$.

^l Cross section of CO momentum transfer used.

^m Branching ratio of 0.09 for $O + H_2$, 0.71 for $O + 2 H$, 0.20 for $OH + H$ [313].

ⁿ Branching ratio of 0.60 for $2 H + OH$, 0.25 for $H_2O + H$, 0.14 for $H_2 + OH$, 0.01 for $H_2 + O + H$ [314].

^o Cross section of NH_3 is used

^p Coefficient based on $Ar_2^* + Ar_2^* \longrightarrow Ar_2^+ + Ar + Ar + e^-$.

^q Coefficient based on metastable quenching rate.

^r Coefficient based on $Ar(^4S[^3P_2]) + O_2 \longrightarrow Ar + O + O$.

^s Fast radiative decay to $N_2(A)$ assumed.

^t Coefficient based on $Ar(^4S[^3P_2]) + N_2 \longrightarrow Ar + N + N$.

^u Coefficient based on $Ar(^4S[^3P_2]) + N_2(A) \longrightarrow Ar + N_2^+ + e^-$.

^v Coefficients same as for reactions with $Ar(^4S[^3P_2])$.

^w Coefficient based on $Ar^+ + O \longrightarrow O^+ + Ar$.

^x   Coefficient based on $Ar^+ + N_2(A) \longrightarrow Ar + N_2^+$.

^y   Fast radiative decay of $O(^1D)$ to ground state assumed.

^z   Estimation of endproducts.

^{aa}   Coefficient based on $O + O + M \longrightarrow O_2(a) + M$.

^{ab}   Based on values from [181]. Note that rotationally and vibrationally excited states, but also H* and H_2* are included for energy loss. Therefore, physical quenching is implemented as a loss for these states.

^{ac}   Coefficient based on quenching by O.

^{ad}   Coefficient based on quenching by N_2.

^{ae}   Coefficient based on $O_2(b) + N_2 \longrightarrow O_2(a) + N_2$.

^{af}   Coefficient based on $N_2(A) + O_2 \longrightarrow N_2 + O_2$.

^{ag}   Coefficient based on $N_2(A)$ quenching.

^{ah}   Coefficient based on $O + N_2(A) \longrightarrow NO + N$.

^{ai}   Coefficient based on $O + N_2(A) \longrightarrow NO + N(^2D)$.

^{aj}   Estimation of branching ratios: 25% (in reference 4 paths suggested, 3 relevant).

^{ak}   Coefficient based on $O_2(a) + N \longrightarrow O + NO$.

^{al}   Coefficient based on $O_2(a) + N_2(A) \longrightarrow N_2 + O + O$.

^{am}   Coefficient based on $O_2(a) + NO \longrightarrow O + NO_2$.

^{an}   Multiple paths suggested in reference, only one relevant: estimates of branching ratios: 50%.

^{ao}   Coefficient based on $O_3 + N_2(A) \longrightarrow N_2 + O_2 + O$.

^{ap}   Coefficient based on $O_3 + N_2(A) \longrightarrow NO + NO + O$.

^{aq}   Estimation of endproducts by analogy and branching ratio of 50% assumed.

^{ar}   Coefficient based on $Ar(^4S[^3P_2]) + H_2 \longrightarrow Ar + H + H$.

^{as}   Coefficient based on $Ar(^4P) + H_2O \longrightarrow Ar + OH + H$.

^{at}   Sum of rate of $Ar_2^+ + H_2O$ reactions is 2.00×10^{-9} [190].

^{au}   Estimation of endproducts by analogy and branching ratio of 33% assumed.

^{av}   Coefficient based on HeH^+ reaction [121].

^{aw}   Coefficient based on $O_2^- + M \longrightarrow O_2 + M + e^-$.

^{ax}   Coefficient based on $OH + N_2(A) \longrightarrow OH(A) + N_2$.

^{ay}   Coefficient based on $OH + N_2(A) \longrightarrow O + H + N_2$.

^{az}   In reference: branching ratio of 0.10 for $H_2O_2 + NO_3$ and 0.90 for $H_2O + NO_2 + O_2$ assumed.

^{ba}   Coefficient based on $HO_2 + O_2(a) \longrightarrow OH + O_2 + O$.

Appendix B

Additional reaction set used in this work, with the rate constants and the corresponding references

This appendix includes the modifications to the reaction set presented in Appendix A. The reasons for these modifications are indicated in the first column.

Change[a]	Reaction name	A[b]	B[b]	C[b]	Ref.
r	$e^- + e^- + O^+ \rightarrow O + e^-$	9.14×10^{-27}	-4.5	0	[105]
R	$e^- + M + O^+ \rightarrow O + M$	7.10×10^{-27}	-4.5	0	[105]
		2.70×10^{-29}	-1.5	0	[105]
r	$e^- + e^- + O_2^+ \rightarrow O_2 + e^-$	4.31×10^{-34}	-1.5	0	[105]
		9.14×10^{-27}	-4.5	0	[105]
R	$e^- + M + O_2^+ \rightarrow O_2 + M$	4.31×10^{-34}	-1.5	0	[105]
		2.70×10^{-29}	-1.5	0	[105]
		7.18×10^{-27}	-4.5	0	[105]
D	$e^- + O_3^- \rightarrow O_3^- + e^-$	$\sigma(\varepsilon)$			[177]
R	$e^- + O_4^+ \rightarrow O_2 + O_2$	2.25×10^{-07}	-0.5	0	[105]
		7.12×10^{-08}	-0.5	0	[105]
R	$e^- + e^- + N^+ \rightarrow N + e^-$	9.14×10^{-27}	-4.5	0	[105]
		5.40×10^{-24}	-4.5	0	[171]
r	$e^- + M + N^+ \rightarrow N + M$	2.70×10^{-29}	-1.5	0	[105]
		2.49×10^{-29}	-1.5	0	[171]
r	$e^- + e^- + N_2^+ \rightarrow N_2 + e^-$	9.14×10^{-27}	-4.5	0	[105]
		7.18×10^{-27}	-4.5	0	[105]
R	$e^- + M + N_2^+ \rightarrow N_2 + M$	2.70×10^{-29}	-1.5	0	[105]
		4.31×10^{-34}	-4.5	0	[105]
R	$e^- + NO^+ \rightarrow N + O$	1.80×10^{-09}	-1.5	0	[105]
		$\sigma(\varepsilon)$	0	0	[178]
r	$e^- + e^- + NO^+ \rightarrow NO + e^-$	9.14×10^{-27}	-4.5	0	[105]
		7.18×10^{-27}	-4.5	0	[105]
r	$e^- + M + NO^+ \rightarrow NO + M$	2.70×10^{-29}	-1.5	0	[105]

Change[a]	Reaction name	A[b]	B[b]	C[b]	Ref.
A	$e^- + NO_2 \rightarrow NO + O^-$	2.52×10^{-29}	-1.5	0	[105]
A	$e^- + NO_2 \rightarrow NO_2^-$	1.00×10^{-11}	0	0	[105]
A	$e^- + NO_2^+ \rightarrow NO + O(^1D)$	3.00×10^{-11}	0	0	[105]
D	$e^- + NO_2^+ \rightarrow NO + O(^1D)$	$\sigma(\varepsilon)$			[179]
A	$e^- + e^- + NO_2^+ \rightarrow NO_2 + e^-$	9.14×10^{-27}	-4.5	0	[105]
A	$e^- + M + NO_2^+ \rightarrow NO_2 + M$	2.70×10^{-29}	-1.5	0	[105]
A	$e^- + NO_3 + M \rightarrow NO_3^- + M$	1.00×10^{-30}	0	0	[116]
r	$e^- + e^- + H^+ \rightarrow H + e^-$	9.14×10^{-27}	-4.5	0	[105]
		8.80×10^{-27}	-4.5	0	[121]
A	$e^- + M + H^+ \rightarrow H + M$	2.70×10^{-29}	-1.5	0	[105]
A	$e^- + e^- + H_2^+ \rightarrow H_2 + e^-$	9.14×10^{-27}	-4.5	0	[105]
A	$e^- + M + H_2^+ \rightarrow H_2 + M$	2.70×10^{-29}	-1.5	0	[105]
A	$e^- + e^- + OH^+ \rightarrow OH + e^-$	9.14×10^{-27}	-4.5	0	[105]
A	$e^- + M + OH^+ \rightarrow OH + M$	2.70×10^{-29}	-1.5	0	[105]
A	$e^- + e^- + H_2O^+ \rightarrow H_2O + e^-$	9.14×10^{-27}	-4.5	0	[105]
A	$e^- + M + H_2O^+ \rightarrow H_2O + M$	2.70×10^{-29}	-1.5	0	[105]
A	$e^- + HNO_3 \rightarrow NO_2^- + OH$	5.00×10^{-08}	0	0	[180]
A	$Ar^+ + O_3^- \rightarrow Ar + O_3$	2.00×10^{-07}	-0.5	0	[105]
A	$Ar^+ + O_3^- \rightarrow Ar + O + O_2$	1.00×10^{-07}	0	0	[105]
A	$Ar^+ + O_3^- + M \rightarrow Ar + O_3 + M$	2.00×10^{-25}	-2.5	0	[105]
A	$Ar_2^+ + O_3^- \rightarrow Ar + Ar + O_3$	2.00×10^{-07}	-0.5	0	[105]
A	$Ar_2^+ + O_3^- \rightarrow Ar + Ar + O_2 + O$	1.00×10^{-07}	0	0	[105]
A	$Ar_2^+ + O_3^- + M \rightarrow Ar + Ar + O_3 + M$	2.00×10^{-25}	-2.5	0	[105]
A	$Ar_2^+ + NO_3^- + M \rightarrow Ar + Ar + NO_3 + M$	2.00×10^{-25}	-2.5	0	[105]

Change[a]	Reaction name	A[b]	B[b]	C[b]	Ref.
A	$O + O_3 \rightarrow O_2(a) + O_2$	1.00×10^{-11}	0	2300	[170]
A	$O(^1D) + O_4^+ \rightarrow O_3 + O_2^+$	3.00×10^{-10}	0	0	[126]
M	$O_{2,vib} + O_3 \rightarrow O_2 + O_3$				[181]
M	$O_{2,rot} + O_3 \rightarrow O_2 + O_3$				[181]
A	$O_2(a) + O \rightarrow O_2 + O$	7.00×10^{-16}	0	0	[182]
A	$O_3 + O_3^- \rightarrow O_2 + O_2 + O_2 + e^-$	3.00×10^{-10}	0	0	[116]
A	$N_2 + N_4^+ \rightarrow N_2^+ + N_2 + N_2$	2.10×10^{-16}	0	-121	[171]
A	$N_2(A) + N_2^+ \rightarrow N_3^+ + N$	3.00×10^{-10}	0	0	[116]
R	$N_2(A) + N \rightarrow N_2 + N$	2.00×10^{-12}	0	0	[182]
		2.00×10^{-11}			[183]
P	$N_2(A) + N_2(A) \rightarrow N_2 + N_2$	2.00×10^{-12}	0	0	[184]
	$N_2(A) + N_2(A) \rightarrow N_2 + N_2(A)$				[184]
R	$N_4^+ + M \rightarrow N_2^+ + M + N_2$	4.88×10^{-09}	1.5	12638	[185]
		2.50×10^{-15}	0	0	[105]
A	$O + N_2(A) \rightarrow N_2 + O(^1D)$	2.30×10^{-11}	0	0	[116]
R	$O + N_2(A) \rightarrow NO + N(^2D)$	7.00×10^{-12}	0	0	[105]
		1.00×10^{-12}	0	0	[105]
A	$O + NO_3 \rightarrow NO + O_3^-$	2.50×10^{-12}	0	0	[186]
A	$O^- + NO_3 \rightarrow NO_3^- + O$	3.00×10^{-10}	0	0	[116]
A	$O_2^- + N \rightarrow NO + O_2^-$	1.00×10^{-10}	0	0	[126]
r	$O_2^- + N_2O \rightarrow O_3^- + N_2$	1.00×10^{-14}	0	0	[186]
		9.00×10^{-13}	0	0	[105]
A	$O_3 + NO_2^- \rightarrow O_3^- + NO_2$	9.00×10^{-11}	0	0	[126]
A	$O_3 + N_4^+ \rightarrow N_2 + N_2 + O_2 + O$	1.00×10^{-07}	0	0	[105]

Change[a]	Reaction name	A[b]	B[b]	C[b]	Ref.
A	$O_3^- + N_2O \rightarrow O_2 + O_2 + N_2 + e^-$	2.00×10^{-14}	0	0	[126]
A	$O_3^- + N_2O \rightarrow O_2^- + O_2 + N_2$	2.00×10^{-14}	0	0	[126]
A	$O_3^- + N_2O \rightarrow NO + NO_3^-$	2.00×10^{-14}	0	0	[126]
A	$O_4^+ + NO_2 \rightarrow NO_2^+ + O_2 + O_2$	3.00×10^{-10}	0	0	[116]
A	$N + NO_2^- \rightarrow N_2 + O_2 + e^-$	1.00×10^{-12}	0	0	[116]
R	$N_3^+ + NO \rightarrow N + N_2 + NO^+$	7.00×10^{-11}	0	0	[116]
		1.40×10^{-10}	0	0	[187]
A	$N_3^+ + NO_2^- + M \rightarrow N_2 + N + NO_2 + M$	2.00×10^{-25}	-2.5	0	[105]
A	$N_3^+ + NO_3^- + M \rightarrow N_2 + N + NO_3 + M$	2.00×10^{-25}	-2.5	0	[105]
A	$N_4^+ + NO_2^- + M \rightarrow N_2 + N_2 + NO_2 + M$	2.00×10^{-25}	-2.5	0	[105]
A	$N_4^+ + NO_3^- + M \rightarrow N_2 + N_2 + NO_3 + M$	2.00×10^{-25}	-2.5	0	[105]
M	$NO + NO + O_2 \rightarrow NO_2 + NO_2$				[188]
D	$NO + NO_2 \rightarrow N_2O_3$	7.90×10^{-12}	1.40		[189]
R	$NO_2^+ + NO_2^- \rightarrow NO_2 + NO + O$	2.00×10^{-07}	0	0	[105]
		1.00×10^{-07}	0	0	[105]
A	$H + O_3^- \rightarrow OH^- + O_2$	8.40×10^{-10}	0	0	[116]
R	$H + NO_2^- \rightarrow HNO_2 + e^-$	1.85×10^{-10}	0	0	[190]
		3.70×10^{-10}	0	0	[186]
A	$H^+ + NO_2 \rightarrow NO_2^+ + H$	1.85×10^{-09}	0	0	[180]
M	$H^+ + H + M \rightarrow H_2^+ + M$				[121]
P	$H^- + OH^+ \rightarrow H + O + H$	1.00×10^{-07}	0	0	[105]
	$H^- + OH^+ \rightarrow H + OH$				[105]
A	$H_2 + N_4^+ \rightarrow N_2 + H_2^+ + N_2$	3.00×10^{-10}	0	1800	[116]
M	$H_2^+ + OH^- + M \rightarrow H_2 + OH + M$				[105]

Change[a]	Reaction name	A[b]	B[b]	C[b]	Ref.
A	$H_3^+ + O^- + M \rightarrow H_2 + H + O + M$	2.00×10^{-25}	-2.5	0	[105]
A	$H_3^+ + O_2^- + M \rightarrow H_2 + H + O_2 + M$	2.00×10^{-25}	-2.5	0	[105]
A	$H_3^+ + NO_2^- + M \rightarrow H_2 + H + NO_2 + M$	2.00×10^{-25}	-2.5	0	[105]
A	$H_3^+ + NO_3^- + M \rightarrow H_2 + H + NO_3 + M$	2.00×10^{-25}	-2.5	0	[105]
R	$OH + N^+ \rightarrow N + OH^+$	3.40×10^{-10}	0	0	[116]
		3.70×10^{-11}	0	0	[180]
R	$OH + N^+ \rightarrow NO^+ + H$	3.40×10^{-10}	0	0	[116]
		3.40×10^{-11}	0	0	[191]
r	$OH + HNO_3 \rightarrow H_2O + NO_3$	1.50×10^{-14}	0	-650	[116]
		1.50×10^{-13}	0	0	[188]
R	$OH(A) + N_2 \rightarrow OH + N_2$	2.49×10^{-13}	-0.5	0	[192]
		2.49×10^{-14}	-0.5	0	[192]
A	$OH^+ + NO_2 \rightarrow NO^+ + HO_2$	1.30×10^{-09}	0	0	[116]
A	$OH^- + O_3 \rightarrow O_3^- + OH$	9.00×10^{-10}	0	0	[116]
A	$HO_2 + NO \rightarrow OH + NO_2$	3.60×10^{-12}	0	-270	[183]
A	$H_2O + O(^1D) \rightarrow OH + OH$	2.20×10^{-10}	0	0	[188]
M	$H_2O + O_2^- \rightarrow H_2O + O_2 + e^-$				[121]
r	$H_2O + N^+ \rightarrow NO^+ + H_2$	4.00×10^{-10}	0	0	[191]
		4.00×10^{-10}	0.52	0	[191]
A	$H_3O^+ + N_2O_5 \rightarrow H_2O + HNO_3 + NO_2^+$	5.50×10^{-10}	0	0	[116]
A	$O_2(b) \rightarrow O_2(a)$	1.50×10^{-03}	0	0	[182]
A	$N_2(A) \rightarrow N_2$	5.00×10^{-01}	0	0	[182]
A	$N_2(a') \rightarrow N_2$	$1.00\times10^{+02}$	0	0	[182]
P	$H_2O_3^+ + e^- \rightarrow H_2O + O_2$	7.22×10^{-07}	-0.2	0	[121]

Change[a]	Reaction name	A[b]	B[b]	C[b]	Ref.
	$H_2O_3^+ + e^- \rightarrow H + OH + O_2$				[105]
P	$H_5O_2^+ + e^- \rightarrow 2\,H_2O + H$	2.00×10^{-07}	-0.5	0	[121]
	$H_5O_2^+ + e^- \rightarrow H_2O + H + H + OH$				[105]
P	$H_7O_3^+ + e^- \rightarrow 3\,H_2O + H$	2.00×10^{-07}	-0.5	0	[121]
	$H_7O_3^+ + e^- \rightarrow 2\,H_2O + H + H + OH$				[105]
P	$H_9O_4^+ + e^- \rightarrow 4\,H_2O + H$	2.00×10^{-07}	-0.5	0	[121]
	$H_9O_4^+ + e^- \rightarrow 3\,H_2O + H + H + OH$				[105]
P	$H_{11}O_5^+ + e^- \rightarrow 5\,H_2O + H$	2.00×10^{-07}	-0.5	0	[121]
	$H_{11}O_5^+ + e^- \rightarrow 4\,H_2O + H + H + OH$				[105]
P	$H_{13}O_6^+ + e^- \rightarrow 6\,H_2O + H$	2.00×10^{-07}	-0.5	0	[121]
	$H_{13}O_6^+ + e^- \rightarrow 5\,H_2O + H + H + OH$				[105]
P	$H_{15}O_7^+ + e^- \rightarrow 7\,H_2O + H$	2.00×10^{-07}	-0.5	0	[121]
	$H_{15}O_7^+ + e^- \rightarrow 6\,H_2O + H + H + OH$				[105]
A	$H_2O_3^+ + O_2 \rightarrow O_4^+ + H_2O$	2.00×10^{-10}	0	2300	[126]
P	$H_2NO_2^+ + O^- + M \rightarrow NO + O + H_2O + M$	2.00×10^{-25}	-2.5	0	[105]
	$H_2NO_2^+ + O^- + M \rightarrow NO_2 + H_2O + M$				[105]
P	$H_2NO_2^+ + O_2^- + M \rightarrow NO + O_2 + H_2O + M$	2.00×10^{-25}	-2.5	0	[105]
	$H_2NO_2^+ + O_2^- + M \rightarrow NO_3 + H_2O + M$				[105]
P	$H_2NO_2^+ + O_3^- + M \rightarrow NO + O_3 + H_2O + M$	2.00×10^{-25}	-2.5	0	[105]
	$H_2NO_2^+ + O_3^- + M \rightarrow NO_2 + O_2 + H_2O + M$				[105]
P	$H_2NO_2^+ + NO_3^- + M \rightarrow NO + NO_3 + H_2O + M$	2.00×10^{-25}	-2.5	0	[105]
	$H_2NO_2^+ + NO_3^- + M \rightarrow NO_2 + NO_2 + H_2O + H_2O + M$				[105]
P	$H_2NO_2^+ + H^- + M \rightarrow H + NO + H_2O + M$	2.00×10^{-25}	-2.5	0	[105]
	$H_2NO_2^+ + H^- + M \rightarrow HNO + H_2O + M$				[105]

Change[a]	Reaction name	A[b]	B[b]	C[b]	Ref.
P	$H_2NO_2^+ + OH^- + M \rightarrow OH + NO + H_2O + M$	2.00×10^{-25}	-2.5	0	[105]
	$H_2NO_2^+ + OH^- + M \rightarrow HNO_2 + H_2O + M$				[105]
P	$H_4NO_3^+ + O^- + M \rightarrow NO + O + 2\,H_2O + M$	2.00×10^{-25}	-2.5	0	[105]
	$H_4NO_3^+ + O^- + M \rightarrow NO_2 + 2\,H_2O + M$				[105]
P	$H_4NO_3^+ + O_2^- + M \rightarrow NO + O_2 + 2\,H_2O + M$	2.00×10^{-25}	-2.5	0	[105]
	$H_4NO_3^+ + O_2^- + M \rightarrow NO_3 + 2\,H_2O + M$				[105]
P	$H_4NO_3^+ + O_3^- + M \rightarrow NO + O + O_2 + 2\,H_2O + M$	2.00×10^{-25}	-2.5	0	[105]
	$H_4NO_3^+ + O_3^- + M \rightarrow NO_2 + O_2 + 2\,H_2O + M$				[105]
P	$H_4NO_3^+ + NO_3^- + M \rightarrow NO + NO_3 + 2\,H_2O + M$	2.00×10^{-25}	-2.5	0	[105]
	$H_4NO_3^+ + NO_3^- + M \rightarrow NO_2 + NO_2 + 2\,H_2O + M$				[105]
P	$H_4NO_3^+ + H^- + M \rightarrow H + NO + 2\,H_2O + M$	2.00×10^{-25}	-2.5	0	[105]
	$H_4NO_3^+ + H^- + M \rightarrow HNO + 2\,H_2O + M$				[105]
P	$H_4NO_3^+ + OH^- + M \rightarrow OH + NO + 2\,H_2O + M$	2.00×10^{-25}	-2.5	0	[105]
	$H_4NO_3^+ + OH^- + M \rightarrow HNO_2 + 2\,H_2O + M$				[105]
P	$H_6NO_4^+ + O^- + M \rightarrow NO + O + 3\,H_2O + M$	2.00×10^{-25}	-2.5	0	[105]
	$H_6NO_4^+ + O^- + M \rightarrow NO_2 + 3\,H_2O + M$				[105]
P	$H_6NO_4^+ + O_2^- + M \rightarrow NO + O_2 + 3\,H_2O + M$	2.00×10^{-25}	-2.5	0	[105]
	$H_6NO_4^+ + O_2^- + M \rightarrow NO_3 + 3\,H_2O + M$				[105]
P	$H_6NO_4^+ + O_3^- + M \rightarrow NO + O + O_2 + 3\,H_2O + M$	2.00×10^{-25}	-2.5	0	[105]
	$H_6NO_4^+ + O_3^- + M \rightarrow NO_2 + O_2 + 3\,H_2O + M$				[105]
P	$H_6NO_4^+ + NO_3^- + M \rightarrow NO + NO_3 + 3\,H_2O + M$	2.00×10^{-25}	-2.5	0	[105]
	$H_6NO_4^+ + NO_3^- + M \rightarrow NO_2 + NO_2 + 3\,H_2O + M$				[105]
P	$H_6NO_4^+ + H^- + M \rightarrow H + NO + 3\,H_2O + M$	2.00×10^{-25}	-2.5	0	[105]
	$H_6NO_4^+ + H^- + M \rightarrow HNO + 3\,H_2O + M$				[105]

Change[a]	Reaction name	A[b]	B[b]	C[b]	Ref.
P	$H_6NO_4^+ + OH^- + M \rightarrow OH + NO + 3\ H_2O + M$	2.00×10^{-25}	-2.5	0	[105]
	$H_6NO_4^+ + OH^- + M \rightarrow HNO_2 + 3\ H_2O + M$				[105]

ᵃ   The changes made with respect to Appendix A are done due to some small errors and inconsistencies in the reaction set and mostly for reactions with minor importance. Nevertheless, they are presented here for the sake of correctness. As a result they do not affect the density calculations significantly. This column indicates the specific change: (A) added new reaction, (r) minor change in rate coefficient for consistency, (R) larger change in rate coefficient, (D) reaction deleted, (M) multiple reactions detected thus reduced to only one, (P) reaction products modified.

ᵃ   Reaction rate coefficients are usually in the Arrhenius form, for heavy particle collisions: k=A$\times$(T$_g$/300)$^B\times$exp(-C/T$_g$), for electron impact collisions: k=A$\times$(T$_e$)$^B\times$exp(-C/T$_e$). The unit of A is (s^{-1}),(cm^3.s^{-1}) or (cm^6.s^{-1}) for first, second or third order reactions. The unit of C is K, except for electron impact reactions where the unit is eV. Thus, the units of T$_g$ and T$_e$ are also K and eV, respectively In the case that reaction rate coefficients are calculated by the Boltzmann solver with cross sectional data this is indicated by $\sigma(\varepsilon)$ where ε is the mean electron energy.

Bibliography

[1] Lu X, Laroussi M and Puech V 2012 *Plasma Sourc. Sci. Tech.* **21** 034005

[2] Nie Q Y, Ren C S, Wang D Z, Li S Z, Zhang J L and Kong M G 2007 *Appl. Phys. Lett.* **90** 221504

[3] Sousa J S, Niemi K, Cox L J, Algwari Q T, Gans T and O'Connell D 2011 *J. Appl. Phys.* **109** 123302

[4] Qian M, Ren C, Wang D, Zhang J and Wei G 2010 *J. Appl. Phys.* **107** 063303

[5] Li Q, Li J T, Zhu W C, Zhu X M and Pu Y K 2009 *Appl. Phys. Lett.* **95** 141502

[6] Teschke M, Kedzierski J, Korzec D and Engemann J 2005 *IEEE Trans. Plasma Sci.* **33** 310

[7] Laimer J, Reicher H and Störi H 2009 *Vacuum* **84** 104

[8] Kim H, Brockhaus A and Engemann J 2009 *Appl. Phys. Lett.* **95** 211501

[9] Bibinov N, Dudek D, Awakowicz P and Engemann J 2007 *J. Phys. D: Appl. Phys.* **40** 7372

[10] Georgescu N, Lungu C P, Lupu A R and Osiac M 2010 *IEEE Trans. Plasma Sci.* **38** 3156

[11] Ni T L, Ding F, Zhu X D, Wen X H and Zhou H Y 2008 *Appl. Phys. Lett.* **92** 241503

[12] Coulombe S, Léveillé V, Yonson S and Leask R L 2006 *Pure Appl. Chem* **78** 1147

[13] Hong Y C, Uhm H S and Yi W J 2008 *Appl. Phys. Lett.* **93** 051504

[14] Xiong Q, Nikiforov a Y, Lu X P and Leys C 2010 *J. Phys. D: Appl. Phys.* **43** 415201

[15] Shashurin A, Shneider M N, Dogariu a, Miles R B and Keidar M 2009 *Appl. Phys. Lett.* **94** 231504

[16] Lu X, Jiang Z, Xiong Q, Tang Z, Hu X and Pan Y 2008 *Appl. Phys. Lett.* **92** 081502

[17] Robert E, Barbosa E, Dozias S A, Vandamme M, Cachoncinlle C, Viladrosa R and Pouvesle J M 2009 *Plasma Process. Polym.* **6** 795

[18] Schulz-von der Gathen V, Buck V, Gans T, Knake N, Niemi K, Reuter S, Schaper L and Winter J 2007 *Contrib. Plasma Phys.* **47** 510

[19] Laroussi M and Lu X 2005 *Appl. Phys. Lett.* **87** 113902

[20] Schneider S, Lackmann J W, Narberhaus F, Bandow J E, Denis B and Benedikt J 2011 *J. Phys. D: Appl. Phys.* **44** 379501

[21] http://bioplasma.pointblank.ie/

[22] Ellerweg D, von Keudell A and Benedikt J 2012 *Plasma Sourc. Sci. Tech.* **21** 034019

[23] Lee H W, Park G Y, Seo Y S, Im Y H, Shim S B and Lee H J (2011) *J. Phys. D: Appl. Phys.* **44** 053001

[24] Lu X and Laroussi M 2006 *J. Appl. Phys.* **100** 063302

[25] Brok W J M, Bowden M D, van Dijk J, van der Mullen J J a M and Kroesen G M W 2005 *J. Appl. Phys.* **98** 013302

[26] Stoffels E, Flikweert A J, Stoffels W W and Kroesen G M W 2002 *Plasma Sourc. Sci. Tech.* **11** 383

[27] Lu X, Member S, Cao Y, Yang P, Xiong Q, Xiong Z, Xian Y and Pan Y 2009 *IEEE Trans. Plasma Sci.* **37** 668

[28] Bussiahn R, Brandenburg R, Gerling T, Kindel E, Lange H, Lembke N, Weltmann K D, von Woedtke T and Kocher T 2010 *Appl. Phys. Lett.* **96** 143701

[29] Babaeva N Y and Mark M J K 2010 *J. Phys. D: Appl. Phys.* **43** 185206

[30] Cao Z, Nie Q, Bayliss D L, Walsh J L, Ren C S, Wang D Z and Kong M G 2010 *Plasma Sourc. Sci. Tech.* **19** 025003

[31] Cao Z, Walsh J L and Kong M G 2009 *Appl. Phys. Lett.* **94** 021501

[32] Kushner M J 2011 *30th Int. Conf. on Phenomena in Ionized Gases, Belfast, UK*

[33] van Gessel a F H, van Grootel S C and Bruggeman P J 2013 *Plasma Sourc. Sci. Tech.* **22** 055010

[34] Shimizu T, Steffes B, Pompl R, Jamitzky F, Bunk W, Ramrath K, Georgi M, Stolz W, Schmidt H U, Urayama T, Fujii S and Morfill G E 2008 *Plasma Process. Polym.* **5** 577

[35] Shashurin A, Keidar M, Bronnikov S, Jurjus R a and Stepp M a 2008 *Appl. Phys. Lett.* **93** 181501

[36] Tsai J H, Hsu C M and Hsu C C 2013 *Plasma Chem. Plasma P.* **33** 1121

[37] Robert E, Sarron V, Darny T, Riès D, Dozias S, Fontane J, Joly L and Pouvesle J M 2014 *Plasma Sourc. Sci. Tech.* **23** 012003

[38] Hofmann S, van Gessel A F H, Verreycken T and Bruggeman P 2011 *Plasma Sourc. Sci. Tech.* **20** 065010

[39] Hofmann S and Bruggeman P 2011 *IEEE Trans. Plasma Sci.* **39** 2332

[40] Zhang S, van Gaens W, van Gessel B, Hofmann S, van Veldhuizen E, Bogaerts A and Bruggeman P 2013 *J. Phys. D: Appl. Phys.* **46** 205202

[41] van Gessel a F H, Alards K M J and Bruggeman P J 2013 *J. Phys. D: Appl. Phys.* **46** 265202

[42] Hofmann S, van Gils K, van der Linden S, Iseni S and Bruggeman P 2014 *Eur. Phys. J. D* **68** 56

[43] von Woedtke T, Reuter S, Masur K and Weltmann K D 2013 *Phys. Rep.* **530** 291

[44] Weltmann K D, Kindel E, Brandenburg R, Meyer C, Bussiahn R, Wilke C and von Woedtke T 2009 *Contrib. Plasma Phys.* **49** 631

[45] Liu X Y, Pei X K, Lu X P and Liu D W 2014 *Plasma Sourc. Sci. Tech.* **23** 035007

[46] Laroussi M, Hynes W, Akan T and Tendero C 2008 *IEEE Trans. Plasma Sci.* **36** 1298

[47] Naidis G V 2010 *J. Phys. D: Appl. Phys.* **43** 402001

[48] Naidis G V 2011 *J. Phys. D: Appl. Phys.* **44** 215203

[49] Boeuf J P, Yang L L and Pitchford L C 2013 *J. Phys. D: Appl. Phys.* **46** 015201

[50] Breden D, Miki K and Raja L L 2012 *Plasma Sourc. Sci. Tech.* **21** 034011

[51] Yousfi M, Eichwald O, Merbahi N and Jomaa N 2012 *Plasma Sourc. Sci. Tech.* **21** 045003

[52] Morfill G E, Shimizu T, Steffes B and Schmidt H U 2009 *New J. Phys.* **11** 115019

[53] Xiong Z, Robert E, Sarron V, Pouvesle J M and Kushner M J 2013 *J. Phys. D: Appl. Phys.* **46** 155203

[54] Xiong Z and Kushner M J 2012 *Plasma Sourc. Sci. Tech.* **21** 034001

[55] Xiong, Z, Robert E, Sarron V, Pouvesle J M and Kushner M J 2012 *J. Phys. D: Appl. Phys.* **45** 275201

[56] Babaeva N Y and Kushner M J 2014 *Plasma Sourc. Sci. Tech.* **23** 015007

[57] Isbary G, Köritzer J, Mitra a, Li Y F, Shimizu T, Schroeder J, Schlegel J, Morfill G, Stolz W and Zimmermann J 2013 *Clin. Plasma Med.* **1** 36

[58] Emmert S, Brehmer F, Hanssle H, Helmke A, Mertens N, Ahmed R, Simon D, Wandke D, Schon M P, Maus-Friedrichs W, Viol W and Daschlein G 2012 *Plasma Med.* **2** 19

[59] Fridman G, Shereshevsky A, Jost M M, Brooks A D, Fridman A, Gutsol A, Vasilets V and Friedman G 2007 *Plasma Chem. Plasma P.* **27** 163

[60] Waskoenig J, O'Connell D, Schulz- von der Gathen V, Winter J, Park S J and Eden J G 2008 *Appl. Phys. Lett.* **92** 101503

[61] Oehmigen K, Hähnel M, Brandenburg R, Wilke C, Weltmann K D and von Woedtke T 2010 *Plasma Process. Polym.* **7** 250

[62] Polak M, Winter J, Schnabel U, Ehlbeck J and Weltmann K–D 2012 *Plasma Process. Polym.* **9** 67

[63] Kovalóvá Z, Zahoran M, Zahoranová a and Machala Z 2014 *J. Phys. D: Appl. Phys.* **47** 224014

[64] Machala Z, Tarabova B, Hensel K, Spetlikova E, Sikurova L and Lukes P 2013 *Plasma Process. Polym.* **10** 649

[65] Traylor M J, Pavlovich M J, Karim S, Hait P, Sakiyama Y, Clark D S and Graves, D B 2011 *J. Phys. D: Appl. Phys.* **44** 472001

[66] Kim G J, Kim W, Kim K T and Lee J K 2010 *Appl. Phys. Lett.* **96** 021502

[67] Dobrynin D, Arjunan K, Fridman A, Friedman G and Clyne A M 2011 *J. Phys. D: Appl. Phys.* **44** 075201

[68] Graves D B 2012 *J. Phys. D: Appl. Phys.* **45** 263001

[69] Kalghatgi S, Kelly C M, Cerchar E, Torabi B, Alekseev O, Fridman A, Friedman G and Azizkhan-Clifford J 2011 *PloS one* **6** e16270

[70] Lukes P, Dolezalova E, Sisrova I and Clupek M 2014 *Plasma Sourc. Sci. Tech.* **23** 015019

[71] Van Gils C a J, Hofmann S, Boekema B K H L, Brandenburg R and Bruggeman P J 2013 *J. Phys. D: Appl. Phys.* **46** 175203

[72] Fridman G, Peddinghaus M, Balasubramanian M, Ayan H, Fridman A, Gutsol A and Brooks A 2006 *Plasma Chem. Plasma P.* **26** 425

[73] De Geyter N and Morent R 2012 *Annu. Rev. Biomed. Eng.* **14** 255

[74] Zimmermann J L, Dumler K, Shimizu T, Morfill G E, Wolf A, Box-hammer V, Schlegel J, Gansbacher B and Anton M 2011 *J. Phys. D: Appl. Phys.* **44** 505201

[75] Bayliss D L, Walsh J L, Shama G, Iza F and Kong M G 2009 *New J. Phys.* **11** 115024

[76] Cha S and Park Y S 2014 *Clin. Plasma Med.*

[77] Stoffels E, Kieft I E and Sladek R E J 2003 *J. Phys. D: Appl. Phys.* **36** 2908

[78] Stoffels E, Kieft I E, Sladek R E J, van den Bedem L J M, van der Laan E P and Steinbuch M 2006 *Plasma Sourc. Sci. Tech.* **15** S169

[79] O'Connell D, Cox L J, Hyland W B, McMahon S J, Reuter S, Graham W G, Gans T and Currell F J 2011 *Appl. Phys. Lett.* **98** 043701

[80] Leduc M, Guay D, Coulombe S and Leask R L 2010 *Plasma Process. Polym.* **7** 899

[81] Kalghatgi S, Kelly C M, Cerchar E, Torabi B, Alekseev O, Fridman A and Azizkhan-Clifford J 2011 *PloS One* **6** e16270

[82] Kim K, Choi J D, Hong Y C, Kim G, Noh E J, Lee J S and Yang S S 2011 *Appl. Phys. Lett.* **98** 073701

[83] Ahn H J, Kim K I, Kim G, Moon E, Yang S S and Lee J S 2011 *PloS one* **6** e28154

[84] Sladek R, Stoffels E, Walraven R, Tielbeek P and Koolhoven R 2004 *IEEE Trans. Plasma Sci.* **32** 1540

[85] Keidar M, Shashurin A, Volotskova O, Ann Stepp M, Srinivasan P, Sandler A and Trink B 2013 *Phys. Plasmas* **20** 057101

[86] Kajiyama H, Nakamura K, Utsumi F, Tanaka H, Hori M and Kikkawa F 2014 *Jpn. J. Appl. Phys.* **53** 05FA05

[87] Robert E, Vandamme M, Brullé L, Lerondel S, Le Pape a, Sarron V and Pouvesle J M 2013 *Clin. Plasma Med.* **1** 8

300

[88] Collet G, Robert E, Lenoir a, Vandamme M, Darny T, Dozias S, Kieda C and Pouvesle J M 2014 *Plasma Sourc. Sci. Tech.* **23** 012005

[89] Kalghatgi S, Friedman G, Fridman A and Clyne A M 2010 *Ann. Biomed. Eng.* **38** 748

[90] Tipa R S and Kroesen G M W 2011 *IEEE Trans. Plasma Sci.* **39** 2978

[91] Nastuta A V, Topala I, Grigoras C, Pohoata V and Popa G 2011 *J. Phys. D: Appl. Phys.* **44** 105204

[92] Witte M B and Barbul A 2002 *Am J. Surg.* **183** 406

[93] Nosenko T, Shimizu T and Morfill G E 2009 *New J. Phys.* **11** 115013

[94] Lloyd G, Friedman G, Jafri S, Schultz G, Fridman A and Harding K 2010 *Plasma Process. Polym.* **7** 194

[95] Heinlin J, Isbary G, Stolz W, Morfill G, Landthaler M, Shimizu T, Steffes B, Nosenko T, Zimmermann J and Karrer S 2011 *J. Eur. Acad. Dermatol. Venereol.* **25** 1

[96] Emmert S, Brehmer F, Hänß le H, Helmke A, Mertens N, Ahmed R, Simon D, Wandke D, Maus-Friedrichs W, Däschlein G, Schön M P and Viöl W 2013 *Clin. Plasma Med.* **1** 24

[97] Isbary G, Shimizu T, Zimmermann J, Heinlin J, Al-Zaabi S, Rechfeld M, Morfill G, Karrer S and Stolz W 2014 *Clin. Plasma Med.* 1

[98] Isbary G, Morfill G, Zimmermann J, Shimizu T and Stolz W 2011 *Arch. Dermatol.* **147** 388

[99] Lademann J, Ulrich C, Patzelt a, Richter H, Kluschke F, Klebes M, Lademann O, Kramer a, Weltmann K and Lange-Asschenfeldt B 2013 *Clin. Plasma Med.* **1** 5

[100] Tümmel S, Mertens N, Wang J and Viöl W 2007 *Plasma Process. Polym.* **4** S465

[101] Isbary G, Morfill G, Schmidt H U, Georgi M, Ramrath K, Heinlin J, Karrer S, Landthaler M, Shimizu T, Steffes B, Bunk W, Monetti R, Zimmermann J L, Pompl R and Stolz W 2010 *Br. J. Dermatol.* **163** 78

[102] Eliasson B and Kogelschatz U 1986 *Basic data for modelling of electrical discharges in gases: oxygen* Asea Brown Boveri Research Report KLR 86-11C

[103] Eliasson B, Hirth M and Kogelschatz U 1987 *J. Phys. D: Appl. Phys.* **20** 1421–1437

[104] Kogelschatz U, Eliasson B and Hirth M 1988 *Ozone Sci. Eng.* **10** 367–377

[105] Kossyi I A, Kostinsky A Y, Matveyev A A and Silakov V P 1992 *Plasma Sourc. Sci. Tech.* **1** 207–220

[106] Gentile A C and Kushner M J 1995 *J. Appl. Phys.* **78** 2074

[107] Atkinson R, Baulch D L, Cox R A, Hampson R F, Kerr J A, Rossi M J and Troe J 1997 *J. Phys. Chem. Ref. Data* **26** 1329

[108] Baulch D L, Cox R A, Hampson R F, Kerr J A, Troe J and Watson R T 1984 *J. Phys. Chem. Ref. Data* **13** 1259

[109] Baulch D L 2005 *J. Phys. Chem. Ref. Data* **34** 757

[110] Herron J T 1999 *J. Phys. Chem. Ref. Data* **28** 1453

[111] Herron J T 2001 *Plasma Chem. Plasma Proc.* **21** 581–609

[112] Herron J T and Green D S 2001 *Plasma Chem. Plasma Proc.* **21** 459–481

[113] Sieck L W, Herron J T and Green D S 2000 *Plasma Chem. Plasma Proc.* **20** 235–258

[114] Tsang W and Hampson R F 1986 *J. Phys. Chem. Ref. Data* **15** 1087

[115] Tsang W and Herron J T 1991 *J. Phys. Chem. Ref. Data* **20** 609

[116] Sakiyama Y, Graves D B, Chang H W, Shimizu T and Morfill G E 2012 *J. Phys. D: Appl. Phys.* **45** 425201

[117] Babaeva N Y and Kushner M J 2013 *J. Phys. D: Appl. Phys.* **46** 025401

[118] Babaeva N Y, Ning N, Graves D B and Kushner M J 2012 *J. Phys. D: Appl. Phys.* **45** 115203

[119] Babaeva N Y, Tian W and Kushner M J 2014 *J. Phys. D: Appl. Phys.* **47** 235201

[120] Naidis G V 2013 *Plasma Sourc. Sci. Tech.* **22** 035015

[121] Liu D X, Bruggeman P, Iza F, Rong M Z and Kong M G 2010 *Plasma Sourc. Sci. Tech.* **19** 025018

[122] Waskoenig J, Niemi K, Knake N, Graham L M, Reuter S, Schulz-von der Gathen V and Gans T 2010 *Plasma Sourc. Sci. Tech.* **19** 045018

[123] McKay K, Liu D X, Rong M Z, Iza F and Kong M G 2012 *J. Phys. D: Appl. Phys.* **45** 172001

[124] Murakami T, Niemi K, Gans T, O'Connell D and Graham W G 2014 *Plasma Sourc. Sci. Tech.* **23** 025005

[125] Murakami T, Niemi K, Gans T, O'Connell D and Graham W G 2013 *Plasma Sourc. Sci. Tech.* **22** 045010

[126] Murakami T, Niemi K, Gans T, O'Connell D and Graham W G 2013 *Plasma Sourc. Sci. Tech.* **22** 015003

[127] Sakiyama Y and Graves D B 2006 *J. Phys. D: Appl. Phys.* **39** 3451

[128] Sakiyama Y and Graves D B 2006 *J. Phys. D: Appl. Phys.* **39** 3644

[129] Sakiyama Y and Graves D B 2007 *IEEE Trans. Plasma Sci.* **35** 1279

[130] Sakiyama Y and Graves D B 2007 *J. Appl. Phys.* **101** 073306

[131] Sakiyama Y and Graves D B 2009 *Plasma Sourc. Sci. Tech.* **18** 025022

[132] Schmidt-Bleker A, Winter J, Iseni S, Dünnbier M, Weltmann K D and Reuter S 2014 *J. Phys. D: Appl. Phys.* **47** 145201

[133] Hamaguchi S 2013 *AIP Conf. Proc.* **1545** 214

[134] Yusupov M, Bogaerts A, Huygh S, Snoeckx R, van Duin A C T and Neyts E C 2013 *J. Phys. Chem. C* **117** 5993

[135] Yusupov M, Neyts E C, Khalilov U, Snoeckx R, van Duin a C T and Bogaerts a 2012 *New J. Phys.* **14** 093043

[136] Yusupov M, Neyts E C, Simon P, Berdiyorov G, Snoeckx R, van Duin A C T and Bogaerts A 2014. *J. Phys. D: Appl. Phys.* **47** 025205

[137] Van der Paal J, Aernouts S, van Duin A C T, Neyts E C and Bogaerts A 2013 *J. Phys. D: Appl. Phys.* **46** 395201

[138] Neyts E C, Yusupov M, Verlackt C C and Bogaerts A 2014 *J. Phys. D: Appl. Phys.* **47** 293001

[139] Dorai R and Kushner M J 2003 *J. Phys. D: Appl. Phys.* **36** 666–685

[140] Stafford D S and Kushner M J 2004 *J. Appl. Phys.* **96** 2451

[141] Arakoni R, Stafford D S, Babaeva N Y and Kushner M J 2005 *J. Appl. Phys.* **98** 073304

[142] Reuter S, Winter J, Schmidt-Bleker A, Schroeder D, Lange H, Knake N, Schulz-von der Gathen V and Weltmann K D 2012 *Plasma Sourc. Sci. Tech.* **21** 024005

[143] Kong M G, Ganguly B N and Hicks R F 2012 *Plasma Sourc. Sci. Tech.* **21** 030201

[144] Farouk T, Farouk B, Gutsol A and Fridman A 2008 *Plasma Sourc. Sci. Tech.* **17** 035015

[145] Zhu X M, Pu Y K, Balcon N and Boswell R 2009 *J. Phys. D: Appl. Phys.* **42** 142003

[146] Pekárek S 2003 *Acta Polytech.* **43** 47

[147] Aerts R, Martens T and Bogaerts A 2012 *J. Phys. Chem. C* **116** 23257

[148] Stoffels E, Gonzalvo Y A, Whitmore T D, Seymour D L and Rees J A 2007 *Plasma Sourc. Sci. Tech.* **16** 549

[149] Bruggeman P, Iza F, Lauwers D and Gonzalvo Y A 2010 *J. Phys. D: Appl. Phys.* **43** 012003

[150] Schaper L, Reuter S, Waskoenig J, Niemi K, Schulz-von der Gathen V and Gans T 2009 *J. Phys.: Conf. Ser.* **162** 012013

[151] Vieceli J, Roeselova M, Potter N, Dang L X, Garrett B C and Tobias D J 2005 *J. Phys. Chem. B* **109** 15876

[152] Van Gaens W and Bogaerts a 2013 *J. Phys. D: Appl. Phys.* **46** 275201

[153] Maletić D, Puač N, Lazović S, Malović G, Gans T, Schulz-von der Gathen V and Petrović Z L 2012 *Plasma Phys. Contr. Fusion* **54** 124046

[154] Ellerweg D, Benedikt J, von Keudell a, Knake N and Schulz-von der Gathen V 2010 *New J. Phys.* **12** 013021

[155] Sousa J S, Douat C, Bauville G, Fleury M and Puech V 2013 Singlet delta oxygen absolute density measurements in the effluent of cold atmospheric pressure microplasma jets *31th Int. Conf. on Ionized Gases, Granada*

[156] van Gessel A F H, Alards K M J and Bruggeman P J 2013 *J. Phys. D: Appl. Phys.* **46** 265202

[157] Reuter S, Winter J, Iseni S, Peters S, Schmidt-Bleker a, Dünnbier M, Schäfer J, Foest R and Weltmann K D 2012 *Plasma Sourc. Sci. Tech.* **21** 034015

[158] Yonemori S, Nakagawa Y, Ono R and Oda T 2012 *J. Phys. D: Appl. Phys.* **45** 225202

[159] Wagenaars E, Gans T, O'Connell D and Niemi K 2012 *Plasma Sourc. Sci. Tech.* **21** 042002

[160] Pipa A V, Reuter S, Foest R and Weltmann K-D 2012 *J. Phys. D: Appl. Phys.* **45** 085201

[161] Sousa J S, Niemi K, Cox L J, Algwari Q T, Gans T and O'Connell D 2011 *J. Appl. Phys.* **109** 123302

[162] Reuter S, Winter J, Schmidt-Bleker A, Tresp H, Hammer M U and Weltmann K-D 2012 *IEEE Trans. Plasma Sci.* **40** 2788

[163] Winter J, Wende K, Masur K, Iseni S, Dünnbier M, Hammer M U, Tresp H, Weltmann K D and Reuter S 2013 *J. Phys. D: Appl. Phys.* **46** 295401

[164] Xiong Q, Nikiforov a Y, Li L, Vanraes P, Britun N, Snyders R, Lu X P and Leys C 2012 *Eur. Phys. J. D* **66** 281

[165] Van Gils C a J, Hofmann S, Boekema B K H L, Brandenburg R and Bruggeman P J 2013. *J. Phys. D: Appl. Phys.* **46** 175203

[166] Hofmann S, van Gils K, van der Linden S, Iseni S and Bruggeman P 2014 *Eur. Phys. J. D* **68** 56

[167] Deng X L, Nikiforov A, Vanraes P and Leys C 2013 *J. Appl. Phys.* **113** 023305

[168] Li L, Nikiforov A, Xiong Q, Britun N, Snyders R, Lu X and Leys C 2013 *Phys. Plasmas* **20** 093502

[169] http://www.graphviz.org/

[170] Bogaerts A 2009 *Spectroc. Acta B* **64** 1266

[171] Bogaerts A 2009 *Spectroc. Acta B* **64** 126

[172] Itikawa Y 2005 *J. Phys. Chem. Ref. Data* **34** 1

[173] Ono R and Oda T 2003 *J. Appl. Phys.* **93** 5876

[174] Komuro A, Ono R and Oda T 2013 *J. Phys. D: Appl. Phys.* **46** 175206

[175] Fresnet F, Baravian G, Magne L, Pasquiers S, Postel C, Puech V and Rousseau A 2002 *Plasma Sourc. Sci. Tech.* **11** 152

[176] Bartis E A J, Graves D B, Seog J and Oehrlein G S 2013 *J. Phys. D: Appl. Phys.* **46** 312002

[177] Kushner M J 1999 Strategies for Rapidly Developing Plasma Chemistry Models *Bull. Am. Phys. Soc.* **44** 63

[178] Brian J 1990 *Phys. Rep.* **186** 215

[179] Person J C and Ham D O 1988 *Int. J. Radiat. Appl. Instr.* **31** 1

[180] Woodall J, Agúndez M, Markwick-Kemper A J and Millar T J 2007 *Astronom. Astrophys.* **466** 1197

[181] Fridman A 2008 *Plasma Chemistry* (Cambridge: Cambridge University Press)

[182] Capitelli M, Ferreira C M, Gordiets B F and Osipov A I 2000 *Plasma Kinetics in Atmospheric Gases* (*Springer Series on Atomic, Optical, and Plasma Physics* vol 31) ed Drake G F and Ecker G (Berlin: Springer)

[183] Gordillo-Vázquez F J 2008 *J. Phys. D: Appl. Phys.* **41** 234016

[184] Lowke J and Morrow R 1995 *IEEE Trans. Plasma Sci.* **23** 661

[185] Bhoj A N B 2006 *Multiscale simulation of atmospheric pressure pulsed discharges used in polymer surface functionalization* Ph.D. thesis University of Illinois

[186] Albritton D 1978 *At. Data and Nucl. Data Tables* **22** 1

[187] Gentile A C 1995 *Kinetic processes and plasma remediation of toxic gases* Ph.D. thesis University of Illinois

[188] Atkinson R, Baulch D L, Cox R A, Crowley J N, Hampson R F, Hynes R G, Jenkin M E, Rossi M J and Troe J 2004 *Atmos. Chem. Phys.* **4** 1461

[189] Rasmussen C L, Hansen J r, Marshall P and Glarborg P 2008 *Int. J. Chem. Kinet.* **40** 454

[190] Ikezoe Y, Matsuoka S, Takebe M and Viggiano A (eds) 1987 *Gas Phase Ion-Molecule Reaction Rate Constants Through 1986* (Tokyo: Maruzen Company Ltd)

[191] Eichwald O, Yousfi M, Hennad A and Benabdessadok M D 1997 *J. Appl. Phys.* **82** 4781

[192] Koike T and Morinaga K 1982 *Bull. Chem. Soc. Jpn.* **55** 52

[193] Li Q, Li J-T, Zhu W-C, Zhu X-M and Pu Y-K 2009 *Appl. Phys. Lett.* **95** 141502

[194] A F H van Gessel 2013 *Laser diagnostics on atmospheric pressure plasma jets* Ph.D. thesis Eindhoven University of Technology

[195] Weltmann K D, Kindel E, von Woedtke T, Hähnel M, Stieber M and Brandenburg R 2010 *Pure and Applied Chemistry* **82** 1223

[196] Reuter S, Niemi K, Schulz–von der Gathen V and Döbele H F 2009 *Plasma Sources Science and Technology* **18** 015006

[197] Moisan M, Boudam K, Carignan D, Kéroack D, Levif P, Barbeau J, Séguin J, Kutasi K, Elmoualij B, Thellin O and Zorzi W 2013 *Eur. Phys. J. Appl. Phys.* **63** 10001

[198] Walsh J L and Kong M G 2008 *Appl. Phys. Lett.* **93** 111501

[199] Zhang S *et al* 2014 *accepted in Plasma Sourc. Sci. Tech.*

[200] Marinov D, Guerra V, Guaitella O, Booth J P and Rousseau A 2013 *Plasma Sourc. Sci. Tech.* **22** 055018

[201] Guerra V, Kutasi K, Sá P and Lino da Silva M 2011 *Eur. Phys. J. Appl. Phys.* **56** 24004

[202] Zeldovich Ya B, Sadovnikov P Y and Frank-Kamenetskii D A 1947 *Oxidation of Nitrogen in Combustion* (Moscow-Leningrad: Academy of Sciences of USSR, Institute of Chemical Physics)

[203] Komuro A, Ono R and Oda T 2013 *J. Phys. D: Appl. Phys.* **46** 175206

[204] Verreycken T and Bruggeman P J 2014 *Plasma Chem. Plasma Process.* 1

[205] Waskoenig J, Niemi K, Knake N, Graham L M, Reuter S, Schulz-von der Gathen V and Gans T 2010 *Plasma Sourc. Sci. Tech.* **19** 045018

[206] Shimizu T, Sakiyama Y, Graves D B, Zimmermann J L and Morfill G E 2012 *New Journal of Physics* **14** 103028

[207] Tian W and Kushner M J 2014 *Journal of Physics D: Applied Physics* **47** 165201

[208] Reuter S, Winter J, Schmidt-Bleker A, Tresp H, Hammer M U and Weltmann K D 2012 *IEEE Transactions on Plasma Science* **40** 2788

[209] Reuter S, Winter J, Iseni S, Schmidt-Bleker A, Dünnbier M, Masur K, Wende K and Weltmann K 2014 *IEEE Transaction on Plasma Science*

[210] Iséni S, Reuter S and Weltmann K D 2014 *Journal of Physics D: Applied Physics* **47** 075203

[211] Normand E, McCulloch M, Duxbury G and Langford N 2003 *Optics Letters* **16** 16

[212] Röpcke J, Davies P B, Lang N, Rousseau A and Welzel S 2012 *Journal of Physics D: Applied Physics* **45** 423001

[213] Rothman L, Gordon I, Barbe A, Benner D, Bernath P, Birk M, Boudon V, Brown L, Campargue A, Champion J P, Chance K, Coudert L, Dana V, Devi V, Fally S, Flaud J M, Gamache R, Goldman A, Jacquemart D, Kleiner I, Lacome N, Lafferty W, Mandin J Y, Massie S, Mikhailenko S, Miller C, Moazzen-Ahmadi N, Naumenko O, Nikitin A, Orphal J, Perevalov V, Perrin A, Predoi-Cross A, Rinsland C, Rotger M, Šimečková M, Smith M, Sung K, Tashkun S, Tennyson J, Toth R, Vandaele A and Vander Auwera J 2009 *Journal of Quantitative Spectroscopy and Radiative Transfer* **110** 533

[214] neoplas control GmbH, Q-MACSoft Monitor software, version 1.2.8.929, 2011, http://www.neoplas-control.de/

[215] neoplas control GmbH, Q-MACSoft HT software, version 1.2.8.929, 2011, http://www.neoplas-control.de/

[216] Van Gaens W, Bruggeman P J and Bogaerts A 2014 *New Journal of Physics* **16** 063054

[217] Lu X, Laroussi M and Puech V 2012 *Plasma Sources Science and Technology* **21** 034005

[218] Dünnbier M, Schmidt-Bleker A, Winter J, Wolfram M, Hippler R, Weltmann K-D and Reuter S 2013 *Journal of Physics D: Applied Physics* **43** 435203

[219] Iséni S, Zhang S, van Gessel A F H, Hofmann S, van Ham B T J, Reuter S, Weltmann K D and Bruggeman P J 2014 *New Journal of Physics*, *submitted*

[220] Iseni S, Schmidt-Bleker A, Winter J, Weltmann K D and Reuter S 2014 *Journal of Physics D: Applied Physics* **47** 152001

[221] Shimizu T, Sakiyama Y, Graves D B, Zimmermann J L and Morfill G E 2012 *New J. Phys.* **14** 103028

[222] Phelps A `ftp://jila.colorado.edu/collision_data`

[223] Petrov G M, Giuliani J L and Dasgupta A 2002 *J. Appl. Phys.* **91** 2662

[224] Rapp D and Englander-Golden P 1965 *J. Chem. Phys.* **43** 1464

[225] Bogaerts A, Gijbels R and Vlcek J 1998 *J. Appl. Phys.* **84** 121

[226] Bacri J and Medani A 1982 *Physica B+C* **112** 101

[227] Vriens L 1964 *Phys. Lett.* **8** 260

[228] Biondi M A 1976 *Principles of laser plasmas* (Chichester, Sussex, UK: Wiley) p xvii+695

[229] Kannari F, Obara M and Fujioka T 1985 *J. Appl. Phys.* **57** 4309

[230] Itikawa Y and Ichimura A 1990 *J. Phys. Chem. Ref. Data* **19** 637

[231] Laher R R and Gilmore F R 1990 *J. Phys. Chem. Ref. Data* **19** 277

[232] Deutsch H, Scheier P, Becker K and Märk T 2003 *Chem. Phys. Lett.* **382** 26

[233] Itikawa Y, Ichimura A, Onda K, Sakimoto K, Takayanagi K, Hatano Y, Hayashi M, Nishimura H and Tsurubuchi S 1989 *J. Phys. Chem. Ref. Data* **18** 23

[234] Krishnakumar E and Srivastava S 1992 *Int. J. Mass Spectrom.* **113** 1

[235] Schulz G 1962 *Phys. Rev.* **128** 178

[236] Burrow P D 1973 *J. Chem. Phys.* **59** 4922

[237] Hall R I and Trajmar S 1975 *J. Phys. B* **8** L293

[238] Jacobs H, Miethke F, Rutscher A and Wagner H E 1996 *Contrib. Plasma Phys.* **36** 471

[239] Matejcik S, Kiendler A, Cicman P, Skalny J, Stampfli P, Illenberger E, Chu Y, Stamatovic A and Märk T D 1997 *Plasma Sourc. Sci. Tech.* **6** 140

[240] Geltman S 1973 *J. Quant. Spectrosc. Radiat. Transf.* **13** 601

[241] Henry R, Burke P and Sinfailam A L 1969 *Phys. Rev.* **178** 218

[242] Smith A, Caplinger E, Neynaber R, Rothe E and Trujillo S 1962 *Phys. Rev.* **127** 1647

[243] Itikawa Y, Hayashi M, Ichimura A, Onda K, Sakimoto K, Takayanagi K, Nakamura M, Nishimura H and Takayanagi T 1986 *J. Phys. Chem. Ref. Data* **15** 985

[244] Tabata T, Shirai T, Sataka M and Kubo H 2006 *At. Data and Nucl. Data Tables* **92** 375

[245] Ton-That D and Flannery M 1977 *Phys. Rev. A* **15** 517

[246] Josić L, Wróblewski T, Petrović Z, Mechlinska-Drewko J and Karwasz G 2001 *Chem. Phys. Lett.* **350** 318

[247] Rapp D and Briglia D D 1965 *J. Chem. Phys.* **43** 1480

[248] Lindsay B G, Mangan M A, Straub H C and Stebbings R F 2000 *J. Chem. Phys.* **112** 9404

[249] Sakai Y, Okumura T and Tagashira H 1995 *Aust. J. Phys.* **48** 419

[250] Hayashi M and Niwa A 1987 Gaseous Dielectrics V ed Christophorou L G Bouldin D W (New York: Pergamon) p 27

[251] Banks P 1966 *Planet. Space Sci.* **14** 1085

[252] Itikawa Y 1971 *Planet. Space Sci.* **19** 993

[253] Janev R K, Reiter D and Samm U 2003 *Collision Processes in Low-Temperature Hydrogen Plasmas* Technical report Forschungszentrum Juelich GmbH

[254] Hayashi M 1979 *J. Phys. Colloques* **40** C7–45

[255] Corrigan S J B 1965 *J. Chem. Phys.* **43** 4381

[256] Chan C F 1983 *Reaction cross-sections and rate coefficients related to the production of positive ions* Lawrence Berkeley Laboratory Report No. LBID-632

[257] Tawara H, Itikawa Y, Nishimura H and Yoshino M 1990 *J. Phys. Chem. Ref. Data* **19** 617

[258] Jain A and Norcross D 1992 *Phys. Rev. A* **45** 1644

[259] Riahi R, Teulet P, Ben Lakhdar Z and Gleizes A 2006 *Eur. Phys. J. D* **40** 223

[260] Pedersen H, Djurić N, Jensen M, Kella D, Safvan C, Schmidt H, Vejby-Christensen L and Andersen L 1999 *Phys. Rev. A* **60** 2882

[261] Nandi D, Krishnakumar E, Rosa A, Schmidt W F and Illenberger E 2003 *Chem. Phys. Lett.* **373** 454

[262] Hayashi M 1990 Nonequilibrium Processes in Partially Ionized Gases (NATO Advanced Science Institutes Series, Series B, Physics vol 220) ed Capitelli M and Bardsley J N (New York: Plenum) 333

[263] Tarnovsky V, Deutsch H and Becker K 1997 *Int. J. Mass Spectrom.* **167-168** 69

[264] Gudmundsson J T and Thorsteinsson E G 2007 *Plasma Sourc. Sci. Tech.* **16** 399

[265] Arakoni R A, Bhoj A N and Kushner M J 2007 *J. Phys. D: Appl. Phys.* **40** 2476

[266] Zhao G B, Argyle M D and Radosz M 2006 *J. Appl. Phys.* **99** 113302

[267] Kannari F, Suda A, Obara M and Fujioka T 1983 *IEEE J. Quantum Electron.* **19** 1587

[268] Xu X P, Rauf S and Kushner M J 2000 *J. Vac. Sci. Technol. A* **18** 213

[269] Sankaran A and Kushner M J 2002 *J. Appl. Phys.* **92** 736

[270] Chen H L C 2008 *Investigation on Performance Enhancement of Non-thermal Plasma with the Assistance of Numerical Simulation* Ph.D. thesis National Taiwan University

[271] Shul R J, Passarella R, Upschulte B L, Keesee R G and Castleman a W 1987 *J. Chem. Phys.* **86** 4446

[272] Keto J W 1981 *J. Chem. Phys.* **74** 4433

[273] Arakoni R A 2007 *Simulation of flowing plasma discharges with applications to lasers, fuel cells, and microthrusters* Ph.D. thesis University of Illinois

[274] Pasquiers S *Personal communication*

[275] Avtaeva S V, General A A and Kel'man V A 2010 *J. Phys. D: Appl. Phys.* **43** 315201

[276] Ferguson E E 1973 *At. Data and Nucl. Data Tables* **12** 159

[277] Demore W B, Margitan J J, Molina M J, Watson R T, Golden D M, Hampson R F, Kurylo M J, Howard C J and Ravishankara A R 1985 *Int. J. Chem. Kinet.* **17** 1135

[278] Dorai R 2002 *Modeling of atmospheric pressure plasma processing of gases and surfaces* Ph.D. thesis University of Illinois

[279] Eichwald O, Guntoro N A, Yousfi M and Benhenni M 2002 *J. Phys. D: Appl. Phys.* **35** 439

[280] Soloshenko I A, Tsiolko V V, Pogulay S S, Terent'yeva A G, Bazhenov V Y, Shchedrin a I, Ryabtsev a V and Kuzmichev a I 2007 *Plasma Sourc. Sci. Tech.* **16** 56

[281] Xu X 2000 *Dynamics of high- and low-pressure plasma remediation* Ph.D. thesis University of Illinois

[282] Soloshenko I, Tsiolko V, Khomich V, Bazhenov V, Ryabtsev A, Schedrin A and Mikhno I 2002 *IEEE Trans. Plasma Sci.* **30** 1440

[283] NIST Chemical Kinetics Database, Standard Reference Database 17, Version 7.0 (Web Version), Release 1.6.5 `http://kinetics.nist.gov/kinetics/`

[284] Moreau N, Pasquiers S, Blin-Simiand N, Magne L, Jorand F, Postel C and Vacher J R 2010 *J. Phys. D: Appl. Phys.* **43** 285201

[285] Moravej M, Yang X, Barankin M, Penelon J, Babayan S E and Hicks R F 2006 *Plasma Sourc. Sci. Tech.* **15** 204

[286] Magne L, Pasquiers S, Blin-Simiand N and Postel C 2007 *J. Phys. D: Appl. Phys.* **40** 3112

[287] Anderson W R, Mcquaid M J, Nusca M J and Kotlar A J 2010 *A Detailed, Finite-Rate, Chemical Kinetics Mechanism for Monomethylhydrazine-Red Fuming Nitric Acid Systems* U.S. Army Research Laboratory Report

[288] Konnov A 2009 *Combust. Flame* **156** 2093

[289] Raud J, Laan M and Jõgi I 2011 *J. Phys. D: Appl. Phys.* **44** 345201

[290] Blin-Simiand N, Jorand F, Magne L, Pasquiers S, Postel C and Vacher J R 2008 *Plasma Chem. Plasma Proc.* **28** 429

[291] Goswami M, Volkov E N, Konnov A A, Bastiaans R and de Goey L 2008 *Updated Kinetic Mechanism for NOx Prediction and Hydrogen Combustion Milestone M2.2* Report Technical University of Eindhoven

[292] Vranckx S, Peeters J and Carl S A 2008 *Atmos. Chem. Phys.* **8** 6261

[293] Smith G P, Golden D M, Frenklach M, Moriarty N W, Eiteneer B, Goldenberg M, Bowman T C, Hanson R K, Song S, Gardiner W C, Lissianski V V and Qin Z GRI-Mech 3.0 `http://www.me.berkeley.edu/gri_mech/`

[294] van den Berg A, Dentener F and Lelieveld J 2000 *J. Geophys. Res.* **105** 11671

[295] Velazco J E, Kolts J H and Setser D W 1978 *J. Chem. Phys.* **69** 4357

[296] Sadeghi N, Setser D W, Francis A, Czarnetzki U and Döbele H F 2001 *J. Chem. Phys.* **115** 3144

[297] Magne L, Pasquiers S, Gadonna K, Jeanney P, Blin-Simiand N, Jorand F and Postel C 2009 *J. Phys. D: Appl. Phys.* **42** 165203

[298] Trevor P L and Barker J R 1981 *Int. J. Chem. Kinet.* **13** 1163

[299] Dunkin D B 1970 *J. Chem. Phys.* **53** 987

[300] Hjartarson A T, Thorsteinsson E G and Gudmundsson J T 2010 *Plasma Sourc. Sci. Tech.* **19** 065008

[301] Bogaerts A and Gijbels R 2000 *J. Anal. At. Spectrom.* **15** 441

[302] Ho G H and Golde M F 1991 *J. Chem. Phys.* **95** 8866

[303] Gilles M K and Ravishankara A R 2000 *Phys. Chem. Chem. Phys.* **2** 4045

[304] McKendrick C B, Kerr E A and Wilkinson J P T 1984 *J. Phys. Chem.* **88** 3930

[305] Becker K, Haaks D and Tatarczyk T 1974 *Chem. Phys. Lett.* **25** 564

[306] Jowko A, Wnorowski K, Kowalczyk J and Wojciechowski K 2001 *Radiat. Phys. Chem.* **61** 27

[307] Shul R J, Passarella R, DiFazio L T, Keesee R G and Castleman A W 1988 *J. Phys. Chem.* **92** 4947

[308] Anicich V G 1993 *J. Phys. Chem. Ref. Data* **22** 1469

[309] Mellouki A, Le Bras G and Poulet G 1988 *J. Phys. Chem.* **92** 2229

[310] Kaiser E W and Wu C H 1977 *J. Phys. Chem.* **81** 1701

[311] Okada S, Tezaki A, Miyoshi A and Matsui H 1994 *J. Chem. Phys.* **101** 9582

[312] Meaburn G M and Gordon S 1968 *J. Phys. Chem.* **72** 1592

[313] Rosen S, Derkatch A, Semaniak J, Neau A, Al-Khalili A, Le Padellec A, Vikor L, Thomas R, Danared H, af Ugglas M and Larsson M 2000 *Faraday Discuss.* **115** 295; discussion 303

[314] Jensen M J, Bilodeau R C, Safvan C P, Seiersen K, Andersen L H, Pedersen H B and Heber O 2000 *The Astrophysical Journal* **543** 764

List of Publications

1. Bogaerts A, Aerts R, Snoeckx R, Somers W, **Van Gaens W**, Yusupov M and Neyts E 2012 'Modeling of plasma and plasma-surface interactions for medical, environmental and nano applications' *Journal of Physics: Conference Series* 399:012011

2. Zhang S, **Van Gaens W**, van Gessel B, Hofmann S, van Veldhuizen E, Bogaerts A and Bruggeman P J 2013 'Spatially resolved ozone densities and gas temperatures in a time modulated RF driven atmospheric pressure plasma jet: an analysis of the production and destruction mechanisms' *Journal of Physics D: Applied Physics* 46(20):205202

3. **Van Gaens W** and Bogaerts A 2013 'Kinetic modelling for an atmospheric pressure argon plasma jet in humid air.' *Journal of Physics D: Applied Physics* 46(27):275201

4. Aerts R, Tu X, **Van Gaens W**, Whitehead J C and Bogaerts A 2013 'Gas purification by nonthermal plasma: a case study of ethylene' *Environmental Science and Technology* 47(12):6478

5. **Van Gaens W** and Bogaerts A 2014 'Reaction pathways of biomedically active species in an Ar plasma jet' *Plasma Sources Science and Technology* 23(3):035015

6. **Van Gaens W**, Bruggeman P J and Bogaerts A 2014 'Numerical analysis of the NO and O generation mechanism in a needle-type plasma jet' *New Journal of Physics* 16(6):063054

7. Vandenbroucke A, Aerts R, **Van Gaens W**, De Geyter N, Leys C, Morent R and Bogaerts A 'Modeling and experimental study of TCE abatement with a negative DC corona discharge', *submitted to Plasma Chemistry and Plasma Processing*

8. **Van Gaens W**, Iséni S, Schmidt-Bleker A, Weltmann K–D, Reuter S and Bogaerts A 'Numerical analysis of the effect of nitrogen and oxygen admixtures on the chemistry of an argon plasma jet operating at atmospheric pressure', *submitted to New Journal of Physics*

List of Conference Contributions

1. **Van Gaens W** and Bogaerts A (oral) 'Development of an $Ar/N_2/O_2/H_2O$ plasma chemistry for the numerical simulation of a plasma needle', European Plasma Conference HTPP-11, Brussels, Belgium, June 2010

2. **Van Gaens W** and Bogaerts A (poster) 'Influence of diffusive air components on a Ar plasma needle: numerical simulations', International Conference on Plasma Medicine 3 (ICPM 3), Greifswald, Germany, October 2010

3. **Van Gaens W** and Bogaerts A (oral) 'Numerical modeling of a plasmajet device: on the fluid dynamics and argon/humid air plasma chemistry', International Conference on Plasma Chemistry, Philadelphia, United States, July 2011

4. **Van Gaens W** and Bogaerts A (poster) 'Numerical simulations on a plasmajet device, focussing on the mixing of the argon discharge and humid air', International Conference on Phenomena in Ionized Gases (ICPIG 30), Belfast, United Kingdom, September 2011

5. **Van Gaens W** and Bogaerts A (poster) 'Numerical modelling on the topic of biomedical plasma applications at PLASMANT Research Group', COST Action Bioplasma Scientific Kickoff Meeting, Bari, Italy, February 2012

6. **Van Gaens W** and Bogaerts A (oral) 'Modelling of RF cold atmospheric pressure plasmajet in air', ChemCYS, Blankenberge, Belgium, March 2012

7. **Van Gaens W** and Bogaerts A (poster) 'Insight in the complex argon/humid air plasma chemistry, by means of numerical fluid modeling', International Conference on Plasma Medicine 4 (ICPM 4), Orléans, France, June 2012

8. **Van Gaens W** and Bogaerts A (oral) '(Bio)Plasma Chemistry', Leiden, The Netherlands, Plasma to Plasma workshop, January 2013

9. **Van Gaens W** and Bogaerts A (poster) 'Chemical kinetics modelling of argon atmospheric pressure plasma jets', International Conference on Phenomena in Ionized Gases (ICPIG 31), Granada, Spain, July 2013

10. **Van Gaens W** and Bogaerts A (oral) 'Chemical kinetics modeling of argon atmospheric pressure plasma jets', 2nd Young Professionals Workshop on Plasma-Medicine, Kolpinsee, Germany, September 2013

11. **Van Gaens W**, Bruggeman P and Bogaerts A (poster) 'Numerical analysis of NO and O generation in a needle-type plasma jet', International Conference on Plasma Medicine 5 (ICPM 5), Nara, Japan, May 2014

12. **Van Gaens W**, Bruggeman P and Bogaerts A (poster) 'Influence of H_2O impurities on RONS generation in a plasma jet', International Workshop on Diagnostics and Modelling for Plasma Medicine (DMPM2014), Nara, Japan, May 2014